# Formation of Supermassive Black Hole Seeds in the First Galaxies

# Formation of Supermassive Black Hole Seeds in the First Galaxies

a dissertation presented
by
Fernando Becerra
to
The Department of Astronomy

in partial fulfillment of the requirements
for the degree of
Doctor of Philosophy
in the subject of
Astronomy and Astrophysics

Harvard University
Cambridge, Massachusetts
May 2018

# Formation of Supermassive Black Hole Seeds in the First Galaxies


## Abstract

Frontier observations of quasars at redshifts $z \gtrsim 6$ suggest the existence of supermassive black holes of masses $\simeq 10^9\,\mathrm{M}_\odot$ when the Universe was less than a billion years old. These objects most likely grew from smaller black hole seeds, although the origin of these seeds still remains unclear. We investigate the process of formation and evolution of supermassive black hole seeds in the first galaxies. First, we perform the highest-resolution hydrodynamical simulation to date to analyze the formation of a supermassive protostar of $\simeq 0.1\,\mathrm{M}_\odot$ at the center of an atomic cooling halo. We show that, although the gas fragments and forms a protostellar system, the system still accretes mass at rates high enough to become a massive black hole seed within a few hundred thousand years. Unfortunately, due to the high resolution achieved, these simulations become prohibitively expensive after $\simeq 20\,\mathrm{yr}$ and we are not able to follow its development at later times. Instead, we describe the subsequent evolution using analytical methods and a one-zone model. We deduce a mass-radius relation for the growth of the protostar and utilize such relation to derive a sub-grid recipe for the accretion radius of sink particles in numerical simulations. Then, we use this sub-grid

model in cosmological simulations where the maximum resolution has been limited in order to follow the growth of the protostar for a longer time. We present a suite of six simulations using three different thresholds for the resolution and two methods to model the central object. Using this approach, we describe the early, intermediate, and late stages of the buildup of black hole seeds, from its formation as a massive protostar of $\simeq 10\,\mathrm{M}_{\odot}$ and until it becomes a massive black hole seed of $\simeq 10^5\,\mathrm{M}_{\odot}$. Finally, we complement this picture by adding the effect of radiative feedback from the central source in the surrounding gas. We outline the implementation of the radiative transfer equations in our hydrodynamical simulations and show preliminary results of our calculations. Fully coupled radiation-hydrodynamical simulations will give us a complete description of the assembly of supermassive black hole seeds in the early Universe.

# Contents

In loving memory of Elisa del Carmen Araya Cortés

# Acknowledgments

Almost six years have passed since I started graduate school at Harvard. It has been a period full of challenges, both academically and personally, and rich experiences that have made me grow as a person. Now that I am about to finish, I look back and realize that most of what I learned did not come from what I did, but from the people I met. I am grateful to every single person that shared time with me, doing science, drinking tea, playing fútbol, eating asados, watching movies, talking, or just hanging out. They all contributed to this dissertation and this achievement is also theirs.

I am deeply grateful to Lars Hernquist, my advisor, for being so supportive, for reading every single document I sent him, for writing recommendation letters, for encouraging me to attend conferences, for the moments at wine and cheese, and many other reasons. He was the one who dropped by my office accompanied by a new postdoc in the group at that time, and suggested that I should start working with him. That was the beginning of the process that led to this dissertation. I would also like to thank Volker Bromm, who selflessly accepted to be my co-advisor in the last few years, for helping me in the always difficult process of doing research, for hosting me every time I visited Austin, and for encouraging me to give always the best of me.

I would also like to mention the postdocs I collaborated with: Thomas Greif, who taught me how to do excellent science during the early years of my PhD and gave me the initial motivation to start working on the exciting topic of formation of supermassive black hole seeds; Federico Marinacci, who helped me in dealing with AREPO and always gave me feedback on the papers we co-authored; Kohei Inayoshi, who contributed to improve the primordial chemistry network; and Rahul Kannan, who is helping me to implement radiative feedback in our simulations. Finally, I am thankful to my thesis committee: Edo Berger, Daniel Eisenstein, and Avi Loeb, for providing guidance, and Anna Frebel, for agreeing to be the external reader.

I am also indebted to the whole CfA community for making these years an unforgettable experience. My classmates, the climbing group, the hiking group, the movie group, my office neighbors: Kate Alexander, Jenny Bergner, Pierre Christian, Hannah Diamond-Lowe, Marion Dierickx, Anastasia Fialkov, Xinyi Guo, Harshil Kamdar, Luke Kelley, Amber Medina, Philip Mocz, Roxana Pop, Stephen Portillo, and Yuan-Sen Ting. To the Hernquist group and all the people who have been part of it, including Annalisa Pillepich, Laura Sales, and Sarah Wellons. To the rest of the graduate students body, who play a really important part on making the department a nice place to work. To the CfA football group, especially Iouli Gordon, Rafael Martínez, and Gonzalo González, for those fútbol games at the QRAC and Danehy Park. To the administrative staff: Robb Scholten, Peg Herlihy, Nina Zonnevylle, and Lisa Catella, for running the department so smoothly and for being such wonder-

ful human beings. To all the other people working at the CfA, including Jesús with whom I commented fútbol matches almost every day.

Thanks to Mia for hosting me in her nice place and for being the best landlady ever. Thanks to the "Chilean" gang in Boston for all the moments of happiness and laughter: David Albrecht, Manuel Bugueño, Fernanda Cerda, Ricardo Faúndez, Joe Fournier, Viviana Guzmán, Gastón Keller, Alexandra Pontefract, Camila Rasner, Mike Rasner, and Nomi Zuckerman. Thanks to all the people who are not in Boston, because distance has only strengthened our friendship: my friends from Cerro Calán, including Nicola Astudillo, Claudia Avendaño, and Fernando Olguín; my College friends, including Lisset Manzano and Natalia Zúñiga; and my high school friends, including Felipe Antimán, César Casanova, Felipe Mancilla, Pablo Muñoz, Héctor Pérez, Kenneth Reese, Sebastián Román, Javier Sánchez, and Héctor Sotomayor.

Special thanks go to Jieun Choi, Natalia Cornejo, and Karen Pérez de Arce. I do not have words to express how grateful I am of your help and support. You were there for me when I needed it most, and I could not have done it without you.

To my parents, Fernando Becerra and Nilda Saavedra, and my brothers, Álex Becerra y Jaime Becerra. They have always been there supporting me, encouraging me, and trusting in me. If it were not because of you, I would not be here.

To Katy Newlin, for being such an amazing and lovely person. Thank you for being yourself. Thank you from the bottom of my heart.

# Author List

The following authors contributed to Chapter 2:
Thomas H. Greif
Volker Springel
Lars E. Hernquist

The following authors contributed to Chapter 3:
Federico Marinacci
Kohei Inayoshi
Volker Bromm
Lars E. Hernquist

The following authors contributed to Chapter 4:
Federico Marinacci
Volker Bromm
Lars E. Hernquist

The following authors contributed to Chapter 5:
Federico Marinacci
Rahul Kannan
Volker Bromm
Lars E. Hernquist

*¿Cómo y por qué llegué hasta allí? Por los mismos motivos por los que he llegado a tantas partes.*

Manuel Rojas

# 1 Introduction

## 1.1 The first billion years

Reconstructing the whole history of the Universe is an extremely challenging task. Hints provided by powerful ground- and space-based telescopes have shed light into the early moments, allowing scientists to come up with a rough picture of the Universe from the Big Bang to the present day, depicted in Figure 1.1. The earliest ob-

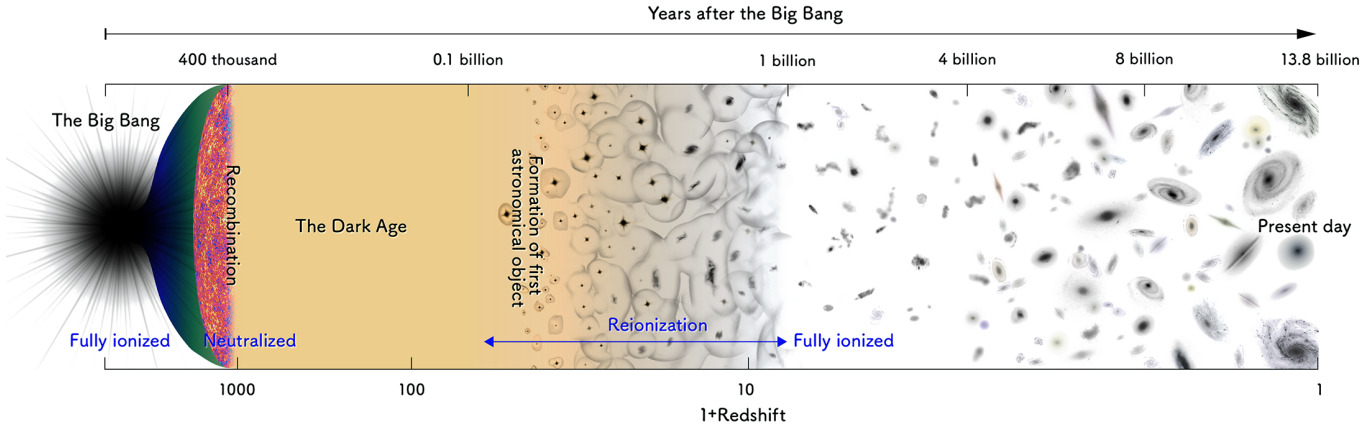


**Figure 1.1:** History of the Universe from the Big Bang to the present day. For a few hundred thousand years after the Big Bang, the cosmic hydrogen is fully ionized and the Universe is opaque to electron scattering. Around 300,000 years after the beginning of the Universe, the temperature drops and electrons and protons are able to attract each other and form hydrogen, a process called recombination. The Universe enters then a period of darkness that is not visible to the human eye, the so-called dark ages. The first stars are thought to form during this time at redshifts around $z \simeq 15 - 30$, followed by the formation of the first galaxies at $z \simeq 10 - 20$. Strong radiative feedback form the first luminous objects start reionizing the Universe, in what is called the Epoch of Reionization. This epoch extends between $z \simeq 6 - 15$ and marks the transition to an era where baryonic matter plays a prominent role in structure formation and evolution. (Credits: NAOJ; inverted from original.)

servational signature detected so far is located about 300000 years after the Big Bang and is known as the cosmic microwave background (CMB, Spergel et al. 2003; Planck Collaboration et al. 2014, 2016). Before that, the cosmic hydrogen was fully ionized and the Universe was opaque to scattering by free electrons. Around that time the temperature dropped below a few thousand degrees Kelvin, under which conditions electrons and protons moved more slowly and attracted each other to form hydrogen, a process known as recombination. As a consequence, scattering of energetic photons was highly reduced and photons decoupled from baryonic matter. The photons that were last scattered continued traveling in a straight line, only affected by cosmic expansion. As a result, their wavelength shifted to the microwave regime, leaving the CMB as a relic signature of the epoch of last scattering at redshift $z \simeq 1100$.

The next set of deep observations of distant galaxies (Lehnert et al. 2010; Oesch et al. 2016), quasars (Fan et al. 2006; Mortlock et al. 2011; Bañados et al. 2018), and gamma-ray bursts (Tanvir et al. 2009; Salvaterra et al. 2009) takes us to when the Universe was less than a billion years old . At that moment the Universe is composed by stars, galaxies, and even supermassive black holes. This epoch is characterized by strong radiative and mechanical feedback from the first objects that reionize the Universe, known as the epoch of reionization (EoR). The current constraints locate the EoR within the redshift range $z \simeq 6 - 15$. Initially during the EoR, the intergalactic medium (IGM) is neutral everywhere, except in the regions around the first objects. As reionization progresses, an evolving patchwork of neutral (HI) and ionized (HII)

hydrogen unfolds, and, once a sufficient number of radiation sources form, the ionized regions permeate to fill the whole Universe. This process provides an important milestone: it marks the transition to an era in which the role of baryonic matter in the formation and evolution of structures becomes prominent.

Between the CMB and the beginning of the EoR, the Universe enters a period where it is completely dark to the human eye, the so-called dark ages. Very little is known about this gap of several hundred thousand years, except by the fact that this is when the first stars form, and the first generation of galaxies and supermassive black holes (SMBHs) are assembled. The anisotropies of the CMB provide essential information about the initial conditions for the formation of all these cosmic structures. In the current standard model of cosmology, so-called Lambda Cold Dark Matter ($\Lambda$CDM), structures form hierarchically through mergers of smaller DM halos into increasing larger ones. The first "dark" objects are defined as halos with no star formation and of very small masses, set by the initial thermal motion of DM particles. The formation of the first luminous objects is much more complicated and requires a variety of physical processes in addition to gravity. In particular, the first generation of stars formed out of pristine gas constituted only by hydrogen and helium. These objects completely transformed the early Universe through strong radiative and supernova (SN) feedback: the buildup of HII regions around stars initiate the process of cosmic reionization, while explosions of SNe disperse heavy elements into the IGM. Both reionization and the enrichment of primordial gas with metals play a crucial role

in the assembly of the first galaxies and the later evolution of the Universe. Therefore, the properties of the subsequent generation of stars, the first galaxies, as well as the first SMBHs are likely to be shape in large part by the first generation of stars.

## 1.2 The first stars

On large scales the Universe appears nearly uniform and isotropic, but stars and galaxies suggest that they grew from deviations from its uniformity. The first stars are expected to be formed in halos where the primordial density field was randomly enhanced over the surrounding matter. These perturbations were amplified by gravity and, once overdensities become large enough, they decoupled from the background and collapsed under its own gravity. The collapse occurred in many dimensions, leading to the formation of sheets in one dimension, filaments when two sheets collapsed, and DM halos at the intersection of filaments. The first stars are expected to form in so-called minihalos – halos of masses $\simeq 10^6\,\mathrm{M}_\odot$ that collapsed at redshifts $z \simeq 20 - 30$. In those halos gas is entrained with the dynamically dominant DM component and reaches a state of 'virial equilibrium', characterized by the balance of gravitational potential and kinetic energy:

$$\frac{GM_{\rm vir}}{R_{\rm vir}} \sim v_{\rm vir}^2, \tag{1.1}$$

where $M_{\rm vir}$ is the mass of the halo, $v_{\rm vir}$ the virial velocity, and $R_{\rm vir}$ the virial radius given by

$$R_{\rm vir} \simeq 100\,{\rm pc} \left(\frac{M_{\rm vir}}{10^6\,{\rm M}_\odot}\right)^{1/3} \left(\frac{1+z}{20}\right)^{-1}. \tag{1.2}$$

As a consequence of the collapse, the gas heats up to the virial temperature $T_{\rm vir} \sim m_{\rm H} v_{\rm vir}/k_{\rm B}$, where $m_{\rm H}$ is the mass of the hydrogen atom and $k_{\rm B}$ the Boltzmann constant. Following Equations 1.1 and 1.2, this can be rewritten as

$$T_{\rm vir} \simeq 2 \times 10^3\,{\rm K} \left(\frac{M_{\rm vir}}{10^6\,{\rm M}_\odot}\right)^{2/3} \left(\frac{1+z}{20}\right). \tag{1.3}$$

For a typical minihalo, gas temperatures are below the threshold $\simeq 10^4\,{\rm K}$ for efficient cooling due to atomic hydrogen. Hence, in order to collapse and form a hydrostatic object, the gas needs to rely in a different cooling mechanism to radiate away its thermal energy. As suggested by Saslaw & Zipoy (1967), such coolant may be molecular hydrogen ($H_2$). In primordial star formation, the most important $H_2$ formation channel is via the intermediary reaction of radiative association of free electrons with neutral hydrogen atoms (McDowell 1961; Peebles & Dicke 1968)

$$H + e^- \rightarrow H^- + \gamma, \tag{1.4}$$

followed by the associative detachment of the $H^-$ atoms with neutral hydrogen atoms:

$$\mathrm{H} + \mathrm{H}^- \rightarrow \mathrm{H}_2 + \mathrm{e}^-. \tag{1.5}$$

The process of primordial star formation begins with an initial collapse where gas is heated via adiabatic compression until it reaches a density $n_{\mathrm{H}} \simeq 1\,\mathrm{cm}^{-3}$, achieving temperatures $T \simeq 1000$ K, which are of the order of the virial value. The gas then cools through $\mathrm{H}_2$ ro-vibrationals transitions to a minimum temperature $T \simeq 200\,\mathrm{K}$ at densities $n_{\mathrm{H}} \simeq 10^4\,\mathrm{cm}^{-3}$. At this point, the Jeans mass can be estimated as $M_{\mathrm{J}} \sim c_{\mathrm{s}}^3 G^{-2/3} \rho^{-1/2}$ with $c_{\mathrm{s}}$ the baryonic sound speed and $\rho$ the total gas density, or, analogously, as:

$$M_{\mathrm{J}} \simeq 500\,\mathrm{M}_\odot \left(\frac{T}{200\,\mathrm{K}}\right)^{3/2} \left(\frac{n_{\mathrm{H}}}{10^4\,\mathrm{cm}^{-3}}\right)^{-1/2}, \tag{1.6}$$

which sets the mass scale of a Pop III-equivalent to a pre-stellar core. Once this mass is accreted, the cloud collapses under its own gravity and gas temperature increases due to compressional heating until $n_{\mathrm{H}} \simeq 10^8\,\mathrm{cm}^{-2}$. At that point three-body processes become important, converting most atomic gas to molecular hydrogen. $\mathrm{H}_2$ cooling, first as line emission up to $n_{\mathrm{H}} \simeq 10^{10}\,\mathrm{cm}^{-3}$ and then as collision induced emission for $n_{\mathrm{H}} \gtrsim 10^{14}\,\mathrm{cm}^{-3}$, allows the gas to reach temperatures $\gtrsim 2000\,\mathrm{K}$ at $n_{\mathrm{H}} \simeq 10^{16}\,\mathrm{cm}^{-3}$. Then, collisional dissociation of $\mathrm{H}_2$ reverts the previous three-body formation process and the temperature rises steeply with increasing density. At $n_{\mathrm{H}} \simeq 10^{20}\,\mathrm{cm}^{-3}$, collapse stalls and an accretion shock forms that heats up the gas to $\gtrsim 10^4$ K (Omukai & Nishi 1998; Yoshida et al. 2008), marking the formation of a protostar with initial

mass of $\simeq 10^{-2}\,\mathrm{M}_{\odot}$ at the center of the cloud.

One of the main parameters that govern the final masses of the first stars is the accretion rate. The growth of the protostar can be estimated by assuming that a Jeans mass worth of gas collapses on its free-fall timescale (Shu 1977):

$$\dot{M} \sim \frac{M_{\mathrm{J}}}{t_{\mathrm{ff}}} \sim \frac{c_{\mathrm{s}}^3}{G} \propto T^{3/2}. \tag{1.7}$$

Evaluating this expression when the gas first becomes gravitationally unstable, i.e. when $T \simeq 200$ K and $n_{\mathrm{H}} \simeq 10^4\,\mathrm{cm}^{-3}$, gives an estimated accretion rate of $\dot{M} \simeq 10^{-3}\,\mathrm{M}_{\odot}\,\mathrm{yr}^{-1}$, which is roughly 100 times higher than the values in present-day star-forming regions. Omukai & Nishi (1998) estimated the final mass using the self-similar solution for a spherically symmetric infall problem, obtaining $M_{\star} \simeq 500\,\mathrm{M}_{\odot}$ after $10^5$ yrs. However, stellar radiation can influence this evolution by dissociating $\mathrm{H}_2$ and heating up the surrounding gas. When accounting for those effects, the resulting masses are in the range $10 - 1000\,\mathrm{M}_{\odot}$ (Hirano et al. 2014; Susa et al. 2014). Furthermore, secondary protostars created by fragmentation shortly after the formation of the first protostar may accrete material in the surrounding envelope before they reach the cloud center and reduce even more the mass of the central protostar. In that case, after a few hundred years, the final masses of the protostars range from $\simeq 0.02$ to $\simeq 10\,\mathrm{M}_{\odot}$, and are characterized by a flat initial mass function, implying that most of the mass is locked up in high-mass protostars (Clark et al. 2008; Greif et al. 2011).

## 1.3 The first galaxies

Before studying the first galaxies, we need to define what a 'first galaxy' is, but there is currently no agreement on that topic (Bromm & Yoshida 2011). From an observational perspective, the first galaxy might imply a search for galaxies either with zero metallicity or hosting predominantly primordial stars; however, most first galaxies could be already metal-enriched by SNe triggered by the first stars. From a theoretical point of view, to define a galaxy we require some ingredients: the presence of a DM halo hosting a long-lived stellar system, gas, and a DM potential well deep enough to retain gas that was heated to temperatures $\gtrsim 10^4$ K. Some models have proposed that minihalos hosting the first stars can be considered the first galaxies, which would require the initial mass function of primordial stars to be similar to the locally observed one in order to sustain star formation and effectively self-enrich. However, as discussed in the previous section, Pop III stars were predominantly massive and hence feedback from them is likely to shut off the potential for subsequent star formation.

Another theories suggest that DM halos with virial temperatures $\gtrsim 10^4$ K might be able to revirialize the gas affected by stellar feedback. At those temperatures, the onset of atomic hydrogen cooling occurs and hence these halos do not depend on the presence of molecular hydrogen to cool gas. In addition, these so-called atomic cooling halos have sufficiently deep potential wells to retain photoheated gas and allow the

existence of a self-sustained cycle of star formation and feedback. Using Equation 1.3, the corresponding relation between virial mass and temperature can be written as

$$M_{\rm vir} \simeq 5 \times 10^7 \, {\rm M}_\odot \left( \frac{T_{\rm vir}}{10^4 \, {\rm K}} \right)^{3/2} \left( \frac{1+z}{10} \right)^{-3/2} , \tag{1.8}$$

from which the characteristic virial mass of these halos is $M_{\rm vir} \simeq 10^7 - 10^8 \, {\rm M}_\odot$, with a typical formation redshift $\simeq 10 - 15$. This is the definition adopted in this dissertation, and hence the terms 'first galaxies' and 'atomic cooling halos' will refer indistinctly to the same objects in the following chapters.

## 1.4 The first supermassive black holes

The evidence suggesting that SMBHs play a crucial role in the formation and evolution of galaxies is overwhelming. Dynamical measurements indicate that SMBHs reside in the center of almost every massive galaxy (e.g., Kormendy & Ho 2013), and that there is a tight correlation between the mass of the central back hole (BH) and the stellar velocity dispersion in galaxy bulges in the local Universe (Ferrarese & Merritt 2000; Gebhardt et al. 2000). These observations favor a picture where BHs and their host galaxies co-exist and co-evolve. Although the masses of these BHs are less than 1% of the baryonic mass in the galaxy (Magorrian et al. 1998; Marconi & Hunt 2003; Häring & Rix 2004), they are a powerful source of feedback that suppresses star formation and contributes to the reionization of the Universe. Furthermore, recent

observations of quasars at redshift $z \gtrsim 6$ powered by SMBHs with masses $\gtrsim 10^9\,\mathrm{M}_\odot$ (e.g., Fan et al. 2003, 2006; Mortlock et al. 2011; Wu et al. 2015; Bañados et al. 2018) reveal that this has been the case since when the Universe was less than one billion years old. Therefore, understanding the physical processes governing the formation and growth of SMBHs is essential to answer fundamental questions about the formation and evolution of galaxies in the Universe.

The presence of SMBHs so early in the evolution of the Universe suggests that they most likely grew from smaller seed BHs formed at redshifts $\gtrsim 15$. The mass scale of these seeds can vary between 10 and $10^5\,\mathrm{M}_\odot$, depending on the formation mechanism and environment in which they were born. Their growth rate is mainly determined by intense accretion and merging until they reach a few billion solar masses. Although most BH seeds are expected grow at relatively modest rates, some of them may quickly grow due to accretion flows that feed material onto the seed. For example, to form a $\simeq 10^9\,\mathrm{M}_\odot$ SMBH at $z \simeq 7$, a seed of a few hundred solar masses should continuously accrete at the Eddington rate throughout its lifetime. Therefore, the existence of quasars at $z \gtrsim 6$ could be explained by the presence of massive seed BHs at $z \gtrsim 15$.

Many pathways have been proposed to explain the formation of these seeds in the literature, but their origin still remains unclear (Haiman 2006, 2009, 2013; Volonteri 2012; Volonteri & Bellovary 2012; Latif & Ferrara 2016). Figure 1.2 illustrates three of the most popular BH seeds formation scenarios: (i) the remnant of the first genera-

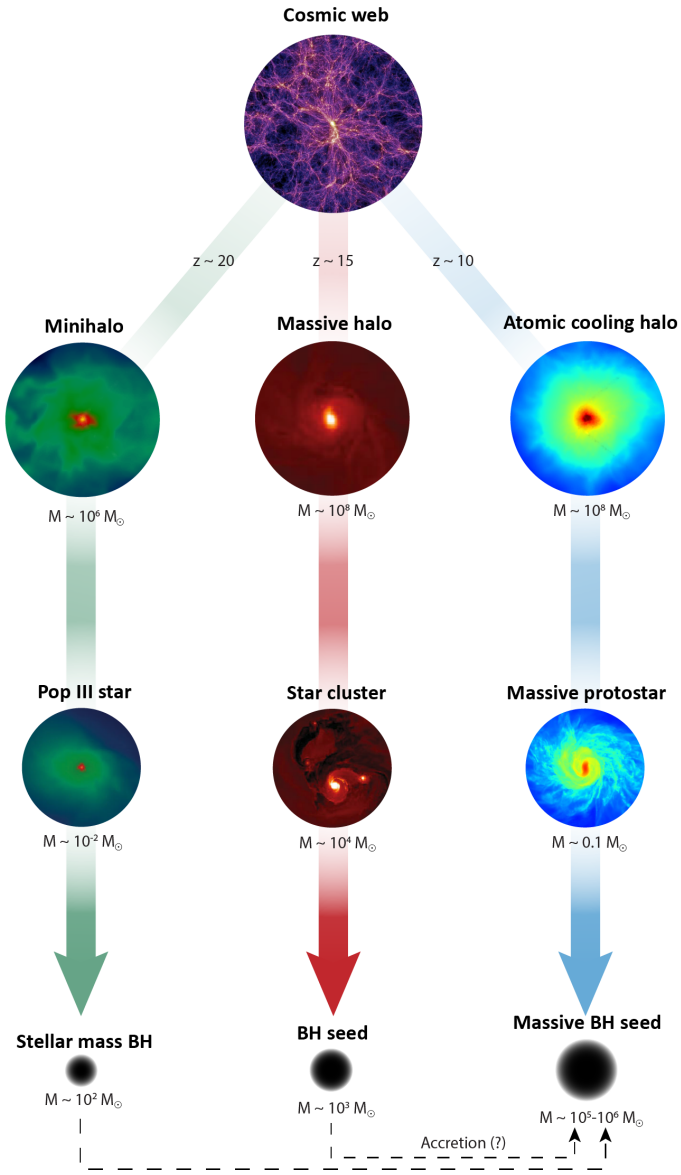


**Figure 1.2:** Pathways of massive black hole seeds formation. The three main theories concerning the formation MBH seeds in the early Universe are: remnants of Pop III stars (left), dynamical processes in stellar clusters (middle), and direct collapse of gas in atomic cooling halos (right). In the first case, the collapse of primordial stars in minihalos of masses $\simeq 10^8$ M$_\odot$ at redshifts $z \simeq 20$ can lead to the formation of stellar mass BHs of $M_\star \simeq 10^2$ M$_\odot$. In more massive, metal-enriched halos of $\simeq 10^8$ M$_\odot$ at $z \simeq 15$, dense stellar clusters can dynamically collapse to form BH seeds of $M_\star \simeq 10^3$ M$_\odot$. Finally, if molecular hydrogen is dissociated in a $10^8$ M$_\odot$ halo, gas can directly collapse and form a supermassive star, which then becoemes a massive BH seeds of $M_\star \simeq 10^5$ M$_\odot$. (Credits: Simulation images adapted from Springel et al. (2005); Greif et al. (2011); Becerra et al. (2015).)

tion (Pop III) stars (Madau & Rees 2001; Li et al. 2007; Johnson et al. 2012), (ii) the dynamical evolution of dense nuclear stellar clusters (Omukai et al. 2008; Devecchi & Volonteri 2009), and (iii) the direct collapse of metal-free gas in halos with virial temperatures $T_{\rm vir} \gtrsim 10^4$ K, the so-called atomic cooling halos (Bromm & Loeb 2003; Begelman et al. 2006; Spaans & Silk 2006).

### 1.4.1 Origin of SMBH seeds

#### Remnants of Pop III stars

It seems intuitive to think that SMBHs grow from remnants of the first stars. The final fate of low-metallicity, non-rotating Pop III stars will primarily depend on its mass: between $40 - 140\,{\rm M}_\odot$ they are expected to directly collapse into BHs to similar masses, below $\simeq 40\,{\rm M}_\odot$ a SN partially disrupts the star and a fraction of the star collapses into a BH, and for masses $\gtrsim 260\,{\rm M}_\odot$ the star directly collapses to a BH without any significant explosion (Heger et al. 2003). In order to reach the mass of the SMBH seeds at $z \simeq 7$, these BH seeds of a few hundred solar masses formed at redshifts $z \simeq 20 - 30$ should continuously grow at or above the Eddington limit. However, three-dimensional numerical simulations have shown that feedback from the progenitor star photo-evaporates the surrounding gas, thus halting accretion onto the star (Johnson & Bromm 2007; Alvarez et al. 2009). As a result, accretion rates are several orders of magnitude below the Eddington value, which makes their growth extremely

difficult and poses a serious complication of the Pop III stellar remnant scenario.

### Stellar clusters

An additional route for the formation of massive seeds is given by self-gravitating stellar systems with negative heat capacity. Those systems are susceptible to gravitational collapse when the core collapse timescale ($t_{\rm cc}$) is comparable to the two-body relaxation time (Binney & Tremaine 1987). An additional requirement is that the $t_{\rm cc}$ has to be shorter than the typical timescales for massive stars to reach the main sequence, otherwise mass loss from supernova may halt the collapse. The more compact the cluster, the shorter the core collapse timescale, implying that clusters with size $\lesssim$ 1 pc are the ideal places for this mechanism to occur. In the context of high-redshift BH formation, these dense stellar clusters are expected to form at $z \simeq 10-15$ in halos of masses $\simeq 10^8\,{\rm M}_\odot$ enriched by trace amount of metals (Omukai et al. 2008; Devecchi & Volonteri 2009). If core collapse proceeds unimpeded, higher stellar density at the center leads to runaway stellar collisions and the formation of a very massive star (VMS), which later may evolve via mergers or accretion to form a massive BH seed of $\lesssim 1000\,{\rm M}_\odot$.

### Direct collapse scenario

Another theory postulates that massive BH seeds of $10^5 - 10^6\,{\rm M}_\odot$ form as a result of large inflows of dense gas that collapses directly into a single massive object (Rees

1984; Loeb & Rasio 1994; Eisenstein & Loeb 1995; Bromm & Loeb 2003; Koushiappas et al. 2004; Begelman et al. 2006; Lodato & Natarajan 2006). A prerequisite is that gas should efficiently shed angular momentum and collapse rapidly to prevent fragmentation into stars. Additionally, large mass accretion rates of $\gtrsim 0.1\,\mathrm{M}_\odot\,\mathrm{yr}^{-1}$ are required for this formation mechanism to work (Begelman 2010; Hosokawa et al. 2013; Schleicher et al. 2013). Since the accretion rate scales as $\dot{M} \propto T^{3/2}$, both of these requirements (avoiding fragmentation and large accretion rates) can be achieved in a high-temperature environment where cooling has been inhibited, either by requiring no metals or preventing $H_2$ formation (Bromm & Loeb 2003; Volonteri et al. 2008; Regan & Haehnelt 2009).

In particular, this process can occur in massive metal-free halos with virial temperatures $\gtrsim 10^4$ K exposed to a substantial Lyman-Werner (LW) background that photo-dissociates $H_2$ (Omukai 2001; Bromm & Loeb 2003; Volonteri & Rees 2005; Spaans & Silk 2006; Schleicher et al. 2010), also known as atomic cooling halos. The destruction channel for molecular hydrogen can occur through the Salomon process, which involves absorption of photons with energies between $11.2 - 13.6$ eV that photo-dissociates $H_2$ shortly after putting it into an excited state:

$$\mathrm{H_2} + \gamma_{\mathrm{LW}} \rightarrow \mathrm{H} + \mathrm{H}. \tag{1.9}$$

In particular, massive stars with a hard spectrum of characteristic temperature $T_{\mathrm{rad}} =$

$10^5$ K are more efficient at photo-dissociating $H_2$ via this process. The complete quenching of $H_2$ requires a critical value of UV flux ($J_{21}^{crit}$) that might vary between $J_{21}^{crit} \simeq 30 - 10^5$, depending on the shape of the radiation spectrum, mode of star formation, and metallicity of stars (e.g. Omukai 2001; Johnson et al. 2013; Shang et al. 2010; Van Borm & Spaans 2013; Sugimura et al. 2014; Agarwal & Khochfar 2015). An intense background of UV radiation like that one could be supplied in a small subset of halos by a neighboring star-forming galaxy (e.g. Dijkstra et al. 2008; Agarwal et al. 2012).

In the absence of $H_2$ the gas is expected to undergo an isothermal monolithic collapse until it becomes optically thick to radiative cooling, from where it evolves adiabatically. If radiation pressure is strong enough to temporarily counteract gravity, a supermassive protostar forms at the center of the atomic cooling halo. From estimations using Equation 1.7, the expected accretion rate lies between $0.1 - 1\,M_\odot\,yr^{-1}$, which is a few orders of magnitude higher than in the case of gas in halos with efficient $H_2$ cooling (see Section 1.2). The outcome is a supermassive star (SMS) of $\simeq 10^5\,M_\odot$ within 1 Myr after its birth, which can then collapse directly into a seed BH of similar mass by post-Newtonian instabilities, a so-called direct collapse black hole (DCBH).

### 1.4.2 Growth of SMBH seeds

Once a massive BH seed has formed it needs to grow rapidly to match the observations of high-redshift quasars. Accretion of mass at the Eddington rate causes a black hole mass to increase in time as

$$M_{\rm BH}(t) = M_{\rm BH}(0) \exp\left(\frac{1-\epsilon}{\epsilon}\frac{t}{t_{\rm Edd}}\right), \tag{1.10}$$

where $t_{\rm Edd} = 0.45$ Gyr and $\epsilon$ is the radiative efficiency. For a standard radiative efficiency $\epsilon \sim 0.1$ and a seed mass $M_{\rm BH}(0) \simeq 10^2 - 10^5\,{\rm M}_\odot$, it takes at least 0.5 Gyr to grow to $\simeq 10^9\,{\rm M}_\odot$. Unfortunately, black holes are unlikely to accrete at the Eddington rate throughout its life; instead, its accretion rate is limited by both external and internal factors. For instance, external conditions determine how much gas is initially available to be accreted by the BH (Wise et al. 2008; Greif et al. 2008), while internal radiative feedback from the newly-born star itself can inhibit accretion (Pelupessy et al. 2007; Johnson & Bromm 2007). Given the limited amount of time that BH seeds have to grow to match the requirements set by $z \simeq 6$ observations, some authors have also explored early phases of super-critical accretion growth (e.g. Volonteri & Rees 2005). In general, there is encouraging consistency between the models of BH seed formation and growth, and the observational data from high-redshift quasars. Large scale cosmological simulations strengthen this picture: the masses of BH seeds

adopted in relatively low-resolution simulations are often consistent with the masses expected for seeds formed from the collapse of SMSs in the direct collapse model.

## 1.5 This dissertation

In this dissertation we study the process of formation and evolution of supermassive black hole seeds in the first galaxies, with a focus on the direct collapse scenario. In particular, we investigate the collapse of gas in atomic cooling halos in which formation of $H_2$ has been suppressed by a strong LW background radiation field. We use two methods to explore the stages in the evolution of these seeds: high-resolution three-dimensional numerical simulations and analytical models. Both approaches complement each other: the former provide a self-consistent picture of the assembly of SMBH seeds starting from cosmological initial conditions, while the latter can model processes that are not resolved by simulations. In this way we can get a full picture of how SMBH seeds formed and evolved in the early Universe. Each chapter of this dissertation is dedicated to different stages in the evolution of the seeds: formation of a massive protostar, properties of the protostar during its early growth, intermediate and late stages in the assembly of SMBH seeds, and the effect of radiative feedback in its evolution.

Chapter 2 explores the formation of a supermassive protostar at the center of an atomic cooling halo. For that, we use the highest-resolution three-dimensional sim-

ulation to date of the collapse of one of such halos. A key ingredient to model the different cooling processes involved in the assembly of these objects is the primordial chemistry network, which is evolved with a newly-introduced module in the moving-mesh code AREPO. Additionally, a strong LW background radiation field is introduced to suppress molecular hydrogen cooling. With this setup, we report the formation of a massive protostar at the center of the halo, with an initial mass of $\simeq 0.1\,\mathrm{M}_{\odot}$ and surrounded by a gas disk. The high resolution achieved by the simulations reveal for the first time the process of fragmentation of the disk and the formation of a proto-stellar system at small scales. After $\simeq 17$ yrs, the central protostar maintains a high accretion rate, suggesting that fragmentation is not a significant barrier for forming a massive black hole seed.

Following the evolution of the protostar for a longer period of time becomes prohibitively expensive due to the resolution achieved by such simulations. A complementary strategy to describe the early stages of these objects is to derive its properties using a theoretical approach. In Chapter 3 we develop an analytical model to characterize the early growth of supermassive protostars since their formation at $M_{\star} \simeq 0.1\,\mathrm{M}_{\odot}$ until they reach $M_{\star} \simeq 10^{5}\,\mathrm{M}_{\odot}$. For that purpose, first, we calculate the properties of the object at the moment of creation, when the gas becomes optically thick to $\mathrm{H}^{-}$ cooling, based on idealized thermodynamic considerations and a detailed one-zone model. The subsequent evolution of the protostar is mainly determined by accretion onto the object and can be describe by the relation $R_{\star} \propto M_{\star}^{1/3}$ during the

early stages, and $R_\star \propto M_\star^{1/2}$ once internal luminosity becomes dominant. We then employ this model to construct a sub-grid recipe for sink particles that can be used in future simulations that lack the power to resolve the central protostar.

In Chapter 4, we use the sub-grid recipe previously developed to study the intermediate and late stages of the assembly of SMBH seeds. For that purpose, we perform cosmological simulations of gas collapsing in atomic cooling halos with an improved primordial chemistry network. In order to follow the central object for a longer time, the simulations should not become too computationally expensive. One way to overcome this issue is to truncate the evolution of the gas above a certain threshold density, $n_{\rm th}$. We use two techniques to model the central object above such threshold: sink particles and an artificially-stiffened equation of state (EOS). We present a suite of six simulations using both approaches and three different values for $n_{\rm th}$ to explore the initial, intermediate, and late stages in the assembly of SMBH seeds. We report the growth of the central protostar from masses $\simeq 10\,{\rm M}_\odot$ to $\simeq 10^5\,{\rm M}_\odot$, with an average accretion rate of $\langle \dot{M}_\star \rangle \simeq 2\,{\rm M}_\odot\,{\rm yr}^{-1}$ for sink particles, and $\simeq 0.8 - 1.4\,{\rm M}_\odot\,{\rm yr}^{-1}$ for the stiff EOS. We further estimate how the emission coming from the central object, and subsequent development of an HII region, might affection its evolution. At the end of the runs, the HII region has long detached from the protostellar photosphere, but the ionizing radiation remains trapped in the inner host halo and has thus not yet escaped into the intergalactic medium.

A self-consistent description of how ionizing radiation might influence the growth

of the central object requires fully coupled radiation-hydrodynamics (RHD) simulations. We present the current implementation of RHD simulations of the formation of SMBH seeds in Chapter 5. In particular, we delineate the numerical methods employed to couple the radiative transfer equations to the hydrodynamics of the gas. We further describe how photons emitted by the central source are injected and transported in the surrounding gas, and how the absorption of such photons influence the chemical composition of the cells. Additionally, we show preliminary results of adding radiation to one of the sink particle simulations used for the previous chapter.

Finally, in Chapter 6, we draw conclusions from the work presented in this dissertation, and discuss what should be done in the future to get a full description of the formation and evolution of SMBH seeds in the early Universe.

*"El día en que lo iban a matar, Santiago Nasar*
*se levantó a las 5.30 de la mañana para esperar*
*el buque en que llegaba el obispo."*

Gabriel García Márquez

# 2

# Formation of massive protostars in atomic cooling haloes

This chapter has been published as

Becerra, F., Greif, T. H., Springel, V., & Hernquist, L. E. (2015). Formation of massive protostars in atomic cooling haloes. *MNRAS*, 446, 2380–2393.

ABSTRACT

We present the highest-resolution three-dimensional simulation to date of the collapse of an atomic cooling halo in the early Universe. We use the moving-mesh code AREPO with the primordial chemistry module introduced in Greif (2014), which evolves the chemical and thermal rate equations for over more than 20 orders of magnitude in density. Molecular hydrogen cooling is suppressed by a strong Lyman-Werner background, which facilitates the near-isothermal collapse of the gas at a temperature of about $10^4$ K. Once the central gas cloud becomes optically thick to continuum emission, it settles into a Keplerian disc around the primary protostar. The initial mass of the protostar is about $0.1\,\mathrm{M}_\odot$, which is an order of magnitude higher than in minihaloes that cool via molecular hydrogen. The high accretion rate and efficient cooling of the gas catalyse the fragmentation of the disc into a small protostellar system with $5-10$ members. After about 12 yr, strong gravitational interactions disrupt the disc and temporarily eject the primary protostar from the centre of the cloud. By the end of the simulation, a secondary clump has collapsed at a distance of $\simeq 150$ au from the primary clump. If this clump undergoes a similar evolution as the first, the central gas cloud may evolve into a wide binary system. High accretion rates of both the primary and secondary clumps suggest that fragmentation is not a significant barrier for forming at least one massive black hole seed.

## 2.1 Introduction

Black holes (BHs) are a key ingredient in the formation and evolution of galaxies. In the local Universe, the stellar velocity dispersion in galaxy bulges is correlated with the mass of the BH at their centre (Ferrarese & Merritt 2000; Gebhardt et al. 2000). BHs also power luminous quasars by accreting gas from their host galaxies. Recent observations suggest that quasars powered by BHs with masses $\gtrsim 10^9\,\mathrm{M}_\odot$ were already present when the Universe was less than one billion year old (Fan et al. 2003, 2006). These supermassive black holes most likely grew from smaller seed BHs that formed earlier, but the origin of these seeds remains unclear (Haiman 2006, 2009; Greene 2012; Volonteri 2012; Volonteri & Bellovary 2012). One possible candidate are the remnants of massive Population III stars (Madau & Rees 2001; Li et al. 2007; Johnson et al. 2012), or the direct collapse of primordial gas in haloes with virial temperatures $T_\mathrm{vir} \gtrsim 10^4\,\mathrm{K}$, so-called atomic cooling haloes (Bromm & Loeb 2003; Bromm & Yoshida 2011). In the former case, the seeds have initial masses of the order of $100\,\mathrm{M}_\odot$, and grow at or above the Eddington limit for the remaining $\simeq 500\,\mathrm{Myr}$ between seed formation and $z \simeq 6$. However, numerical simulations have shown that accretion on to early BHs is inefficient, due to the low density of the gas surrounding the BH remnant, which is caused by photoionization heating from the progenitor star (Johnson & Bromm 2007; Alvarez et al. 2009). Accretion rates are thus not high enough to allow efficient growth of the seed, which poses a serious complication for

the Population III stellar remnant scenario.

In the direct collapse scenario, haloes with virial temperatures $\gtrsim 10^4$ K may host seed BHs that are substantially more massive. A prerequisite is that the accretion rate on to the central object is high enough that radiative feedback does not severely impede the accretion flow (Johnson et al. 2011, 2012; Hosokawa et al. 2012, 2013). In this case, a supermassive star or 'quasi-star' forms, which may collapse into a BH of mass $\sim 10^5 - 10^6\,\mathrm{M}_\odot$ (Heger et al. 2003; Begelman et al. 2006, 2008; Begelman 2010; Volonteri & Begelman 2010; Montero et al. 2012; Volonteri 2012; Inayoshi et al. 2013; Schleicher et al. 2013; Chen et al. 2014). Since the accretion rate in a Jeans-unstable cloud scales as $\dot{M} \propto T^{3/2}$, molecular hydrogen cooling must be suppressed until the virial temperature of the halo is high enough that Ly$\alpha$ cooling becomes important. This may be achieved by a Lyman-Werner (LW) radiation background (Omukai 2001; Bromm & Loeb 2003; Volonteri & Rees 2005; Spaans & Silk 2006; Schleicher et al. 2010; Johnson et al. 2013). Simple one-zone models have found that the critical flux is of the order of $J_{21,\mathrm{crit}} = 10^5$ in units of $J_{21} = 10^{-21}\,\mathrm{erg\,s^{-1}\,cm^{-2}\,Hz^{-1}\,sr^{-1}}$ for a blackbody spectrum with $10^5$ K (Omukai 2001). For Population I/II stars, recent studies have found that the critical flux may be somewhat lower (Shang et al. 2010; Wolcott-Green & Haiman 2012; Van Borm & Spaans 2013; Agarwal & Khochfar 2015; Latif et al. 2014a, 2015; Regan et al. 2014b; Sugimura et al. 2014). Even though the LW flux on cosmological scales is well below this value, local star formation may raise the flux to supercritical levels (Dijkstra et al. 2008, 2014; Agarwal et al. 2012, 2014;

Visbal et al. 2014).

If the LW flux is high enough, the halo gas collapses nearly isothermally at $\simeq 10^4\,\mathrm{K}$ up to a density of $n_\mathrm{H} \simeq 10^6\,\mathrm{cm}^{-3}$, where the gas becomes optically thick to Ly$\alpha$ emission (Omukai 2001). At this point, continuum cooling via free-bound emission of $\mathrm{H}^-$ takes over, and allows the gas to again contract nearly isothermally up to a density of $n_\mathrm{H} \simeq 10^{16}\,\mathrm{cm}^{-3}$. Once the continuum emission becomes trapped, the gas evolves nearly adiabatically and a protostar forms at the centre of the halo. During the initial collapse, the angular momentum is constantly redistributed by turbulence and bar-like instabilities, such that the cloud contracts nearly unhindered (Oh & Haiman 2002; Koushiappas et al. 2004; Begelman et al. 2006; Lodato & Natarajan 2006; Wise et al. 2008; Begelman & Shlosman 2009; Choi et al. 2013; Latif et al. 2013a; Prieto et al. 2013).

The subsequent accretion phase was investigated by Regan & Haehnelt (2009) and Latif et al. (2013a,b). They found that a Keplerian disc forms around the primary protostar, which becomes gravitationally unstable and fragments into a small system of protostars. The secondary protostars merge on a short time-scale and do not prevent the growth of the primary protostar. These studies employed a pressure floor beyond a certain refinement level, such that the maximum density was limited to $n_\mathrm{H} \sim 10^6 - 10^9\,\mathrm{cm}^{-3}$. The simulations of Regan et al. (2014a) also displayed the formation of a disc-like object at the centre of the halo, which in some cases fragmented on a scale of 100 au. However, these simulations also suffered from limited

resolution, and did not include the relevant $H_2$ cooling and chemistry. Recently, Inayoshi et al. (2014) used the most detailed chemical and thermal model to date, but stopped the simulation once the primary protostar had formed. In addition, they did not use cosmological initial conditions. We here attempt to improve upon these studies by carrying out a simulation that starts from cosmological initial conditions and is not resolution-limited. We use a slightly less sophisticated chemical model as Inayoshi et al. (2014), but evolve the simulation well beyond the formation of the first protostar at the centre of the halo.

This chapter is organized as follows. In Section 2.2, we describe the simulation setup and the chemistry and cooling network. In Section 2.3, we analyse the simulation and discuss the collapse of the central gas cloud, the formation and fragmentation of the disc, the development of the protostellar system, and the collapse of a secondary clump towards the end of the simulation. Finally, in Section 2.4 we summarize and draw conclusions. All distances are quoted in proper units, unless noted otherwise.

## 2.2 Simulations

We perform three-dimensional, cosmological hydrodynamical simulations to investigate the collapse of gas in atomic cooling haloes in which the formation of $H_2$ has been suppressed by a LW background. For this purpose we employ the moving-mesh

code AREPO (Springel 2010). We also include the recently developed primordial chemistry and cooling network of Greif (2014). In the following, we briefly describe the initialization of the simulations, the extraction procedure and refinement criteria used to achieve densities $n_{\rm H} \gtrsim 10^{21}$ cm$^{-3}$, and the chemistry and cooling network.

### 2.2.1 Dark matter simulations

We first initialize a dark matter (DM)-only simulation at a redshift of $z = 99$ in a standard $\Lambda$ cold dark matter ($\Lambda$CDM) cosmology. We adopt cosmological parameters based on the *Wilkinson Microwave Anisotropy Probe* results (Komatsu et al. 2009). We use a matter density $\Omega_{\rm m} = 1 - \Omega_\Lambda = 0.27$, baryon density $\Omega_{\rm b} = 0.046$, Hubble parameter $h = H_0/100$ km s$^{-1}$ Mpc$^{-1}$ $= 0.7$ (where $H_0$ is the present Hubble expansion rate), spectral index $n_{\rm s} = 0.96$, and normalization $\sigma_8 = 0.81$. The simulation is initialized in a box of side length 2 Mpc (comoving) with a total of $512^3$ DM particles of mass $\simeq 2.2 \times 10^3$ M$_\odot$. The gravitational softening length is set to $\simeq 195$ pc (comoving), which corresponds to 5% of the initial mean inter-particle separation. We stop the simulation when the first halo with virial mass exceeding $10^8$ M$_\odot$ collapses. This occurs at $z_{\rm coll} \simeq 12.4$, when the first halo reaches $M_{\rm vir} \simeq 1.7 \times 10^8$ M$_\odot$. At this point the halo has a virial radius of $R_{\rm vir} \simeq 1.4$ kpc and a spin parameter $\lambda \simeq 0.05$.

### 2.2.2 Resimulations

The second step is to locate the target halo and flag it for further refinement. We select the particles belonging to that halo and a sufficiently large boundary region around it, and trace them back to their initial conditions. Once the particle locations have been determined, we reinitialize the simulation centred on the target halo. In order to acquire higher resolution we replace each DM particle by 64 less-massive DM particles and 64 mesh-generating points. The resolution is gradually decreased as the distance from the high-resolution region increases, replacing cells and DM particles by higher-mass particles outside the target region. The resimulation has lower resolution towards the edges of the box than the original DM-only simulation, but the accuracy of the gravitational tidal field around the target halo is preserved. The refined DM particle mass is given by $M_{\rm dm,ref} = (1 - \Omega_{\rm b}/\Omega_{\rm m})M_{\rm dm}/64 \simeq 28\ {\rm M}_\odot$, and the gravitational softening length is set to $\simeq 49\,{\rm pc}$ (comoving). The refined mass of each cell is given by $M_{\rm gas,ref} = (\Omega_{\rm b}/\Omega_{\rm m})M_{\rm dm}/64 \simeq 6\,{\rm M}_\odot$.

We stop the resimulation once the first cell has exceeded a density of $n_{\rm H} \simeq 10^9\,{\rm cm}^{-3}$. We then proceed to extract the particles in the central 3 pc and reinitialize the simulation with reflective boundary conditions. Hence, the central region of the final output in the first resimulation becomes the initial condition for a second resimulation with a box size of 3 pc. Furthermore, at those densities the gas component is already well decoupled from the DM component (Greif et al. 2011), so we discard the DM and keep

only the gas particles. We evolve the second resimulation until it exceeds a density of $n_{\rm H} \simeq 10^{19}\,{\rm cm}^{-3}$, after which we conduct a second extraction similar in nature to the first, but cut out the central $5 \times 10^{-3}\,{\rm pc}$ of the second resimulation. We then use this as the side length for the third resimulation. This approach has the risk that perturbations from the edges of the box might influence the central regions. However, we explicitly avoid this issue by assuring that the sound crossing time through the box is much longer than the free-fall time of the central high-density cloud.

### 2.2.3 Refinement

An essential refinement criterion that grid codes have to fulfill to resolve gravitational instability and avoid artificial fragmentation is the so-called Truelove criterion (Truelove et al. 1997). This criterion states that the local Jeans length needs to be resolved by at least four cells, where the cell size is approximately given by $h = (3V/4\pi)^{1/3}$, and $V$ is the volume of the cell. In order to adequately resolve turbulence, recent studies using grid codes with a fixed mesh have found that the Jeans length must be resolved by at least 32 cells (Federrath et al. 2011; Turk et al. 2012; Latif et al. 2013a). A disadvantage of using refinement based on the Jeans length is that shock-heated regions may be much less resolved than adjacent cold regions. In order to avoid this problem, we follow the refinement criterion proposed by Turk et al. (2010), who suggest using the minimum temperature of the gas to evaluate the Jeans length. We slightly modify this criterion by using $T_{\rm min} = 5000\,{\rm K}$ for

cells with $T \leq T_{\rm min}$, but the correct temperature for cells with $T > T_{\rm min}$. This ensures that the initial collapse phase is adequately resolved, while at high densities the resolution does not become excessively high and slows down the calculation. Below $n_{\rm H} = 10^{15}\,{\rm cm}^{-3}$, we employ 64 cells per Jeans length, which is degraded to 8 cells above $n_{\rm H} = 10^{18}\,{\rm cm}^{-3}$. We use a linear extrapolation between these densities. The maximum spatial resolution achieved with this refinement strategy is $\simeq 6.6 \times 10^{-4}\,{\rm au}$. Next to the Jeans refinement, we refine a cell if its mass increases to more than twice its initial mass.

### 2.2.4 Chemistry and cooling

A detailed description of the chemical and thermal model used here can be found in Greif (2014) (see also the Section 2.5). Here, we only briefly describe the most important reactions and cooling processes. The chemical network employs a non-equilibrium solver at low densities and an equilibrium solver at high densities for the species H, $H_2$, $H^-$, $H^+$, and $e^-$. The transition from non-equilibrium to equilibrium $H_2$ chemistry occurs at $n_{\rm H_2,eq} = 10^{15}\ {\rm cm}^{-3}$, since three-body reactions depend on the cube of the density and would otherwise prohibitively decrease the time-step of the non-equilibrium solver. For densities above $n_{\rm H^+,eq} = 10^{18}\ {\rm cm}^{-3}$, the electron and $H^+$ abundances are also considered to be in equilibrium. The main reactions include the formation of $H_2$ via associative detachment as well as three-body reactions, the destruction of $H_2$ via collisions and photodissociation, and the formation and destruc-

tion of $H^+$ by collisional ionizations and recombinations.

The relevant cooling processes are $H_2$ line cooling, $H_2$ collision-induced emission, Ly$\alpha$ cooling, and inverse Compton cooling. $H_2$ cooling plays a substantial role up to $n_{\rm H} \simeq 10^{15}$ cm$^{-3}$, where the gas becomes optically thick to the $H_2$ line emission, while collision-induced emission becomes important at $n_{\rm H} \gtrsim 10^{14}$ cm$^{-3}$ and provides the last radiative cooling channel (Omukai & Nishi 1998; Ripamonti & Abel 2004). Although we include molecular hydrogen cooling, its effect does not become important during the evolution of the simulation due to the presence of a strong LW background that dissociates $H_2$ via the Solomon process (Abel et al. 1997). Previous studies found that a strong LW flux with $J_{21} \gtrsim 10^3$ is required to dissociate molecular hydrogen in the progenitors of an atomic cooling halo (Omukai 2001; Johnson & Bromm 2007; Dijkstra et al. 2008; Latif et al. 2013b; Wolcott-Green et al. 2011). Here, we assume a constant LW flux of $J_{21} = 10^5$ for a blackbody spectrum with $T_{\rm rad} = 10^5$ K, which is commonly used to estimate the spectra of Population III stars. In this case, the $H^-$ photodissociation rate is much smaller than the $H_2$ photodissociation rate (Sugimura et al. 2014). We approximate the combined effects of Ly$\alpha$ cooling and continuum cooling by assuming that Ly$\alpha$ cooling remains optically thin up to densities $n_{\rm H} \simeq 10^{16}\,{\rm cm}^{-3}$. The cooling rate is exponentially suppressed at densities $n_{\rm H} \simeq 10^{16}\,{\rm cm}^{-3}$ to approximately reproduce the density-temperature relation found in Omukai (2001). Due to this simplification, we may somewhat underestimate the true cooling rate.

## 2.3 Results

### 2.3.1 Collapse of central gas cloud

A number of studies have discussed the properties of the collapse of primordial gas clouds in atomic cooling haloes (e.g., Bromm & Loeb 2003; Regan & Haehnelt 2009; Choi et al. 2013; Latif et al. 2013a; Inayoshi et al. 2014; Regan et al. 2014a). Here, we investigate the collapse of the gas over an unprecedented range in scale, as shown in Figure 2.1. The six panels show a zoom-in on the central gas cloud, ranging from 10 pc down to scales of 10 au. The panel on the bottom-left side of the figure shows the primary protostar surrounded by an accretion disc. The cloud shows an irregular morphology and changes shape as it collapses. Its filamentary structure is indicative of turbulence, which is especially pronounced during the later stages of the collapse. On the largest scales, the cloud shows less substructure and is more spherically symmetric.

Figure 2.2 shows various physical quantities as a function of distance from the densest cell in the halo. The radial profiles are constructed from data of the three resimulations. We proceed by extracting the inner $\simeq$ 300 au from the last resimulation, while the range between $\simeq$ 300 and $\simeq 10^5$ au is taken from the second resimulation. To complete the profiles, the outer region corresponds to data from the first resimulation up to $\simeq 10^{10}$ au. Due to the self-similarity of the collapse, moving from large to

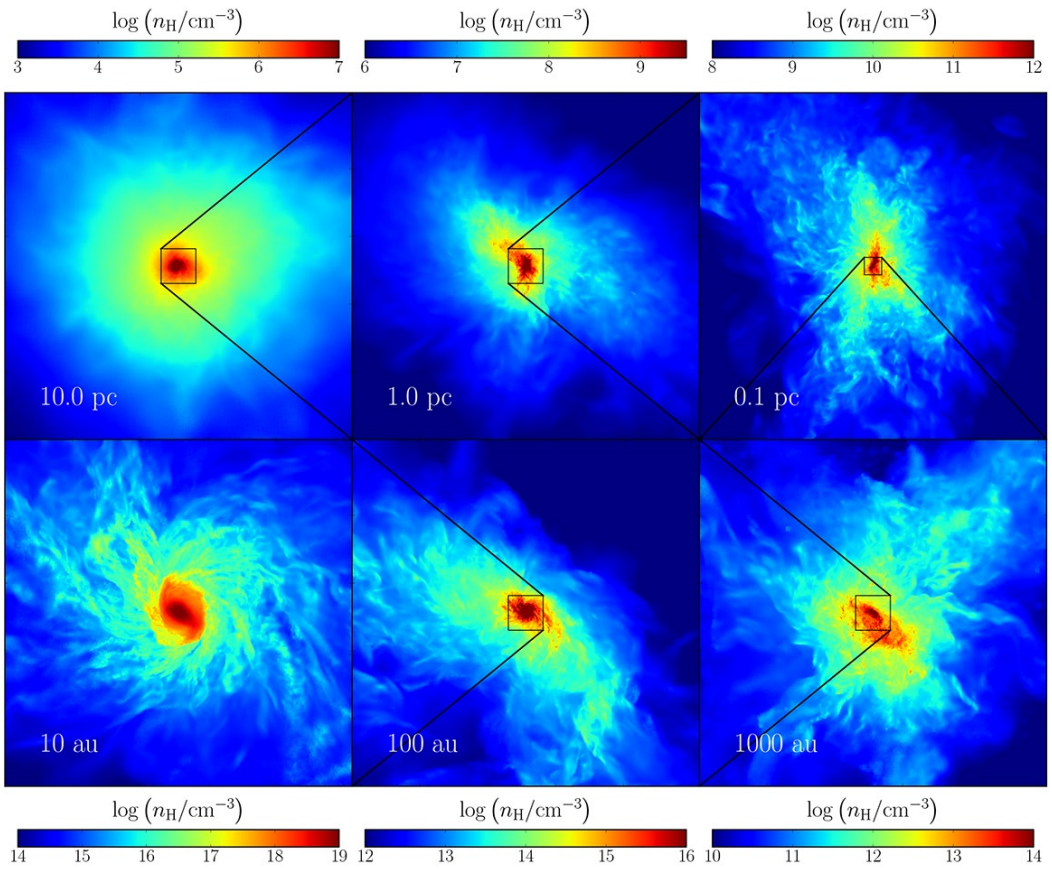


**Figure 2.1:** Zoom-in on the gas cloud that forms at the centre of the atomic cooling halo. The number density of hydrogen nuclei is weighted with the square of the density along the line of sight, which is perpendicular to the plane of the disc. Clockwise from the top left, the width of the individual cubes are $10$ pc, $1$ pc, $0.1$ pc, $1000$ au, $100$ au, and $10$ au. The cloud has an irregular morphology that continues to change shape and orientation throughout the collapse. The filamentary structure indicates that turbulence is present on all scales.

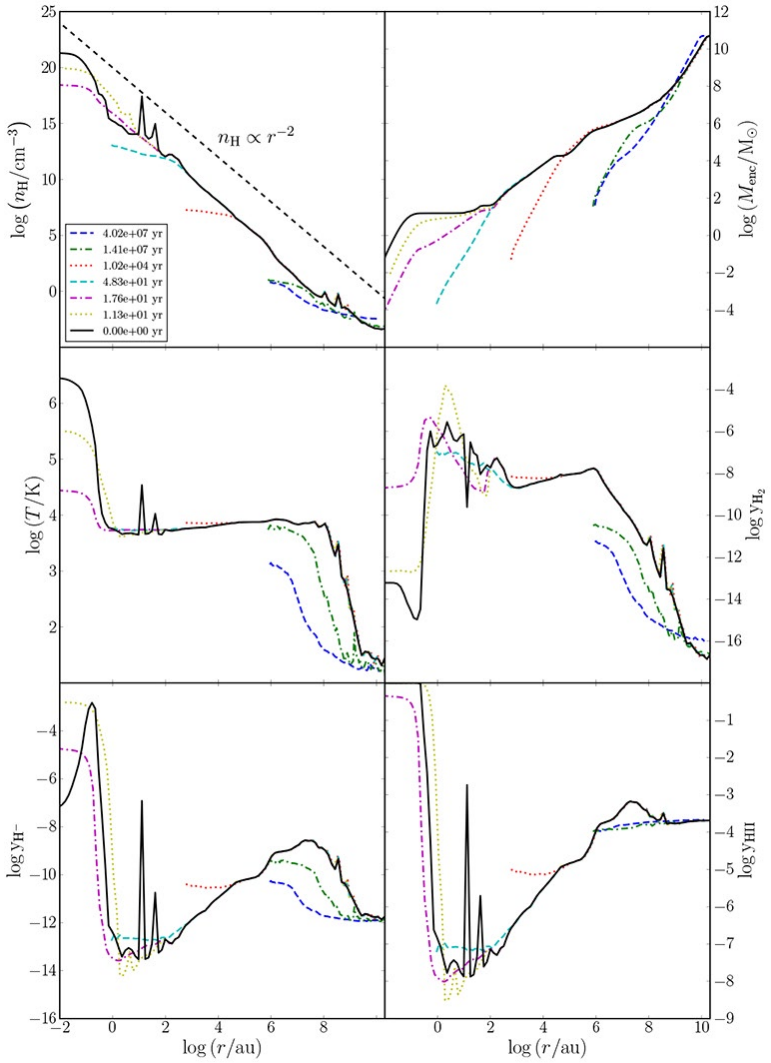


**Figure 2.2:** Radial profiles for the mass-weighted number density of hydrogen nuclei, enclosed gas mass, temperature, and $H_2$, $H^-$, and HII abundances between about $0.01$ au and $\sim$ $100$ kpc. The various line styles and colours denote different epochs of the evolution of the halo, labelled by their lookback time as measured from the end of the run according to the legend. The blue dashed line corresponds to redshift $\simeq$ $26$, the green dash-dotted line to $z$ $\simeq$ $15$, the red dotted line to when the number density first exceeds $10^9$ cm$^{-3}$, the cyan dashed line to $\simeq 9 \times 10^3$ yr after that, the purple dash-dotted line to when the number density first exceeds $10^{19}$ cm$^{-3}$, the yellow dotted line to $\simeq$ $6$ yr after the formation of first protostar, and the black solid line to the end of the simulation after approximately $18$ yr. The halo follows several evolutionary stages from large to small scales: shock-heating to the virial temperature, onset of cooling, Jeans instability, isothermal contraction, formation of the primary protostar and disc, and fragmentation of the disc (see Section 2.3 for details).

small radii is equivalent to moving from early to late times. Properties plotted in the figure are the number density of hydrogen nuclei, enclosed gas mass, temperature, $H_2$ abundance, $H^-$ abundance, and HII abundance. These profiles have been calculated using mass-weighted averages of the cells contributing to the radial bins. Colours and line styles represent different evolutionary stages of the gas cloud as described in the legend and the caption of the figure.

As the gas collapses into the DM halo, it is shock-heated to the virial temperature. In the central parts of the halo, Ly$\alpha$ cooling becomes important and keeps the gas nearly isothermal at $\simeq 10^4\,\mathrm{K}$ (Wise & Abel 2007). During this period, the $H_2$ abundance builds up from $\simeq 10^{-16}$ to $\simeq 10^{-8}$, with small spikes due to the existence of shocks in the outer regions of the halo. The HII abundance increases by about one order of magnitude. The collapse then approximately follows the Larson-Penston solution for an isothermal, self-gravitating gas cloud (Larson 1969; Penston 1969), which is described by a density profile following $\rho \propto r^{-2}$. The strong LW background suppresses the formation of $H_2$ and maintains an abundance of $\simeq 10^{-8}$ down to scales of $\simeq 10^3\,\mathrm{au}$. This prevents $H_2$ cooling, which in turn leads to a roughly isothermal collapse between $\simeq 10^8$ and $\simeq 1\,\mathrm{au}$. Over these scales, the $H^-$ and HII abundances drop by many orders of magnitude due to recombination. On a scale of $\simeq 10^3\,\mathrm{au}$, the $H_2$ fraction increases due to three-body reactions. Up to this point, the radial profiles agree well with those of previous studies (Wise et al. 2008; Latif et al. 2013a; Regan et al. 2014a; Inayoshi et al. 2014). In the final stage of the collapse, when

the primary protostar forms, the gas becomes optically thick to continuum cooling at $\simeq 1\,\mathrm{au}$, which results in a rise in temperature of more than two orders of magnitude to $\gtrsim 10^6\,\mathrm{K}$. This is accompanied by a drop in the $H_2$ abundance and an increase in both the $H^-$ and HII abundances. At the end of the simulation, two pronounced spikes in the density profile are clearly visible in the central $\simeq 100\,\mathrm{au}$. These correspond to secondary protostars that have formed due to fragmentation in the disc. This will be discussed in detail in Section 2.3.2.

In Figure 2.3, we show the temperature-density distribution of the gas at the end of the simulation, next to those of the $H_2$, $H^-$, and HII abundances. At low densities, the temperature distribution spans almost six orders of magnitude, reaching as high as $\simeq 10^4$ K. A similarly high scatter is present in the $H_2$ and $H^-$ abundances, while the HII abundance varies only by two orders of magnitude. Up to $n_\mathrm{H} \simeq 10^{15}\,\mathrm{cm}^{-3}$, the temperature distribution becomes much narrower, showing the near-isothermal collapse of the gas. Once three-body reactions become important, the distribution of the $H_2$ fraction widens for densities in the range $10^5 - 10^{15}\,\mathrm{cm}^{-3}$, with particles reaching abundances as high as $y_{H_2} \simeq 0.1$. The resulting temperature dispersion leads to an increasing dispersion in the $H^-$ and HII abundances, while their average values continue to decrease due to recombinations. The values of the $H_2$ abundance are somewhat smaller than those found in Inayoshi et al. (2014), but agree with Latif et al. (2013a). We therefore do not distinguish between two thermal phases of the gas as in Inayoshi et al. (2014). For densities $\gtrsim 10^{18}\,\mathrm{cm}^{-3}$, the formation of the primary and secondary

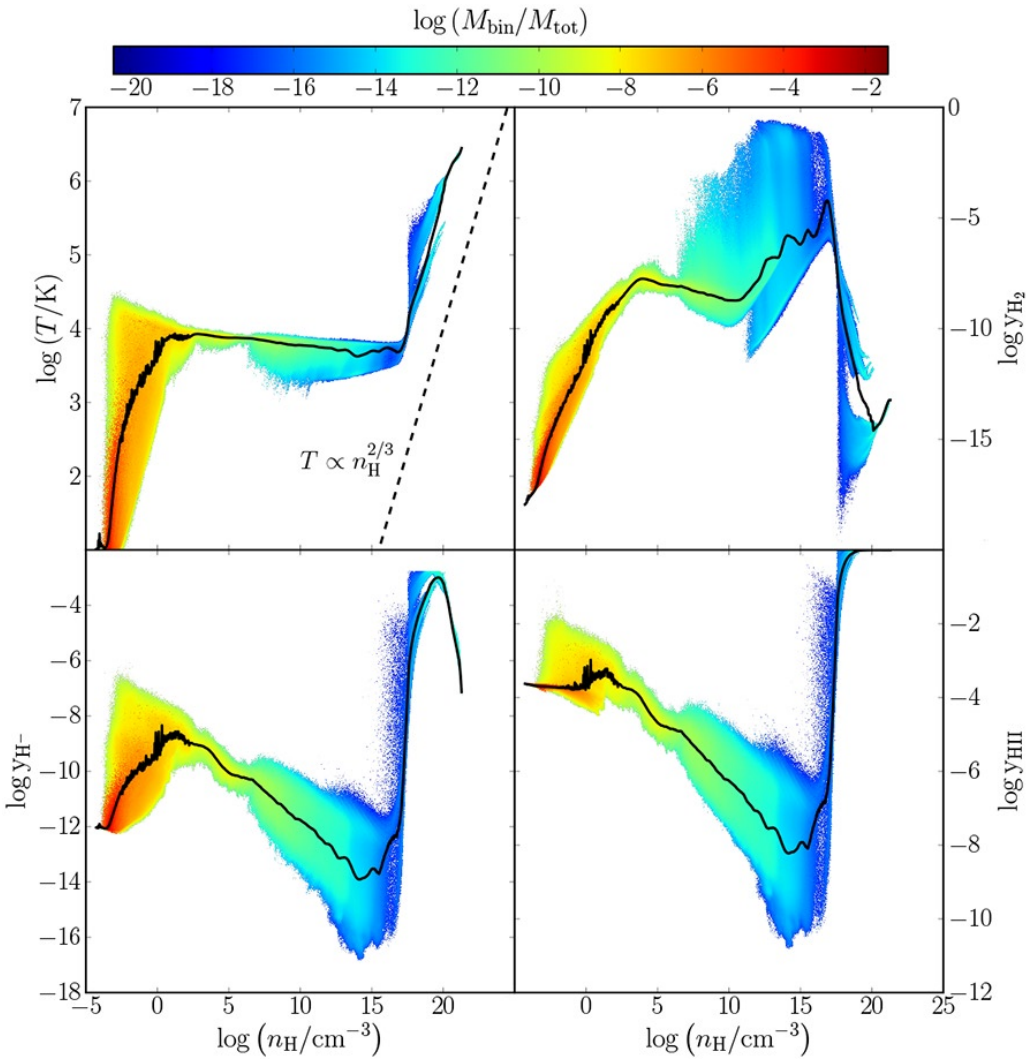


**Figure 2.3:** Clockwise from the top left panel: distribution of the gas in temperature, $H_2$, HII, and $H^-$ abundances versus number density of hydrogen nuclei at the end of the simulation. The mass per bin over the total mass in the computational domain is colour-coded from blue (lowest) to red (highest). The solid black lines show the mass-weighted average values. After shock-heating to the virial temperature of $\simeq 10^4$ K, the gas collapses nearly isothermally to densities of $n \simeq 10^{16}$ cm$^{-3}$. The gas then becomes optically thick to continuum emission and evolves nearly adiabatically. At this point, the HII abundance dramatically increases from $\sim 10^{-14}$ to unity. The $H_2$ abundance stays below $\simeq 10^{-7}$ due to the LW background, but then increase to $\simeq 10^{-4}$ as three-body reactions set in. However, the $H_2$ abundance never becomes high enough for $H_2$ cooling to become important. The 'fingers' visible in the various distributions show the evolutionary paths of individual protostars.

protostars can be recognized as 'fingers' of gas in the individual panels, which evolve nearly adiabatically. The high temperatures in the interior of the protostars results in a decrease of the $H_2$ and $H^-$ abundances, and an increase of the HII abundance to unity.

The radial profiles of the magnitude of the radial velocity, rotational velocity, Keplerian velocity, turbulent velocity, and sound speed at the end of the simulation are shown in the left-hand panel of Figure 2.4. In addition, the right-hand panel shows the Mach numbers of each velocity component. The turbulent Mach number is given by

$$\mathcal{M}_{\rm turb}^2 c_{\rm s}^2 = \sum_i \frac{m_i}{M} (\mathbf{v}_i - \mathbf{v}_i^{\rm rad} - \mathbf{v}_i^{\rm rot})^2, \tag{2.1}$$

where $c_{\rm s}$ denotes the sound speed of the radial bin, $M$ the total mass, $i$ the index of a cell contributing to the bin, $m_i$ its mass, $\mathbf{v}_i$ the velocity, $\mathbf{v}_i^{\rm rad}$ the radial velocity vector, and $\mathbf{v}_i^{\rm rot}$ the rotational velocity vector. During the initial free-fall phase, the turbulent component is supersonic with $\mathcal{M} \simeq 3$. In contrast, the Mach number of the rotational velocity remains below unity, indicating the poor rotational support of the cloud at that stage. The trend for each component is roughly maintained once the halo has entered the isothermal collapse phase, with the exception of the Mach number of the radial velocity, which briefly drops to below unity. Down to $\simeq 100\,{\rm au}$, the rotational velocity oscillates between 0.2 and 0.5 of the Keplerian velocity, indicating a substantial degree of rotational support. It reaches its peak at the edge of the disc

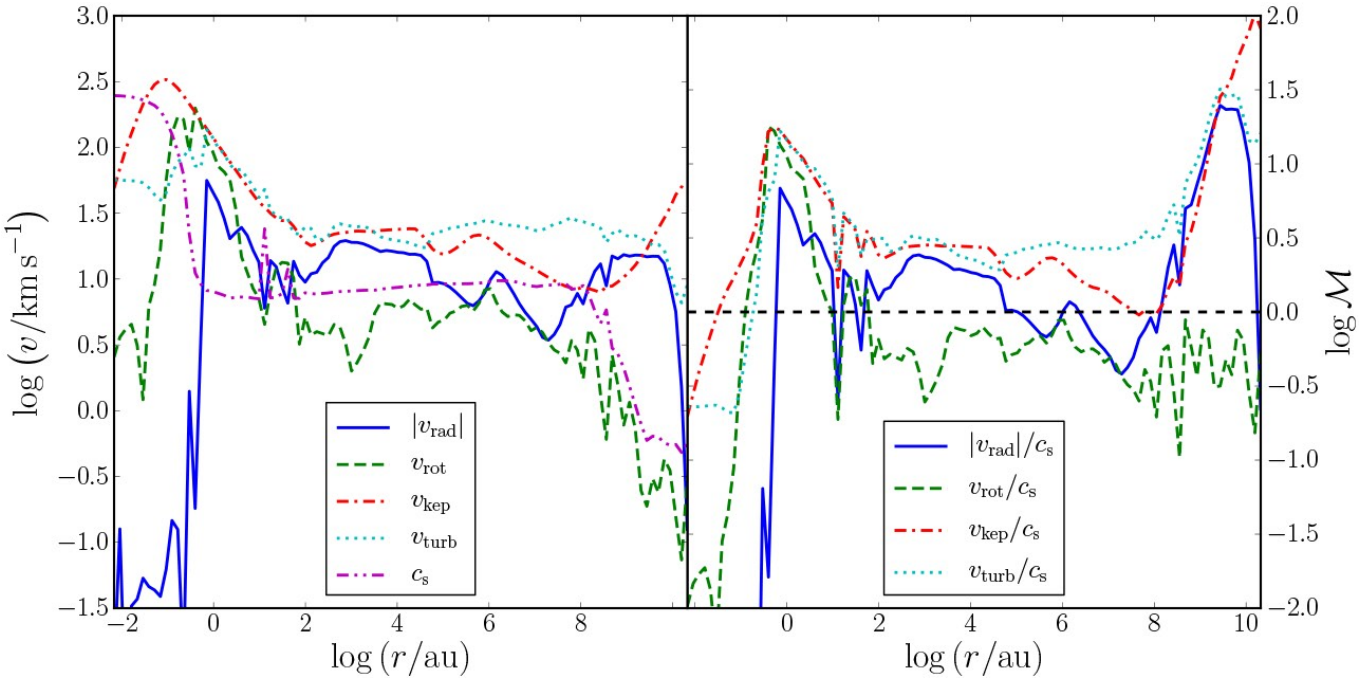


**Figure 2.4:** Mass-weighted average radial velocity, rotational velocity, Keplerian velocity, turbulent velocity, and sound speed versus radius (left-hand panel), as well as the corresponding Mach numbers (right-hand panel). The turbulent velocity is supersonic with a Mach number of $\simeq 3$ throughout the collapse, while the radial velocity briefly becomes subsonic. Once the disc forms, the rotational velocity becomes nearly equal to the Keplerian velocity, and comparable to the turbulent velocity.

on scales $\simeq 1\,\mathrm{au}$, where $v_{\mathrm{rot}} \simeq v_{\mathrm{kep}}$. On smaller scales, the primary protostar is characterized by an increase in temperature and thus sound speed, such that all velocity components become subsonic. In addition, $v_{\mathrm{rad}}$ drops precipitously, which shows that the infall rate decreases rapidly within the primary protostar. Similar values for the velocity have been found in previous studies (e.g. Regan et al. 2014a).

Overall, we find good agreement between our results and previous work. However, some differences exist. The morphology of the halo between $\simeq 10\,\mathrm{au}$ and $\simeq 10\,\mathrm{pc}$ is similar to that of Inayoshi et al. (2014), but we do not find clumps on larger scales as pointed out by Regan & Haehnelt (2009), Latif et al. (2013a), and Regan et al. (2014a). However, this is not surprising, since in our case the gas has not yet had time to settle into a disc on these scales. The radial profiles resemble those of Latif et al. (2013a) quite well, while Inayoshi et al. (2014) found a slightly higher $H_2$ abundance, which is also reflected in lower temperatures during the isothermal collapse phase. These differences may be caused by the different chemical networks used in our study (see Section 2.3.6).

### 2.3.2 Disc formation and fragmentation

After the formation of the first protostar, the gas becomes fully rotationally supported in a Keplerian disc. We study its stability by computing Toomre's parameter (Toomre 1964):

$$Q = \frac{c_{\mathrm{s}}\kappa}{\pi G \Sigma}, \tag{2.2}$$

where $c_s$ is the sound speed of the gas, $\kappa$ the epicyclic frequency of the disc, $G$ the gravitational constant, and $\Sigma$ the surface density of the gas. For the case of a Keplerian disc, the epicyclic frequency may be replaced by the orbital frequency $\Omega$. The $Q$ parameter was originally proposed to determine whether perturbations can grow in an infinitely thin, isothermal disc. Later studies have extended this criterion for thick discs, finding that it only deviates by a factor of order unity from the above equation (Wang et al. 2010). For values greater than $Q_{\rm crit} = 1$, the system is stable due to gas pressure and shear by the differential rotation of the disc, while for lower values the system is unstable and hence susceptible to the growth of perturbations. These lead to the formation of spiral arms that transport mass inwards and angular momentum outwards.

Radial profiles for the gas surface density, sound speed, orbital frequency, and Toomre parameter are shown in the left-hand panel of Figure 2.5. We compute the profiles using mass-weighted spherical shells centred on the densest cell in the halo of the final resimulation. The surface density increases as $\Sigma \propto r$ in the interior of the protostar, where the density is almost constant. On larger scales, the radial dependence changes to $\Sigma \propto r^{-1}$, as deduced from the relation $\rho \propto r^{-2}$ for isothermal collapse, while the orbital frequency roughly follows $\Omega \propto r^{-1}$. On scales between 0.1 and 100 au, the radial dependence of $\Sigma$ and $\Omega$ thus cancel each other, such that $Q$ remains roughly constant around unity. In the interior of the protostar, $Q$ increases due to the increase in the sound speed and the different radial scaling between $\Sigma$ and $\Omega$. Since

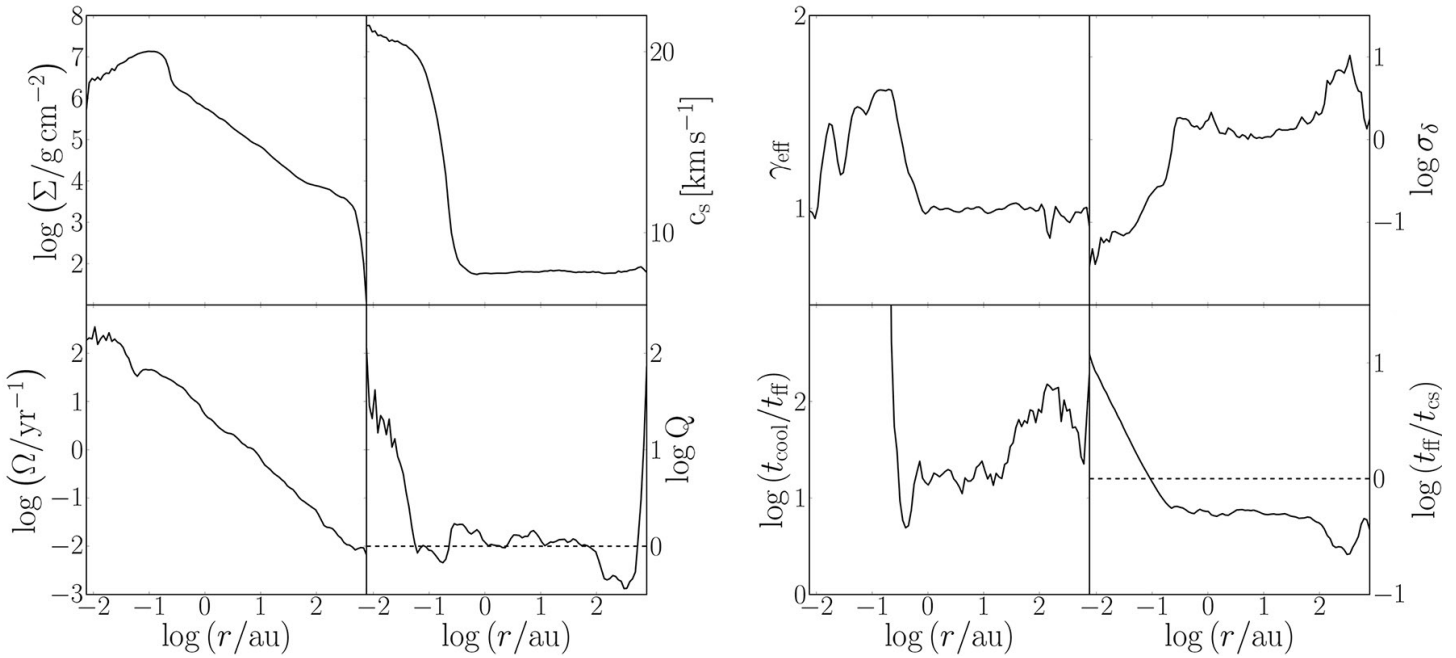


**Figure 2.5:** Left: from top left to bottom right, the panels show the mass-weighted average surface density, sound speed, orbital frequency, and Toomre parameter versus radius just before the disc fragments. Above $\simeq 0.1$ au, the power-law profiles of the surface density and rotation speed yield a Toomre parameter that is close to unity, which indicates that perturbations in the disc can grow. Right: effective equation of state, root-mean-squared density contrast, cooling time over free-fall time, and free-fall time over sound-crossing time. The isothermal collapse of the gas on scales $\gtrsim 1$ au results in $\gamma_{\rm eff} \simeq 1$, while the increasing optical depth of the gas to continuum emission on smaller scales results in an exponent that is closer to that of an adiabatic gas. The cooling time over the free fall time has a local minimum on a scale of $\simeq 1$ au: this is approximately the radius at which the first fragment forms. The density contrast created by the supersonic turbulence is between $\simeq 1$ and $\simeq 10$. The free-fall time exceeds the sound crossing time on a scale of $\simeq 0.1$ au, which shows the size of the central, Jeans-unstable clump.

the value of $Q$ is roughly equal to the critical value, the disc is prone to perturbation growth.

Further properties at the time when the primary protostar has just formed and is surrounded by a disc that has not yet fragmented are shown in the right-hand panel of Figure 2.5. From the top left to the bottom right, the panels show the effective equation of state, root-mean-squared density contrast, cooling time over free-fall time, and free-fall time over sound-crossing time. In the outer region of the disc, on scales $\gtrsim 1\,\mathrm{au}$, the equation of state is characterized by $\gamma_{\mathrm{eff}} \simeq 1$, as expected for isothermal collapse. The density contrast is roughly constant around unity, while the interior of the primary protostar is characterized by values close to 0.1. Here, $\gamma_{\mathrm{eff}}$ increases to $\simeq 1.2 - 1.5$ as a reflection of the temperature increase by almost two orders of magnitude in the central $\simeq 1\,\mathrm{au}$. The cooling time remains well above the free-fall time in the inner 100 au of the halo and down to $\simeq 1\,\mathrm{au}$, the scale at which the gas becomes optically thick to continuum cooling. The free-fall time remains below the sound-crossing time down to $\simeq 0.1\,\mathrm{au}$, showing the gravitational instability of the cloud down to this scale.

### 2.3.3 Minimum fragment mass

Further evidence for the gravitational instability of the gas is presented in Figure 2.6, where we plot the enclosed gas mass over the locally estimated Bonnor-Ebert (BE; Ebert 1955; Bonnor 1956) mass as a function of enclosed gas mass. Colours and line

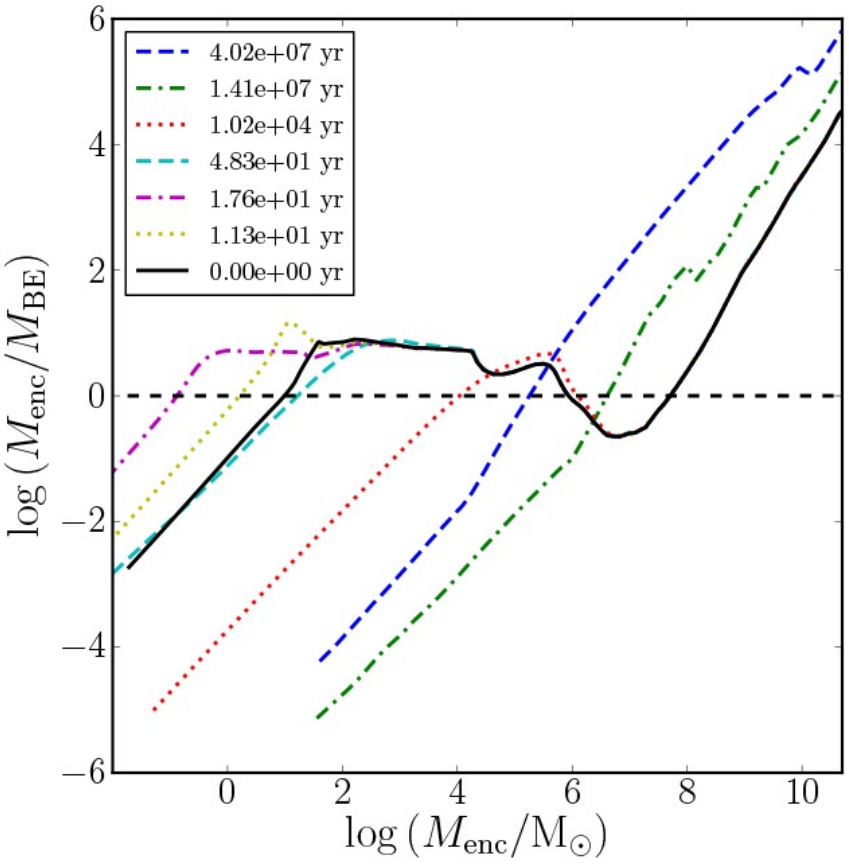


**Figure 2.6:** Enclosed gas mass over the mass-weighted average BE mass as a function of enclosed gas mass. Colours and line styles are the same as in Figure 2.2. As the halo grows in mass, the BE mass increases due to the rise in the virial temperature, which reduces $M_{\rm enc}/M_{\rm BE}$. Once the atomic cooling halo is assembled, this ratio exceeds unity on a scale of $\simeq 10^8$ $M_\odot$. Following the onset of runaway cooling due to Ly$\alpha$ emission, the central $10^6$ $M_\odot$ become Jeans-unstable (red dotted line). The minimum Jeans mass of the cloud is indicated by the purple dash-dotted line as $\simeq 0.1$ $M_\odot$, which coincides with the initial mass of the primary protostar.

styles are the same as in Figure 2.2. The profiles have been computed using spherical shells centred on the densest cell, where the BE mass is calculated as the mass-weighted average among cells within a given radius according to:

$$M_{\rm BE} \simeq 15\,{\rm M}_\odot \left(\frac{n_{\rm H}}{\rm cm^{-3}}\right)^{-1/2} \left(\frac{T}{\rm K}\right)^{3/2} \mu^{-3/2}\gamma^2. \tag{2.3}$$

During the initial collapse, the ratio of enclosed gas mass to BE mass decreases as a consequence of the rise in temperature as the gas is shock-heated. The enclosed gas mass surpasses $M_{\rm BE}$ at $M_{\rm enc} \simeq 10^8\,{\rm M}_\odot$, which is in agreement with the mass of the halo. As the halo keeps accreting, another region where the ratio exceeds unity emerges at about $\simeq 10^6\,{\rm M}_\odot$. This marks the initial Jeans instability of the cloud. From $\simeq 10^6\,{\rm M}_\odot$, the point where $M_{\rm enc}$ surpasses $M_{\rm BE}$ moves down to $\simeq 0.1\,{\rm M}_\odot$ when the densest cell first reaches $10^{19}\,{\rm cm^{-3}}$. This is the minimum fragment mass and coincides with the initial mass of the protostar formed at the centre of the halo. From then on the temperature of the central object increases, which is translated into an increase of the BE mass, and hence a decrease of the $M_{\rm enc}/M_{\rm BE}$ ratio. As a result, the point at which this ratio equals unity briefly moves up to $\simeq 10\,{\rm M}_\odot$ and always stays above $\simeq 1\,{\rm M}_\odot$.

### 2.3.4 Protostellar system

The fragmentation of the disc into a small protostellar system is shown in Figure 2.7. The top three rows show cubes of side length 20 au centred on the position of the primary protostar, while the cubes of the last row are 50 au wide with the centre fixed on the position of the primary protostar after $\simeq$ 12 yr. In total, we present 16 different output times, which are measured with respect to the point in time at which the densest cell first exceeds $10^{19}\,\mathrm{cm}^{-3}$. During the first $\simeq$ 6 yr, perturbations grow between 1 and 10 au in the form of spiral arms. After $\simeq$ 7 yr, they become gravitationally unstable and the first secondary protostar forms. In the next $\simeq$ 2 yr, the efficient cooling of the gas results in the formation of additional protostars, and after $\simeq$ 12 yr a small protostellar system with six members has emerged. Shortly thereafter, three-body interactions and strong tidal forces during a close passage of a secondary protostar and the primary results in the disruption of the disc. Both protostars are ejected from the centre of the cloud. The sequence in the bottom row of Figure 2.7 shows the evolution of this interaction and how both protostars move away from each other.

To quantify the interaction between both protostars, Figure 2.8 shows the relative distance and velocity between the protostars over time. For comparison, we also include the escape velocity of both protostars, using the enclosed mass in a spherical region around their respective centres, with radii equal to their separation. Once the secondary protostar forms, it orbits at a roughly constant distance of $\simeq$ 4 au

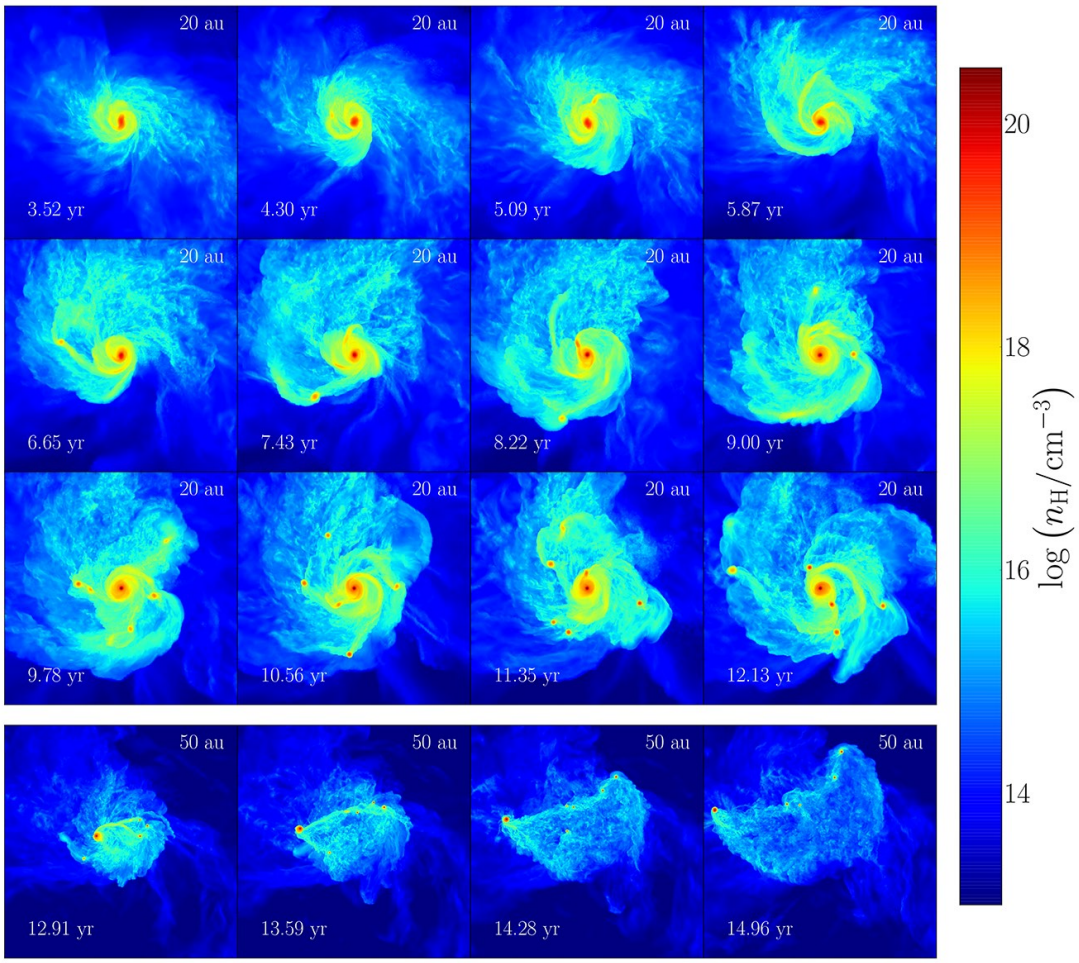


**Figure 2.7:** Evolution of the protostellar system that forms at the centre of the atomic cooling halo. The number density of hydrogen nuclei is weighted with the square of the density along the line of sight, which is perpendicular to the plane of the disc. The top three rows show cubes with a side length of $20$ au, centred on the position of the first protostar. The bottom row shows the later evolution of the protostellar system on a somewhat larger scale of $50$ au, where the centre has been fixed on the position of the primary protostar after $\simeq 12$ yr. The time is measured from the instant when the density first exceeds $10^{19}$ cm$^{-3}$. The formation of a Keplerian disc around the primary protostar is clearly visible. Shortly thereafter, the disc becomes Toomre-unstable and spiral arms form that transport mass inwards and angular momentum outwards. After $\simeq 6$ yr, the disc becomes gravitationally unstable and fragments due to the high mass accretion rate from the surrounding cloud on to the disc, and the efficient cooling of the disc by continuum emission. Over the next $\simeq 7$ yr, an additional five protostars form before three-body interactions lead to the temporary ejection of the primary protostar from the cloud, which disrupts the disc.

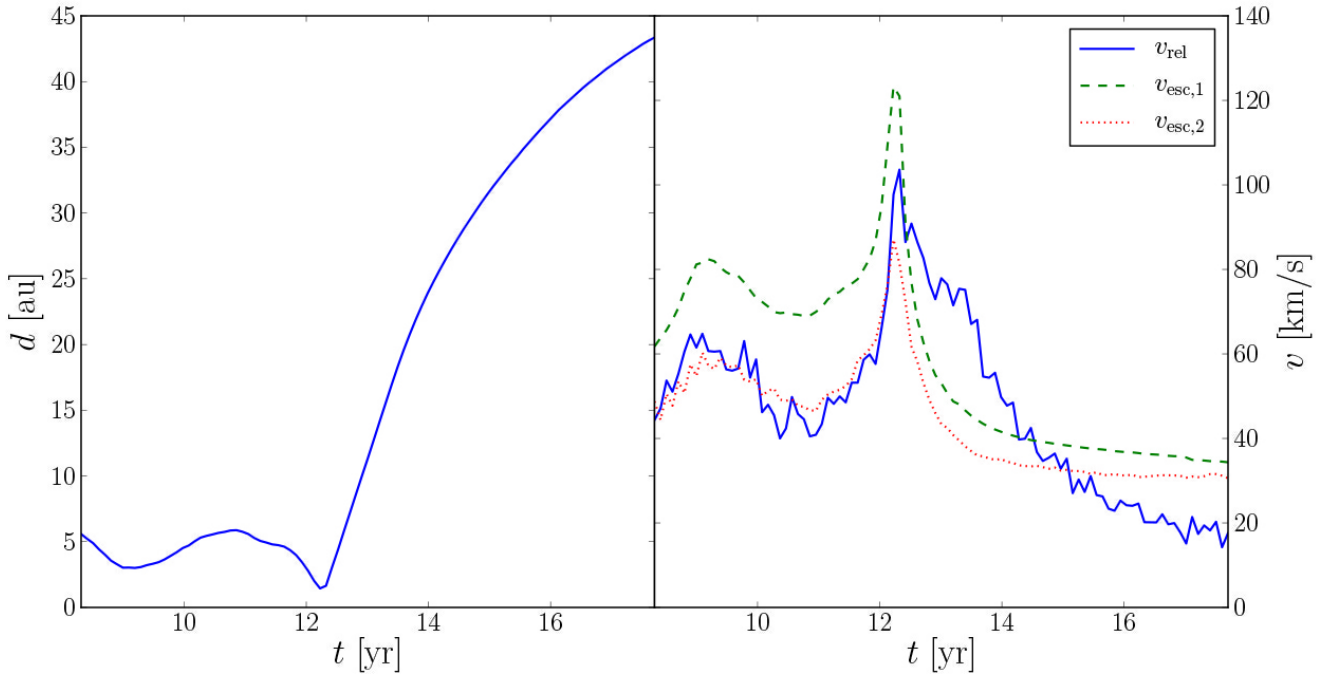


**Figure 2.8:** Relative distance (left-hand panel) and velocity (right-hand panel, blue solid) between the primary and a secondary protostar. The latter initially orbits around the primary protostar at a distance of $\simeq 4$ au, but strong gravitational forces due to three-body interactions temporarily eject both protostars from the centre of the cloud after $\simeq 12$ yr. The relative velocity reaches a peak value of about $\simeq 100\,\mathrm{km\,s^{-1}}$, which declines to $20\,\mathrm{km\,s^{-1}}$ towards the end of the simulation. For comparison, we also show the escape velocities of both protostars. The green dashed line corresponds to the primary protostar, and the red dotted line to the secondary protostar. Since the relative velocity decreases to well below the escape velocity, both protostars will likely return to the centre of the cloud.

from the primary protostar, but they soon move together and their separation decreases to $\simeq$ 1 au. Shortly thereafter, three-body interactions eject both protostars from the centre of the halo. This is reflected by a high relative velocity with a peak value of $\simeq$ 100 km s$^{-1}$, which is followed by a gradual drop in the relative velocity. The parabolic shape of the relative distance suggests that it may reach a point of turnaround and the protostars will begin to re-collapse towards the centre. This trend is supported by the declining profile of the relative velocity and the fact that it has fallen well below the escape velocity by the end of the simulation.

In Figure 2.9, we show the mass, radius, and accretion rate of all protostars over time. The solid lines correspond to individual protostars, while the black dashed lines denote the total mass and accretion rate, respectively. The radius of a protostar is calculated as the distance at which the Rosseland mean opacity reaches its maximum value (Stacy et al. 2013). The protostellar mass is given by the mass enclosed within that radius, and the accretion rate by the time derivative of the enclosed mass. A total of eight secondary protostars form during the evolution and fragmentation of the disc. Out of these, four survive until the end of the simulation. The rest merge with other protostars or are tidally disrupted. During the first $\simeq$ 6 yr after the formation of the primary protostar, its mass builds up from $\simeq$ 0.1 to $\simeq$ 6.4 M$_\odot$ at a rate of roughly 1 M$_\odot$ yr$^{-1}$, in agreement with previous work (Latif et al. 2013a; Inayoshi et al. 2014). Its radius increases from $\simeq$ 32 to $\simeq$ 136 R$_\odot$. The second protostar forms after $\simeq$ 7 yr with an initial mass of $\simeq$ 0.02 M$_\odot$ and a radius of $\simeq$ 22 R$_\odot$. Most of the gas is ac-

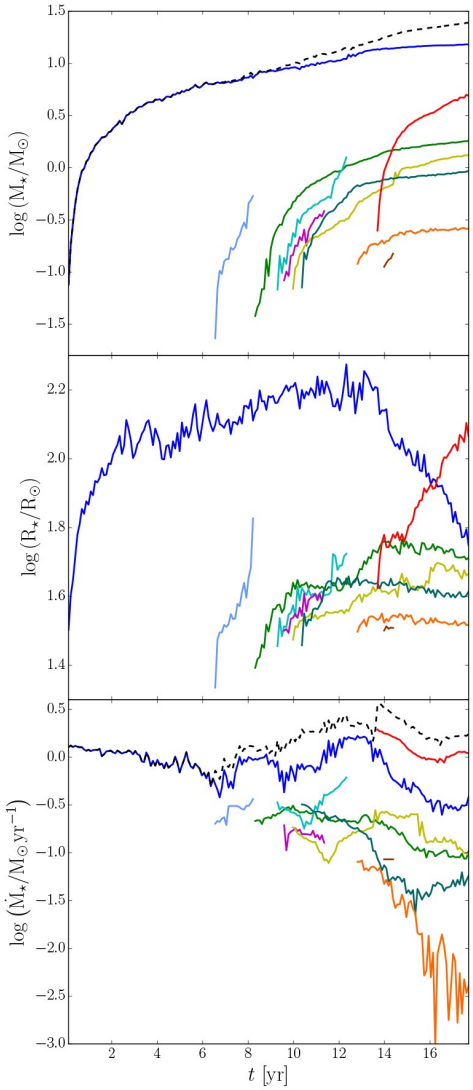


**Figure 2.9:** Stellar mass, radius, and accretion rate of all protostars formed in the simulation. Each line corresponds to an individual protostar, and the black dashed lines shows the total mass and accretion rate, respectively. Initially, the mass budget is entirely dominated by the primary protostar (blue line), which grows from $\simeq 0.1$ to $\simeq 15\,\mathrm{M}_\odot$ at a rate of $\simeq 1\,\mathrm{M}_\odot\,\mathrm{yr}^{-1}$, while its radius swells to well over $100$ au. Once the primary protostar is expelled from the centre, its accretion rate and size drop significantly. The protostar formed in the secondary clump (red line) grows to about $5\,\mathrm{M}_\odot$ at a rate of $\gtrsim 1\,\mathrm{M}_\odot\,\mathrm{yr}^{-1}$. The other protostars stay below $\simeq 2\,\mathrm{M}_\odot$, and thus do not contribute significantly to the total protostellar mass.

creted by the primary protostar, while the second protostar only accretes at a rate of $\simeq 0.3\,\mathrm{M_\odot\,yr^{-1}}$ before it is tidally disrupted.

Shortly thereafter, the disc fragments vigorously and gives rise to a protostellar system characterized by a massive primary protostar with $\simeq 9.2\,\mathrm{M_\odot}$ and a radius of $\simeq 160\,\mathrm{R_\odot}$, while the secondary protostars only have masses between $\simeq 0.06$ and $\simeq 0.6\,\mathrm{M_\odot}$, and radii in the range $\simeq 26 - 41\,\mathrm{R_\odot}$. The accretion on to the secondary protostars results in a slight decrease of the accretion rate on to the primary protostar of $\simeq 0.5\,\mathrm{M_\odot\,yr^{-1}}$, while the total accretion rate remains roughly constant at $1.5\,\mathrm{M_\odot\,yr^{-1}}$. After $\simeq 13$ yr, the primary protostar is expelled from the centre of the halo and the disc is disrupted (see bottom row of Figure 2.7). As the primary protostar is deprived of gas, its accretion rate drops to $\lesssim 0.3\,\mathrm{M_\odot\,yr^{-1}}$, and its radius decreases from $\simeq 160$ to $\simeq 56\,\mathrm{R_\odot}$. Its final mass is $\simeq 15\,\mathrm{M_\odot}$.

The formation of a protostellar system has recently been reported in studies of minihaloes that cool via $H_2$ lines (Clark et al. 2008, 2011; Greif et al. 2011). Initial masses of protostars in atomic cooling haloes are an order of magnitude higher, while the accretion rates exceed those in minihaloes by about three orders of magnitude. Other studies have found similar values for the initial protostellar masses and accretion rates (Regan & Haehnelt 2009; Latif et al. 2013a; Regan et al. 2014a; Inayoshi et al. 2014).

### 2.3.5 Secondary clump

About 13 yr into the evolution of the protostellar system, a second clump collapses at a distance of about 150 au from the primary clump. Figure 2.10 shows both clumps in a cube with a side length of 300 au at the end of the simulation, with smaller cubes showing zoom-ins on to the individual clumps. The zoom-in of the secondary clump shows a protostar with a disc and spiral arms similar to the early evolutionary stages of the primary clump. The protostar in the secondary clump is denoted by the red line in Figure 2.9. Its mass quickly grows from $\simeq 0.2$ to $\simeq 4.9\,\mathrm{M}_{\odot}$, and its radius increases from $\simeq 42$ to $\simeq 116\,\mathrm{R}_{\odot}$. Despite its later formation, it accretes more rapidly than the first protostar. Ultimately, both clumps may evolve into a wide binary system.

### 2.3.6 Caveats

Previous studies that investigated the collapse and fragmentation of gas in atomic cooling haloes did not have sufficiently high resolution to self-consistently follow the formation of protostars at the centre of the cloud. We have attempted to address this shortcoming by performing a simulation that is not resolution-limited. Nevertheless, we have neglected some physical processes that might affect the fragmentation of the cloud. In particular, we have assumed that the optically thin regime for atomic hydrogen cooling extends up to densities $\simeq 10^{16}\,\mathrm{cm}^{-3}$. In reality, the gas becomes optically

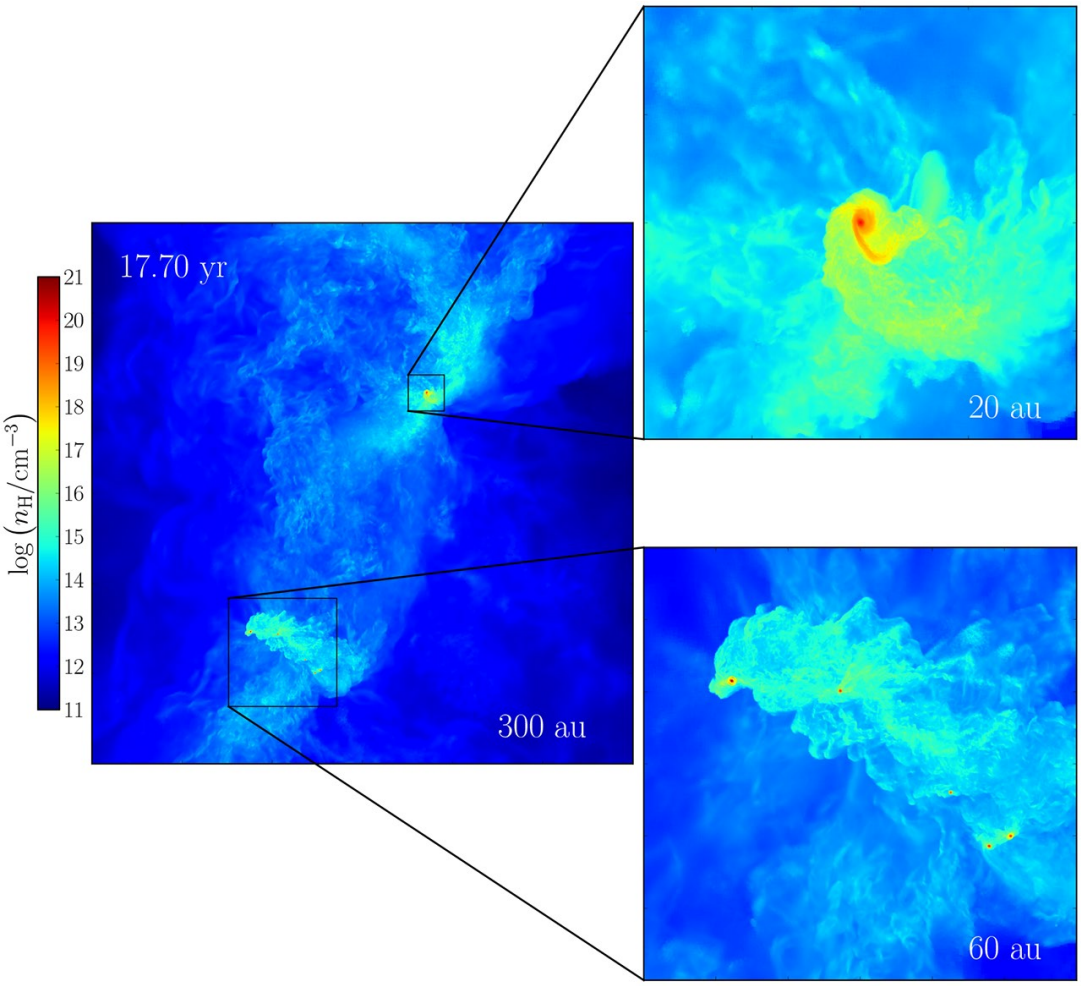


**Figure 2.10:** Simultaneous collapse of a secondary gas clump at a distance of $150$ au from the primary clump in the atomic cooling halo. The number density of hydrogen nuclei is weighted with the square of the density along the line of sight in a cube with a side length of $300$ au. The panels on the right show zoom-ins on the primary and secondary clumps with a side length of 60 and $20$ au, respectively. While strong interactions occur in the central protostellar system, a second clump has collapsed and is in the early stages of its evolution. Ultimately, the clumps may evolve into a wide binary system.

thick to Ly$\alpha$ radiation at densities of $\simeq 10^6\,\mathrm{cm}^{-3}$, and then free-bound continuum emission of $H^-$ becomes the main cooling agent. Previous studies have found that this kind of cooling may lower the temperature by up to a factor of 2 in the range $n \simeq 10^{15} - 10^{20}\,\mathrm{cm}^{-3}$ compared to our study (Omukai 2001; Inayoshi et al. 2014). A lower temperature should translate into a lower Toomre parameter, which would enhance the fragmentation seen in our simulation. In addition, at $n_\mathrm{H} \gtrsim 10^{16}\,\mathrm{cm}^{-3}$ we have introduced an artificial cut-off for continuum cooling in order to approximately reproduce the density-temperature relation found in Omukai (2001). This simplification may also affect the thermal and gravitational stability of the gas.

Another factor that might influence the temperature of the disc is the heating from the accretion luminosity of the primary protostar. The accretion luminosity is given by

$$\Gamma_\mathrm{acc} = \kappa_\mathrm{P} \left( \frac{L_\mathrm{acc}}{4\pi r^2} \right), \tag{2.4}$$

where $\kappa_\mathrm{P}$ is the Planck mean opacity, $r$ the distance from the source, and $L_\mathrm{acc} = GM_\star \dot{M}_\star / R_\star$ the accretion luminosity. The effects of the accretion luminosity have been discussed in similar studies that focused on minihaloes (Greif et al. 2011; Smith et al. 2011). They found that the additional heating of the gas may slightly delay fragmentation, but does not prevent it. The photospheric temperature of the protostar of $\simeq 8000\,\mathrm{K}$ during the early stages of the collapse is too low to produce significant amounts of ionizing radiation. Latif et al. (2013a) investigated the influence of

accretion luminosity in atomic cooling haloes. Assuming a power-law relation between the mass and the radius of the star, and an accretion rate of $\simeq 1\,\mathrm{M}_\odot\,\mathrm{yr}^{-1}$, they computed an accretion luminosity of $\simeq 2 \times 10^{-4}\,\mathrm{erg\,cm^{-3}\,s^{-1}}$ for a $500\,\mathrm{M}_\odot$ clump with a size of $\simeq 100\,\mathrm{au}$ and a temperature of $\simeq 8000\,\mathrm{K}$. This value is comparable to the energy emitted by Ly$\alpha$ cooling, and may exceed it once the mass of the clump reaches $\simeq 1000\,\mathrm{M}_\odot$. However, Latif et al. (2013a) found that this difference only translates into an increase of the temperature by $\simeq 500\,\mathrm{K}$. Since we investigate the evolution of the protostellar system at even earlier times, when the mass of the protostar is much lower, the effects of the accretion luminosity are expected to be even smaller.

Next to the aforementioned cooling and heating processes, we do not include the effects of magnetic fields. These are expected to become dynamically important in minihaloes as well as atomic cooling haloes (e.g. Xu et al. 2008; Schleicher et al. 2010; Sur et al. 2010; Peters et al. 2012, 2014; Schober et al. 2012; Turk et al. 2012; Latif et al. 2013c). Indeed, Latif et al. (2014b) found that the magnetic pressure provides additional support against gravity and delays or suppresses fragmentation. Future simulations should therefore include magnetic fields as well as a more detailed chemical and thermal model.

## 2.4 Summary and Conclusions

We have performed the highest-resolution cosmological simulation to date of the formation and evolution of a protostellar system in an atomic cooling halo. We follow the collapse of the gas from a few Mpc down to $\lesssim 0.01\,\mathrm{au}$, spanning almost 13 orders of magnitude in scale, and reaching densities as high as $n_{\mathrm{H}} \simeq 10^{22}\,\mathrm{cm}^{-3}$. The simulation includes an equilibrium/non-equilibrium primordial chemistry solver that evolves five species (H, $H_2$, $H^-$, $H^+$, and $e^-$), and includes $H_2$ line emission, $H_2$ collision-induced emission, Ly$\alpha$ cooling, and inverse Compton cooling. Additionally, we have included a uniform LW background of strength $J_{21} = 10^5$ to prevent star formation in progenitor haloes.

During the initial collapse, the gas is shock-heated to the virial temperature of about $10^4$ K. The molecular hydrogen abundance briefly increases due to the presence of supersonic shocks, but the external radiation background photodissociates $H_2$ to a level of $y_{\mathrm{H}_2} \sim 10^{-7}$ within the halo. As a result, runaway collapse due to Ly$\alpha$ cooling ensues once the virial mass has risen to $\simeq 5 \times 10^7\,\mathrm{M}_\odot$. The central gas cloud becomes Jeans-unstable with a mass of $\simeq 10^6\,\mathrm{M}_\odot$ and collapses nearly isothermally over many orders of magnitude in density, characterized by a profile of the form $\rho \propto r^{-2}$. At densities $n_{\mathrm{H}} \sim 10^6\,\mathrm{cm}^{-3}$, the gas becomes optically thick to Ly$\alpha$ emission and effectively cools via free-bound continuum emission of $H^-$ up to a density of $n_{\mathrm{H}} \sim 10^{16}\,\mathrm{cm}^{-3}$, where the continuum emission is trapped. The average $H_2$ abun-

dance increases to $y_{H_2} \sim 10^{-4}$ at $n_H \gtrsim 10^{10}\,cm^{-3}$ due to three-body reactions, but never becomes high enough for $H_2$ line emission to become important. The $H^+$ abundance declines to $\simeq 10^{-8}$ due to recombinations before increasing to unity for densities $\gtrsim 10^{16}\,cm^{-3}$, where the gas evolves nearly adiabatically and a protostar with an initial mass of $\simeq 0.1\,M_\odot$ is formed.

Following the formation of the primary protostar, the gas settles into a Keplerian disc. The Toomre parameter within the disc is close to unity, such that perturbations can grow. The emerging spiral arms feed gas on to the primary protostar at a rate of $\simeq 1\,M_\odot\,yr^{-1}$. However, this is not sufficient to process the mass that accretes from the surrounding cloud on to the disc. In combinations with the efficient cooling of the gas via continuum emission, the disc becomes gravitationally unstable and a secondary protostar forms after only $\simeq 7\,yr$. The disc continues to fragment, such that after $\simeq 18\,yr$ a total of eight secondary protostars have formed. By the end of the simulation, four of these have survived, while the rest have merged away or are tidally disrupted. The primary protostar has grown to a mass of $\simeq 15\,M_\odot$, while all other secondary protostars have masses $\lesssim 2\,M_\odot$. Three-body interactions lead to the temporary ejection of the primary protostar from the disc after $\simeq 12\,yr$, which is disrupted in the process. However, an analysis of the relative velocity of the protostars shows that it is well below the escape velocity. It will therefore likely return to the centre of the cloud. After $\simeq 13\,yr$, a second clumps collapses at a distance of $\simeq 150\,au$ from the primary clump. It has not yet fragmented and contains a single protostar that

rapidly grows to $\simeq 5\,\mathrm{M}_\odot$. If this clump show a similar pattern of rapid migration and merging, the cloud may evolve into a wide binary system.

Despite the temporary ejection of the primary protostar from the centre of the cloud, subfragmentation likely does not substantially impede its growth. Once it returns to the centre of the cloud, its accretion rate will likely again increase to $\simeq 1\,\mathrm{M}_\odot\,\mathrm{yr}^{-1}$. In addition, the secondary protostars formed in the disc quickly migrate to the centre of the cloud, where they merge with the primary protostar. They are also typically 10 times less massive than the primary protostar, which has accreted $\simeq 15\,\mathrm{M}_\odot$ by the end of the simulation, while the most massive secondary protostar has only grown to $\simeq 1.5\,\mathrm{M}_\odot$. Most of the accreted material thus does not stem from other protostars, but from the bar-like instabilities in the disc. The secondary clump may be a much more potent candidate for accreting mass that may have otherwise been accreted by the primary clump, but even in this case the growth of the most massive protostar would be reduced by at most a factor of 2. It thus appears that fragmentation is not a significant barrier for forming at least one massive BH seed per atomic cooling halo, assuming that the LW background is high enough to prevent $H_2$ cooling. Recent simulations have shown that this may indeed be the much more limiting factor (Latif et al. 2014a, 2015; Regan et al. 2014b).

One of the main caveats of this study is the simplified chemistry and cooling network. Future work should include a more detailed chemical model, such as that used in Inayoshi et al. (2014). It may also become possible to treat the radiative transfer

of the various line and continuum processes (e.g. Greif 2014). Finally, the influence of magnetic fields may be investigated with modules that have already been implemented in AREPO (Pakmor et al. 2011). The influence of the radiation may not be that strong, since it is difficult to heat the gas above $\simeq 10^4$ K, while magnetic fields may have a substantial effect on the thermal and gravitational stability of the cloud (e.g. Latif et al. 2013c, 2014b). The additional support provided by magnetic fields may reduce the ability of the gas to fragment, and further increase the accretion rate of the primary protostar.

## 2.5 Appendix: Chemical solver

We here describe a new solver implemented in AREPO that combines a non-equilibrium solver for low densities with an equilibrium solver for high densities. This tiered approach allows us to seamlessly model the extremely large dynamic range of more than 20 orders of magnitude in density that builds up in self-gravitating, primordial gas clouds.

### 2.5.1 Methodology

We use an operator-split approach to solve for the coupled evolution of the chemical abundances and internal energy of the gas, represented by a system of first-order dif-

ferential equations:

$$\dot{\mathbf{y}} = \mathbf{F}(t, \mathbf{y}), \tag{2.5}$$

where $\mathbf{y}$ denotes the chemical species and internal energy, $\mathbf{F}$ is a function that incorporates the rate equations, and $t$ denotes the time. The time dependency implicitly includes all external dependencies, such as on density and redshift. For a given hydrodynamic time step $\Delta t$, the above differential equation is integrated using the publicly available solver SUNDIALS CVODE, which employs a variable order, variable step multistep backward differencing scheme (Hindmarsh et al. 2005). We model three independent chemical species: $H^-$, $H_2$, and $H^+$. The abundance of $H^-$ may be trivially derived from that of $H^+$, such that only the abundances of $H_2$ and $H^+$ are included in $\mathbf{y}$. The electron abundance is trivially given by $y_e = y_{H^+}$, and that of neutral hydrogen by $y_{H\,I} = 1 - 2y_{H_2} - y_{H^+}$, where $y_X = n_X/n_H$ denotes the ratio of the number density of chemical species $X$ to the number density of hydrogen nuclei. The latter is given by $n_H = X_H \rho / m_H$, where $X_H = 0.76$ is the cosmological mass fraction of hydrogen, $\rho$ the volumetric mass density, and $m_H$ the mass of the hydrogen atom. Since reactions involving helium are comparatively unimportant at the densities and temperatures modelled here, we assume that it remains chemically inert and is in the ground electronic state. Because of the tight coupling of some of the chemical rates to the internal energy, a relative accuracy of $f_{acc,neq} = 10^{-4}$ is necessary to avoid significant spurious oscillations. Below $y_{abs} = 10^{-20}$, the chemical species are no longer

| No. | Process | Rate coefficient | Units | Reference |
|---|---|---|---|---|
| 1 | $H + e^- \rightarrow H^- + \gamma$ | $1.4 \times 10^{-18} T_K^{0.928} \exp(-T_K/1.62 \times 10^4)$ | $cm^3\,s^{-1}$ | Galli & Palla (1998) |
| 2 | $H + H^- \rightarrow H_2 + e^-$ | $1.35 \times 10^{-9}(T_K^{0.098493} + 0.32852 T_K^{0.5561}$ $+2.771 \times 10^{-7} T_K^{2.1826})/(1 + 6.191 \times 10^{-3} T_K^{1.0461}$ $+8.9712 \times 10^{-11} T_K^{3.0424} + 3.2576 \times 10^{-14} T_K^{3.7741})$ | $cm^3\,s^{-1}$ | Kreckel et al. (2010) |
| 3 | $3H \rightarrow H + H_2$ | $6 \times 10^{-32} T_K^{-0.25} + 2 \times 10^{-31} T_K^{-0.5}$ | $cm^6\,s^{-1}$ | Forrey (2013) |
| 4 | $2H + H_2 \rightarrow 2H_2$ | $k_3/8$ | $cm^6\,s^{-1}$ | Jacobs et al. (1967) |
| 5 | $H + H_2 \rightarrow 3H$ | $q_{H_2} k_3$ | $cm^3\,s^{-1}$ | Detailed balance with (3) |
| 6 | $2H_2 \rightarrow 2H + H_2$ | $q_{H_2} k_4$ | $cm^3\,s^{-1}$ | Detailed balance with (4) |
| 7 | $H_2 + \gamma \rightarrow 2H$ | $1.38 \times 10^{-12}$ | $s^{-1}$ | Abel et al. (1997) |
| 8 | $H + e^- \rightarrow H^+ + 2e^-$ | $\exp[-32.71396786 + 13.536556 \ln T_{eV}$ $-5.73932875(\ln T_{eV})^2 + 1.56315498(\ln T_{eV})^3$ $-0.2877056(\ln T_{eV})^4 + 0.0348255977(\ln T_{eV})^5$ $-2.63197617 \times 10^{-3}(\ln T_{eV})^6$ $+1.11954395 \times 10^{-4}(\ln T_{eV})^7$ $-2.03914985 \times 10^{-6}(\ln T_{eV})^8]$ | $cm^3\,s^{-1}$ | Janev et al. (1987) |
| 9 | $H^+ + e^- \rightarrow H + \gamma$ | $2.753 \times 10^{-14}(3.15614 \times 10^5/T_K)^{1.5}$ $\times(1 + (1.15188 \times 10^5/T_K)^{0.407})^{-2.242}$ | $cm^3\,s^{-1}$ | Ferland et al. (1992) |
| 10 | $H^+ + e^- \rightarrow H + \gamma$ | $k_8/q_H$ | $cm^6\,s^{-1}$ | Detailed balance with (8) |
| 11 | $H_2$ line cooling | $\mathrm{dex}[-103 + 97.59 \log T_K - 48.05(\log T_K)^2$ $+10.8(\log T_K)^3 - 0.9032(\log T_K)^4]$ | $erg\,cm^3\,s^{-1}$ | Galli & Palla (1998) |
| 12 | $H_2$ CIE | $5.3 \times 10^{-49} T_K^4$ | $erg\,cm^3\,s^{-1}$ | Ripamonti & Abel (2004) |
| 13 | Ly$\alpha$ cooling | $7.5 \times 10^{-19} \exp(-1.18348 \times 10^5/T_K)$ $/\left[1 + (T_K/10^5)^{0.5}\right]$ | $erg\,cm^3\,s^{-1}$ | Cen (1992) |
| 14 | IC cooling | $5.65 \times 10^{-36} T_{CMB,K}^4 (T_K - T_{CMB,K})$ | $erg\,s^{-1}$ | Peebles (1971) |

**Table 2.1:** Chemistry and cooling network, and the corresponding rate coefficients. $T_K$ denotes the temperature in units of K, $T_{eV}$ the temperature in units of eV, and $T_{CMB,K} = 2.725(1+z)^4$ the temperature of the CMB in units of K. The equilibrium constants $q_{H_2}$ and $q_H$ are introduced in Section 2.5.2.

evolved accurately, which avoids an unnecessary computational overhead.

### 2.5.2 Chemistry

The chemical and thermal processes included in our reaction network are shown in Table 2.1, together with the corresponding rate coefficients and references. To enable fast look-up, the rates are linearly interpolated from a table with 5000 logarithmically spaced temperature bins between 10 and $10^8$ K. Because of the comparatively large reaction rates, we assume that $H^-$ is in chemical equilibrium:

$$y_{H^-} = \frac{k_1}{k_2} y_{H^+}, \tag{2.6}$$

where $k_1$ denotes the rate coefficient for the formation of $H^-$ via radiative association of H I and free electrons, and $k_2$ the rate coefficient for the destruction of $H^-$ by associative detachment with H I. The latter reaction results in the formation of $H_2$. Molecular hydrogen may also be formed by three-body reactions involving three hydrogen atoms or two hydrogen atoms and one hydrogen molecule, while it is destroyed by collisions with hydrogen atoms and molecules, as well as radiation in the Lyman–Werner (LW) bands:

$$\begin{aligned}\dot{y}_{H_2} = {} & k_2 y_{H^-} y_{H\,I} n_H + (k_3 y_{H\,I}^3 + k_4 y_{H_2} y_{H\,I}^2) n_H^2 \\ & - k_5 y_{H_2} y_{H\,I} n_H - k_6 y_{H_2}^2 n_H - k_7 J_{21} f_{sh} y_{H_2},\end{aligned} \tag{2.7}$$

where $J_{21}$ denotes the specific intensity in units of $10^{-21}\,\mathrm{erg\,s^{-1}\,cm^{-2}\,Hz^{-1}\,sr^{-1}}$ in the LW bands. We use the recently updated rate coefficients for associative detachment and three-body $H_2$ formation of Kreckel et al. (2010) and Forrey (2013), respectively. The shielding factor for incident LW radiation is given by

$$f_{sh} = \frac{0.965}{(1 + x/b_5)^{1.1}} + \frac{0.035}{(1+x)^{0.5}} \times \exp\left[-8.5 \times 10^{-4} (1+x)^{0.5}\right], \tag{2.8}$$

where $x = N_{\mathrm{H_2,eff}}/5 \times 10^{14}\,\mathrm{cm}^{-2}$, $N_{\mathrm{H_2,eff}}$ is the effective $H_2$ column density (see Section **??**), $b_5 = v_{\mathrm{th}}/\left(\mathrm{km\,s}^{-1}\right)$, and $v_{\mathrm{th}}$ the thermal velocity of the $H_2$ molecules:

$$v_{\mathrm{th}} = \sqrt{2k_{\mathrm{B}}T/m_{\mathrm{H_2}}}. \tag{2.9}$$

Here, $m_{\mathrm{H_2}}$ denotes the mass of the $H_2$ molecule, $k_{\mathrm{B}}$ Boltzmann's constant, and $T$ the temperature of the gas (Draine & Bertoldi 1996; Wolcott-Green et al. 2011).

The collisional dissociation rates are obtained from the three-body formation rates by applying the principle of detailed balance:

$$k_{\mathrm{diss}} = q_{\mathrm{H_2}} k_{\mathrm{3b}}, \tag{2.10}$$

where $q_{\mathrm{H_2}}$ is the equilibrium constant:

$$q_{\mathrm{H_2}} = \frac{n_{\mathrm{H\,I}}^2}{n_{\mathrm{H_2}}} = \frac{Z_{\mathrm{H}}^2}{Z_{\mathrm{H_2}}} \left(\frac{\pi m_{\mathrm{H}} k_{\mathrm{B}} T}{h_{\mathrm{p}}^2}\right)^{3/2} \exp\left(-\chi_{\mathrm{H_2}}/k_{\mathrm{B}}T\right), \tag{2.11}$$

and $h_{\mathrm{p}}$ denotes Planck's constant, $\chi_{\mathrm{H_2}} = 4.48\,\mathrm{eV}$ the binding energy of $H_2$, and $Z_{\mathrm{H}}$ and $Z_{\mathrm{H_2}}$ the partition functions of atomic and molecular hydrogen, respectively:

$$Z = \sum_i g_i \exp\left(-\frac{E_i}{k_{\mathrm{B}}T}\right), \tag{2.12}$$

where $g_i$ is the degeneracy of state $i$ with energy $E_i$. In the case of atomic hydrogen,

$g_i = 2i^2$, $E_i = \chi_{\rm H}/i^2$, and $\chi_{\rm H} = 13.6\,{\rm eV}$ denote the ionization energy of atomic hydrogen, and the sum is truncated at $i = 5$. In the case of $H_2$, only the ro-vibrational transitions of the electronic ground state are modelled, such that $g_i = 2J_i + 1$, where $J$ denotes the rotational quantum number. The energy levels are taken from Borysow et al. (1989), using vibrational quantum numbers $0 \leq v \leq 2$ and rotational quantum numbers $0 \leq J < 20$, which is sufficient for the regime in which $H_2$ cooling is important.

The formation and destruction of ionized hydrogen is governed by collisional ionization with electrons and the inverse process, recombinations. The recombination rate at high densities is obtained by applying the principle of detailed balance to the collisional ionization rate of Janev et al. (1987) :

$$k_{\rm rec} = k_{\rm coll}/q_{\rm H}, \tag{2.13}$$

where

$$q_{\rm H} = \frac{n_{\rm H^+}^2}{n_{\rm H\,I}} = \frac{2}{Z_{\rm H}} \left( \frac{2\pi m_{\rm e} k_{\rm B} T}{h_{\rm p}^2} \right)^{1.5} \exp\left(-\chi_{\rm H}/k_{\rm B}T\right), \tag{2.14}$$

and $m_{\rm e}$ is the mass of the electron. At low densities, the case B recombination rate of Ferland et al. (1992) is used, which includes recombinations to all levels except the ground state. The two regimes are smoothly adjoined by a transition function, such

that the net $H^+$ formation rate is given by

$$\dot{y}_{H^+} = k_8 y_{H^+} y_{H\,I} n_H - (k_9 y_{H^+}^2 n_H)^d (k_{10} y_{H^+}^3 n_H^2)^{1-d}, \tag{2.15}$$

where

$$d = \frac{1}{1 + n_H / n_{H,trans}}, \tag{2.16}$$

and $n_{H,trans} = 10^{17}\,cm^{-3}$. This ensures that the $H^+$ abundance approaches the thermal equilibrium abundance at high densities, since we do not include the inverse reactions for recombinations to all hydrogen levels (reaction 9 in Table 2.1).

### 2.5.3 Heating and cooling

The rate of change of the volumetric internal energy density $u$ is given by

$$\dot{u} = \Gamma_{chem} - \Lambda_{cool}, \tag{2.17}$$

where $\Gamma_{chem}$ denotes heating due to chemical processes, and $\Lambda_{cool}$ cooling due to radiative processes. We only include the chemical heating and cooling of the gas due to the formation and destruction of $H_2$, since significant amounts of $H^+$ are formed only at very high densities, where the abundances become inaccurate due to various non-ideal gas effects (Ripamonti et al. 2002). The chemical heating rate may therefore be

conveniently written as

$$\Gamma_{\rm chem} = \chi_{\rm H_2} \dot{y}_{\rm H_2} n_{\rm H}. \tag{2.18}$$

The radiative cooling rate is given by

$$\Lambda_{\rm cool} = \Lambda_{\rm line} + \Lambda_{\rm CIE} + \Lambda_{{\rm Ly}\alpha} + \Lambda_{\rm IC}, \tag{2.19}$$

and includes $H_2$ line cooling, $H_2$ collision-induced emission, Ly$\alpha$ cooling, and inverse Compton scattering of electrons with cosmic microwave background (CMB) photons. The $H_2$ line cooling rate is discussed in detail in Section 2.5.4. The cooling rate due to collision-induced emission is given by

$$\Lambda_{\rm CIE} = k_{12} y_{\rm H_2} n_{\rm H}^2 f_{\rm esc}, \tag{2.20}$$

where $k_{12}$ and the escape fraction are taken from Ripamonti & Abel (2004). The latter is given by

$$f_{\rm esc} = \frac{1 - \exp\left(-\tau_{\rm cont}\right)}{\tau_{\rm cont}}, \tag{2.21}$$

where

$$\tau_{\rm cont} = \left( \frac{n_{\rm H}}{n_{\rm H,cont}} \right)^{2.8} \tag{2.22}$$

and $n_{\rm H,cont} = 1.5 \times 10^{16}\,{\rm cm}^{-3}$. The Ly$\alpha$ cooling rate is given by:

$$\Lambda_{{\rm Ly}\alpha} = k_{13} y_{\rm H^+} y_{\rm H\,I} n_{\rm H}^2 f_{\rm esc}, \tag{2.23}$$

where $k_{13}$ is taken from Cen (1992), and

$$f_{\rm esc} = \exp\left(-n_{\rm H}/n_{\rm H,cont}\right). \tag{2.24}$$

The latter approximately reproduces the temperature–density relation found in the one-zone models of Omukai (2001). Finally, the IC cooling rate is given by

$$\Lambda_{\rm IC} = k_{14} y_{\rm H^+} n_{\rm H}, \tag{2.25}$$

where $k_{14}$ is taken from Peebles (1971).

### 2.5.4 $H_2$ LINE COOLING

The $H_2$ line cooling rate is obtained by adjoining the rate in the limit $n_{\rm H} \to 0$ with the LTE rate (Galli & Palla 1998):

$$\Lambda_{\rm line} = \frac{\Lambda_{\rm LTE}}{1 + \Lambda_{\rm LTE}/\Lambda_{n\to 0}}. \tag{2.26}$$

In the above equation, the low-density rate is given by

$$\Lambda_{\mathrm{n}\to 0} = k_{11} y_{\mathrm{H\,I}} y_{\mathrm{H_2}} n_{\mathrm{H}}^2, \tag{2.27}$$

where $k_{11}$ is taken from Galli & Palla (1998). If the gas is optically thin, the cooling rate may be calculated directly from the Einstein coefficients corresponding to the individual ro-vibrational transitions of $H_2$:

$$\Lambda_{\mathrm{LTE,thin}} = \sum_{\mathrm{u,l}} E_{\mathrm{ul}} A_{\mathrm{ul}} n_{\mathrm{u}} \tag{2.28}$$

where $E_{\mathrm{ul}}$ denotes the energy emitted by the transition from the upper state u to the lower state l, $A_{\mathrm{ul}}$ the Einstein coefficient, and $n_{\mathrm{u}}$ the number density of $H_2$ molecules in the upper state. The Einstein coefficients are taken from Turner et al. (1977). The relative numbers of $H_2$ molecules in the upper and lower states are given by

$$B_{\mathrm{u,l}} = \frac{n_{\mathrm{u,l}}}{n_{\mathrm{H_2}}} = \frac{g_{\mathrm{u,l}}}{Z_{\mathrm{H_2}}} \exp\left(-\frac{E_{\mathrm{u,l}}}{k_{\mathrm{B}} T}\right). \tag{2.29}$$

This allows the cooling rate per $H_2$ molecule to be tabulated as a function of temperature:

$$\epsilon_{\mathrm{LTE,thin}} = \sum_{\mathrm{u,l}} E_{\mathrm{ul}} A_{\mathrm{ul}} B_{\mathrm{u}}. \tag{2.30}$$

Ripamonti & Abel (2004) assumed that the optically thick cooling rate can be obtained from the optically thin cooling rate via

$$\epsilon_{\rm LTE} = f_{\rm esc}\epsilon_{\rm LTE,thin}, \tag{2.31}$$

where

$$f_{\rm esc} = \frac{bx}{x^b + b - 1} \tag{2.32}$$

for $x \geq 1$ and $f_{\rm esc} = 1$ for $x < 1$. The parameter $x$ is given by

$$x = b^{1/(b-1)} \frac{n_{\rm H}}{X_{\rm H} n_{\rm H,line}}, \tag{2.33}$$

where $b = 1.45$ and $n_{\rm H,line} = 8 \times 10^9\,{\rm cm}^{-3}$. This formula reproduces the slope of the fit to the detailed one-dimensional calculations of Ripamonti et al. (2002), but has the advantage of a continuous derivative at $x = 1$.

### 2.5.5 Adiabatic index

The pressure, temperature, and internal energy density of the gas are related via

$$P = \rho \frac{k_{\rm B} T}{\mu m_{\rm H}} = (\gamma - 1)u, \tag{2.34}$$

where $\mu$ and $\gamma$ denote the mean molecular weight and adiabatic index of the gas, respectively. The latter is given by

$$\frac{1}{\gamma - 1} = \frac{\sum_i y_i/(\gamma_i - 1)}{\sum_i y_i}, \tag{2.35}$$

where the sum extends over all chemical species. In our case, the adiabatic index is given by

$$\frac{1}{\gamma - 1} = \frac{1 + y_{\rm He} - 2y_{\rm H_2} + y_{\rm H^+}}{y_n\,(\gamma_{\rm m} - 1)} + \frac{y_{\rm H_2}}{y_n\,(\gamma_{\rm H_2} - 1)}, \tag{2.36}$$

where $y_n = 1 + y_{\rm He} - y_{\rm H_2} + y_{\rm H^+}$ and $y_{\rm He} = (1/X_{\rm H} - 1)\,/4$. The adiabatic index for a monatomic gas is given by $\gamma_{\rm m} = 5/3$, and for $\rm H_2$ by

$$\frac{1}{\gamma_{\rm H_2} - 1} = \frac{5}{2} + \frac{x^2 {\rm e}^x}{({\rm e}^x - 1)^2}, \tag{2.37}$$

where $x = 6.1 \times 10^3\,{\rm K}/T$. The second term in this equation accounts for the vibrational degrees of freedom of $\rm H_2$ (Yoshida et al. 2006). In analogy to the adiabatic index, the mean molecular weight of the gas is given by

$$\mu = \frac{\sum_i m_i y_i}{m_{\rm H} \sum_i y_i}, \tag{2.38}$$

where $m_i$ denotes the particle mass of species $i$. Here, this simplifies to

$$\mu = \frac{1 + 4y_{\mathrm{He}}}{1 + y_{\mathrm{He}} - y_{\mathrm{H_2}} + y_{\mathrm{H^+}}}. \tag{2.39}$$

### 2.5.6 Equilibrium chemistry

Once the density exceeds $n_{\mathrm{H_2,eq}} = 10^{15}\,\mathrm{cm}^{-3}$, the $H_2$ abundance may be safely assumed to be in thermal equilibrium (Omukai & Nishi 1998). This simplifies the chemistry, since updating the $H_2$ abundance only requires the solution of an implicit equation instead of a coupled differential equation. For a new internal energy, the updated $H_2$ abundance must be consistent with the chemical heating and cooling of the gas due to the formation and dissociation of $H_2$:

$$u - u_{\mathrm{init}} = \chi_{\mathrm{H_2}}(y_{\mathrm{H_2}} - y_{\mathrm{H_2,init}})n_{\mathrm{H}}, \tag{2.40}$$

where $u_{\mathrm{init}}$ and $y_{\mathrm{H_2,init}}$ are the internal energy density and $H_2$ abundance at the beginning of the time step. According to equation 2.11, the $H_2$ abundance is related to the temperature via

$$\frac{(1 - 2y_{\mathrm{H_2}} - y_{\mathrm{H^+}})^2}{y_{\mathrm{H_2}}} = \frac{q_{\mathrm{H_2}}}{n_{\mathrm{H}}}, \tag{2.41}$$

which is solved with a bisection method that uses $u = (u_{\mathrm{max}} - u_{\mathrm{min}})/2$ as an initial guess for the internal energy. Here, $u_{\mathrm{min}} = f_{\mathrm{bi}} u_{\mathrm{init}}$, $u_{\mathrm{max}} = u_{\mathrm{init}}/f_{\mathrm{bi}}$, and $f_{\mathrm{bi}} = 0.1$

gives robust minimum and maximum values.

For each new guess of the internal energy, the adiabatic index, mean molecular weight, and temperature are updated using the $H_2$ fraction at the beginning of the time step. This does not result in a substantial error, since the adiabatic index and mean molecular weight do not change much over a single time step. The updated temperature is used to compute the equilibrium constant $q_{H_2}$, which is then used to solve the above equation. The physically meaningful solution is the negative branch of

$$y_{H_2} = \frac{-B \pm E}{2A}, \tag{2.42}$$

where the coefficients are given by

$$A = 4, \tag{2.43}$$

$$B = -4\left(1 - y_{H^+}\right) - q_{H_2}/n_H, \tag{2.44}$$

$$C = \left(1 - y_{H^+}\right)^2, \tag{2.45}$$

$$D = 4AC, \tag{2.46}$$

$$E = \left(B^2 - D\right)^{1/2}. \tag{2.47}$$

A subtle problem arises if $D$ is much smaller than $B^2$. In this case, $E$ may be truncated due to rounding errors, which results in $E = B^2$ and $y_{H_2} = 0$. This unphysical

solution is avoided by a Taylor expansion of $E$ around $D = 0$:

$$E = |B| - \frac{D}{2\,|B|}. \tag{2.48}$$

For $D < 10^{-10} B^2$, the $H_2$ abundance is therefore given by

$$y_{H_2} = \frac{D}{4A\,|B|}, \tag{2.49}$$

where we have exploited the fact that $B < 0$. Once the new $H_2$ abundance has been obtained, the new internal energy density is used as a solution if $(u_{\rm new} - u_{\rm init})\,/u_{\rm init} < f_{\rm acc,eq} = 10^{-7}$. This comparatively high accuracy is necessary to obtain a self-consistent solution at the very high densities and temperatures within metal-free protostars. After the equilibrium step is completed, the non-equilibrium solver is used to update the $H^+$ abundance as well as the internal energy density, which is subject to radiative cooling. The equilibrium and non-equilibrium steps are subcycled on a time step:

$$\Delta t_{\rm sub} = f_{\rm sub} \Delta t, \tag{2.50}$$

where we have found that $f_{\rm sub} = 0.2$ suppresses visible fluctuations.

For $n_{\rm H} \gtrsim n_{\rm H^+,eq} = 10^{18}\,{\rm cm}^{-3}$, the $H^+$ abundance also converges to the thermal equilibrium value (Omukai & Nishi 1998). As opposed to $H_2$, we do not account for the chemical heating and cooling of the gas due to changes in the $H^+$ abundance. A

further simplification arises due to the fact that the $H_2$ abundance generally decreases to well below unity as the $H^+$ abundance increases to unity. The resulting equation is therefore comparatively simple:

$$\frac{y_{H^+}^2}{1 - y_{H^+}} = \frac{q_H}{n_H}. \tag{2.51}$$

The root of this equation is found using the same bisection method as for the $H_2$ abundance, but with $f_{bi} = 0.01$. Since the $H_2$ abundance may depend sensitively on the $H^+$ abundance, the latter is updated first.

*"Aujourd'hui, maman est morte. Ou peut-être*

*hier, je ne sais pas."*

Albert Camus

# 3

# Opacity limit for supermassive protostars

This chapter has been published as

Becerra, F., Marinacci, F., Inayoshi, K., Bromm, V., & Hernquist, L. E. (2018). Opacity limit for supermassive protostars. *ApJ*, 857, 138.

ABSTRACT

We present a model for the evolution of supermassive protostars from their formation at $M_\star \simeq 0.1\,\mathrm{M}_\odot$ until their growth to $M_\star \simeq 10^5\,\mathrm{M}_\odot$. To calculate the initial properties of the object in the optically thick regime, we follow two approaches: one based on idealized thermodynamic considerations, and another based on a more detailed one-zone model. Both methods derive a similar value of $n_\mathrm{F} \simeq 2 \times 10^{17}\,\mathrm{cm}^{-3}$ for the density of the object when opacity becomes important, i.e. the opacity limit. The subsequent evolution of the growing protostar is determined by the accretion of gas onto the object and can be described by a mass-radius relation of the form $R_\star \propto M_\star^{1/3}$ during the early stages, and of the form $R_\star \propto M_\star^{1/2}$ when internal luminosity becomes important. For the case of a supermassive protostar, this implies that the radius of the star grows from $R_\star \simeq 0.65\,\mathrm{AU}$ to $R_\star \simeq 250\,\mathrm{AU}$ during its evolution. Finally, we use this model to construct a sub-grid recipe for accreting sink particles in numerical simulations. A prime ingredient thereof is a physically motivated prescription for the accretion radius and the effective temperature of the growing protostar embedded inside it. From the latter, we can conclude that photo-ionization feedback can be neglected until very late in the assembly process of the supermassive object.

## 3.1 Introduction

Recent observations at redshifts $z \gtrsim 6$ suggest that quasars were already powered by supermassive black holes (SMBHs) with masses $\gtrsim 10^9\,\mathrm{M}_\odot$ when the Universe was less than one billion years old (Fan et al. 2003, 2006; Mortlock et al. 2011; Wu et al. 2015). These SMBHs most likely grew from smaller seed BHs that formed earlier, but the origin of these seeds remains unclear (Haiman 2006, 2009; Bromm & Yoshida 2011; Greene 2012; Volonteri 2012; Volonteri & Bellovary 2012). Furthermore, feedback and self-regulation of the seeds make the study of their formation and growth even more complex (Milosavljević et al. 2009). The two most promising theories concerning the formation of seed BHs at high redshift are the remnants of massive Population III stars (Madau & Rees 2001; Li et al. 2007; Johnson et al. 2012), and the direct collapse of primordial gas in haloes with virial temperatures $T_{\mathrm{vir}} \gtrsim 10^4\,\mathrm{K}$, the so-called atomic cooling haloes (Bromm & Loeb 2003; Begelman et al. 2006; Spaans & Silk 2006).

In the direct collapse scenario, high temperatures are reached in haloes where cooling by molecular hydrogen and metal lines to below $\simeq 10^4\,\mathrm{K}$ has been suppressed, which implies that the only coolant acting on the gas is atomic hydrogen (Omukai 2001; Oh & Haiman 2002). In the case of molecular hydrogen, which naturally forms at the center of the halo, its photo-dissociation can be achieved by an external soft ultraviolet (UV) background in the Lyman-Werner (LW) bands. Previous studies

have found that this leads to a nearly isothermal collapse at $T_{\rm vir} \simeq 10^4\,{\rm K}$ due to initially Lyman-$\alpha$ cooling, and subsequently $H^-$ bound-free and free-free emission, when higher densities are reached (Regan & Haehnelt 2009; Latif et al. 2013b; Inayoshi et al. 2014; Becerra et al. 2015; Chon et al. 2016). High-resolution simulations have shown that, as the gas collapses and reaches densities of $\simeq 10^{17}{\rm cm}^{-3}$, it becomes optically thick to $H^-$ radiation, and a massive protostar with an accretion rate of $\simeq 1\,{\rm M}_\odot\,{\rm yr}^{-1}$ forms at the center of the halo (Inayoshi et al. 2014; Van Borm et al. 2014; Becerra et al. 2015; Latif et al. 2016). Due to this high accretion rate, the central object can easily become a supermassive star of $\simeq 10^5 - 10^6\,{\rm M}_\odot$ within a million years (Regan & Haehnelt 2009; Latif et al. 2013b), which later might collapse into an SMBH due to relativistic instabilities (Baumgarte & Shapiro 1999; Umeda et al. 2016; Woods et al. 2017, see also Figure 3.1).

In this work, we study the physics of the central object when it approaches the optically thick regime. In particular, we investigate the properties of the emerging protostar when the optical depth due to $H^-$ emission becomes unity, thus extending the classical theory of opacity-limited fragmentation developed for present-day star formation (Low & Lynden-Bell 1976; Rees 1976). Previous studies have explored this scenario using detailed one-zone models (e.g. Omukai 2001). Here, we present an alternative approach based on both simplified dimensional arguments and a fitting formula for the cooling and heating processes within the non-equilibrium chemistry of H and $H^-$ ions. In addition, we develop an idealized model for the subsequent evolution

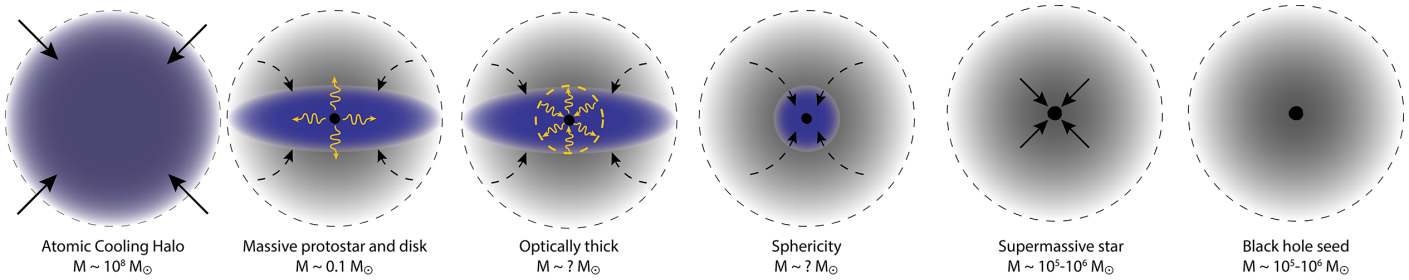


**Figure 3.1:** Overview of the formation of a supermassive black hole seed. An atomic cooling halo of virial (total) mass $M \simeq 10^8 \mathrm{M}_\odot$ and exposed to strong Lyman-Werner background radiation collapses. The gas reaches the optically thick regime first on small scales, such that a central protostar of initial mass $M \simeq 0.1\,\mathrm{M}_\odot$ and accretion rate $\dot{M} \simeq 1\,\mathrm{M}_\odot\,\mathrm{yr}^{-1}$ is formed, surrounded by a disk-like structure. Photons coming from the protostar due to accretion are radiated away, until the gas becomes optically thick to $\mathrm{H}^-$ radiation at intermediate scales. Eventually, the central object eats up the entire disk and tends toward sphericity, although the mass of the object at each of these later stages still remains to be determined. The massive protostar keeps accreting the surrounding gas and becomes a supermassive star of $M \simeq 10^5 - 10^6\,\mathrm{M}_\odot$ after $\simeq 10^5 - 10^6\,\mathrm{yr}$. Finally, it collapses into a massive black hole seed due to relativistic instabilities.

of the accreting protostar, until the formation of a supermassive object. Based on this modeling of the growing protostar, we deduce parameters for a physically motivated sink particle algorithm, to be used as a sub-grid recipe in large-scale, hydrodynamic simulations of the formation of SMBH seeds in a fully cosmological context. Such simulations are needed to derive detailed diagnostics for the SMBH assembly process at high redshifts, to be probed with next-generation observational facilities (Pacucci et al. 2015), such as the *James Webb Space Telescope (JWST)*, the ATHENA X-ray mission, and the Laser Interferometer Space Antenna (LISA) gravitational-wave observatory.

## 3.2 Physics of the opacity limit

### 3.2.1 Classical picture

In the theory of star formation, it has been a long-standing quest to understand the limits to fragmentation in a given cloud setting. An influential idea was that fragmentation proceeds hierarchically in a collapsing cloud, as the Jeans mass decreases with increasing density as long as the cloud can collapse almost isothermally (Hoyle 1953). The minimum fragment mass is then set by the scale when opacity prevents the release of the gravitational energy via radiation, such that the Jeans mass would increase again upon further compression (Low & Lynden-Bell 1976; Rees 1976). Fragmentation can be seeded in a number of ways, including from non-spherical perturba-

tions of the Larson-Penston solution (Hanawa & Matsumoto 2000; Lai 2000). We here follow a similar reasoning, applied to the peculiar conditions of isothermally collapsing primordial gas in atomic cooling haloes. Our goal is to robustly derive the characteristic density $n_{\rm F}$, mass $M_{\rm F}$, and radius $R_{\rm F}$ of the emerging protostar, when the gas first becomes optically thick (see third panel of Figure 3.1). These values will mark the initial stage in the build-up process of the supermassive object.

We start by considering the simple relation between these three quantities:

$$M_{\rm F} = \frac{4\pi}{3}\frac{m_{\rm H}}{X} n_{\rm F} R_{\rm F}^3 \ , \tag{3.1}$$

where we have used $\rho = m_{\rm H} n / X$, with $X = 0.76$ being the primordial hydrogen mass fraction, to translate total mass density to hydrogen number density.

We furthermore assume that the optically thick cloud is gravitationally bound, such that the characteristic mass is of the order of the Jeans mass $M_{\rm J}$,

$$M_{\rm F} \simeq M_{\rm J} = \left(\frac{\pi k_{\rm B}}{G m_{\rm H} \mu}\right)^{3/2} T^{3/2} n_{\rm F}^{-1/2} \ , \tag{3.2}$$

where $\mu \simeq 1.22$ is the mean molecular weight for a fully-neutral primordial mixture of atomic hydrogen and helium.

Finally, we need to account for energy equilibrium. The energy that is to be radiated away originates in the gravitational collapse of the cloud. In this case, the gravi-

tational energy is emitted in a collapse timescale $t_{\rm col}$, as long as the gas remains optically thin to its cooling radiation. Right before the gas cloud becomes opaque, the energy is radiated from the surface as a fraction $f_{\rm BB}$ of the black-body radiation. Hence, we can equate the gravitational compressional heating rate with the radiation cooling rate

$$\frac{4\pi}{3} R_{\rm F}^3 \cdot \frac{n_{\rm F} k_{\rm B} T}{t_{\rm col}} = f_{\rm BB} 4\pi R_{\rm F}^2 \sigma_{\rm SB} T^4 \ , \tag{3.3}$$

where $\sigma_{\rm SB}$ is the Stefan-Boltzmann constant. In a one-zone model, where the thermal evolution of the central core of a collapsing cloud is calculated, the collapse timescale is commonly assumed to be $t_{\rm col} = \sqrt{3\pi/32G\rho}$, which is the time for the density of an initially static cloud to reach infinity. On the other hand, the dynamical timescale in the free-fall collapse is $t_{\rm col} = 1/\sqrt{24G\rho}$, which is shorter by a factor of $3\pi/2 \simeq 4.7$. In reality, the collapse timescale can be between these values. Here, we set the collapse timescale to $t_{\rm col} = f_{\rm col}\sqrt{3\pi/32G\rho}$ in order to consider this uncertainty, where $0.2 \lesssim f_{\rm col} \lesssim 1$.

We then proceed to solve the system of Equations (3.1), (3.2), and (3.3), and obtain analytic expressions of the characteristic density, radius, and mass

$$n_{\rm F} \simeq 4.6 \times 10^{16} \ f \left( \frac{T}{3000 \ {\rm K}} \right)^{5/2} \ {\rm cm}^{-3}, \tag{3.4}$$

$$R_{\rm F} \simeq 0.33\ f^{-1} \left(\frac{T}{3000\ {\rm K}}\right)^{-3/4}\ {\rm AU} \tag{3.5}$$

$$M_{\rm F} \simeq 0.045\ f^{-1/2} \left(\frac{T}{3000\ {\rm K}}\right)^{1/4}\ {\rm M}_\odot\ , \tag{3.6}$$

where we have normalized $T$ to the typical value of isothermally collapsing gas in the high density regime in an atomic cooling halo and we have used $f = f_{\rm col} f_{\rm BB} \lesssim 1$. We note that this argument for the universal line in the density-temperature plane (Equation (3.4)), on which the gas cloud becomes optically thick to any continuum opacities (gas and dust grains) has already been discussed by Omukai et al. (2005), and we here reproduce the key result in a simplified way to highlight the basic physics involved.

Figure 3.2 shows the density-temperature diagram of a collapsing cloud in an atomic cooling halo when a protostar, composed of a hydrostatic and adiabatic core, forms at the center of the cloud (red dashed curve). The data is taken from a three-dimensional (3D) hydrodynamical simulation by Inayoshi et al. (2014), including all relevant cooling and chemical reaction networks. In this case, the gas becomes opaque at $n \simeq 5 \times 10^{15}$ cm$^{-3}$ (open circle), which agrees with $n_{\rm F} = 9.2 \times 10^{15}$ cm$^{-3}$ for $f = 0.2$ within a factor of two (see Equation (3.4)). Moreover, the radius and mass of the opaque core estimated from Equations (3.5) and (3.6) are $R_F = 1.7$ AU and $M_F = 0.1$ M$_\odot$ for $f = 0.2$, respectively. Both values also reasonably agree with the 3D simulation

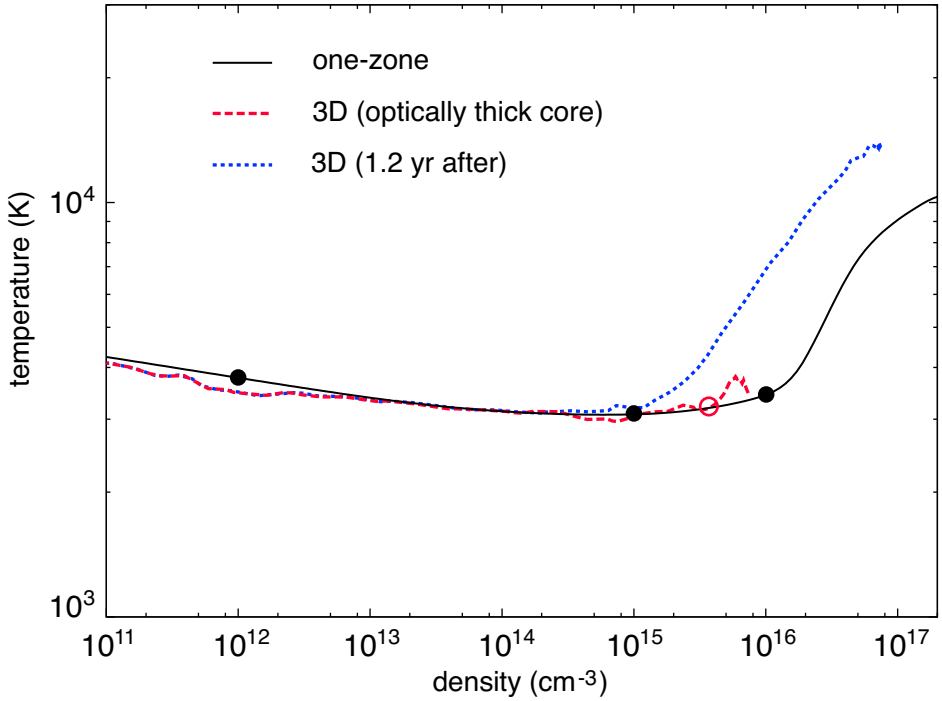


**Figure 3.2:** Density-temperature diagram of a collapsing cloud in an atomic cooling halo. Solid curve (black) presents the thermal history obtained from a one-zone calculation including $H^-$ continuum cooling and opacity effects (see Section 3.2.2). Dashed curves (red and blue, respectively) show the snapshots of a three-dimensional (3D) simulation by Inayoshi et al. (2014) when (1) a hydrostatic protostar forms due to the opacity limit (long, red), and (2) $1.2$ years after protostellar formation (short, blue). The open circle marks the density above which the gas becomes opaque in the 3D simulation. Filled circles mark the three epochs at which we show the optical depth due to absorption and scattering in Figure 3.3. The density at the opacity limit in the 3D simulation is lower than that in the one-zone calculation because the collapse timescale in the 3D simulation is shorter than what is assumed in the one-zone model.

results, where $R_F \simeq 1$ AU and $M_\star \simeq 0.2$ $M_\odot$ right after protostellar formation.

### 3.2.2 Detailed modeling: One-zone model

Next, we gain further insight by considering the detailed physics of $H^-$ opacity, based on the actual microphysical cross section for this process. To this extent, we re-derive the opacity limit by using a one-zone model for the collapse of gas into an atomic cooling halo.

Following previous works (Omukai 2001; Inayoshi et al. 2014), we implement the cooling function due to $H^-$ free-bound (fb) and free-free (ff) emission

$$H + e^- \rightarrow H^- + \gamma, \tag{3.7}$$

$$H + e^- \rightarrow H + e^- + \gamma, \tag{3.8}$$

and consider three opacity sources associated with $H^-$ bound-free, free-free transition and H Rayleigh scattering

$$H^- + \gamma \rightarrow H + e^-, \tag{3.9}$$

$$H + e^- + \gamma \rightarrow H + e^-, \tag{3.10}$$

$$\mathrm{H} + \gamma \rightarrow \mathrm{H} + \gamma'. \tag{3.11}$$

These processes are treated in a self-consistent way with chemical reaction networks. An updated set of chemical reaction rate coefficients and cross sections is summarized in Inayoshi et al. (2014, 2016).

In what follows, we briefly describe the method introduced by Inayoshi et al. (2014) to calculate the cooling function both in the optically thin and thick regimes. We summarize specific functional forms for the cooling rates and opacities in Section 3.5. In the optically thin limit, the $\mathrm{H}^-$ cooling rate is estimated by integrating emissivities over frequency as

$$\Lambda_{\rm thin} \equiv 4\pi \int (\eta_\nu^{\rm fb} + \eta_\nu^{\rm ff}) d\nu. \tag{3.12}$$

We here divide the frequency range into two: $D_l = [0, 0.75]$ eV and $D_h = [0.75, 13.6]$ eV, called "low" and "high" frequency, respectively. That is,

$$\begin{aligned} \Lambda_{\rm thin} &= \int_{D_l} + \int_{D_h} 4\pi (\eta_\nu^{\rm fb} + \eta_\nu^{\rm ff}) d\nu, \\ &\equiv \Lambda_{\rm thin}^{(l)} + \Lambda_{\rm thin}^{(h)}. \end{aligned} \tag{3.13}$$

This distinction between the two ranges is required to calculate the cooling rate in the optically thick case. Figure 3.3 shows the optical depth at the core of the collapsing

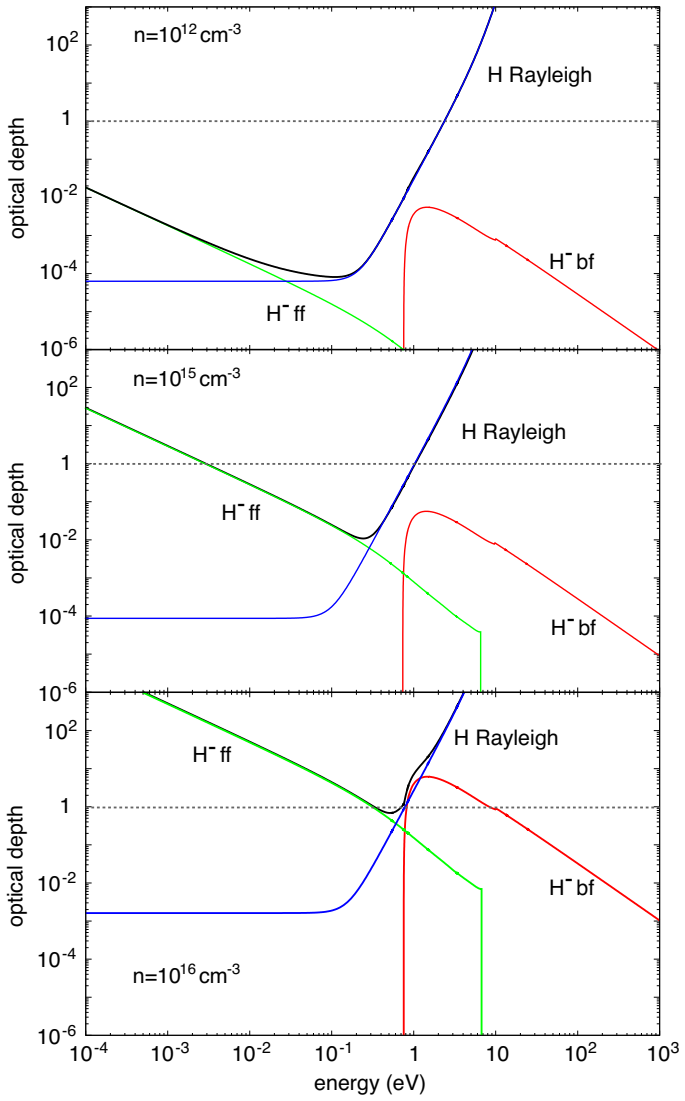


**Figure 3.3:** Frequency-dependent optical depth due to $H^-$ bound-free (red), $H^-$ free-free (green) and H Rayleigh scattering (blue) for three different densities with $n = 10^{12}$ cm$^{-3}$ (top), $10^{15}$ cm$^{-3}$ (middle), and $10^{16}$ cm$^{-3}$ (bottom). The horizontal dashed line shows the line on which $\tau_\nu (= n\sigma_\nu \lambda_{\rm J}) = 1$.

cloud due to the $H^-$ bound-free/free-free transition and H Rayleigh scattering for three different densities. For the lowest density ($n = 10^{12}$ cm$^{-3}$, top panel), the gas is optically thin ($\tau_\nu = n\sigma_\nu\lambda_{\rm J} < 1$) to all the continuum opacities at frequencies $\lesssim 2$ eV. As the density increases to $n = 10^{15}$ cm$^{-3}$ (middle panel), the optical depth at higher frequencies ($\gtrsim 1$ eV) exceeds unity, but the $H^-$ free-free emission still works as radiation cooling. For the highest density ($n = 10^{16}$ cm$^{-3}$, bottom panel), the gas core becomes completely opaque to all the continuum, and hence enters the opacity limit.

In the optically thick limit, the cooling function is approximated as

$$\Lambda_{\rm thick} \simeq \int_{D_l} + \int_{D_h} \frac{-4\pi}{3(\kappa_\nu^{\rm a} + \kappa_\nu^{\rm s})} \frac{\partial^2 B_\nu(T)}{\partial z^2} d\nu, \tag{3.14}$$

where $\kappa_\nu^{\rm a(s)}$ is the absorption (scattering) coefficients, $B_\nu(T)$ is the Planck function, and $z$ is the coordinate along the temperature gradient. Here, we approximate Equation (3.14) as

$$\Lambda_{\rm thick} \simeq \sum_{i=l,h} \frac{4\pi \int_{D_i} B_\nu(T) d\nu}{3\kappa_R^{(i)} \ell^2} = \sum_{i=l,h} \frac{4\pi \int_{D_i} \eta_\nu d\nu}{3\kappa_R^{(i)} \kappa_P^{(i)} \ell^2}, \tag{3.15}$$

where the partial derivative $\partial/\partial z$ is replaced with a characteristic length $\ell$, and $\kappa_R^{l(h)}$ and $\kappa_P^{l(h)}$ are Rosseland and Planck mean opacities in the low- and high-frequency regimes, respectively. Note that, in this limit, the emissivity is expressed as $\eta_\nu = \kappa_\nu^{\rm a} B_\nu(T)$ because the source function is given by $B_\nu(T)$.

Finally, in order to connect both the optically thin and thick regimes, we adopt the following functional form

$$\Lambda_{\rm tot} \simeq \sum_{i=l,h} \frac{4\pi \int_{D_i} \eta_\nu d\nu}{1+3\kappa_R^{(i)}\kappa_P^{(i)}\ell^2}, \\ = \sum_{i=l,h} \frac{\Lambda_{\rm thin}^{(i)}}{1+3\kappa_R^{(i)}\kappa_P^{(i)}\ell^2} \equiv \Lambda^{(l)} + \Lambda^{(h)}, \tag{3.16}$$

where the first (second) term in the right-hand side in Equation (3.16) mainly corresponds to $H^-$ free-bound (free-free) emission. Figure 3.4 shows the evolution of the cooling rates for a collapsing cloud in our one-zone calculation (see solid curve in Figure 3.2). Each solid curve presents the total cooling rate (red), the rate of $\Lambda^{(h)}$ (green) and $\Lambda^{(l)}$ (blue). The $H^-$ free-bound cooling saturates and decreases at $n > 6 \times 10^{15}$ cm$^{-3}$ because of H Rayleigh scattering and $H^-$ bound-free absorption. At $9 \times 10^{15}$ cm$^{-3} \lesssim n \lesssim 2 \times 10^{16}$ cm$^{-3}$, the $H^-$ free-free emission acts as the main cooling process instead of $H^-$ free-bound. Since the compressional heating, given by $\Gamma_{\rm comp} = nk_{\rm B}T/t_{\rm ff}$ (dashed curve in Figure 3.4), dominates the total cooling rate during this transition, the temperature begins to increase gradually. Eventually, the gas becomes completely opaque at $n > 2 \times 10^{16}$ cm$^{-3}$, where $T \propto n^{2/3}$. Note that this density, here derived by considering the detailed microphysics involved, is very similar to the estimate in Section 3.2.1. We can thus robustly characterize the conditions at the onset of supermassive protostar formation.

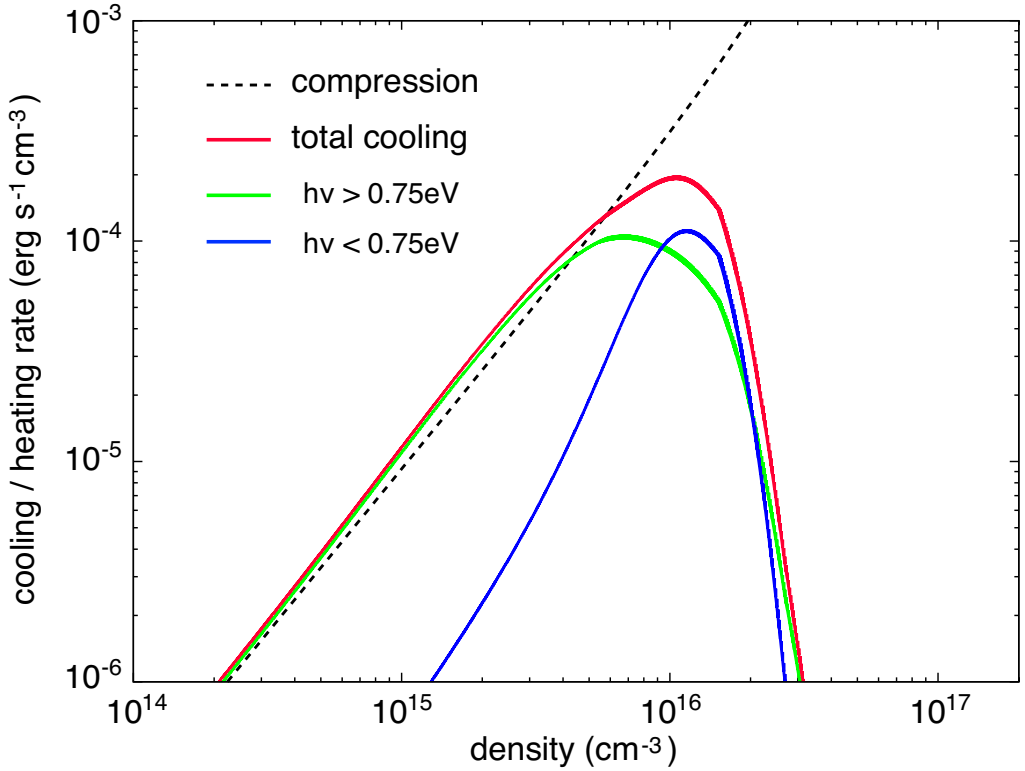


**Figure 3.4:** Radiative cooling rates (solid) and heating rate due to gravitational compression (dashed) in a collapsing cloud. Cooling rates represented are the total cooling rate ($\Lambda_{\rm tot}$, red solid), the rate due to higher-frequency photons with $h\nu > 0.75$ eV ($\Lambda^{(h)}$, green solid) and with $h\nu < 0.75$ eV ($\Lambda^{(l)}$, blue solid).

### 3.2.3 Protostellar evolution

After the collapse and formation of the optically thick object, its mass grows through accretion of the surrounding gas and new sources of energy start becoming important (see fourth panel of Figure 3.1). In that case, its evolution will not be determined by the energy radiated away from the collapse, but by the interplay between internal and accretion radiation from the protostar. During the first stage of protostellar evolution, the energy powering the object will dominantly come from accretion rather than self-gravitating collapse. At some point toward the later evolution of the system, the accretion timescale, $t_{\rm acc} = M_\star/\dot{M}_\star$, becomes larger than the Kelvin-Helmholtz (KH) timescale, $t_{\rm KH} = GM_\star^2/R_\star L_\star$, and hence the protostellar model needs to be augmented by internal contributions (e.g., Omukai & Palla 2003).

Right after a protostar forms, the accretion timescale is shorter than the KH timescale. In this accretion phase ($t_{\rm acc} \lesssim t_{\rm KH}$), we modify the left-hand side of Equation (3.3) and consider the accretion luminosity released at the stellar surface:

$$\frac{GM_\star\dot{M}_\star}{R_\star} \simeq 4\pi R_{\rm ph}^2 \sigma_{\rm SB} T_\star^4, \tag{3.17}$$

where $R_{\rm ph}$ is the photospheric radius. In the early stages of the accretion phase, we assume $R_{\rm ph} \simeq 1.4\ R_\star$ (Stahler et al. 1986), which is derived for a spherically symmetric, quasi-steady model of an accreting protostar. Specifically, a freely-falling enve-

lope is depositing material onto a growing hydrostatic core in an accretion shock. The latter is surrounded by a radiative precursor, transitioning into the optically thin envelope at the photosphere. Here, the factor of 1.4 is determined by $H^-$ opacity, but during later evolutionary stages, other opacity effects like electron scattering will play a role. In accretion problems, other radii like the trapping radius, defined as the point where the radiative diffusion and dynamical timescales are of the same order, might be important. During the evolution of the system, the effective opacity can be written as a function of the opacity due to absorption ($\tau_{\rm abs}$) and to electron scattering ($\tau_{\rm es}$) as $\tau_{\rm eff} = \sqrt{\tau_{\rm abs}(\tau_{\rm abs} + \tau_{\rm es})}$. Inside the photosphere, the gas is ionized and hence electron scattering dominates over absorption ($\tau_{\rm es} \gg \tau_{\rm abs}$). We can then estimate the trapping radius due to electron scattering as $R_{\rm tr}^{\rm es} = \dot{M}_\star \sigma_{\rm T}/4\pi m_{\rm H} c \simeq 4.45\,{\rm AU}\left(\frac{\dot{M}_\star}{{\rm M}_\odot/{\rm yr}}\right)$ (Begelman 1978). For our assumed accretion rate of $\dot{M}_\star \simeq 1\,{\rm M}_\odot\,{\rm yr}^{-1}$, the trapping radius due to electron scattering is of the order of a few astronomical units, which is consistent with the approximation $R_{\rm tr}^{\rm es} \lesssim R_{\rm ph} \sim R_\star$. On the other hand, we can also estimate the trapping radius due to $H^-$ absorption, given by equating the diffusion timescale and the free-fall time as $\tau_{\rm H^-} R/c \simeq \sqrt{3\pi/32G\rho}$. To evaluate this expression, we take the results from the one-zone model and solve for the radius. This gives us a value of $R_{\rm tr}^{\rm H^-} \simeq 4 \times 10^{-2}\,{\rm AU}$, which lies inside the photospheric radius at all times. As a result, we can adequately assume that the trapping radius might not influence the evolution of the object throughout the protostellar assembly. Future, self-consistent radiation-hydrodynamical simulations will provide a more complete understanding.

With these assumptions, we then evaluate the stellar radius as a function of stellar mass $M_\star$, accretion rate $\dot{M}_\star$, and surface temperature $T_\star$:

$$R_\star \simeq 1.1 \left(\frac{M_\star}{\mathrm{M}_\odot}\right)^{1/3} \left(\frac{\dot{M}_\star}{\mathrm{M}_\odot\,\mathrm{yr}^{-1}}\right)^{1/3} \left(\frac{T_\star}{6000\,\mathrm{K}}\right)^{-4/3} \mathrm{AU}. \tag{3.18}$$

Later in the evolution of the object, the internal luminosity from the star begins to dominate because the opacity decreases as the temperature increases inside the star ($\kappa \propto T^{-7/2}$), resulting in $t_{\rm acc} > t_{\rm KH}$. In a typical case for Population III star formation with a moderate accretion rate of $\dot{M}_\star \simeq 10^{-3}\ \mathrm{M}_\odot\,\mathrm{yr}^{-1}$, the star contracts losing the thermal energy via radiative diffusion and forms a main-sequence star. However, when the accretion rate is sufficiently high, the total luminosity (i.e., the accretion luminosity and the internal luminosity) tends to exceed the Eddington luminosity during the KH contraction. Then, the stellar surface expands in order to regulate the increase of the total luminosity, and the protostar evolves into a red-giant-like structure with a contracting core and an expanding envelope. The critical accretion rate to bifurcate the protostellar evolution is estimated as $\dot{M}_\star \gtrsim 4 \times 10^{-3}\ \mathrm{M}_\odot\,\mathrm{yr}^{-1}$ (Omukai & Palla 2003). According to stellar evolution calculations, even if $t_{\rm acc} > t_{\rm KH}$, the stellar surface continues to expand without contraction phases when the accretion rate is higher than $\dot{M}_\star \gtrsim 10^{-2}\ \mathrm{M}_\odot\,\mathrm{yr}^{-1}$ (Hosokawa et al. 2012). In this case, the stellar luminosity approaches the Eddington value for the corresponding mass. Hence, the energy

equilibrium equation can be written as

$$L_{\mathrm{Edd},\star} = \frac{4\pi G M_\star m_\mathrm{H} c}{\sigma_\mathrm{T}} \simeq 4\pi R_\star^2 \sigma_\mathrm{SB} T_\star^4, \tag{3.19}$$

from where we can derive an expression for the stellar radius during the expansion phase, as a function of the mass of the star and the surface temperature (Hosokawa et al. 2012, 2013):

$$R_\star \simeq 0.78 \left(\frac{M_\star}{\mathrm{M}_\odot}\right)^{1/2} \left(\frac{T_\star}{6000\,\mathrm{K}}\right)^{-2} \mathrm{AU}. \tag{3.20}$$

In Figure 3.5, we compare the stellar radius (blue solid) for $T_\star \simeq 6000\,\mathrm{K}$ to other important length scales in our problem. Among them, we consider the Schwarzschild radius, $R_\mathrm{Sch} = 2GM_\star/c^2$ (red solid), the innermost stable circular orbit (ISCO) radius, $R_\mathrm{ISCO} = 6GM_\star/c^2$ (green solid), and the Bondi radius, $R_\mathrm{B} = GM_\star/c_\mathrm{s}^2$ (purple solid). The protostar's radius grows from $R_\star \simeq 0.65\,\mathrm{AU}$ at $M_\star \simeq 0.1\mathrm{M}_\odot$ to $R_\star \simeq 250\,\mathrm{AU}$ at $M_\star \simeq 10^5\mathrm{M}_\odot$, well below the Bondi radius, but above both the Schwarzschild and ISCO radii for the whole range of masses. Additionally, the massive protostar does not enter the region where it becomes GR unstable (pink shaded region) during its evolution. This might indicate that the whole star does not collapse due to GR instability, but only its core, in agreement with Hosokawa et al. (2013).

For the Bondi radius, we here assume for simplicity a nearly-constant sound speed, corresponding to $T(r) \simeq T_\star \simeq 6000\,\mathrm{K}$ (black dashed line in Figure 3.6). This argument

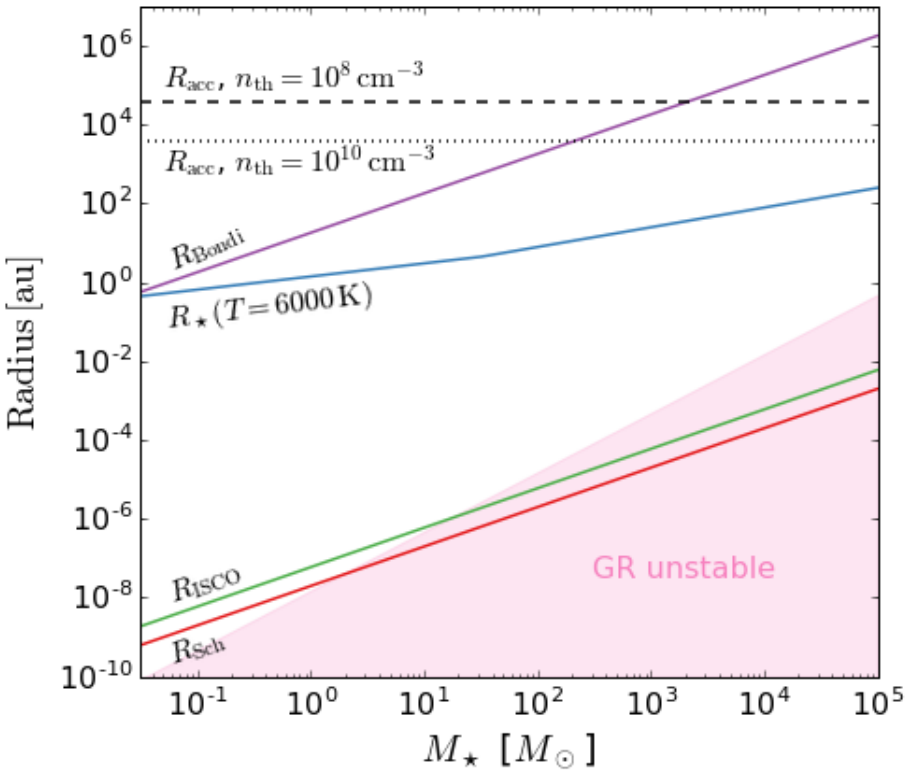


**Figure 3.5:** Characteristic scales related to the evolution of an accreting protostar: stellar radius for a typical temperature of $T \simeq 6000$ K (blue), Schwarzschild radius (red), radius of the innermost stable circular orbit (ISCO, green), and Bondi radius (purple). In addition, we have included the accretion radius as defined in Equation (3.27) for a density threshold of $n_{\rm th} = 10^8$ cm$^{-3}$ (black dashed) and $n_{\rm th} = 10^{10}$ cm$^{-3}$ (black dotted). The pink shaded area indicates the region of the parameter space where the star becomes GR unstable for $n = 3$ polytropic stars (Fricke 1973).

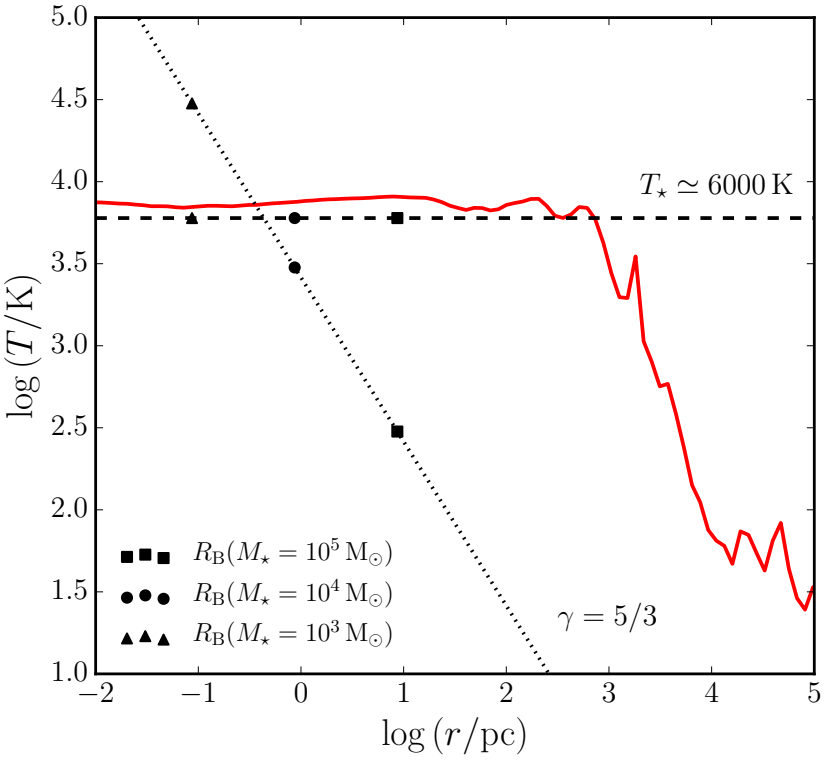


**Figure 3.6:** Radial profiles of the temperature for our assumption $T_\star \simeq 6000\,\mathrm{K}$ (black dashed), our simulations (red solid, see Section 3.3.2), and the adiabatic evolution of an optically thick object of mass $M_\star \simeq 10^4\,\mathrm{M}_\odot$ (black dotted line). The assumption of a constant temperature is a good approximation up to scales $\simeq 100\,\mathrm{pc}$, which encloses the characteristic scales of the problem (see Figure 3.5). For reference, we have also included the value of the Bondi radius for masses $M_\star = 10^3$ (triangles), $10^4$ (circles), and $10^5\,\mathrm{M}_\odot$ (squares).

is based on the Larson-Penston collapse (Larson 1969; Penston 1969), which approximately describes the evolution of atomic cooling halos. In such a case, the density follows a profile $\rho \propto r^{-2}$ and hence the evolution of the temperature is nearly isothermal, up to radii of a few parsecs. Furthermore, we have verified that our simulations of the initial stages of collapse (see Section 3.3.2) exhibit such near-isothermality out to $\simeq 100\,\mathrm{pc}$, as shown by the red solid line in Figure 3.6. It is clear that we oversimplify the situation here. In reality, the infalling matter will heat up when transitioning to optically thick conditions inside the Bondi radius, and eventually follow an adiabatic evolution. In such a case, $\gamma = 5/3$ and the temperature has a radial dependency $T(r) \propto r^{-1}$ (Shapiro & Teukolsky 1983), as represented for a stellar mass $M_\star \simeq 10^4\,\mathrm{M}_\odot$ by the black dotted line in the same figure. In general, the transonic radius for Bondi accretion is given by $R_\mathrm{s} = \left(\frac{5-3\gamma}{4}\right) \frac{GM}{c_{\mathrm{s},\infty}^2}$ (Shapiro & Teukolsky 1983). If the gas evolution is characterized by a different $\gamma$ value (e.g. $\gamma = 1.1$ for classical Population III star formation, Omukai & Nishi 1998), the Bondi radius might change by a factor of a few. Additionally, the transition to the adiabatic stage depends on how the diffusion and free-fall timescales compare to each other. Since the values for the trapping and photospheric radii are similar, this implies that gas outside the photospheric radius is not affected by this increase in temperature, further validating our assumption.

### 3.2.4 Onset of radiative feedback

One factor that might dramatically influence the evolution described in this section is the radiation emitted from the central accreting protostar. Here, we have assumed a constant surface temperature because of strong temperature dependence of $H^-$ opacity. Throughout the evolution of the central object, however, its temperature will vary and eventually reach a point where radiative feedback becomes important. Previous studies have analyzed the formation of primordial supermassive stars in the rapid mass accretion regime and have found that the effective temperature of the object remains well below $10^4\,\mathrm{K}$, for protostellar masses up to $10^4 M_\odot$, or so (Hosokawa et al. 2012, 2013), suggesting that radiative feedback might not become important up to those mass scales.

It is useful to explore the likely temperature evolution of the growing supermassive protostar, in response to a realistic mass accretion history provided by a cosmological simulation. To this extent, we consider the photospheric temperature, given by the general stellar evolution calculations of Stahler et al. (1986):

$$T_\star \simeq 4000\,\mathrm{K}\left(\frac{M_\star}{M_\odot}\right)^{0.044}\left(\frac{\dot{M}_\star}{M_\odot\,\mathrm{yr}^{-1}}\right)^{-0.055}. \tag{3.21}$$

We have plotted this relation in Figure 3.7 for accretion rates of $10^{-2}$ (red), $10^{-1}$ (blue), and $1\,M_\odot\,\mathrm{yr}^{-1}$ (green). Because this relation is only valid when $t_{\rm acc} \lesssim t_{\rm KH}$, we

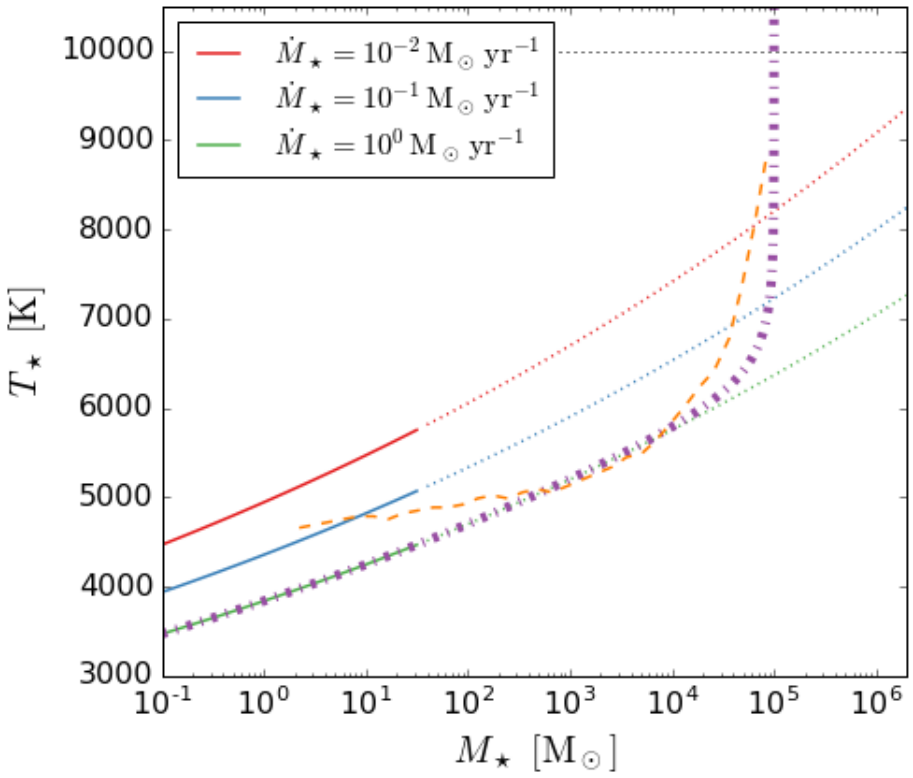


**Figure 3.7:** Photospheric temperature as a function of stellar mass and accretion rate. Colors show the temperature evolution for $\dot{M}_\star = 10^{-2}$ (red solid), $10^{-1}$ (blue solid), and $1\,\mathrm{M}_\odot\ \mathrm{yr}^{-1}$ (green solid) based on Equation (23b) from Stahler et al. (1986). Solid lines represent the stage when $t_{\rm acc} \lesssim t_{\rm KH}$, while dotted lines are a rough extrapolation for higher masses. Additionally, we plot a time-dependent accretion rate of the form $\dot{M}_\star(t) = 1\,\mathrm{M}_\odot\ \mathrm{yr}^{-1} e^{-t/t_{\rm ff,0}}$ (purple dashed-dotted), as an illustrative case, and the results from Hosokawa et al. (2013) (orange dashed). Note that, although both curves seem to agree well, the physical reasons for the rise in temperature are different (see the text for more details). Black dotted line represents the ionizing temperature, $T_{\rm ion} \simeq 10000\,\mathrm{K}$, at which the photosphere starts to emit non-negligible amounts of H ionizing radiation. The surface temperature of the protostar does not become high enough to start emitting hard UV radiation until quite late in the mass build-up. Hence, we can safely neglect its effect on the evolution of the central object early on.

have used solid lines up to the mass where this inequality inverts. For higher masses, we make a rough extrapolation based on the same expression (dotted lines), although the evolution of the temperature for this stage is unclear. As it can be seen, the temperature at which the photosphere begins to emit H-ionizing radiation, $T_{\rm ion} \simeq 10000\,{\rm K}$ (black dotted), is not reached in the range of accretion rates explored here. For lower values of $\dot{M}_\star$ the stellar radius is smaller than the photospheric one, and follows the zero-age main-sequence evolution. In such a case, the ionizing temperature can be reached well before $M_\star \simeq 10^4\,{\rm M}_\odot$.

In addition to our constant accretion rate assumption, we have included a time-dependent toy model of the form $\dot{M}_\star(t) = 1\,{\rm M}_\odot\,{\rm yr}^{-1} e^{-t/t_{\rm ff,0}}$ (purple dashed-dotted line), with $t_{\rm ff,0} = 10^5\,{\rm yr}$ being the free-fall time in the core of the atomic cooling halo before the collapse (e.g. Safranek-Shrader et al. 2012) and $M_\star(t=0) = M_{\rm F} \simeq 0.1\,{\rm M}_\odot$. We also compare with the Hosokawa et al. (2013) results for the effective temperature $T_{\rm eff}$ at $\dot{M}_\star \simeq 1\,{\rm M}_\odot\,{\rm yr}^{-1}$ (orange dashed line). Both models agree well, but in the former case the increase in the effective temperature is due to a drop in the accretion rate, while in the latter case this is a result of the decrease in the opacity because of the expansion of the stellar radius. Similar to the case of constant $\dot{M}_\star$, none of these models reach $T_{\rm ion}$ during the evolution of the protostar up to masses of $10^5\,{\rm M}_\odot$. Since the photospheric temperature at the characteristic accretion rate $\dot{M}_\star \simeq 1\,{\rm M}_\odot\,{\rm yr}^{-1}$ never surpasses $10^4\,{\rm K}$, we can safely neglect photo-ionization feedback from the central protostar during most of its evolution. This radiation only becomes important

for accretion rates a few orders of magnitude lower than $1\,\mathrm{M}_{\odot}\,\mathrm{yr}^{-1}$, or for masses $M_{\star} \simeq 10^{5}\,\mathrm{M}_{\odot}$ in the case of our time-dependent model.

Lastly, the final mass of the protostar can be affected by continuum radiation-driven mass loss once its total luminosity exceeds the Eddington luminosity (e.g., Fiacconi & Rossi 2016), or by mass loss due to pulsations (Inayoshi et al. 2013). As previously discussed, in the early stages of the evolution, the total luminosity remains below the Eddington value and hence it is not affected by radiation-driven mass loss. However, as the mass of the protostar grows its luminosity increases and this scenario changes. In such a case, the final mass of the protostar can vary significantly, as studied by Fiacconi & Rossi (2016). Furthermore, the accreting supermassive protostar might become pulsationally unstable, but the estimated mass-loss rates are too low to effectively prevent protostellar growth (Inayoshi et al. 2013). In summary, mass loss, either due to continuum radiation or pulsations, should not affect the early evolutionary stages, but continuum opacity might become important later on, when the protostellar mass approaches $\simeq 10^{5} - 10^{6}\,\mathrm{M}_{\odot}$ (see the fifth panel of Figure 3.1).

## 3.3 Lessons for the sink algorithm

### 3.3.1 Accretion radius

In the case of numerical simulations, the evolution of the central protostar requires either the implementation of sink particles (e.g. Latif et al. 2013d) or an artificially

stiffened equation of state (e.g. Hirano & Bromm 2017). For the former, we can use the treatment in the previous section of the protostellar evolution to construct a physically motivated sub-grid model.

The formation of the central object in the optically thick regime is characterized by a central fragment of density $n_{\rm F}$ and radius $R_{\rm F}$, and a isothermal profile of the form $n \propto r^{-2}$ outside that scale, as represented by the dashed line in the density-radius diagram in Figure 3.8. The Bondi radius of the object is given by

$$R_{\rm B} \simeq 17 \left(\frac{M_\star}{\rm M_\odot}\right) \left(\frac{T}{6000{\rm K}}\right)^{-1} \ {\rm AU}. \tag{3.22}$$

As seen from Figure 3.8, $R_{\rm B}$ is larger than $R_{\rm F}$, and hence the relation between both quantities follow the isothermal profile, from which we can derive:

$$\begin{aligned} n_{\rm B} &= n_{\rm F} \left(\frac{R_{\rm F}}{R_{\rm B}}\right)^2 \\ &\simeq 4.66 \times 10^{13} f^{-2} \left(\frac{T}{6000{\rm K}}\right)^3 \left(\frac{M_\star}{\rm M_\odot}\right)^{-2} \ {\rm cm}^{-3} \ , \end{aligned} \tag{3.23}$$

where $n_{\rm B} = n(r = R_{\rm B})$ is defined as the density at the Bondi radius.

The solid line in Figure 3.8 corresponds to the subsequent evolution, which is characterized by the growth of the stellar radius following Equation (3.20) for the stage where $t_{\rm acc} \gtrsim t_{\rm KH}$ and accretion rates $\dot{M}_\star \gtrsim 10^{-2}\,{\rm M_\odot\,yr^{-1}}$. Outside the Bondi radius the evolution is still described by the isothermal profile $n \propto r^{-2}$, but inside $R_{\rm B}$ mate-

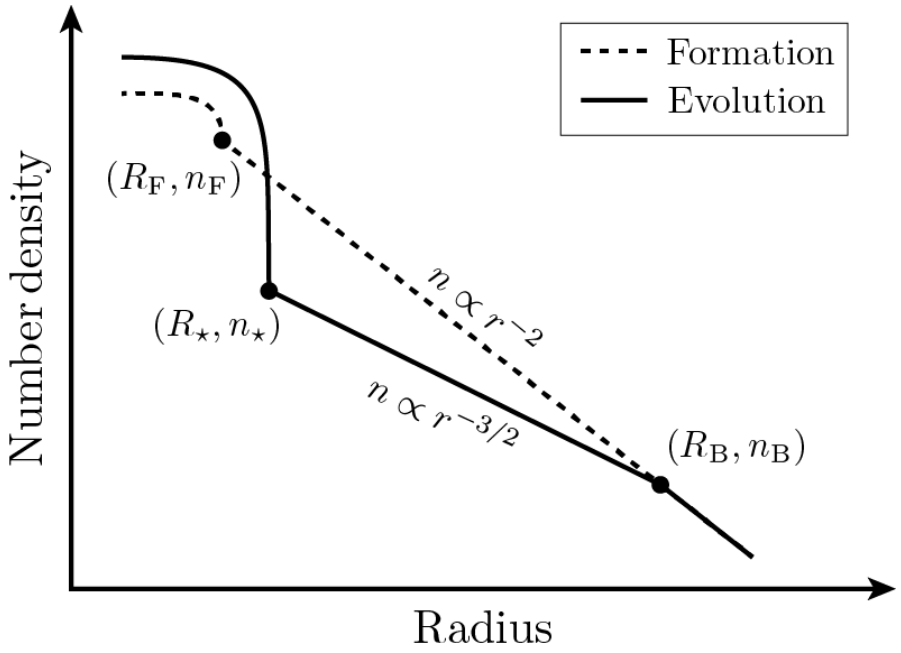


**Figure 3.8:** Density-radius diagram for the protostar at the moment of formation (dashed) and its subsequent evolution (solid). When the fragment forms, its radius ($R_{\rm F}$) is related to the Bondi radius ($R_{\rm B}$) by an isothermal profile of the form $n \propto r^{-2}$. Once protostellar evolution starts, $R_{\rm B}$ increases with mass (and hence with time) but the isothermal profile is kept outside of it, while inside the relation changes to $n \propto r^{-3/2}$ down to the stellar radius $R_\star$.

rial falls within a free-fall time, and hence it is represented by the relation $n \propto r^{-3/2}$ in the density-radius space. This allows us to relate the stellar and the Bondi radius as

$$n_\star = n_{\rm B} \left( \frac{R_{\rm B}}{R_\star} \right)^{3/2} \tag{3.24}$$

$$\simeq 5.13 \times 10^{15} f^{-1} \left( \frac{T}{6000{\rm K}} \right)^{9/2} \left( \frac{M_\star}{{\rm M}_\odot} \right)^{5/4} {\rm cm}^{-3} \ , \tag{3.25}$$

where $n_\star = n(r = R_\star)$ is defined as the density at the stellar radius.

Furthermore, inside the Bondi radius, we can estimate the accretion rate of infalling gas as $\dot{M}_{\rm B} = 4\pi n_{\rm B} m_{\rm H} c_{\rm s} R_{\rm B}^2$. Using Equation (3.23) for $n_{\rm B}$ and Equation (3.22) for $R_{\rm B}$, we derive

$$\dot{M}_{\rm B} \simeq 0.78 f^{-2} \left( \frac{T}{6000{\rm K}} \right)^{3/2} {\rm M}_\odot \, {\rm yr}^{-1} \ , \tag{3.26}$$

The framework depicted here can be used to derive a prescription for the accretion radius of the sink particle, $R_{\rm acc}$. In the ideal case of a simulation with high enough resolution, we would set the accretion radius to $R_{\rm F}$ or $R_\star$. Unfortunately, this case is not always achievable and hence we need to choose $R_{\rm acc} \lesssim R_{\rm B}$ if the simulations resolve densities $n \gtrsim n_{\rm B}$, with an accretion rate estimated by Equation (3.26). On the other hand, the scenario becomes more complex when the simulation is only able to resolve a certain threshold density $n_{\rm th} < n_{\rm B}$. In such a case, the choice of accretion radius should enclose the Bondi radius and, as suggested in Figure 3.8, follow the

isothermal profile. Hence, the value of the accretion rate for a given threshold density can be expressed as $R_{\rm acc} = R_{\rm F}\,(n_{\rm F}/n_{\rm th})^{1/2}$.

In summary, we can write a formula for the accretion radius as based on the threshold density as

$$R_{\rm acc} \simeq \begin{cases} 17\left(\frac{M_\star}{\rm M_\odot}\right)\left(\frac{T}{6000\rm K}\right)^{-1}\ {\rm AU}, & {\rm if}\, n_{\rm th} \gtrsim n_{\rm B} \\ \\ \left(\frac{1.49\times10^{17}\,{\rm cm^{-3}}}{n_{\rm th}}\right)^{1/2} f^{-1/2}\left(\frac{T}{6000\rm K}\right)^{1/2}\ {\rm AU}, & {\rm if}\, n_{\rm th} < n_{\rm B} \end{cases} \tag{3.27}$$

For threshold densities of $n_{\rm th} = 10^8\,{\rm cm^{-3}}$ and $n_{\rm th} = 10^{10}\,{\rm cm^{-3}}$, the initial values of the accretion radius in the low-mass regime (where the Bondi radius is not resolved) are given by $R_{\rm acc} \simeq 3.8\times10^4\,{\rm AU}$ and $R_{\rm acc} \simeq 3.8\times10^3\,{\rm AU}$, respectively. These values are kept until $n_{\rm B} = n_{\rm th}$, which occurs when the mass of the protostar is $\simeq 10^3\,{\rm M_\odot}$ for the former and $\simeq 10^2\,{\rm M_\odot}$ for the latter. From then on, the accretion radius is given by the Bondi radius and the final mass is determined by the Bondi accretion rate, which is independent of the initial resolution of the simulation. Hence, the final mass does not depend on the choice for the threshold density.

The two initial accretion radii for $n_{\rm th} = 10^8\,{\rm cm^{-3}}$ and $n_{\rm th} = 10^{10}\,{\rm cm^{-3}}$ are shown in Figure 3.5 as a black dashed line and a black dotted line respectively. In both cases, the accretion radius is larger than the stellar radius (calculated at $T = 6000\,{\rm K}$) in the mass range $0.1-10^5\,{\rm M_\odot}$ once the sink is formed. As the star evolves, the Bondi radius increases with the mass of the star, eventually reaching the point when it is resolved,

in which case, the accretion radius should transition to $R_{\rm acc} = R_{\rm B}$. This method ensures that the central star, modeled as a sink particle, will always be enclosed by the accretion radius during its evolution, from its formation until it becomes a supermassive star.

Previous works have used different strategies to implement sink particles. For example, Latif et al. (2013d) and Shlosman et al. (2016) assumed $R_{\rm acc} = GM_{\star}/(c_{\rm s}^2 + v_{\infty}^2)$ and then estimated the accretion rate as $\dot{M}_{\star} = 4\pi\rho_{\infty}R_{\rm acc}\sqrt{1.2544c_{\rm s}^2 + v_{\infty}^2}$, while Regan & Downes (2018) used a fixed accretion radius of four cells in the maximum refinement level. We expect all of these recipes to give a similar accretion rate of $\simeq 1 {\rm M}_{\odot}\,{\rm yr}^{-1}$, which corresponds to our estimation from Equation (3.26).

### 3.3.2 Cosmological boundary conditions

We perform a low-resolution simulation of the collapse of an atomic cooling halo following a similar approach to the one described in Becerra et al. (2015). We start from cosmological initial conditions at redshift $z = 99$ and box size of 2 Mpc (comoving) in a $\Lambda$ cold dark matter ($\Lambda$CDM) cosmology. We then follow the evolution of the halo until the highest density cell reaches the threshold density $n_{\rm th} = 10^8\,{\rm cm}^{-3}$. For that, we have used a primordial chemistry network that includes five species (H, $H_2$, $H^-$, $H^+$, and $e^-$) and cooling processes such as $H^-$ cooling, $H_2$ line cooling, $H_2$ collision-induced emission, Ly-$\alpha$ cooling, and inverse Compton cooling. The refinement criteria ensures that the Jeans length is resolved by at least 64 cells at every stage of the evo-

lution.

We show the number density (top) and temperature (bottom) projections of the central object at scales of 200 (left) and 5 pc (right) at that instant in time in Figure 3.9. At large scales, the cloud shows an irregular morphology, but it becomes nearly spherical at scales of $\simeq 10\,\mathrm{pc}$. This implies that the object reaches spherical symmetry at scales larger than the accretion radius at that point ($R_{\mathrm{acc}} \simeq 0.2\,\mathrm{pc}$, as calculated in Section 3.3.1), which is plotted in black dashed lines.

Finally, we analyze the accretion rate onto the object at the moment when the simulation reaches the threshold density in Figure 3.10. The radial profile of the accretion rate is shown as a red solid line, which is calculated as $\dot{M} = -4\pi r^2 \rho v_{\mathrm{rad}}$, where $r$ is the distance to the highest density cell, $\rho$ is the mass density of hydrogen, and $v_{\mathrm{rad}}$ is the radial component of the velocity. For reference, we have also included the Shu accretion rate for spherical collapse, $\dot{M}_{\mathrm{Shu}} \simeq 0.975 c_{\mathrm{s}}^3/G$ (Shu 1977), and the Larson-Penston accretion rate for dynamical collapse, $\dot{M}_{\mathrm{LP}} \simeq 46.9 c_{\mathrm{s}}^3/G$ (Larson 1969; Penston 1969), as blue and green dotted lines, respectively. The mass accretion reaches a maximum of $\dot{M} \simeq 1.4\,\mathrm{M}_\odot\,\mathrm{yr}^{-1}$ at $r \simeq 0.5\,\mathrm{pc}$ and then it decreases to values $\dot{M} \simeq 0.1\,\mathrm{M}_\odot\,\mathrm{yr}^{-1}$ at larger scales, consistent with our estimation from Equation (3.26). Up to scales of $\simeq$15 pc, its value lies in between the Shu and the Larson-Penston accretion rates, which remain roughly constant at $\dot{M}_{\mathrm{Shu}} \simeq 0.18\,\mathrm{M}_\odot\,\mathrm{yr}^{-1}$ and $\dot{M}_{\mathrm{LP}} \simeq 8.5\,\mathrm{M}_\odot\,\mathrm{yr}^{-1}$ for the whole radial range. At the accretion radius (shown as a vertical black dashed line), the value of the mass infall rate is $\dot{M} \simeq 0.6\,\mathrm{M}_\odot\,\mathrm{yr}^{-1}$, which

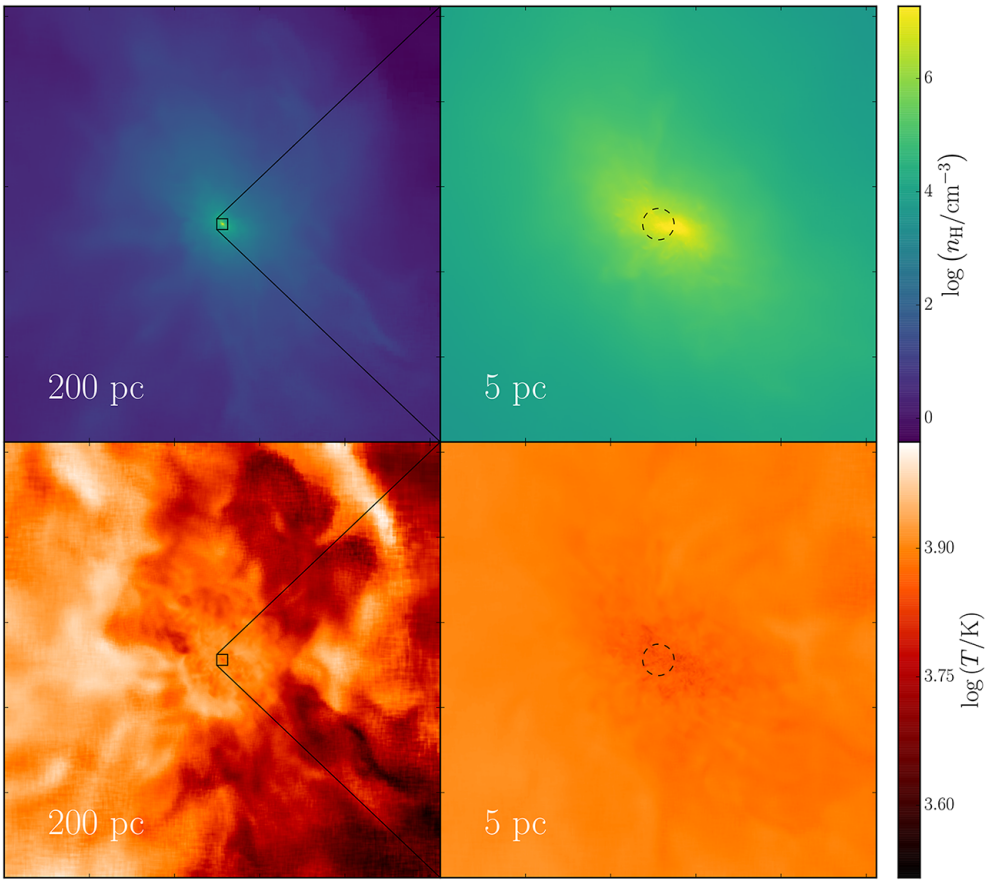


**Figure 3.9:** Density (top) and temperature (bottom) projections of the central 200 (left) and 10 pc (right) for a low-resolution simulation of an atomic-cooling halo when the highest density cell first reaches $10^8$ cm$^{-3}$. From Equation (3.27), the accretion radius at this point is $R_{\rm acc} \simeq 0.2\,{\rm pc}$, which is plotted in dashed black lines in both panels of the right column. At scales of 200 pc the cloud has an irregular morphology but it becomes nearly spherical on the smallest scales. The presence of turbulence can be deduced from the filamentary structure in the large-scale temperature map.

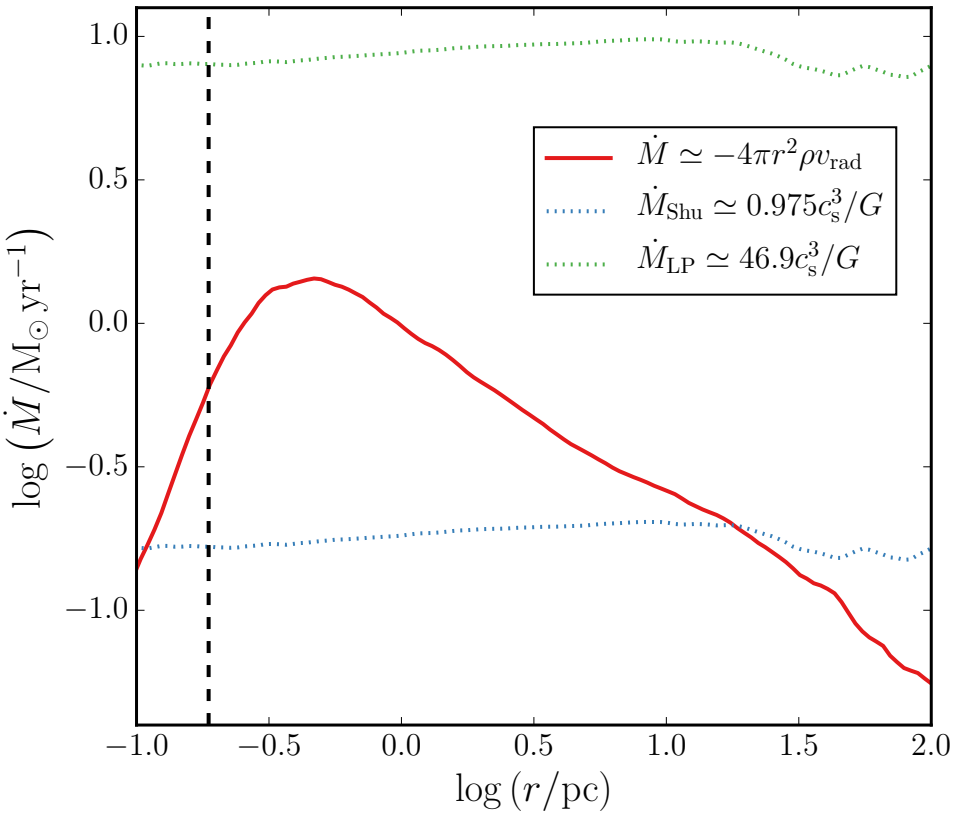


**Figure 3.10:** Mass accretion rate as function of radius, centered on the highest density cell of the halo. The mass accretion rate reaches a maximum of $\dot{M} \simeq 1.4\,\mathrm{M}_\odot\,\mathrm{yr}^{-1}$ at $r \simeq 0.5\,\mathrm{pc}$, and then it decreases to $\dot{M} \simeq 0.1\,\mathrm{M}_\odot\,\mathrm{yr}^{-1}$ at a radial distance of $r \simeq 100\,\mathrm{pc}$. Note that the spatial non-constancy of $\dot{M}$ implies non-steady-state conditions during the initial infall. At the accretion radius (vertical dashed line) the value of the mass infall rate is $\dot{M} \simeq 0.6\,\mathrm{M}_\odot\,\mathrm{yr}^{-1}$. For comparison, we have also plotted $\dot{M}_{\mathrm{Shu}} \simeq 0.975 c_{\mathrm{s}}^3/G$ (blue dotted line), which stays between $0.1\,\mathrm{M}_\odot\,\mathrm{yr}^{-1}$ and $0.2\,\mathrm{M}_\odot\,\mathrm{yr}^{-1}$, and $\dot{M}_{\mathrm{LP}} \simeq 46.9 c_{\mathrm{s}}^3/G$ (green dotted line), which oscillates around $8.5\,\mathrm{M}_\odot\,\mathrm{yr}^{-1}$.

is consistent with the values assumed throughout this study.

### 3.3.3 Disk accretion

Throughout this chapter, we discuss a sub-grid model within a sink assuming spherical symmetric accretion flows. However, gas material with angular momentum forms an accretion disk, through which the central protostar is fed. In supermassive star formation, the disk would be unstable against its self-gravity because of high accretion rates from the parent cloud ($\dot{M}_\star \sim 1\ \mathrm{M}_\odot\,\mathrm{yr}^{-1}$). In such an unstable disk, the disk is likely to fragment into multiple clumps, which could migrate inward losing their orbital angular momentum due to gravitational interaction with the disk and other clumps. Angular momentum redistribution induced by the clumps can drive the evolution of the disk and predict the formation of SMBHs in its nuclei as described by Lodato & Natarajan (2006). Eventually, most of the clumps can feed the gas into the central protostar episodically before the clumps evolve to main-sequence stars, which could suppress the gas accretion through the disk due to ionizing radiation (Inayoshi & Haiman 2014; Latif & Schleicher 2015). Moreover, the radius of the central protostar monotonically increases at $M_\star > 10^2 - 10^3\ \mathrm{M}_\odot$ with an almost constant effective temperature of $T_{\rm eff} \simeq 5000$ K, resulting in weak radiation feedback. Since the average accretion rate through the disk is as high as $\sim 0.1\ \mathrm{M}_\odot\,\mathrm{yr}^{-1}$ and the duration of clump accretion episodes is shorter than the KH timescale at the stellar surface (Sakurai et al. 2016), the evolution of the stellar structure is not affected by details of episodic

accretion (Sakurai et al. 2015).

## 3.4 Summary and Conclusions

In this chapter, we have developed a model for the early evolution of supermassive protostars. After the formation of the initial protostar the surrounding gas becomes optically thick to $H^-$ radiation, at which point we can robustly calculate the properties of the object using the equations of hydrostatic and thermal equilibrium. From that, we obtain a characteristic density, radius, and mass of $n_F \simeq 4.6 \times 10^{16}\,\mathrm{cm}^{-3}$, $R_F \simeq 0.33\,\mathrm{AU}$, and $M_F \simeq 0.045\,M_\odot$, respectively, for a temperature $T = 3000\,\mathrm{K}$. An alternative approach to model the same situation is to use one-zone models. For that, we describe in detail the methods introduced in Inayoshi et al. (2014) and provide explicit numerical fits for the $H^-$ cooling rate and opacity. Combined with the adiabatic heating rate, we can then calculate the critical density at which the gas becomes optically thick, which results in $n_{crit} \simeq 2 \times 10^{16}\,\mathrm{cm}^{-3}$, consistent with the previous estimate. Hence we can robustly characterize the properties of the protostar in the initial optically thick regime.

The early stages of protostellar evolution, where $t_{acc} \lesssim t_{KH}$, are described by the accretion of material onto the central object. For this case, we derive an expression for the protostellar radius as a function of the mass and accretion rate. Using a characteristic value of $\dot{M}_\star \simeq 1\,M_\odot\,\mathrm{yr}^{-1}$ for the accretion rate, we find that the protostellar

radius grows as $R_\star \propto M_\star^{1/4}$ during this phase. Once internal sources of radiation start dominating, $t_{\rm KH} \lesssim t_{\rm acc}$ and hence the radius-mass relation changes to $R_\star \propto M_\star^{1/2}$. For the case of a supermassive protostar, the radius varies from $R_\star \simeq 0.65\,{\rm AU}$ at $M_\star \simeq 0.1{\rm M}_\odot$ to $R_\star \simeq 250\,{\rm AU}$ at $M_\star \simeq 10^5{\rm M}_\odot$. For the surface temperature of the object, we base our analysis on the prescription of Stahler et al. (1986), deducing that it remains well below the ionizing temperature of $T_{\rm ion} \simeq 10^4\,{\rm K}$ during most of its evolution. We can thus safely neglect UV ionizing radiation until the late stages of the assembly process.

In numerical simulations, supermassive protostars are commonly represented by sink particles. Our model allows us to derive the properties of such particles and implement a physically motivated sub-grid model for their evolution in hydrodynamical codes. In particular, we derive an expression for the accretion radius ($R_{\rm acc}$) as a function of the threshold density at which the sink particle is inserted ($n_{\rm th}$), relating it to the physical conditions on the surface of the protostar. For high threshold densities, our model proposes a numerical value based on the isothermal profile of the atomic cooling halo, but this value will eventually transition to $R_{\rm acc} = R_{\rm B}$ once the Bondi radius is resolved further in the evolution of the protostar. We can thus verify throughout the simulation that the accretion radius is well adjusted, in the sense that it is larger than the stellar radius at every moment during its evolution. Our new prescription for sink particles implies changes in the early stages of the evolution up to a protostar mass of $\simeq 10^{2-3}\,{\rm M}_\odot$. After that, it follows the Bondi accretion scenario,

and hence it has an accretion rate of $\simeq 1\,\mathrm{M}_{\odot}\,\mathrm{yr}^{-1}$. The final mass of the object corresponds to $\simeq 10^{5-6}\,\mathrm{M}_{\odot}$, similar to previous estimates in the literature. We will track the accretion and KH timescales during the actual simulation to determine when the accretion rate becomes low enough and the star enters the KH phase. At that point, the radiation hydrodynamic effects from an ionizing central source would have to be taken into account.

The ultimate goal of this line of work is to simulate the assembly process of the first supermassive objects in the Universe in an ab-initio fashion. One key question then is the following: When will this build-up enter a radiation-hydrodynamical phase, where the strong radiative feedback from the growing protostar will eventually turn the object into hyper-luminous beacons from the end of the cosmic dark ages? Those will be probed with next-generation observational facilities, such as the *JWST*, to be launched in 2018. An ideally complementary window into the formation of the first supermassive objects is provided by the gravitational wave signal accompanying the possible merger of binary black holes, which is a prime target for the planned Laser Interferometer Space Antenna (LISA). In light of this suite of next-generation facilities, simulations will have a key role to play in providing physically robust predictions, based on well-motivated sub-grid prescriptions.

## 3.5 Appendix: Opacities and cooling rates

Following our discussion in Section 3.2.2, we can derive numerical fits to the $H^-$ cooling rate based on the description of Equations (3.12) to (3.16) as introduced by Inayoshi et al. (2014). The terms in the right-hand side of Equation (3.13) can be approximated as $\Lambda^{(h)}_{\rm thin} = k^{(h)} n_{\rm HI} n_{\rm e}$ and $\Lambda^{(l)}_{\rm thin} = k^{(l)} n_{\rm HI} n_{\rm e}$, respectively. The cooling rate coefficients are given by

$$k^{(l)} = 0.2345 \times \frac{T_3^{2.265}}{1 + 0.0360\, T_3^{2.149}} \times 10^{-28}\,{\rm erg\,cm^3\,s^{-1}} \tag{3.28}$$

$$\begin{aligned} k^{(h)} &= 10^{-27}\, T_3 \\ &\times \left(1.4924 + 0.07815\, T_3 + 0.0063\, T_3^2\right) \\ &\times \left(1 - 0.1535\, T_3^{0.5}\right)\ {\rm erg\,cm^3\,s^{-1}}, \end{aligned} \tag{3.29}$$

where $T_3 = T/10^3\,{\rm K}$.

Additionally, we estimate the Planck mean opacity for the $H^-$ free-free emission in both the low ($\kappa^{(l)}_{\rm ff,P}$) and high ($\kappa^{(h)}_{\rm ff,P}$) frequency regime, and for the $H^-$ bound-free

emission for the high ($\kappa^{(h)}_{\rm bf,P}$) frequency regime as

$$\kappa^{(l)}_{\rm ff,P} = \frac{10^{-28}}{T^3} \times 28.8 \times \frac{T_3^{-0.88}}{1 + 27.86\, T_3^{-2.15}}\ {\rm cm}^{-1} \tag{3.30}$$

$$\kappa^{(h)}_{\rm ff,P} = \frac{10^{-29}}{T^{2.5}} \exp\left(\frac{-8.761}{T_3}\right) \times 2.868\, T_3^{-0.3326} \times \left(1 + 2.544\, T_3^{1.1413} - 2.3369\, T_3^{1.162}\right)\ {\rm cm}^{-1} \tag{3.31}$$

$$\kappa^{(h)}_{\rm bf,P} = \frac{10^{-11}}{T^{1.5}} \exp\left(\frac{-8.761}{T_3}\right) \times 5.850 \times \left(1 - 0.1042\, T_3^{0.9419} + 0.0727\, T_3^{1.0278}\right)\ {\rm cm}^{-1}. \tag{3.32}$$

Another opacity source is the Rosseland mean opacity for $H^-$ free-free emission in the low frequency regime, which can be modeled as

$$\kappa^{(l)}_{\rm ff,R} = 10^{-44}\, T^2 \times 0.4054\, T_3^{-8.180} \times \left(\frac{1 + 5.552\, T_3^{5.381} + 1.234\, T_3^{8.753}}{1 + 0.0296\, T_3^{1.180}}\right)\ {\rm cm}^{-1}. \tag{3.33}$$

Finally, we also estimate the opacity due to Rayleigh scattering for the high-frequency regime as

$$\kappa^{(h)}_{\rm Ray} = 10^{-42} \exp\left(\frac{8.761}{T_3}\right) \times T^{3.5} \times 1.206 \times \left(\frac{T_3^{0.750}}{1 + 0.139\, T_3^{1.204}}\right)\ {\rm cm}^{-1} \tag{3.34}$$

The total opacities for both regimes can then be written as $\kappa_{\rm R}^{(h)} = \kappa_{\rm Ray}^{(h)}$, $\kappa_{\rm R}^{(l)} = \kappa_{\rm ff,R}^{(l)}$, $\kappa_{\rm P}^{(h)} = \kappa_{\rm ff,P}^{(h)} + \kappa_{\rm bf,P}^{(h)}$, and $\kappa_{\rm P}^{(l)} = \kappa_{\rm ff,P}^{(l)}$. With these approximations and Equation (3.16), we can rewrite the total $H^-$ cooling rate as a function of the optically thin cooling rates and the opacities:

$$\Lambda_{\rm H^-} = \frac{\Lambda_{\rm thin}^{(h)}}{1 + 3\kappa_{\rm R}^{(h)}\kappa_{\rm P}^{(h)}\lambda_{\rm J}\lambda_{\rm J}} + \frac{\Lambda_{\rm thin}^{(l)}}{1 + 3\kappa_{\rm R}^{(l)}\kappa_{\rm P}^{(l)}\lambda_{\rm J}\lambda_{\rm J}} \ . \tag{3.35}$$

Here the characteristic length $\ell$ has been set to the Jeans length $\ell = \lambda_{\rm J} \simeq c_{\rm s} t_{\rm ff}$, with $c_{\rm s} = \sqrt{\gamma k_{\rm B} T / \mu m_{\rm H}}$ being the sound speed.

*"Vine a Comala porque me dijeron que acá vivía*

*mi padre, un tal Pedro Páramo."*

Juan Rulfo

# 4

# Assembly of supermassive black hole seeds

This chapter has been submitted for publication to *MNRAS*

ABSTRACT

We present a suite of six fully cosmological, three-dimensional simulations of the collapse of an atomic cooling halo in the early Universe. We use the moving-mesh code AREPO with an improved primordial chemistry network to evolve the hydrodynamical and chemical equations. The addition of a strong Lyman-Werner background suppresses molecular hydrogen cooling and permits the gas to evolve nearly isothermally at a temperature of about 8000 K. Strong gravitational torques effectively remove angular momentum and lead to the central collapse of gas, forming a supermassive protostar at the center of the halo. We model the protostar using two methods: sink particles that grow through mergers with other sink particles, and a stiff equation of state that leads to the formation of an adiabatic core. We impose threshold densities of $10^8$, $10^{10}$, and $10^{12}\,\mathrm{cm}^{-3}$ for the sink particle formation and the onset of the stiff equation of state to study the late, intermediate, and early stages in the evolution of the protostar, respectively. We follow its growth from masses $\simeq 10\,\mathrm{M}_\odot$ to $\simeq 10^5\,\mathrm{M}_\odot$, with an average accretion rate of $\langle \dot{M}_\star \rangle \simeq 2\,\mathrm{M}_\odot\,\mathrm{yr}^{-1}$ for sink particles, and $\simeq 0.8 - 1.4\,\mathrm{M}_\odot\,\mathrm{yr}^{-1}$ for the adiabatic cores. At the end of the simulations, the HII region generated by radiation from the central object has long detached from the protostellar photosphere, but the ionizing radiation remains trapped in the inner host halo, and has thus not yet escaped into the intergalactic medium. Fully coupled, radiation-hydrodynamics simulations hold the key for further progress.

## 4.1 Introduction

Frontier observations of quasars at redshift z $\gtrsim$ 6 suggest the existence of supermassive black holes (SMBHs) with masses $\gtrsim 10^9\,M_\odot$, when the Universe was less than one billion years old (Fan et al. 2003, 2006; Mortlock et al. 2011; Wu et al. 2015; Bañados et al. 2018). These SMBHs most likely grew from smaller seed BHs, although the origin of these seeds is still unclear (Haiman 2006, 2009; Bromm & Yoshida 2011; Greene 2012; Volonteri 2012; Volonteri & Bellovary 2012; Greif 2015; Johnson & Haardt 2016; Latif & Ferrara 2016; Smith et al. 2017b). The two most promising pathways for the formation of BH seeds at high redshift are the remnants of massive Population III stars (Madau & Rees 2001; Li et al. 2007; Johnson et al. 2012; Alexander & Natarajan 2014), and the direct collapse of primordial gas in haloes with virial temperatures $T_{\rm vir} \gtrsim 10^4\,{\rm K}$, the so-called atomic cooling haloes (Bromm & Loeb 2003; Begelman et al. 2006; Spaans & Silk 2006). A third formation scenario, invoking the high-velocity mergers of massive proto-galaxies, does not require the absence of metals or other low-temperature coolants (e.g. Mayer et al. 2010; Inayoshi et al. 2015).

In the direct collapse scenario, gas falls into the center of haloes where cooling by molecular hydrogen and metal lines to below $\simeq 10^4$ K has been suppressed. The destruction of molecular hydrogen can be achieved by its photo-dissociation due to external soft ultraviolet (UV) background radiation in the Lyman-Werner (LW) bands (Omukai 2001; Bromm & Loeb 2003; Volonteri & Rees 2005; Spaans & Silk 2006;

Schleicher et al. 2010; Johnson et al. 2013; Agarwal et al. 2016; Habouzit et al. 2016; Johnson & Dijkstra 2017). In such a case, the dominant coolant is atomic hydrogen (Omukai 2001; Oh & Haiman 2002), and the gas follows a nearly isothermal collapse at temperatures around the virial value $T_{\rm vir} \simeq 10^4$ K: first, due to Lyman-$\alpha$ cooling up to densities $n_{\rm H} \simeq 10^6\,{\rm cm}^{-3}$, where the gas becomes optically thick to Ly$\alpha$ radiation, and then due to $H^-$ bound-free and free-free emission (Regan & Haehnelt 2009; Latif et al. 2013a; Inayoshi et al. 2014; Becerra et al. 2015, 2018b; Chon et al. 2016). As the gas keeps contracting, it becomes optically thick to $H^-$ continuum emission around $n_{\rm H} \simeq 10^{17}\,{\rm cm}^{-3}$, at which point the gas evolves adiabatically and forms a massive protostar at the center of the halo (Inayoshi et al. 2014; Van Borm et al. 2014; Becerra et al. 2015; Latif et al. 2016). Since the accretion rate in a Jeans-unstable cloud scales as $\dot{M} \propto T^{3/2}$ and the gas in an atomic cooling halo can reach temperatures $T \simeq 10^4$ K, very high values for the accretion rate ($\simeq 1\,{\rm M}_\odot\,{\rm yr}^{-1}$) are achieved. As a consequence, the protostar can grow to $\simeq 10^5 - 10^6\,{\rm M}_\odot$ and become a supermassive star in about a million years (Regan & Haehnelt 2009; Latif et al. 2013b).

Previous high-resolution studies have been able to describe in detail the initial assembly of the protostar up to masses of $M_\star \simeq 0.1\,{\rm M}_\odot$, but, due to the high densities involved in this process, they only follow its evolution for a few years (Inayoshi et al. 2014; Van Borm et al. 2014; Becerra et al. 2015; Latif et al. 2016). In order to investigate the growth of such protostar for longer times, different techniques have been adopted to avoid the creation of high-density regions that prohibitively slow down the

simulations. For example, Regan & Haehnelt (2009); Latif et al. (2013b); Choi et al. (2015) used a pressure floor beyond a certain resolution level, which limited the maximum density to $n_{\rm H} \simeq 10^6 - 10^{12}\,{\rm cm}^{-3}$. Similarly, Latif et al. (2013d); Shlosman et al. (2016); Regan & Downes (2018) employed sink particles that replace gas above a maximum density of $n_{\rm H} \simeq 10^5 - 10^8\,{\rm cm}^{-3}$. One disadvantage of these methods is the limited resolution in regions where density is highest, hence they only describe well the processes on large scales.

In this work, we reconstruct the assembly process of SMBH seeds at high redshifts from masses $M_\star \simeq 10\,{\rm M}_\odot$ to $M_\star \simeq 10^4 - 10^5\,{\rm M}_\odot$. For that purpose, we perform a series of simulations starting from cosmological initial conditions, employing both sink particles and an artificially-stiffened equation of state to model the central object. Additionally, we impose different maximum densities $n_{\rm H} = 10^8$, $10^{10}$, and $10^{12}\,{\rm cm}^{-3}$ to study the late, intermediate, and early stages of the formation of seed BHs, respectively. With this approach, we describe the full picture of the assembly of SMBH seeds. These objects will be prime targets of next-generation observational facilities (Pacucci et al. 2015; Dayal et al. 2017; Natarajan et al. 2017), such as the *James Webb Space Telescope (JWST)*, the ATHENA X-ray mission (e.g. Valiante et al. 2018), and the Laser Interferometer Space Antenna (LISA) gravitational-wave observatory (e.g. Sesana et al. 2011).

This chapter is organized as follows. In Section 4.2, we describe the simulation setup, the chemistry and cooling network, and the techniques used to model the cen-

tral object. In Section 4.3, we analyze the simulation and discuss the collapse of the central gas cloud, the formation and evolution of the central object, the redistribution of angular momentum in the surrounding gas, and the moment when radiation break-out occurs. We discuss the caveats of this work in Section 4.4 and, finally, in Section 4.5 we summarize and draw conclusions.

## 4.2 Numerical Methodology

We investigate the collapse of gas in an atomic cooling halo by performing three-dimensional, cosmological hydrodynamical simulations. Specifically, we use the moving-mesh code AREPO (Springel 2010) with the primordial chemistry network described in detail in Greif (2014). In the following, we briefly summarize the procedure used in Becerra et al. (2015), and describe the modifications added in this work.

### 4.2.1 Simulation set-up

We initialize a dark matter (DM)-only simulation at redshift $z = 99$ in a $\Lambda$ cold dark matter ($\Lambda$CDM) cosmology. We place $512^3$ DM particles of mass $\simeq 2.2 \times 10^3\,\mathrm{M}_\odot$ in a 2 Mpc (comoving) box with a softening length of $\simeq 195$ pc (comoving). We stop the simulation once the first halo to reach a virial mass $\simeq 10^8\,\mathrm{M}_\odot$ collapses. This occurs at $z_{\rm coll} \simeq 11.9$, at which point the halo has a virial mass of $M_{\rm vir} \simeq 1.5 \times 10^8\,\mathrm{M}_\odot$, a virial radius of $R_{\rm vir} \simeq 1.4$ kpc, a virial temperature of $T_{\rm vir} \simeq 3.5 \times 10^4$ K, and a spin

parameter $\lambda \simeq 0.04$.

Once the first $10^8\,\mathrm{M}_\odot$ halo has collapsed, we identify the particles belonging to such halo and trace them back to their initial conditions. We then increase the resolution of the region enclosing the halo by replacing each DM particle by 64 less-massive DM particles and 64 mesh-generating points. With this setup we are able to achieve a DM particle mass of $M_{\mathrm{dm,ref}} \simeq 28\ \mathrm{M}_\odot$, and a refined cell mass given by $M_{\mathrm{gas,ref}} \simeq 6\,\mathrm{M}_\odot$. We then stop the simulation once the first cell exceeds a density of $n_{\mathrm{H}} \simeq 10^8\,\mathrm{cm}^{-3}$, and proceed with a zoom-in simulation by extracting the central 20 pc of the original box. Assuming a temperature of $T \simeq 10^4\,\mathrm{K}$, this box size ensures that material on the edge of the box will not have enough time to fall to the centre of the cut-out, $t \simeq 20\,\mathrm{pc}/c_{\mathrm{s}} \simeq 2\mathrm{Myr}$, where $c_{\mathrm{s}}$ is the sound speed. The artificial boundary will thus, for the duration of the simulation, not affect the halo center, where the protostellar object is created and evolved according to the methodology described in Section 4.2.3.

To achieve such high densities, we enforce the Truelove criterion (Truelove et al. 1997) for refinement, which indicates that the Jeans length needs to be resolved by at least four cells to capture gravitational instabilities. In addition, previous studies have found that the Jeans length must be resolved by at least 32 cells in order to adequately describe the effects of turbulence (Federrath et al. 2011; Safranek-Shrader et al. 2012; Turk et al. 2012; Latif et al. 2013a). Consequently, to fulfill both requirements, and to be on the safe side, we employ a higher resolution of 64 cells per Jeans

length, which is evaluated by using $T_{\rm min} = 5000\,{\rm K}$ for cells with $T \leq T_{\rm min}$, but the actual temperature for cells with $T > T_{\rm min}$. Following this strategy, the maximum spatial resolution reached is $\simeq 10^{-5}\,{\rm pc}$ for our highest resolution simulation.

### 4.2.2 Chemistry

The chemical and thermal model is based on the implementation of Greif (2014) and Becerra et al. (2015). Here, we briefly summarize the main components of the network. We employ a non-equilibrium solver for five species (H, $H_2$, $H^-$, $H^+$, $e^-$), and include reactions such as the formation of $H_2$ via associative detachment as well as three-body reactions, destruction of $H_2$ via collisions and photodissociation, and the formation and destruction of $H^+$ by collisional ionizations and recombinations.

As in Becerra et al. (2015), the cooling processes included are $H_2$ line cooling, $H_2$ collision-induced emission, Ly-$\alpha$ cooling, and inverse Compton cooling. One limitation of that work was the assumption that the optically thin regime for atomic hydrogen cooling extends up to densities $\simeq 10^{16}\,{\rm cm}^{-3}$, while in reality gas becomes optically thick to Ly-$\alpha$ at densities of $\simeq 10^{6}\,{\rm cm}^{-3}$. To improve on that, we have added an artificial cutoff to Ly-$\alpha$ radiation at such density, and from then on free-free and bound-free $H^-$ continuum cooling dominate. The details and formulae used in the implementation of $H^-$ cooling are described in the appendix of Becerra et al. (2018b).

Additionally, we have included a strong Lyman-Werner (LW) background radiation field that dissociates $H_2$ via the Solomon process (Abel et al. 1997). Previous stud-

ies have found that photo-dissociation of molecular hydrogen in the progenitors of an atomic cooling halo requires a LW flux with $J_{21} \gtrsim 10^3$ (Omukai 2001; Johnson & Bromm 2007; Dijkstra et al. 2008; Latif et al. 2013b; Wolcott-Green et al. 2011; Agarwal et al. 2016). Here, we assume a constant LW flux of $J_{21} = 10^5$ for a blackbody spectrum with $T_{\rm rad} = 10^5\,{\rm K}$. Due to this radiation, $H_2$ cooling does not become important during the collapse of the halo, and hence its evolution is mainly determined by $H^-$ cooling.

### 4.2.3 Modeling the central object

Modeling the formation and evolution of a massive protostar from beginning to end implies reaching extremely high densities, which makes the simulations computationally expensive. Since our goal is to describe the evolution of such object until it achieves a mass of $\simeq 10^4 - 10^6\,{\rm M}_\odot$, we need a way to bypass this restriction. To accomplish this, we represent the central object employing two different approaches commonly used in the context of direct collapse BH formation: sink particles (e.g. Latif et al. 2013d; Shlosman et al. 2016; Regan & Downes 2018) and an artificially-stiffened equation of state (e.g. Regan & Haehnelt 2009; Latif et al. 2013a). Both involve a tradeoff: we lose resolution at the center of the object in order to follow its evolution for a longer period. Here we describe the specific implementation of both methods.

### Sink particles

We pre-set a threshold density, $n_{\rm th}$, and create a so-called sink particle (e.g. Bate et al. 1995; Bromm et al. 2002) every time a gas element reaches that value. Once that occurs, we take out all the gas cells within some prescribed radius (centered on the densest cell) that are active at that timestep. The mass of the newly-created sink particle is then the total mass removed, while its position and velocity are determined by the position and velocity of the center of mass of those cells. With those values, and using the temperature of the progenitor cell, we then proceed to calculate an accretion radius, $R_{\rm acc}$, based on the formulation of Becerra et al. (2018b), and assign it to the sink particle. This process is repeated and the accretion radius is re-calculated and updated every time the sink particle becomes active. This occurs quite often since we force the sink particle to have a timestep that is the minimum between the one used for the gravity solver and the smallest between gas cells inside the accretion radius. This procedure effectively results in a variable accretion radius as a function of the sink mass. In this way, we ensure that, at the beginning, $R_{\rm acc}$ is determined by the threshold density, but as the object grows in mass the accretion radius transitions to the Bondi radius.

To avoid problems with the mesh reconstruction algorithm in AREPO, sinks are not allowed to accrete the surrounding gas cells directly. Instead, their growth in mass occurs through mergers with other sink particles. For that purpose, we check if any sink

particles are inside the accretion radius of a neighboring sink particle. If that is the case, one of the sink particles is removed and its mass and momentum are transferred to the other one. As a result, the accretion rate of sink particles is fully determined by mergers with other sinks and we do not impose any value a priori, in contrast to previous studies (e.g. Latif et al. 2013d; Shlosman et al. 2016). This also implies that we can have multiple sink particles for short moments during the evolution of the system. Some of them could be ejected due to gravitational slingshot interactions between them (e.g. Bate et al. 2003), while others may be accreted because of viscous forces (e.g. Hosokawa et al. 2016). Following this approach we reach a resolution of $M_\star \simeq 3\,\mathrm{M}_\odot$ for the initial mass of the sink using $n_{\rm th} = 10^{12}\,\mathrm{cm}^{-3}$.

Because all gas elements with densities larger than $n_{\rm th}$ are replaced by sink particles, this approach allows us to avoid using computational resources on the evolution of high density regions. As a result, the timesteps associated with high-density cells does not become prohibitively small, which allows us to evolve the system for a longer period of time after the formation of the central object. In contrast, the removal of gas cells implies that this methodology might not properly resolve the inner boundary conditions and torques around the sink particle, which might influence the redistribution of gas around the object and hence its accretion rate.

### Stiff equation of state

An alternative approach to model the central object is to artificially introduce an exponential cut-off in the cooling rate above a pre-set threshold density, $n_{\rm th}$. This effectively models the central protostar as an opaque hydrostatic core in which the gas elements with densities higher than $n_{\rm th}$ evolve adiabatically, thus arresting the dynamical collapse. Here, we follow the implementation described in Hirano & Bromm (2017), where they introduce an artificial opacity, $\tau_{\rm art}$, that depends on the local number density defined by

$$\tau_{\rm art} = \left( \frac{n_{\rm H}}{n_{\rm th}} \right)^2 , \tag{4.1}$$

and the corresponding escape fraction, $\beta_{\rm esc.art}$, as

$$\beta_{\rm esc.art} = \frac{1 - \exp\left(-\tau_{\rm art}\right)}{\tau_{\rm art}}. \tag{4.2}$$

Then, we proceed to multiply all cooling rates by this escape fraction to suppress them above $n_{\rm th}$ such that $\Lambda = \beta_{\rm esc.art} \times \Lambda_{\rm cool}$. By reducing the cooling rate above $n_{\rm th}$, gas cells in dense regions experience compressional heating and form an adiabatic core. To fully characterize the central object, we need to define its radius. To that extent, we follow the approach of Greif et al. (2012), in which the photospheric radius of Pop III stars is determined as the point where the optical depth exceeds unity. Here, $\tau_{\rm art} = 1$ corresponds to the condition where the density reaches the threshold density.

Hence, the protostellar radius can be computed using radial profiles and choosing the location where the gas density reaches $n_{\rm th}$.

On the one hand, this allows us to simplify the hydrodynamics governing the evolution of dense regions, which significantly reduces the computational cost of the simulations. On the other hand, as the central object collapses, cells keep being refined and the highest density increases beyond $n_{\rm th}$, but at a reduced rate, so that the overall dynamics can be followed for a much longer duration. Eventually, however, the corresponding timestep becomes smaller and smaller, rendering the simulation too expensive to continue.

## 4.3 Results

We present a suite of six simulations using both approaches to model the central object: sink particles and hydrostatic cores. We use threshold densities of $n_{\rm th} = 10^8$, $10^{10}$, and $10^{12}\,{\rm cm}^{-3}$ for each one of them to describe the late, intermediate, and early stages in the evolution of the growing protostar, respectively. By analyzing the behavior of the object at different stages of its life, we can obtain a fuller picture of the buildup of supermassive black hole seeds.

### 4.3.1 Initial collapse

Figure 4.1 shows the hydrogen number density (left) and temperature (right) projections at the end of the cosmological parent simulations, once the highest density cell reaches $n_{\rm H} \simeq 10^8\,{\rm cm}^{-3}$. From top to bottom, we show box sizes of 20 kpc, 2 kpc, 200 pc, and 20 pc (physical). At large scales we can clearly distinguish the cosmic web surrounding the central halo, composed of filaments and less massive haloes where they intersect. At scales $\gtrsim$ 2 kpc turbulence dominates, which causes the cloud morphology to be highly irregular. During the collapse process, the gas temperature inside the virial radius $R_{\rm vir} \simeq 1.4$ kpc increases to values around $10^4$ K. As we move deeper inside the halo, we see that the morphology changes to a nearly spherical object at $\simeq$ 20 pc, and that there is a slight decrease in temperature at scales less than a few pc. The latter is mainly due to the addition of $H^-$ cooling, as noted by Inayoshi et al. (2014).

A different approach to study the initial collapse is by plotting different halo properties as a function of radius. In Figure 4.2, we present radial profiles for the density (top left), enclosed mass (top right), temperature (bottom left), and $H_2$ abundance (bottom right). The spikes in the profiles are an indication of the turbulent morphology at scales $\gtrsim$ 1 kpc. As the gas collapses into the DM halo, the gas temperature increases to $\simeq$ 8000 K due to shock-heating, slightly below the virial temperature (dashed line). In the central part of the halo, the collapse is nearly isothermal due to

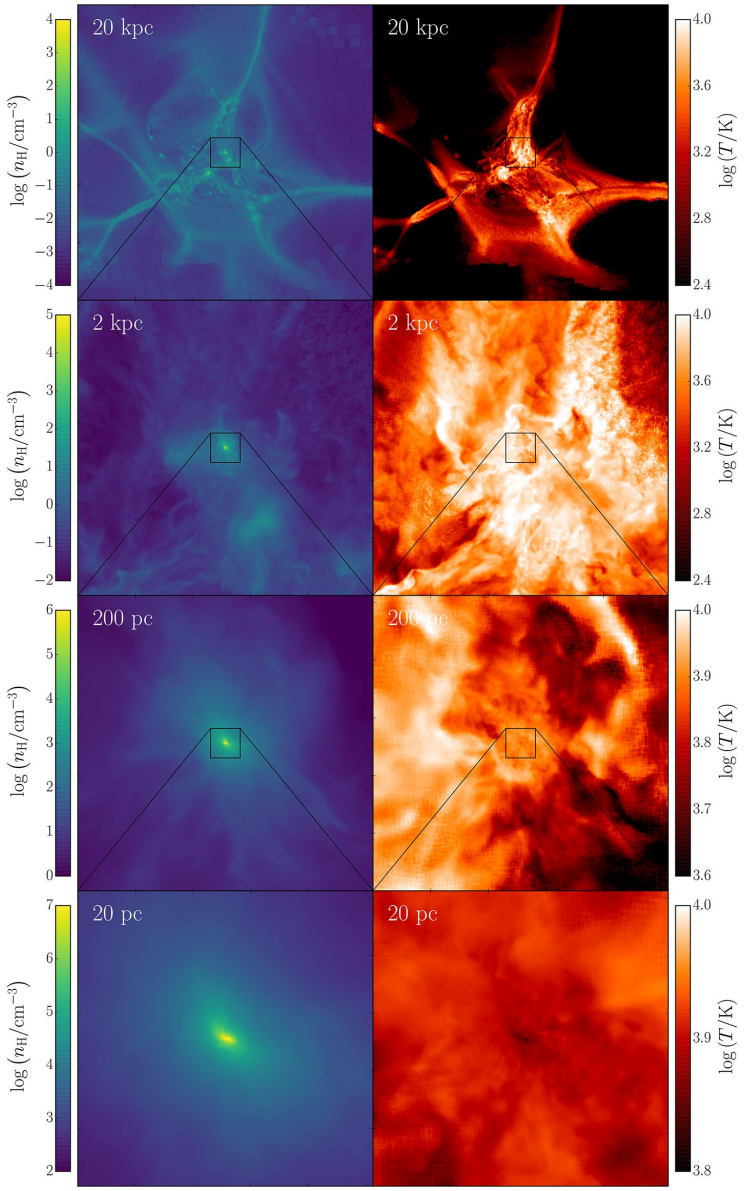


**Figure 4.1:** Overview of the cosmological simulation once the highest density cell reaches $10^8$ cm$^{-3}$. We show density (left) and temperature (right) projections weighted with the square of the density along the line of sight for box sizes of 20 kpc, 2 kpc, 200 pc, and 20 pc, from top to bottom. At large scales, the central halo is surrounded by smaller haloes and filaments, which are characteristic of the cosmic web. Closer to the center, the structure of the cloud changes from highly irregular due to turbulence to nearly spherical (bottom panel).

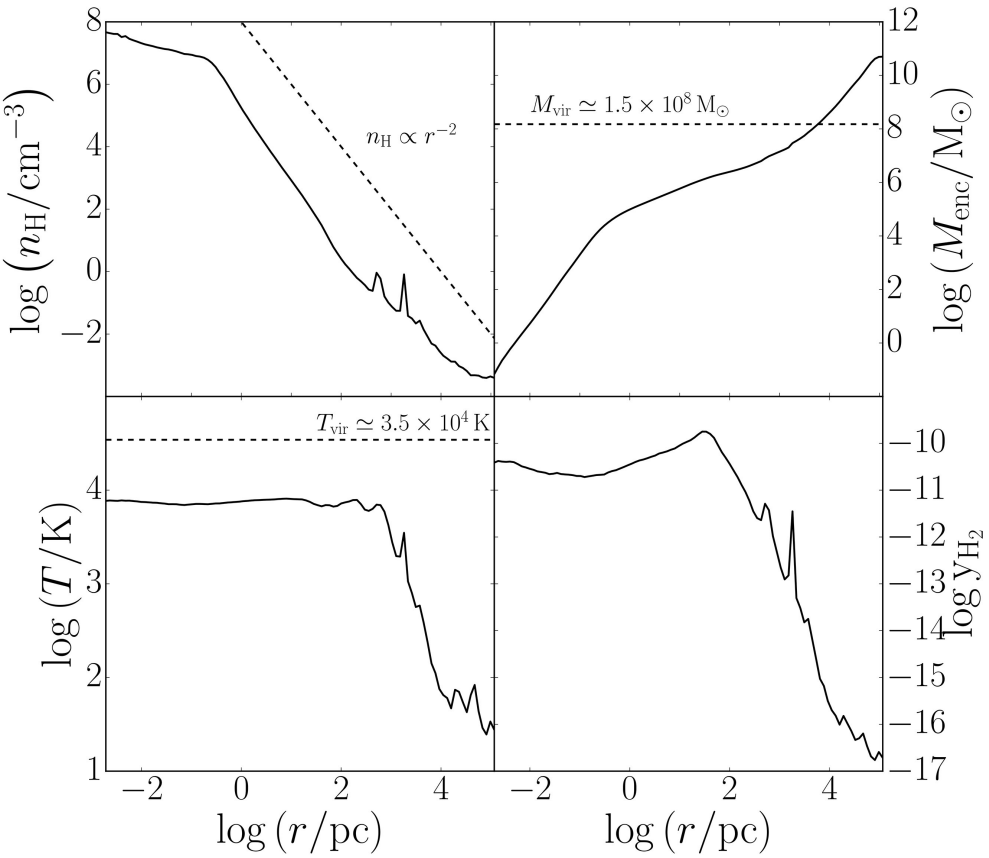


**Figure 4.2:** Environment around the initial protostar. Radial profiles for the mass-weighted number density of hydrogen nuclei, enclosed gas mass, temperature, and $H_2$ abundance once the highest density cell reaches $10^8$ cm$^{-3}$. As the halo collapses, its temperature increase to nearly the virial value, while at the same time $y_{H_2}$ reaches a maximum of $\simeq\ 10^{-10}$. This quantity remains low thanks to the strong LW background radiation, which results in a nearly isothermal evolution of the gas with $T\ \simeq\ 8000$ K, characterized by a density profile $n_{\rm H} \propto r^{-2}$.

$H^-$ cooling. The evolution is then well-described by the Larson-Penston solution for an isothermal, self-gravitating gas cloud (Larson 1969; Penston 1969), and hence the density profile follows the relation $n_H \propto r^{-2}$, as shown by the dashed line in the top left panel. During this period, the $H_2$ abundance, which had increased from $\simeq 10^{-17}$ to $\simeq 10^{-10}$ during the initial collapse, slightly drops to values $\simeq 10^{-11} - 10^{-10}$ due to the strong LW background radiation and collisional dissociation.

### 4.3.2 Central object formation and evolution

The central object is formed as soon as the highest density cell surpasses the threshold density $n_{th}$. In the case of the sink particle simulations, this is defined by the formation and merging of sinks, while in the case of the core simulations the central object is composed by all the gas cells inside the density contour with $n_H = n_{th}$. Figures 4.3 and 4.4 show the density and temperature morphologies, respectively, for sink (top) and core simulations (bottom) at the end of the runs. Columns correspond to threshold densities of $n_{th} = 10^8$ (left), $10^{10}$ (middle), and $10^{12}\,cm^{-3}$ (right), and box sizes of 3, 0.3, and 0.03 pc, respectively. It is worth noting that, since we are plotting different times, a direct comparison between the properties of different simulations at those times is not possible. For a convergence study between simulations with different threshold densities and different central object modeling, we refer the reader to Section 4.6.

The gas morphology around the central object varies for different $n_{th}$. On the left,

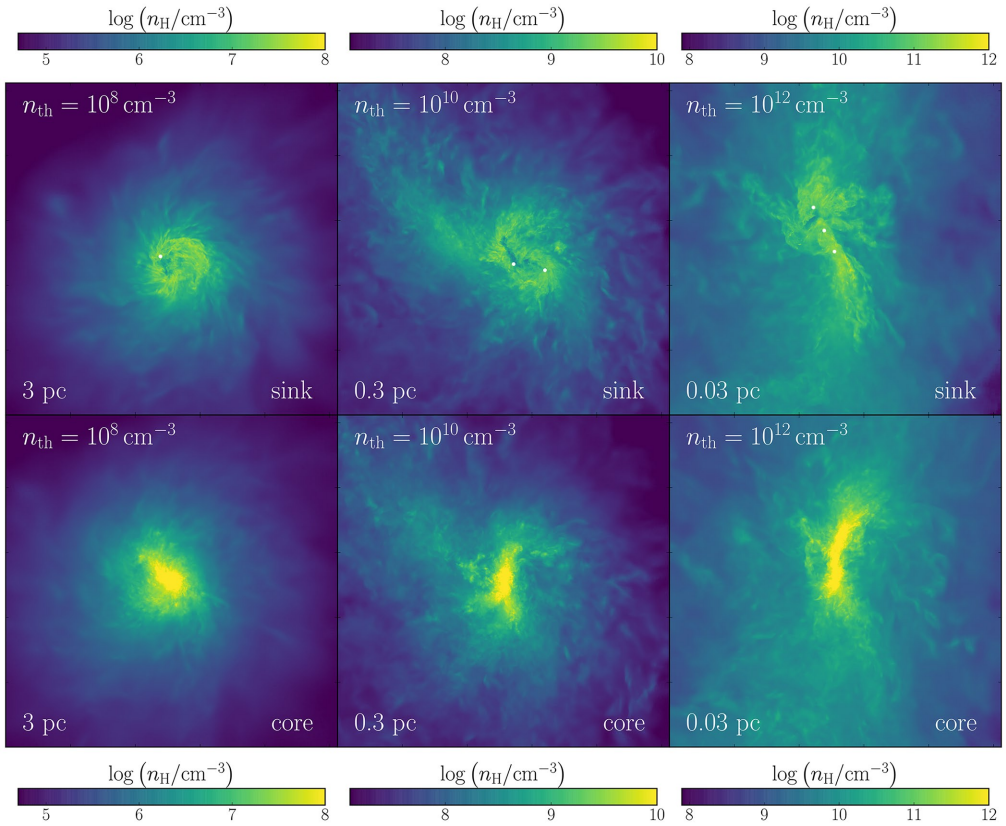


**Figure 4.3:** Projected number density of hydrogen nuclei at the end of each run for sink (top) and artificial core (bottom) simulations. For the sink particles, their location is represented by white dots. Columns represent threshold densities of $n_{\rm th} = 10^8$ (left), $10^{10}$ (middle), and $10^{12}$ cm$^{-3}$ (right), with box sizes of 3 pc, 0.3 pc, and 0.03 pc, respectively. Different scales reveal dissimilar morphologies of the gas around the central object. For example, in the left panels, a disk-like structure can be recognized, while at scales $\lesssim 0.01$ pc the gas tends to form more elongated structures. Note that the accretion onto sink particles produces low-density voids, which are not seen in the case of the core simulations.

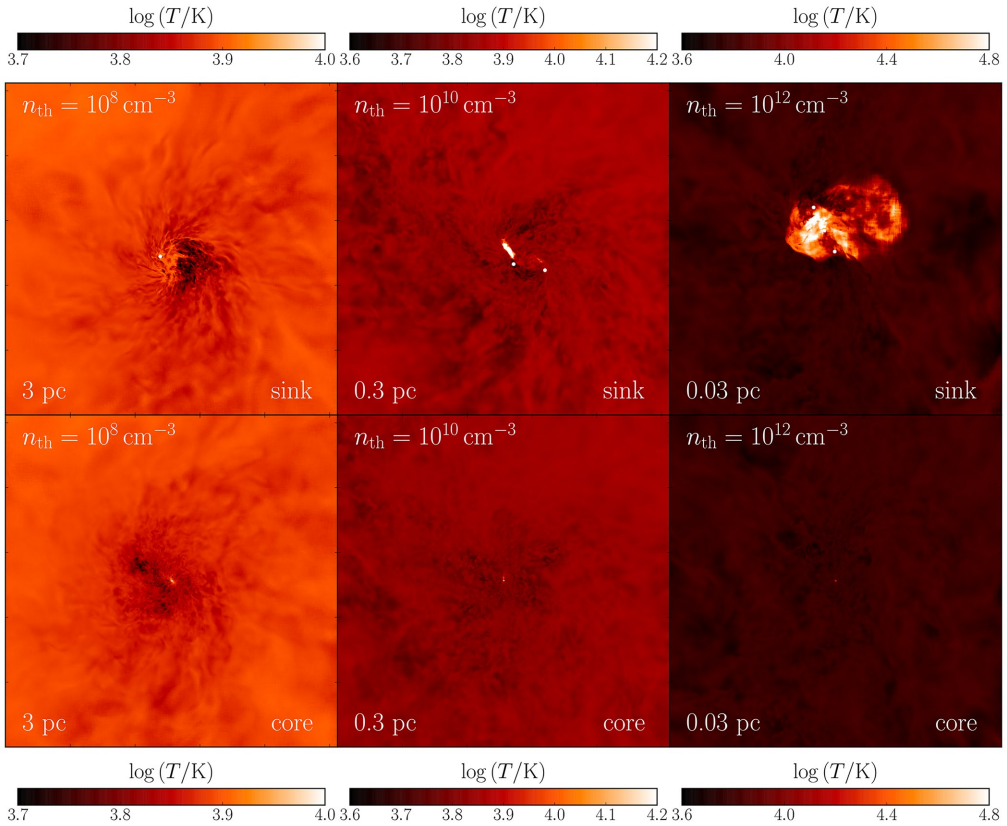


**Figure 4.4:** Temperature projections at the end of each run for the simulations, threshold densities, and box sizes indicated in Figure 4.3. The temperature evolution at these scales is roughly isothermal, although there is an increase at the center. In the case of the sink simulations, this is caused by the dynamical interactions between sink particles that heat up the surrounding gas, while in the case of the core simulations the rise in temperature is due to the adiabatic evolution of the hydrostatic object. Note that in this case, the central temperature rise is barely visible on the scale of the projection.

we can see a disk-like feature of radius $\lesssim$ 0.5 pc, while at smaller scales (or, equivalently, higher $n_{\rm th}$) the gas forms a more elongated structure. In the case of the sink particle simulations, we can discern low-density voids around the sinks, which are caused by gas removal due to sink formation and merging inside the accretion radius. This is not seen in the core simulations, where gas is allowed to keep collapsing, such that some gas cells reach values larger than $n_{\rm th}$ (yellow pixels in bottom row of Figure 4.3). In that case, gas undergoes an adiabatic evolution inside the core and its temperature increases towards the center of the object, visible as a bright dot in the bottom panels of Figure 4.4. A similar but more extended increase in temperature is evident in the sink simulations. In contrast to the core cases, this is due to dynamical interaction between sinks that stir and heat up the surrounding gas, reaching values of $T \simeq 10^{4.4}\,{\rm K}$ at scales $\lesssim 0.01\,{\rm pc}$ in the top right panel of Figure 4.3. A similar dynamical effect in the presence of sink particles was seen in simulations of Pop III protostars (Stacy et al. 2010).

A more quantitative analysis of the evolution of the central object is presented in Figures 4.5 and 4.6. In the former, we plot the mass (top) and accretion rates (bottom) of the most massive sink particle as a function of the time after sink creation for $n_{\rm th} = 10^8$ (red), $10^{10}$ (blue), and $10^{12}\,{\rm cm}^{-3}$ (green), while the latter shows the mass (top) and radius (bottom) of the cores (based on the definitions in Section 4.2.3), as a function of core age for the same threshold densities. The initial sink masses are $\simeq$ 3, 10, and 80 $M_\odot$ from larger to smaller threshold density. This is expected, since these

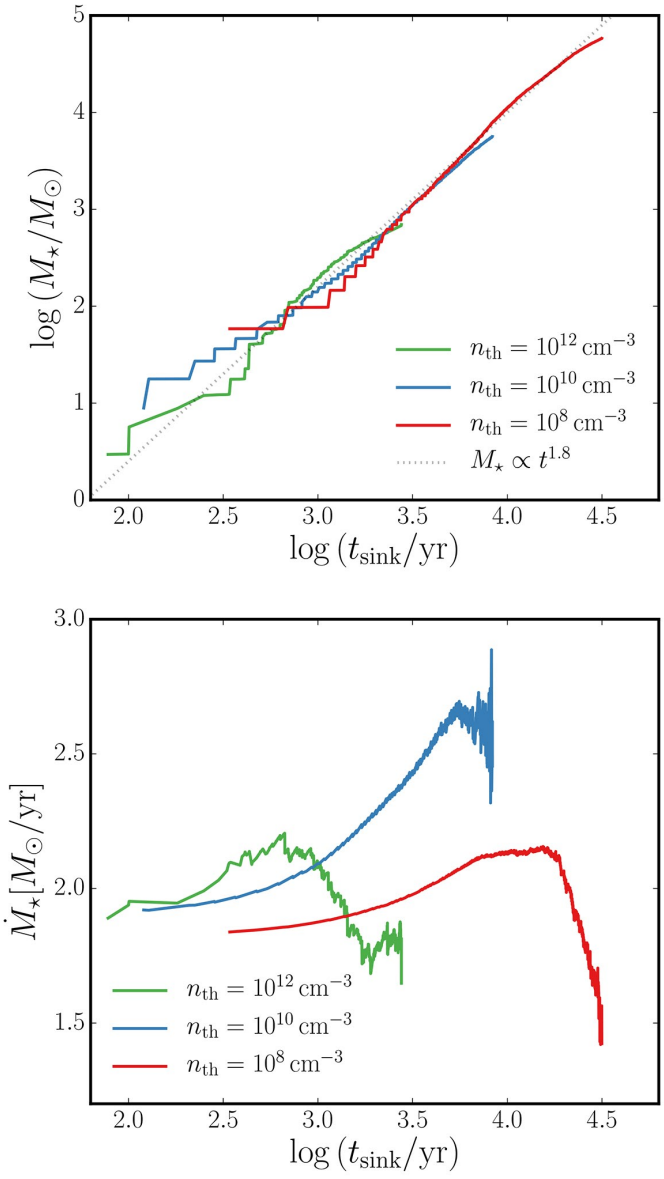


**Figure 4.5:** Sink mass (top) and accretion rate (bottom) as a function of time since initial sink creation, for threshold densities of $n_{\rm th} = 10^8$ cm$^{-3}$ (red), $n_{\rm th} = 10^{10}$ cm$^{-3}$ (blue) and $n_{\rm th} = 10^{12}$ cm$^{-3}$ (green). The sink masses grow from $M_\star \simeq 3$, 10, and 80 M$_\odot$ to $M_\star \simeq 800$, 5000, and 60000 M$_\odot$, with an average accretion rate $\langle \dot{M}_\star \rangle \simeq 2$ M$_\odot$ yr$^{-1}$ for all threshold densities. This evolution is well-described by the relation $M_\star \propto t_{\rm sink}^{1.8}$ (dotted line), which reflects the initial increase in the accretion rate.

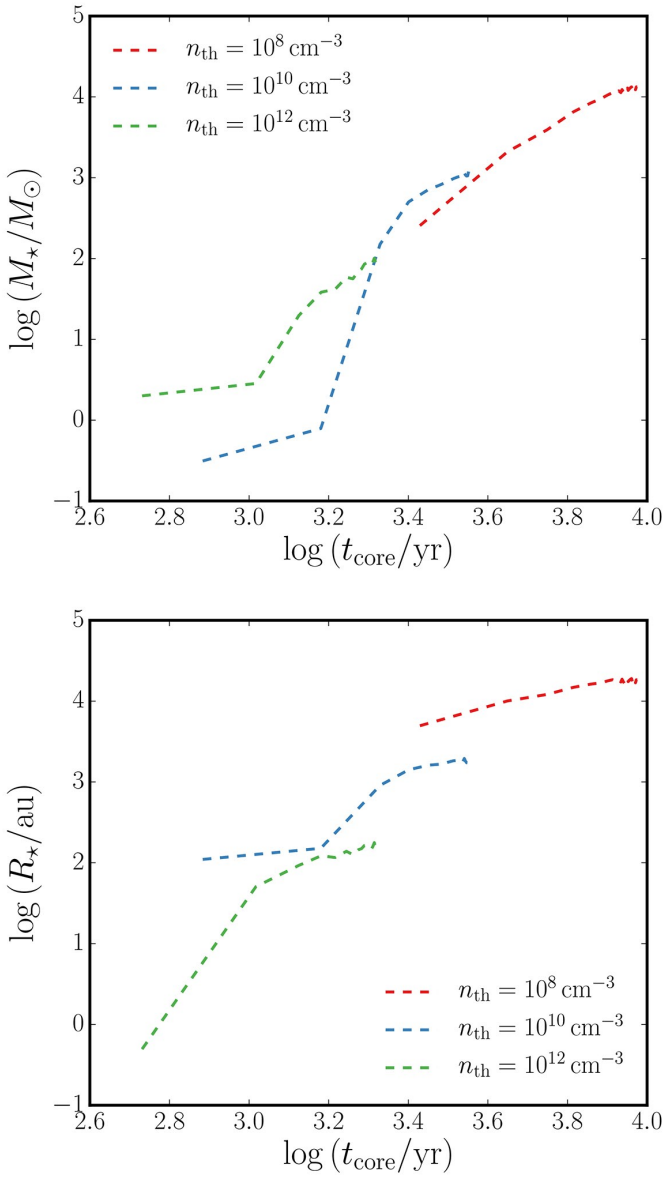


**Figure 4.6:** Hydrostatic core mass (top) and radius (bottom) as a function of time for threshold densities of $n_{\rm th} = 10^8$ cm$^{-3}$ (red), $n_{\rm th} = 10^{10}$ cm$^{-3}$ (blue) and $n_{\rm th} = 10^{12}$ cm$^{-3}$ (green). The early stages are characterized by a steep increase in both mass and radius of the cores. After that, both quantities keep getting larger at a slower pace, finally reaching $M_\star \simeq 10^2, 10^3, 10^4$ M$_\odot$ and $R_\star \simeq 100$, 1,600, 16,500 au, for $n_{\rm th} = 10^{12}, 10^{10}$, and $10^8$ cm$^{-3}$, respectively.

values are determined by the gas mass of the progenitor cells, which are smaller for larger $n_{\rm th}$, and hence higher resolution. We note that our resolution is not sufficient to capture the formation of protostars at the opacity limit (e.g. Becerra et al. 2018b). However, the long-term evolution, studied here, will not be affected by our idealized treatment of the early growth. At the beginning of the runs, all have accretion rates $\simeq 2.0\,{\rm M}_\odot\,{\rm yr}^{-1}$, which subsequently increase somewhat, until reaching a maximum of $\simeq 2.1$, 2.6, and 2.2 ${\rm M}_\odot\,{\rm yr}^{-1}$ for $n_{\rm th} = 10^8$, $10^{10}$, and $10^{12}\,{\rm cm}^{-3}$, respectively. Eventually, most of the gas around the sinks is accreted and their $\dot{M}_\star$ decays to values $\simeq 1$, 2.4, and 1.5 ${\rm M}_\odot\,{\rm yr}^{-1}$. By the end of the runs, their masses have grown to $\simeq 800$, 5000, and 60,000 ${\rm M}_\odot$, with an average accretion rate of $\langle \dot{M}_\star \rangle \simeq 2\,{\rm M}_\odot\,{\rm yr}^{-1}$. Furthermore, their mass growth is well-described as a function of age by the relation $M_\star \propto t_{\rm sink}^{1.8}$, as indicated by the dotted line in the top panel of Figure 4.5. This relation is consistent with the variable accretion rate that we observe in our simulations. More specifically, the physics behind this is as follows. To first order, the accretion rate scales with temperature according to $\dot{M}_\star \propto T^{3/2}$, and the Larson-Penston rarefaction wave reaches slightly hotter regions farther out in the envelope towards later times.

In contrast, the mass of the cores quickly grows during the early stages of their evolution to values $\simeq 30$, 500, and 2000 ${\rm M}_\odot$ for $n_{\rm th} = 10^{12}$, $10^{10}$, and $10^8\,{\rm cm}^{-3}$, respectively. From then on, they steadily acquire additional mass until reaching $M_\star \simeq 10^2$, $10^3$, and $10^4\,{\rm M}_\odot$ at the end of the runs. A similar trend is observed for the radius of the core, which corresponds to values $\simeq 100$, 1,600, and 16,500 au, once the simula-

tions are terminated. The initial rapid evolution of mass and radius corresponds to a stage right after the highest density cell reaches $n_{\rm th}$ and before the core enters its adiabatic evolution. This phase occurs between densities $10^8 - 10^{10}$, $10^{10} - 10^{12}$, and $10^{12} - 10^{13}\,{\rm cm}^{-3}$, from smaller to larger threshold density, respectively, and can be distinguished in the phase space diagram of Figure 4.7. Subsequently, the core enters the adiabatic, slowed contraction phase, characterized by the relation $T \propto n_{\rm H}^{2/3}$, as shown by the dotted lines. The adiabatic evolution coincides with the slower increase in both mass and radius. On average, the cores have accretion rates around $\simeq 0.8 - 1.4\,{\rm M}_\odot\,{\rm yr}^{-1}$, which is smaller than the ones reported for sink particles. This might be due to the definition of the core radius, which is significantly smaller than the accretion radius employed for the sink particles.

### 4.3.3 Fragmentation mass scale

In the case of the core simulations, we can estimate the mass of the collapsed object by calculating the Bonnor-Ebert (BE; Ebert 1955; Bonnor 1956) mass, which is defined as

$$M_{\rm BE} \simeq 15\,{\rm M}_\odot \left(\frac{n_{\rm H}}{{\rm cm}^{-3}}\right)^{-1/2} \left(\frac{T}{\rm K}\right)^{3/2} \mu^{-3/2}\gamma^2, \tag{4.3}$$

where $n_{\rm H}$ is the hydrogen number density, $T$ the temperature, $\mu$ the mean molecular weight, and $\gamma$ the polytropic index. To evaluate this quantity as a function of radius, we calculate the mass-weighted average among cells within a given spherical shell,

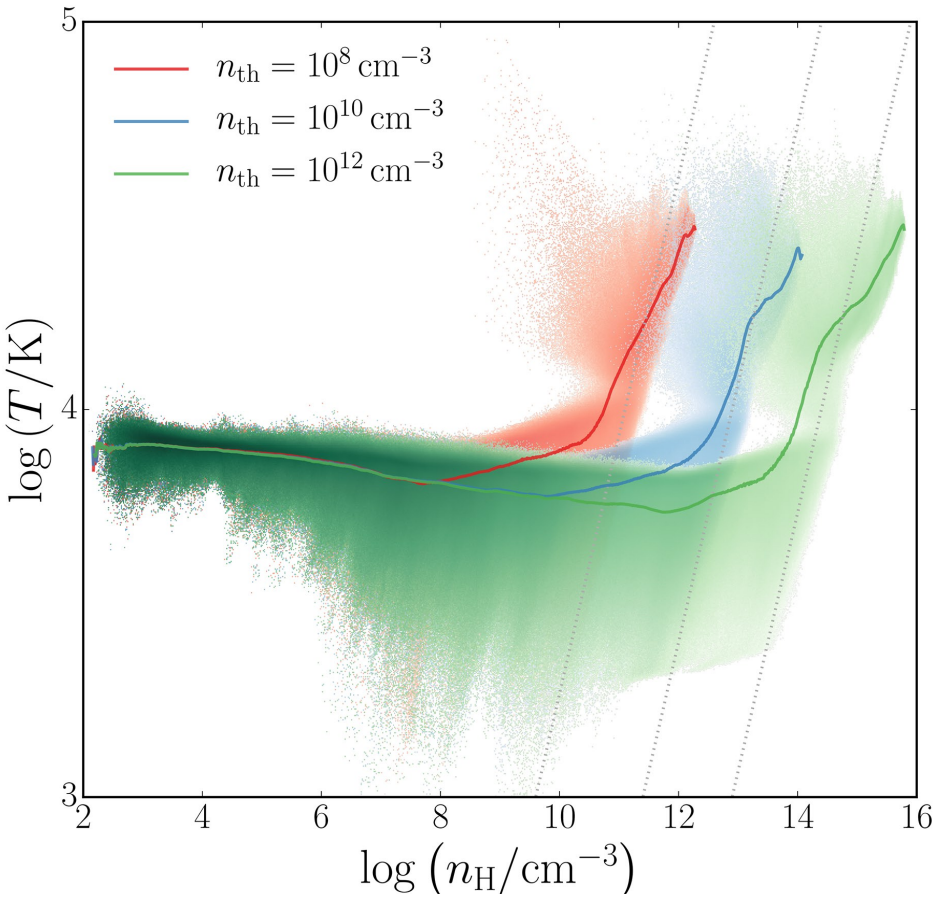


**Figure 4.7:** Thermodynamics of collapsing gas. Shown is the gas temperature as a function of hydrogen number density for core simulations with threshold densities $n_{\rm th} = 10^8$ cm$^{-3}$ (red), $n_{\rm th} = 10^{10}$ cm$^{-3}$ (blue) and $n_{\rm th} = 10^{12}$ cm$^{-3}$ (green). The color-coding indicates mass fractions, from light (lowest) to dark (highest). All simulations show a nearly isothermal evolution until the threshold density is reached. Afterwards, the collapse enters an intermediate stage, where the gas experience a slight increase in temperature over $\simeq 2$ orders of magnitude in density. Finally, for higher densities, the core follows an adiabatic evolution characterized by the relation $T \propto n_{\rm H}^{2/3}$ (black dotted lines).

centered on the highest density cell. In Figure 4.8, we show the ratio of enclosed gas mass to BE mass as a function of enclosed gas mass, for two moments: right after the highest density cell has reached the density threshold (solid), and at the end of the runs (dashed), for $n_{\rm th} = 10^8$ (red), $10^{10}$ (blue), and $10^{12}\,{\rm cm}^{-3}$ (green).

After core formation, the enclosed gas mass surpasses the BE value at $M_{\rm enc} \simeq 2500$, 250, and 30 $M_\odot$, from lower to higher threshold density, which agrees well with the core mass before entering the adiabatic phase, as illustrated in Figure 4.6. As the gas keeps collapsing the temperature increases adiabatically, which is translated into an increase of the BE mass and hence a decrease of the ratio $M_{\rm enc}/M_{\rm BE}$. As a result, the point at which this ratio exceeds unity is shifted to $M_{\rm enc} \simeq 6$, 30, 250 $M_\odot$ at the end of the runs, respectively. This suggests that the central gas could fragment into multiple clumps with characteristic masses around those values. Such sub-fragmentation is indeed seen in our simulations, but any fragments are short-lived, and are quickly swept up by frictional forces into the central core (see Hirano & Bromm 2017).

### 4.3.4 Mass infall rate

To further study how gas is fed into the central object, we analyze the mass infall rate as a function of radius, which can be calculated as

$$\dot{M}_{\rm infall} = -4\pi r^2 \rho v_{\rm rad}, \tag{4.4}$$

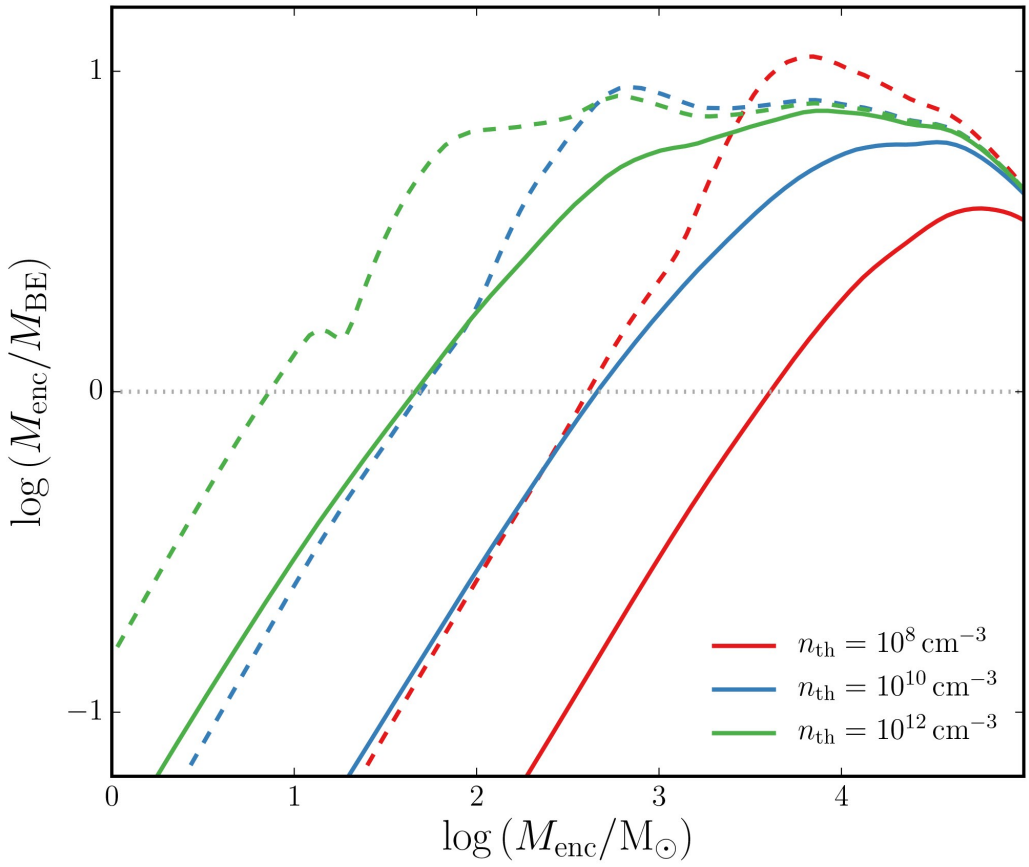


**Figure 4.8:** Enclosed gas mass over mass-weighted average BE mass as a function of enclosed mass for hydrostatic cores, as soon as they reach the threshold density (solid lines) and at the end of the simulations (dashed lines). Initially, this ratio exceeds unity at $M_{\rm enc} \simeq 2500$, 250, and 30 $\mathrm{M}_\odot$ for $n_{\rm th} = 10^8$ cm$^{-3}$ (red), $n_{\rm th} = 10^{10}$ cm$^{-3}$ (blue) and $n_{\rm th} = 10^{12}$ cm$^{-3}$ (green), which is consistent with the mass of the core before entering the adiabatic phase. Then, as the temperature of the core increases, the point where $M_{\rm enc}/M_{\rm BE} = 1$ moves to smaller values of the enclosed gas mass until it reaches $M_{\rm enc} \simeq 6$, 30, 250 $\mathrm{M}_\odot$ at the end of the runs. Some sub-fragmentation is therefore possible towards the later stages of the simulations.

where $r$ is the radius, $\rho$ the volume density, and $v_{\rm rad}$ the radial velocity. In Figure 4.9, we show the radial profiles for this quantity at the end of the runs, for sink (solid) and core (dashed) simulations and threshold densities of $n_{\rm th} = 10^8$ (red), $10^{10}$ (blue), and $10^{12}\,{\rm cm}^{-3}$ (green).

In the case of sink simulations (solid lines), the mass infall rate reaches a peak of $\simeq 2-3\,{\rm M}_\odot\,{\rm yr}^{-1}$ at $r \simeq 0.2$, 0.02, and 0.003 pc from lower to higher threshold density, while at smaller scales the infall rate drastically falls to values $\lesssim 10^{-3}\,{\rm M}_\odot\,{\rm yr}^{-1}$. This decrease is due to the drop in density caused by accretion and merging of sink particles, which constantly removes gas cells inside the accretion radius of the sink particle. In contrast, the core simulations (dashed lines) do not suffer from this limitation and we are able to resolve smaller scales. In such case, the value of the infall rate remains roughly constant around $\dot{M}_{\rm infall} \simeq 2\,{\rm M}_\odot\,{\rm yr}^{-1}$ for all simulations. These values are consistent with the average accretion rates calculated for the sink particles in Section 4.3.2.

### 4.3.5 Angular momentum transport

One of the key effects that determine the mass that is accreted onto the central protostar is the redistribution of angular momentum in the system. If angular momentum were conserved during the initial collapse, we would expect the gas to form a disk that feeds the object at the center. This disk would be unstable against self-gravity due to the high accretion rates and might fragment into multiple clumps. Angular momen-

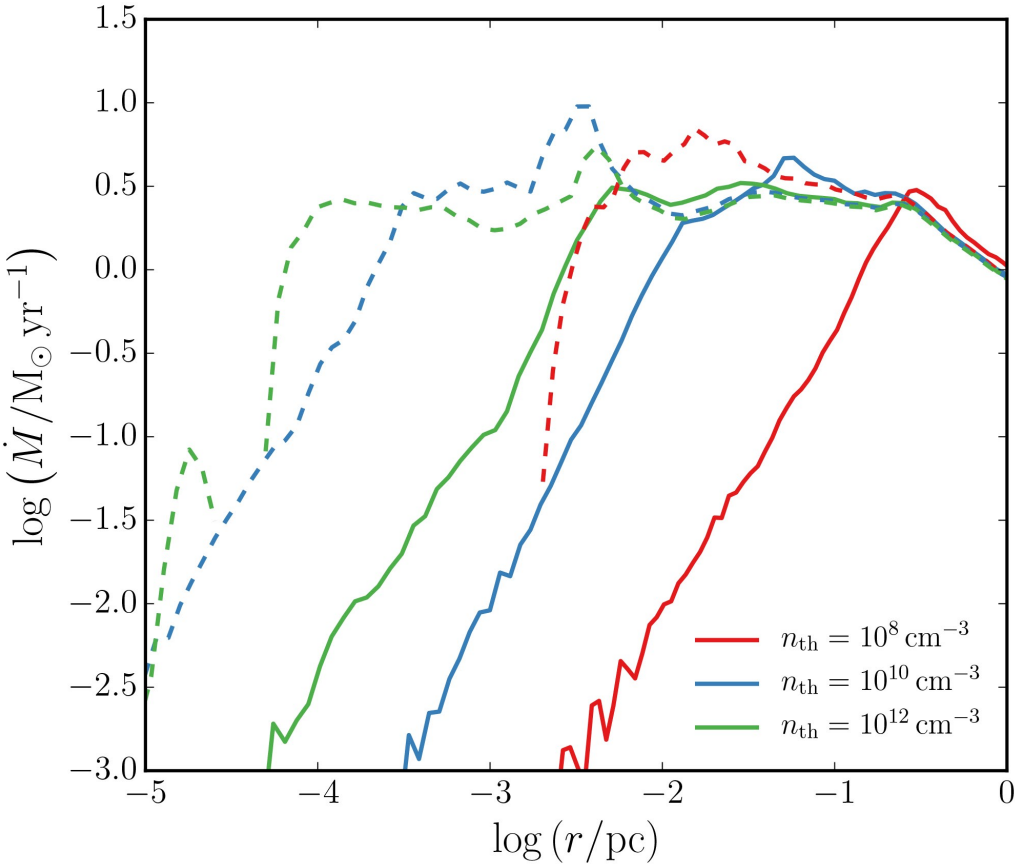


**Figure 4.9:** Mass infall rate as a function of radius at the end of the runs for sink (solid) and core (dashed) simulations, and threshold densities of $n_{\rm th} = 10^8$ cm$^{-3}$ (red), $n_{\rm th} = 10^{10}$ cm$^{-3}$ (blue) and $n_{\rm th} = 10^{12}$ cm$^{-3}$ (green). At large scales, the mass infall rate remains roughly constant at $\dot{M}_{\rm infall} \simeq 2\,{\rm M}_\odot\,{\rm yr}^{-1}$, with a significant drop towards smaller radii to values $\lesssim 10^{-3}\,{\rm M}_\odot\,{\rm yr}^{-1}$. In the case of sink simulations, this decrease occurs at larger scales than in the case of core simulations, and it is caused by the removal of gas cells due to accretion onto sinks.

tum re-distribution induced by these clumps can drive the evolution of the disk and lead to the formation of a supermassive object (Lodato & Natarajan 2006). If we consider that gas, on the scale of the host halo, has a similar spin parameter ($\lambda \simeq 0.05$) than DM, we can deduce $\lambda \sim R_{\rm disk}/R_{\rm vir}$ (Mo et al. 1998), from which the expected radius for the disk would be $R_{\rm disk} \simeq 50\,{\rm pc}$. Since we do not observe this in our simulations, we can deduce that angular momentum is being removed by gravitational ($\boldsymbol{\tau}_{\rm grav}$) and pressure ($\boldsymbol{\tau}_{\rm pres}$) torques on the gas. To quantify the magnitude of the torques, we start by calculating the total baryonic angular momentum at the virial radius, $J_{\rm tot} \simeq 7 \times 10^{67}\,{\rm g\,cm^2 s^{-1}}$, for a virial mass of $\simeq 1.5 \times 10^8\,{\rm M_\odot}$. This quantity needs to be removed in the characteristic timescale of collapse, the free-fall time, $t_{\rm ff} \lesssim 10^8\,{\rm yr}$. Then, we can estimate the torques needed to remove the total angular momentum as $\tau_{\rm tot} \simeq J_{\rm tot}/t_{\rm ff} \simeq 10^{52}\,{\rm g\ cm^2 s^{-2}}$, where $\boldsymbol{\tau}_{\rm tot} = \boldsymbol{\tau}_{\rm grav} + \boldsymbol{\tau}_{\rm pres}$. In terms of required torque per mass, this corresponds to values $\gtrsim 10^{12}\,{\rm cm^2 s^{-2}}$. Let us now assess whether torques of such magnitude are realized in our host haloes.

Previous studies have analyzed how re-distribution of angular momentum affects the evolution of the first stars in the context of minihaloes (e.g. Greif et al. 2012; Hirano & Bromm 2018). In order to analyze this for atomic cooling haloes, we follow a similar approach, and examine the torques acting on the gas around the supermassive black hole seed. Specifically, we focus on two qualitatively different kind of torques:

gravitational and pressure gradient, which are defined as:

$$\boldsymbol{\tau}_{\rm grav} = \frac{1}{\sum_i m_i} \sum_i \boldsymbol{r}_i \times (m_i \boldsymbol{a}_i), \tag{4.5}$$

$$\boldsymbol{\tau}_{\rm pres} = \frac{1}{\sum_i m_i} \sum_i \boldsymbol{r}_i \times \left( m_i \frac{\nabla P_i}{\rho_i} \right), \tag{4.6}$$

where $i$ is the index of the cell, $\boldsymbol{r}_i$ its distance to the sink particle or the highest density cell, $m_i$ its mass, $\boldsymbol{a}_i$ its gravitational acceleration, $\rho_i$ its volume density, and $\nabla P_i$ its pressure gradient. Since we are dividing by the factor $\sum_i m_i$, these quantities represent the torques per unit mass.

The top panels of Figure 4.10 show the gravitational (left) and pressure gradient torque (right), as a function of radius, at the end of the sink (solid) and core (dashed) simulations, for density thresholds of $n_{\rm th} = 10^8$ (red), $10^{10}$ (blue), and $10^{12}\,{\rm cm}^{-3}$ (green). At large scales, the gravitational torque varies between $10^{12}$ and $10^{13}\,{\rm cm}^2\,{\rm s}^{-2}$ for all simulations. Similar to the behavior of the mass infall rate, torques decline towards smaller scales to values $\lesssim 10^{11.5}\,{\rm cm}^2\,{\rm s}^{-2}$. For the sink simulations, this occurs at larger radii compared to the core case, which is due to the removal of gas cells inside the accretion radius. In contrast, the pressure gradient torques remain roughly constant around $\simeq 10^{12}\,{\rm cm}^2\,{\rm s}^{-2}$ for $r \gtrsim 10^{-2}\,{\rm pc}$, and experience a small increase to $\simeq 10^{12} - 10^{12.5}\,{\rm cm}^2\,{\rm s}^{-2}$ at smaller scales. For ease of comparison, we plot the ra-

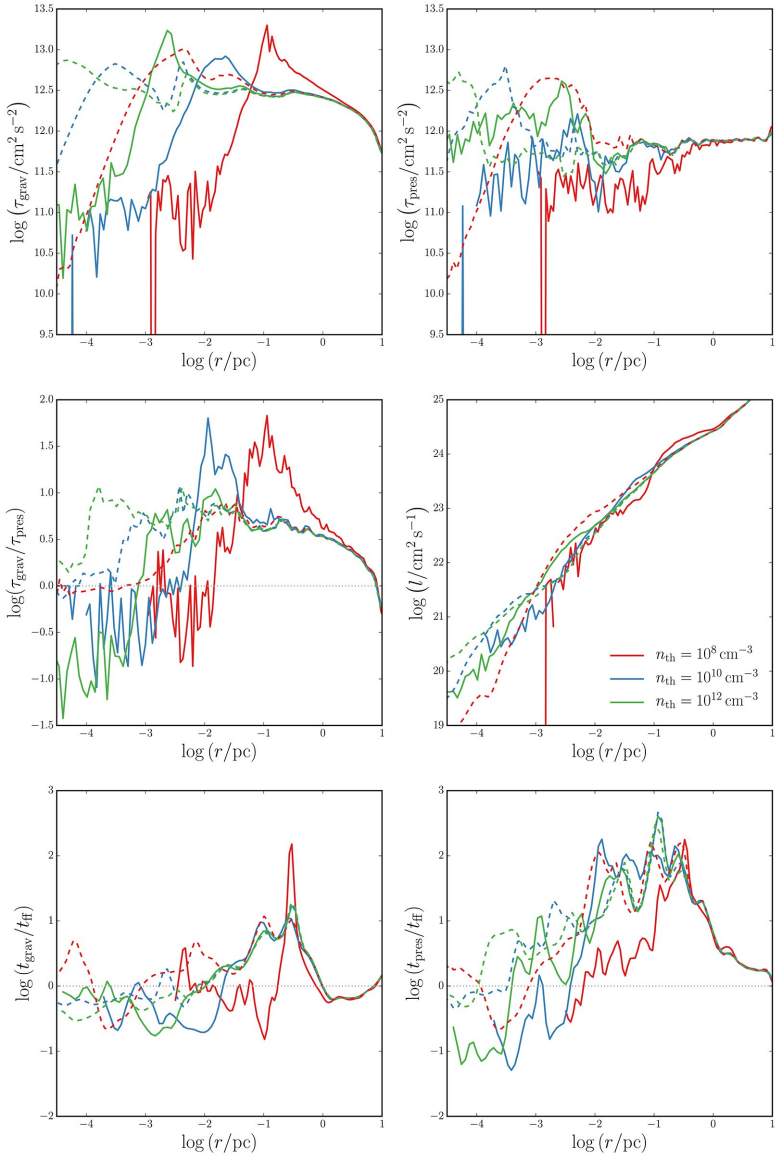


**Figure 4.10:** Physics of angular momentum transport. Radial profiles of the gravitational torques (top left), pressure gradient torques (top right), their ratio $\boldsymbol{\tau}_{\rm grav}/\boldsymbol{\tau}_{\rm pres}$ (middle left), specific angular momentum (middle right), and the timescales for transport driven by $\boldsymbol{\tau}_{\rm grav}$ (bottom left) and $\boldsymbol{\tau}_{\rm pres}$ (bottom right). Timescales are normalized to the local free-fall time, $t_{\rm ff}$. The lines represent the values at the end of the runs for sink (solid) and core simulations (dashed) for $n_{\rm th} = 10^8$ cm$^{-3}$ (red), $n_{\rm th} = 10^{10}$ cm$^{-3}$ (blue) and $n_{\rm th} = 10^{12}$ cm$^{-3}$ (green). Gravitational torques dominate over pressure gradient torques at almost all scales, except in the inner regions of the sink simulations where gravity is not well-resolved due to accretion of gas cells. These torques are responsible for the removal of angular momentum, which allows the gas to collapse onto the central object.

tio $\boldsymbol{\tau}_{\rm grav}/\boldsymbol{\tau}_{\rm pres}$ as a function of radius (left middle panel of Fig. 4.10). From there, it is evident that gravitational torques dominate during the collapse of the cloud at both large and small scales. Sink and core simulations differ most strongly at smaller scales, where $\boldsymbol{\tau}_{\rm grav}$ is not fully resolved because of the constant removal of gas cells due to accretion.

In order to quantify how these torques might affect the redistribution of material around the central object, we analyze their influence on the angular momentum distribution of the collapsing gas. The latter can be calculated as

$$\boldsymbol{l} = \frac{1}{\sum_i m_i} \sum_i \boldsymbol{r}_i \times (m_i \boldsymbol{v}_i), \tag{4.7}$$

where $\boldsymbol{v}_i$ represents the velocity of the cell with respect to the sink particle or the highest density cell's velocity. We can thus derive the timescales on which each torque operates:

$$t_{\rm grav} = \frac{|\boldsymbol{l}|^2}{\boldsymbol{l} \cdot \boldsymbol{\tau}_{\rm grav}}, \qquad t_{\rm pres} = \frac{|\boldsymbol{l}|^2}{\boldsymbol{l} \cdot \boldsymbol{\tau}_{\rm pres}}. \tag{4.8}$$

The right middle panel of Figure 4.10 shows the specific angular momentum, as a function of the radius, for the same snapshots and simulations indicated above. The steady decrease from $l \simeq 10^{25}\,{\rm cm^2\,s^{-1}}$ at $r \simeq 10$ pc to $l \simeq 10^{19}\,{\rm cm^2\,s^{-1}}$ at $r \simeq 10^{19}$ pc shows that gas is losing its angular momentum as it collapses to the center of the cloud. To explain this, we consider the timescales over which the gravitational

(left) and pressure gradient torque (right) act, compared to the free-fall time $t_{\rm ff} = \sqrt{3\pi/32G\rho}$ (bottom panels of Fig. 4.10). In general, $t_{\rm grav} \simeq t_{\rm ff}$, except between 0.01 and 1 pc where $t_{\rm grav} \simeq 10t_{\rm ff}$, while in the case of the pressure gradient torques, the ratio $t_{\rm pres}/t_{\rm ff}$ reaches values $\simeq 100$ in the same region. Gravitational torques, therefore, are more efficient in removing angular momentum, which ultimately impedes the formation of a disk and allows the gas to collapse to the center of the cloud and form a supermassive star.

### 4.3.6 Radiation breakout

As the central object grows, emission coming from it ionizes the surrounding hydrogen developing an HII region. The extent of this region is characterized by the location of the ionization front (IF), which at earlier times is bounded to the central star. However, as the central object accretes mass, its emission grows and the HII region expands from its initial ultra-compact state. A similar early evolution of the developing HII region has been encountered in radiation-hydrodynamic (RHD) simulations of Pop III protostar formation (Stacy et al. 2016). Eventually, the radiation from the fully formed SMBH will break out into the intergalactic medium. Once protostellar radiative feedback becomes important, accretion onto the central object can dramatically change, and the assumptions of our model might not be valid anymore. Here we aim to predict the time of break-out for a supermassive black hole seed by following a similar approach to Smith et al. (2017a), where the ionization front is modeled as the

radius, $r_{\rm IF}$, within which the recombination rate is in equilibrium with the ionization rate.

We begin by writing the recombination rate, as a function of radius $r$, as follows:

$$\dot{N}_{\rm rec} \simeq 4\pi \int_0^r \alpha_{\rm B} n_{\rm H}^2 r'^2 dr', \tag{4.9}$$

where $n_{\rm H}$ is the hydrogen number density, $\alpha_{\rm B} = 2.59 \times 10^{-13} T_4^{-0.7}\,{\rm cm^3 s^{-1}}$ the effective Case B recombination coefficient with $T_4 = T/10^4\,{\rm K}$. In principle the density profile can be obtained from the simulations, but it is not modeled accurately inside the sink accretion radius, one problem being that sink particle mass only grows through mergers with other sink particles. Instead, we use the self-similar solution for a champagne flow (Shu et al. 2002), which assumes a $\rho \propto r^{-2}$ density profile outside a nearly flat inner core. This model has already been used to describe the density evolution in minihaloes (e.g. Alvarez et al. 2006; Wang et al. 2012), and here we apply the same reasoning to atomic cooling haloes. In such a case, the density profile for the isothermal case with temperature $T_{\rm iso}$ is given by

$$n(r) \simeq 7.7 \times 10^4 \left(\frac{T_{\rm iso}}{10^4\,{\rm K}}\right) \left(\frac{r}{1\,{\rm pc}}\right)^{-2} {\rm cm^{-3}}. \tag{4.10}$$

This profile gives a good description of the evolution of an atomic cooling halo with $T_{\rm iso} \simeq T_{\rm vir} \simeq 10^4\,{\rm K}$, as shown in Figure 4.2.

In contrast, the density profile inside the core is described by

$$\frac{m_{\rm H} n(r)}{X} = \frac{\alpha(x)}{4\pi G t^2}, \tag{4.11}$$

where $x = r/c_{\rm s}t$ corresponds to the similarity variable, $c_{\rm s}$ to the sound speed of the ionized gas, $t$ to the time after central object formation, $X = 0.76$ to the hydrogen mass fraction, and $\alpha(x)$ to a function that characterizes the shape of the density profile in the champagne flow. Shu et al. (2002) provides a convenient series expansion for this function, using the boundary condition $\alpha = \alpha_0$ at $x = 0$:

$$\alpha = \alpha_0 + \frac{\alpha_0}{6}\left(\frac{2}{3} - \alpha_0\right) x^2 + \ldots. \tag{4.12}$$

The values for $\alpha_0$ can be extrapolated from table 1 in Shu et al. (2002), based on the value of $\epsilon \equiv (c_{\rm s,i}/c_{\rm s})^2$, where $c_{\rm s,i}$ and $c_{\rm s}$ are the initial and ionized isothermal sound speeds. Here we have used $T_{\rm i} \simeq 10^4\,{\rm K}$ and $T = 3 \times 10^4\,{\rm K}$ for the initial and HII region temperatures, respectively. The transition between both profiles occurs at the shock radius, $r_{\rm sh} = v_{\rm s}t$, where the shock velocity $v_{\rm s} = x_{\rm s}c_{\rm s}$ can be calculated with the value for $x_{\rm s}$ extracted from the same table as above.

Figure 4.11 shows the density profile for the case of an atomic cooling halo in gray lines at times $t = 10^2$, $5\times10^2$, $10^3$, $5\times10^3$, $10^4$, $5\times10^4$, $10^5$, and $5\times10^5\,{\rm yr}$, from top to bottom. For reference, we have included the density profiles from the last snapshot of

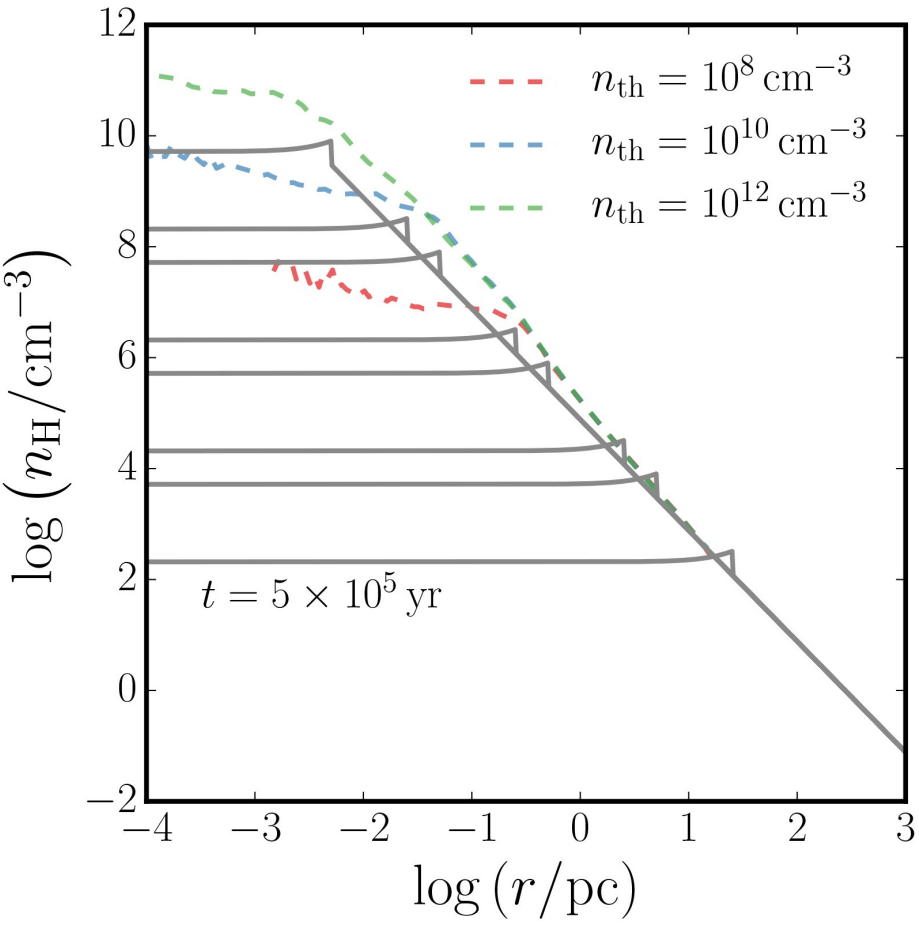


**Figure 4.11:** Density profile as a function of time for the self-similar solution of a champagne flow (Shu et al. 2002). From top to bottom, dark grey lines represent $n_{\rm H}$ at times $t = 10^2, 5 \times 10^2, 10^3, 5 \times 10^3, 10^4, 5 \times 10^4$, $10^5$, and $5 \times 10^5$ yr. The profile is characterized by a nearly flat core that transitions to an isothermal density profile outside the shock radius. The latter is a good approximation for the density profile of our simulations, sufficiently far from a sink (dashed lines).

each sink simulation (dashed lines) for the different threshold densities $n_{\rm th} = 10^8\,{\rm cm}^{-3}$ (red), $10^{10}\,{\rm cm}^{-3}$ (blue), and $10^{12}\,{\rm cm}^{-3}$ (green). Our model predicts that in response to the photo-heating, the density inside the ionized region continuously decreases as time goes by, reaching values as low as $\simeq 10^2\,{\rm cm}^{-3}$ at $t = 5 \times 10^5\,{\rm yr}$. In contrast, the simulations, not taking into account any RHD effects, do not exhibit such a roughly constant-density inner core. Instead, the density keeps increasing near the center, reaching values a few orders of magnitude larger than our analytical model.

Next, we need to account for the ionizing radiation originating from the central object, evaluating the ionizing photon rate according to

$$\dot{N}_{\rm ion} = \frac{\pi L_{\rm Edd}}{\sigma_{\rm SB} T_{\rm eff}^4} \int_{\nu_{\rm min}}^{\infty} \frac{B_\nu}{h\nu} d\nu \tag{4.13}$$

$$\simeq 2.37 \times 10^{54} {\rm s}^{-1} \left( \frac{M_\star}{10^6\,{\rm M}_\odot} \right) \,, \tag{4.14}$$

where $\sigma_{\rm SB}$ is the Stefan-Boltzmann constant, $B_\nu$ the Planck function, and $h\nu_{\rm min} = 13.6$ eV. For simplicity, we here assume a blackbody source with an effective temperature of $T_{\rm eff} = 10^5\,{\rm K}$ emitting at the Eddington luminosity, $L_{\rm Edd} = 4\pi G M_\star m_{\rm H} c/\sigma_T$, where $M_\star$ corresponds to the mass of the sink particle. Such properties are characteristic for very massive stars (e.g. Bromm et al. 2001). Inside the ionization front, the recombination (Equation (4.9)) and ionization (Equation (4.14)) rates are in equilib-

rium, hence

$$4\pi \int_0^{r_{\rm IF}} \alpha_{\rm B} n_{\rm H}^2 r^2 dr \simeq 2.37 \times 10^{54} {\rm s}^{-1} \left( \frac{M_\star}{10^6\,{\rm M}_\odot} \right). \tag{4.15}$$

From this, and using Equations 4.10 and 4.11 to describe the density profile, we can estimate the radius of the ionization front, $r_{\rm IF}$, as a function of time and mass of the star. These results are shown in Figure 4.12 for masses of $M_\star = 10^2$ (red), $10^3$ (blue), $10^4$ (green), $10^5$ (purple), and $10^6\,{\rm M}_\odot$ (orange). The ionization front increases from values $\simeq 10^{-4} - 10^{-3}\,{\rm pc}$ at $t \simeq 100\,{\rm yr}$, to $\simeq 1 - 10\,{\rm pc}$ after $5 \times 10^5\,{\rm yr}$. As the value of $r_{\rm IF}$ grows, it might be able to reach the shock radius, defined in the Shu solution (gray dotted lines). At that point, radiation would be able to escape from the central core, overrunning the halo and reaching the IGM. This occurs at the breakout time $t_{\rm B} \simeq 5 \times 10^4\,{\rm yr}$ and $5 \times 10^3\,{\rm yr}$ for masses $M_\star = 10^5\,{\rm M}_\odot$ and $10^6\,{\rm M}_\odot$, respectively. For lower values of $M_\star$, the ionization front has not reached the shock radius after $5 \times 10^5\,{\rm yr}$, and radiation is still bottled up, but just barely so.

Now, we apply this model to our simulations. In that regard, we extract the sink masses and the times after sink creation from the outputs and insert them into Equation 4.15 to estimate $r_{\rm IF}$. The results are plotted in the left panel of Figure 4.13 for threshold densities of $n_{\rm H} = 10^8$ (red), $10^{10}$ (blue), and $10^{12}\,{\rm cm}^{-3}$ (green). The initial I-front is located at a radius $r_{\rm IF} \simeq 7 \times 10^{-5}\,{\rm pc}$, once the sink is created with $M_\star \simeq 10\,{\rm M}_\odot$ in the $n_{\rm H} = 10^{12}\,{\rm cm}^{-3}$ case. As the sink mass grows to $M_\star \simeq 5 \times 10^5\,{\rm M}_\odot$, $r_{\rm IF}$ increases to $\simeq 1\,{\rm pc}$ but has not yet reached the shock radius (gray dashed lines),

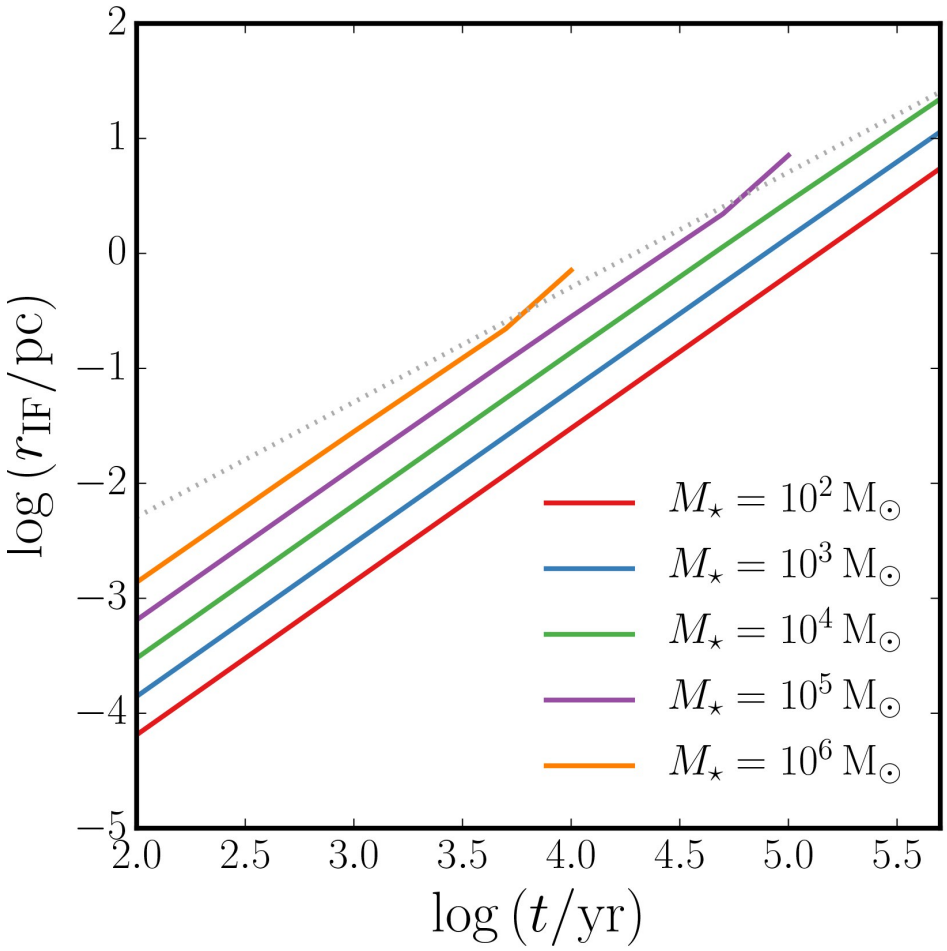


**Figure 4.12:** Ionization front radius as a function of time for masses $M_\star = 10^2$ (red), $10^3$ (blue), $10^4$ (green), $10^5$ (purple), and $10^6$ $M_\odot$ (orange). $r_{\rm IF}$ grows from values $\simeq 10^{-3} - 10^{-4}$ pc to $\simeq 3 - 10$ pc after $5 \times 10^5$ yr. For masses $M_\star = 10^4$ and $10^5$ $M_\odot$, the I-front radius eventually exceeds the shock radius (dotted line), and radiation is able to escape the central core, into the halo and beyond. For smaller masses, radiation break-out has not occurred yet, and radiation remains bottled up.

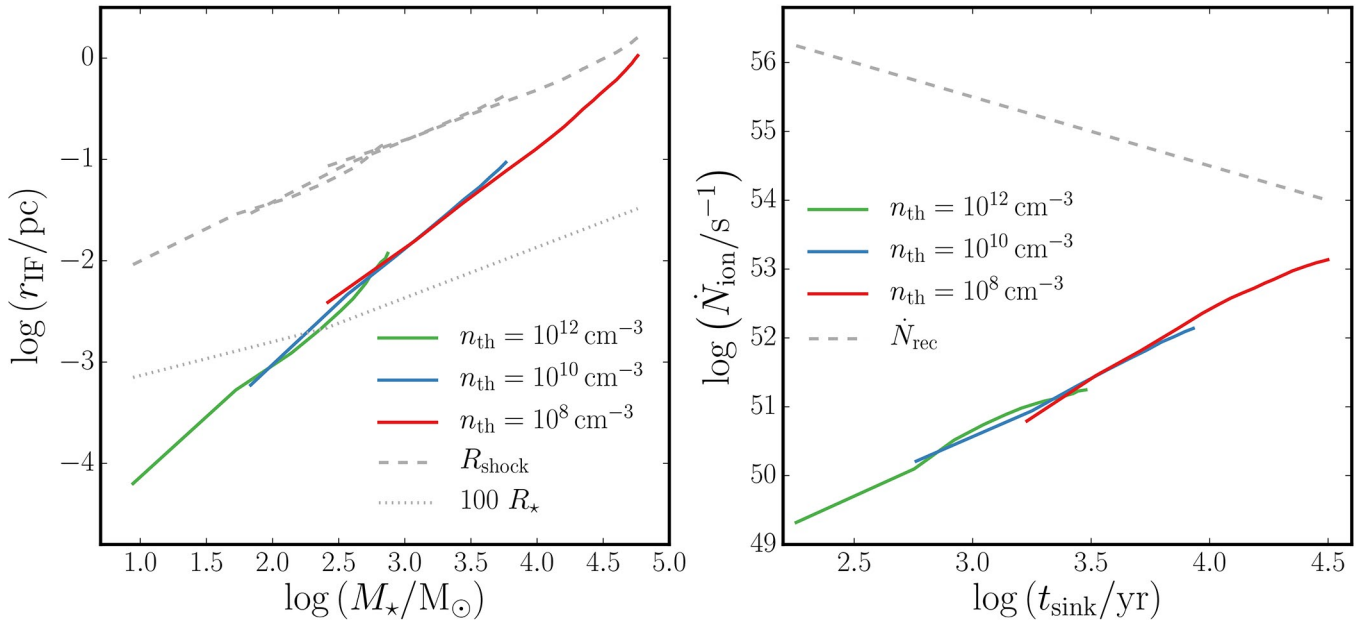


**Figure 4.13:** Structure of the expanding I-front. Left: Ionization front radius as a function of sink mass based on the data from our simulations with threshold density $n_{\rm th} = 10^8$ cm$^{-3}$ (red), $n_{\rm th} = 10^{10}$ cm$^{-3}$ (blue) and $n_{\rm th} = 10^{12}$ cm$^{-3}$ (green). Once the sink mass has reached $M_\star \simeq 5\times10^5$ M$_\odot$, the ionization front radius is of the order of $\simeq 1$ pc and has not reached the shock radius (dashed lines) yet. Although radiation has not broken out, $r_{\rm IF}$ has greatly exceeded 100 $R_\star$ (dotted line) and, as a consequence, it has detached from the stellar photosphere. Right: Ionization rates as a function of time after sink creation based on the data from our simulations for the same $n_{\rm th}$ as in the left-hand panel. After $\simeq 3 \times 10^4$ yr, $\dot{N}_{\rm ion}$ grows to $\simeq 10^{53}$ s$^{-1}$, which is not sufficient to balance the recombination rate (dashed line). This confirms that radiation has not yet broken out of the host halo by the end of our simulations.

which implies that radiation break-out has not happened at the end of our simulations. For reference, we have included $100R_\star$ as a gray dotted line, where $R_\star$ is the radius of the growing protostar, as calculated in Becerra et al. (2018b). We use this radius as an indication of the point at which radiation detaches from the stellar photosphere, which occurs at $M_\star \simeq 200\,\mathrm{M}_\odot$ for our models. From that moment radiation might influence the gas surrounding the central object and affect its growth rate. In the right-hand panel of the same figure, we use our simulation data to calculate the ionization rates as a function of time, with threshold density as a parameter. Additionally, we plot the recombination rates calculated from Equation 4.9, integrated out to $r = R_{\rm vir}$ (gray dashed lines). $\dot{N}_{\rm ion}$ grows from $\simeq 3 \times 10^{51}\,\mathrm{s}^{-1}$ at $t \simeq 200\,\mathrm{yr}$ to $\simeq 10^{53}\,\mathrm{s}^{-1}$ after $\simeq 3 \times 10^4\,\mathrm{yr}$. Nevertheless, this is not sufficient to balance the recombination rate, $\dot{N}_{\rm rec} \simeq 10^{54}\,\mathrm{s}^{-1}$. Hence, radiation has not yet broken out from the host halo.

## 4.4 Caveats

In this work, we have set out to describe the full picture of how a massive protostar of $\simeq 10\,\mathrm{M}_\odot$ becomes a supermassive black hole seed of $\simeq 10^5\,\mathrm{M}_\odot$. In contrast to our previous work in Becerra et al. (2015), we have added an improved treatment for $\mathrm{H}^-$ continuum cooling up to densities of $n_{\rm H} \simeq 10^{16}\,\mathrm{cm}^{-3}$, as detailed in Becerra et al. (2018b). To be able to follow the evolution of the central object for a longer time, we

have implemented sink particles. A drawback of this technique is that the density structure inside the sink particle accretion radius is not accurately captured. For the same reason, quantities that depend on the density, such as the mass infall rate and gravitational torques, are not truly resolved within that distance. To account for that and gain a more complete picture of the processes at small scales, we have run simulations with the same threshold densities, but employing a stiff equation of state to model the central object. Both implementations are complementary, providing us with a broader perspective on the evolution of the protostar.

In addition, we have neglected a number of physical processes that might influence the growth of such an object at some stage during its evolution. In particular, we have not modeled the radiation emerging from the central source. For example, previous studies have discussed that Ly$\alpha$ radiation might be trapped on parsec-scales around the BH seed, which would allow the temperature, and hence the Jeans mass, to increase by a factor of a few. This would result in a change of the adiabatic index to $\gamma = 4/3$, which might delay the initial collapse of the halo (Ge & Wise 2017). Eventually, Ly$\alpha$ radiation might also affect the long-term evolution of the central object by shaping its surroundings (Smith et al. 2017a). Both of these studies used post-processing routines in their analysis. In order to understand the full picture of the formation of SMBH seeds, we will need a fully coupled simulation, where Ly$\alpha$ radiation transport is calculated on-the-fly for self-consistent and higher order description of the processes involved. In this context, Luo et al. (2018); Ardaneh et al. (2018);

Chon et al. (2018) have recently presented pioneering RHD simulations of atomic cooling haloes. We plan to address the impact of radiative feedback in a follow-up study, where we will perform fully-coupled cosmological RHD simulations.

Lastly, we have not included the effects of magnetic fields, which might become important in the direct collapse scenario. For example, magnetic pressure might provide additional support against gravity, which delays the formation of a supermassive star (Latif et al. 2014b). Future work should include a detailed treatment of magneto-hydrodynamic effects in the context of atomic cooling haloes.

## 4.5 Summary and conclusions

We have performed a suite of six simulations to study the buildup of SMBH seeds at high redshifts. We follow the formation and evolution of a supermassive protostar from $M_\star \simeq 10\,\mathrm{M}_\odot$ to $M_\star \simeq 10^5\,\mathrm{M}_\odot$. For this purpose, we model the central object using two methods: sink particles and artificially-stiffened hydrostatic cores, considering three different threshold densities, $n_\mathrm{th} = 10^8$, $10^{10}$, and $10^{12}\,\mathrm{cm}^{-3}$, to address the late, intermediate, and early stages of the BH seed. The simulations employ a primordial chemistry network that evolves five species (H, $H_2$, $H^-$, $H^+$, and $e^-$), and includes $H_2$ line emission, $H_2$ collision-induces emission, Ly$\alpha$ cooling, $H^-$ continuum cooling, as well as inverse Compton cooling. In addition, we have included a uniform LW background radiation field of strength $J_{21} = 10^5$ to prevent the formation of stars

in progenitor minihaloes.

During the initial collapse the gas is shock-heated to a sub-virial temperature $T \simeq$ 8000 K. The molecular hydrogen abundance remains very small throughout the collapse, due to an external LW background radiation that photo-dissociates $H_2$ within the halo, and the collisional dissociation at higher density. As a result, atomic hydrogen cooling dominates in the form of Ly$\alpha$ emission up to densities $n_{\rm H} \simeq 10^6\,{\rm cm}^{-3}$, where the gas becomes optically thick to that radiation, and $H^-$ bound-free and free-free emission up to $n_{\rm H} \simeq 10^{17}\,{\rm cm}^{-3}$. Because of this, the gas evolves nearly isothermally over many orders of magnitude in density, which is reflected in a profile of the form $n_{\rm H} \propto r^{-2}$. Once the highest-density cell reaches a pre-set threshold density, $n_{\rm th}$, we create the central object, which is represented by a sink particle or by a hydrostatic core where cooling has been artificially suppressed.

By analyzing simulations with three threshold densities $n_{\rm th} = 10^8$, $10^{10}$, and $10^{12}\,{\rm cm}^{-3}$, we follow the evolution of the central object from $M_\star \simeq 10\,{\rm M}_\odot$ to $M_\star \simeq 6 \times 10^4\,{\rm M}_\odot$. Its growth is characterized by a relation of the form $M_\star \propto t_{\rm sink}^{1.8}$, where $t_{\rm sink}$ is the age of the sink particle. Accretion rates are in the narrow range $1 - 2.5\,{\rm M}_\odot\,{\rm yr}^{-1}$, with an average value of $\langle \dot{M}_\star \rangle \simeq 2\,{\rm M}_\odot\,{\rm yr}^{-1}$, consistent with the mass infall rates for the collapsing gas. This process is mainly driven by strong gravitational torques, $\boldsymbol{\tau}_{\rm grav} \simeq 10^{12.5}\,{\rm cm}^2\,{\rm s}^{-2}$, acting on timescales comparable to the free-fall time. The initial angular momentum is thus efficiently removed, allowing the gas to feed the central object. As the protostar grows, radiation originating from it ionizes the surround-

ing material, thus creating an initially ultra-compact, but subsequently expanding HII region. Towards the end of the lowest-resolution simulation, the rate of ionizing photons, as estimated with our idealized protostellar evolution sub-grid model, is still below the recombination rate. This would imply that the ionizing radiation is still bottled up, and has not yet escaped from the host halo. On the other hand, this emission detaches from the photosphere of the central object when its mass is $\simeq 200\,\mathrm{M}_{\odot}$. From then on, radiative feedback can influence accretion of gas onto the central object, thus ultimately affecting its final mass. For realistic modeling, the central density structure has to be known. With sinks, however, this structure is not properly resolved at small scales. To approximately assess the situation, we have here used the self-similar solution for a champagne flow to deduce the location of the I-front, and estimate the breakout time. A more accurate description of the radiative feedback from the central source and its effect on the gas requires a fully coupled, on-the-fly implementation of RHD in a cosmological context. Such simulations define the current numerical frontier of the field.

The understanding of how supermassive black holes formed so early in cosmic history is making remarkable progress, based on advances in numerical technology (e.g. Johnson & Haardt 2016; Latif & Ferrara 2016; Smith et al. 2017b; Valiante et al. 2017). Tantalizingly, the early Universe may have provided unique conditions for the accelerated emergence of massive BHs, and it is becoming evident that they have played an important part in shaping early cosmic history. The first SMBHs also pro-

vide luminous beacons of the high-redshift Universe, to be probed with the next generation of observational facilities, such as the *JWST* and the extremely large telescopes currently being built on the ground. To fully harness the promise of these facilities, simulations are vital in elucidating the key observational signatures.

## 4.6 Appendix: Convergence

Following our discussion in Section 4.3.2, we here present evidence that our simulations are converged for different central object models and different threshold densities. For that purpose, we consider number density and temperature projections for sink and stiff equation of state (EOS) simulations, and compare the resulting morphologies at similar times in their evolution. Specifically, in Section 4.6.1 we present a comparison between sink simulations with different $n_{\rm th}$, while in Section 4.6.2 we examine different central object modeling using the same $n_{\rm th}$.

### 4.6.1 Sink particles simulations

Figure 4.14 shows number density (top) and temperature (bottom) projection for sink particle simulations using different threshold densities. The left panel compares a box size of 3 pc for $n_{\rm th} = 10^8\,{\rm cm}^{-3}$ (left column) and $n_{\rm th} = 10^{10}\,{\rm cm}^{-3}$ (right column), while the right panel shows a comparison between $n_{\rm th} = 10^{10}\,{\rm cm}^{-3}$ (left column) and $n_{\rm th} = 10^{12}\,{\rm cm}^{-3}$ (right column) in a 0.3 pc projection. Additionally, we set the upper

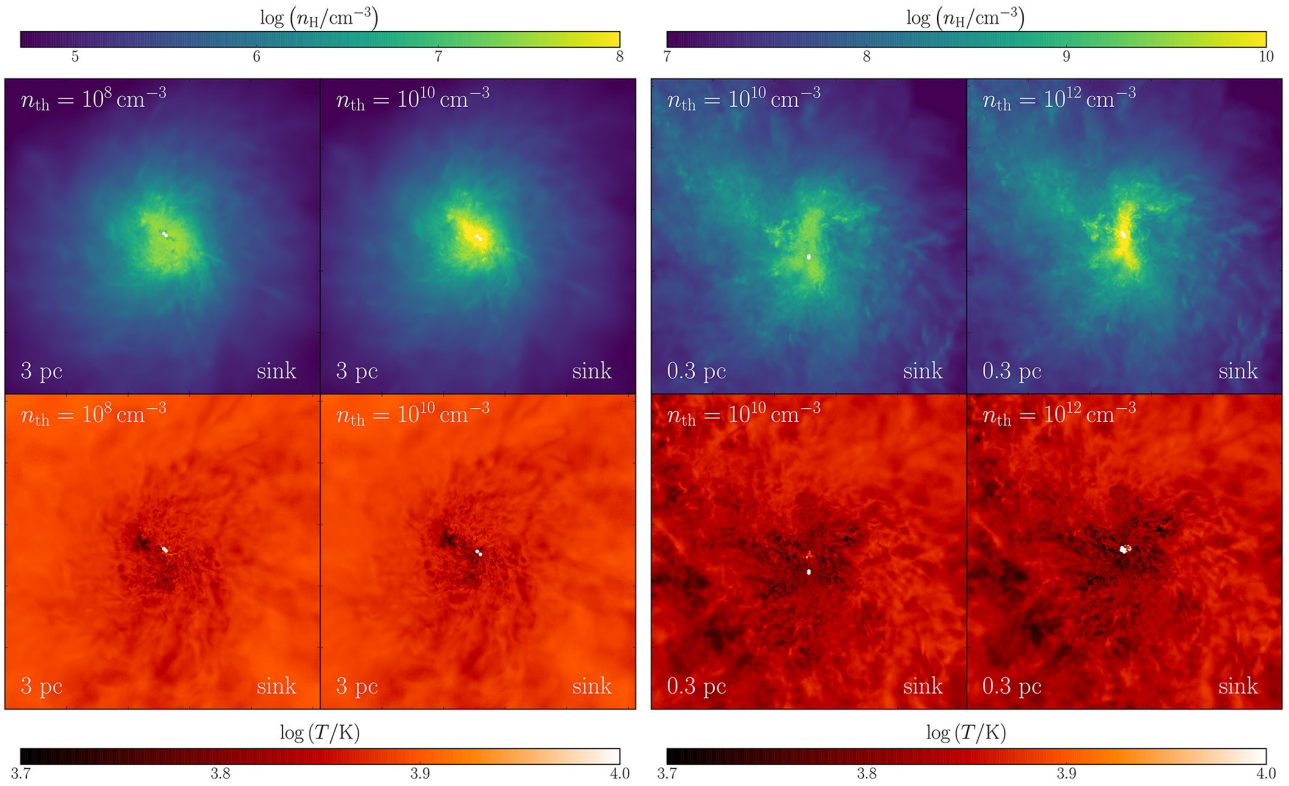


**Figure 4.14:** Number density (top) and temperature (bottom) projections for sink particle simulations with different threshold densities. Left panel shows a comparison between $n_{\rm th} = 10^8$ cm$^{-3}$ (left column) and $n_{\rm th} = 10^{10}$ cm$^{-3}$ (right column) for a box size of 3 pc, while the right panel displays snapshots for $n_{\rm th} = 10^{10}$ cm$^{-3}$ (left column) and $n_{\rm th} = 10^{12}$ cm$^{-3}$ (right column) in a 0.3 pc projection. Both density and temperature fields show similar distribution and values, independent of the threshold density used, demonstrating that these simulations are reasonably converged.

limit of the color bar to the lowest value of $n_{\rm th}$ in each panel in order to distinguish all the gas particles that are above the lowest $n_{\rm th}$ as bright yellow dots in the density projection. In this way, we effectively use bright yellow dots to represent the gas particles in the highest $n_{\rm th}$ simulation that have been replaced by sink particles and accreted by the central object in the lowest $n_{\rm th}$ simulation.

In general, we can see that the gas has a similar morphology in both panels, showing a disk-like structure in the left one, while the right one reveals a bar-like pattern at smaller scales. Similarly, the temperature distribution encloses the same range and distribution of values for both comparisons. Nevertheless, from the images we can see that the location of the central sink particle might change slightly when using different threshold densities. This, however, is small compared to the accretion radius and hence should not influence its evolution and growth.

### 4.6.2 Sink particles and stiff EOS simulations

Figure 4.15 presents a similar comparison between number density (top) and temperature (bottom) projections for different central object modeling and using the same threshold density. We show a box size of 3 pc and $n_{\rm th} = 10^8\,{\rm cm}^{-3}$, 0.3 pc and $n_{\rm th} = 10^{10}\,{\rm cm}^{-3}$, and 0.03 pc and $n_{\rm th} = 10^{12}\,{\rm cm}^{-3}$ in the top left, top right, and bottom panels, respectively. For each panel we display the sink particle method on the left column and the stiff EOS approach on the right one. In addition, we set the upper limit of the color bar to the value of $n_{\rm th}$, hence representing the gas particles

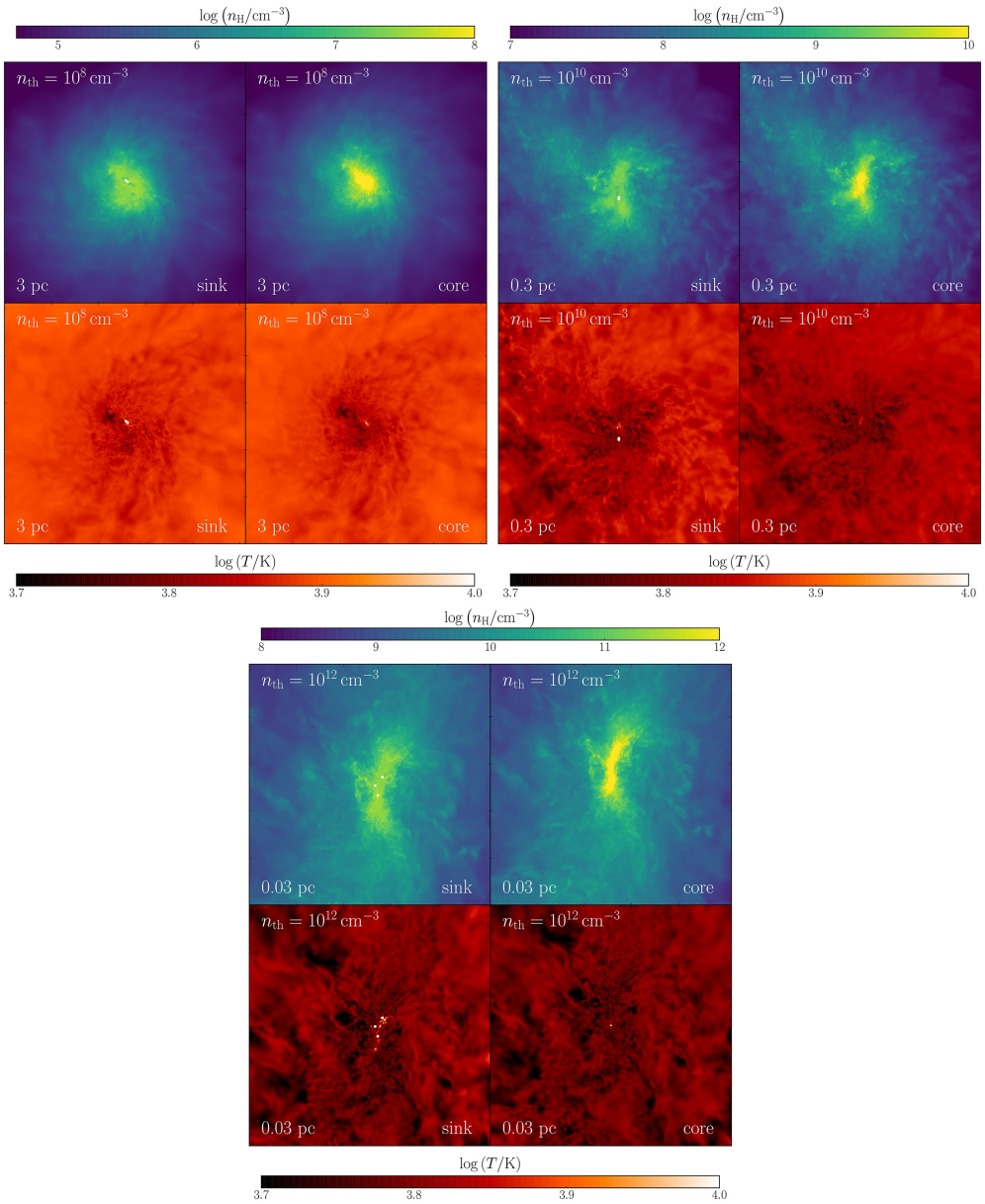


**Figure 4.15:** Number density (top) and temperature (bottom) projections of sink particles and stiff EOS simulations with the same threshold density. We display snapshots using $n_{\rm th} = 10^8$ cm$^{-3}$ in a 3 pc box in the top left panel, $n_{\rm th} = 10^{10}$ cm$^{-3}$ in a 0.3 pc box in the top right panel, and $n_{\rm th} = 10^{12}$ cm$^{-3}$ in a 0.03 pc in the bottom panel. The simulations show a similar distribution in both density and temperature, independent of the central object modeling approach used. Although we can appreciate small differences in temperature for $n_{\rm th} = 10^{12}$ cm$^{-3}$ due to strong gravitational interactions between sink particles, this does not impact the evolution of the central object.

above that threshold as bright yellow dots. These gas cells have become sink particles and been accreted by the central object in the left columns, while in the right one they have become part of the hydrostatic core as defined in Section 4.2.3.

Analogous to the previous figure, it is evident that the simulations using the same threshold density display a similar density and energy distribution. We recover the same disk- and bar-like structures when using the same threshold density, independent of the method used to model the central object. The main difference can be seen in the bottom panel, where multiple sinks have been created. The gravitational interaction between them causes the surrounding gas to heat up, an effect that is not seen in the case with an adiabatic core. However, this difference does not significantly affect the evolution and accretion history of the central object.

*"It was a pleasure to burn."*

Ray Bradbury

# 5

# Radiative feedback from supermassive black hole seeds

## 5.1 Introduction

The presence of supermassive black holes (SMBHs) with masses $\gtrsim 10^9\,\mathrm{M}_\odot$ when the Universe was less than one billion years old has been suggested by frontier observa-

tions of quasars at redshift z $\gtrsim$ 6 (Fan et al. 2003, 2006; Mortlock et al. 2011; Wu et al. 2015; Bañados et al. 2018). These SMBHs most likely grew from smaller seed BHs; however, the origin of these seeds is still unclear (Haiman 2006, 2009; Bromm & Yoshida 2011; Greene 2012; Volonteri 2012; Volonteri & Bellovary 2012; Greif 2015; Johnson & Haardt 2016; Latif & Ferrara 2016; Smith et al. 2017b). Although alternative formation mechanism have been proposed, such as high-velocity mergers of massive proto-galaxies (e.g. Mayer et al. 2010; Inayoshi et al. 2015), the two most promising pathways for the formation of BH seeds at high redshift are still the remnants of massive Population III stars (Madau & Rees 2001; Li et al. 2007; Johnson et al. 2012; Alexander & Natarajan 2014), and the direct collapse of primordial gas in haloes with virial temperatures $T_{\rm vir} \gtrsim 10^4\,{\rm K}$, the so-called atomic cooling haloes (Bromm & Loeb 2003; Begelman et al. 2006; Spaans & Silk 2006).

In the direct collapse scenario, gas falls to the center of haloes with virial temperatures $T_{\rm vir} \simeq 10^4$ K, where cooling by molecular hydrogen and metal lines has been suppressed. The destruction of molecular hydrogen can be achieved by a external soft ultraviolet (UV) background radiation field in the Lyman-Werner (LW) bands, which photo-dissociates molecular hydrogen (Omukai 2001; Bromm & Loeb 2003; Volonteri & Rees 2005; Spaans & Silk 2006; Schleicher et al. 2010; Johnson et al. 2013; Agarwal et al. 2016; Habouzit et al. 2016; Johnson & Dijkstra 2017). With cooling by molecular hydrogen greatly diminished, atomic hydrogen becomes the dominant coolant (Omukai 2001; Oh & Haiman 2002), which provokes the gas to follow a nearly isother-

mal evolution at $\simeq 10^4$ K. First, cooling is mainly driven by Lyman-$\alpha$ emission up to densities $n_{\rm H} \simeq 10^6\,{\rm cm}^{-3}$, where the gas becomes optically thick to Ly$\alpha$ radiation, and then it transitions to $H^-$ bound-free and free-free emission (Regan & Haehnelt 2009; Latif et al. 2013a; Inayoshi et al. 2014; Becerra et al. 2015, 2018b; Chon et al. 2016). At around $n_{\rm H} \simeq 10^{17}\,{\rm cm}^{-3}$ the gas becomes optically thick to $H^-$ continuum emission and from then on it evolves adiabatically, forming a massive protostar at the center of the halo (Inayoshi et al. 2014; Van Borm et al. 2014; Becerra et al. 2015; Latif et al. 2016). Since the accretion rate in a Jeans-unstable cloud scales as $\dot{M} \propto T^{3/2}$, the protostar is characterized by very high accretion rates of the order of $\simeq 1\,{\rm M}_\odot\,{\rm yr}^{-1}$. As a consequence, the protostar can grow to $\simeq 10^5 - 10^6\,{\rm M}_\odot$ and become a supermassive star in about a million years (Regan & Haehnelt 2009; Latif et al. 2013b) Becerra 2018.

As the protostar grows in mass, radiation emitted by the central source becomes important and might influence its evolution. Previous works have investigated the effect of radiative feedback in the development of Pop III stars in minihalos. In this context, one way in which radiation plays a key role is by boosting the dissociation of $H_2$ (and the consequent heating that accompanies the ionization of neutral hydrogen) due to emission in the LW bands. This molecule-dissociating radiation could become significant and indirectly shut down accretion (Susa 2013; Susa et al. 2014); however, other studies have argued that this process is not particularly relevant since the surrounding of the protostar remains optically thick to that radiation (e.g., Hosokawa

et al. 2011). A more important feedback mechanism is the destruction of neutral hydrogen by ionizing photons, accompanied by the corresponding photo-heating process that increases the temperature to values $\gtrsim 10^4$ K. The ionizing radiation then triggers the formation of HII regions around the protostars. These HII regions might not alter the accretion onto the star if they remain compact due to high inflow velocity of the gas (Omukai & Inutsuka 2002), but, if the inflow velocity decreases, then ionizing radiation can escape and photo-evaporate the surrounding gas, halting accretion and limiting the stellar growth rate (McKee & Tan 2008; Hosokawa et al. 2011; Stacy et al. 2012).

Recent works have performed radiation hydrodynamic (RHD) simulations of the collapse of gas in atomic cooling halos to analyze the development of SMBH seeds under those conditions. For instance, Chon et al. (2018) follow the evolution of two gas clouds taken from a 10 Mpc (comoving) cosmological simulation. One of the clouds is strongly affected by tidal forces from a nearby galaxy, which produces more than ten stars with masses of a few $\times 10^3\,\mathrm{M}_\odot$ due to filamentary fragmentation of the gas. In contrast, the second cloud is embedded in a relatively weak tidal field, and hence collapses nearly spherically, forming a single star-disk system. A second example is given by Luo et al. (2018), who use the flux-limited diffusion (FLD) approximation to couple the evolution of gas and radiation in isolated halos. They report the formation of a core of $\simeq 1\,\mathrm{M}_\odot$, whose evolution differs significantly from adiabatic models. The main difference between them and the FLD models is that in the latter radia-

tion might escape due to anisotropies in the optical depth. Finally, Ardaneh et al. (2018) gives a complementary view by analyzing the formation of cosmological halos using the same procedure to solve RHD. In contrast to their adiabatic counterparts, the cosmological FLD halos do not present fragmentation, forming a central core that reaches masses of $\simeq 10\,\mathrm{M}_{\odot}$ and with a photosphere of $\simeq 10$ au. Its evolution is characterized by strong outflows driven by radiation force that form dense expanding shells and transfer momentum outwards.

In this work we study the effect of radiative feedback in SMBH seeds. For that purpose, we perform three-dimensional radiation hydrodynamical simulations of the collapse of an atomic cooling halo. We utilize a similar setup to the one employed in Becerra et al. (2018a) and use those simulations as the non-radiation analog to the runs presented here. We use the newly-implemented AREPO-RT module (Kannan et al. 2018) to solve the radiative transfer equations. In particular, we model photon injection and transport, which are then coupled to the primordial chemistry network implemented in our previous work (Greif 2014; Becerra et al. 2015, 2018b). Using this approach we plan to resolve the formation of HII regions around supermassive protostars and analyze how they affect its growth. These objects will be prime targets of next-generation observational facilites (Pacucci et al. 2015; Dayal et al. 2017; Natarajan et al. 2017), such as the *James Webb Space Telescope (JWST)*, the ATHENA X-ray mission (e.g. Valiante et al. 2018), and the Laser Interferometer Space Antenna (LISA) gravitational-wave observatory (e.g. Sesana et al. 2011).

## 5.2 Numerical methodology

We investigate the effect of radiative feedback in the formation and evolution of SMBH seeds by performing three-dimensional, cosmological radiation hydrodynamics (RHD) simulations. We use the outputs from Becerra et al. (2018a), which employ the moving-mesh code AREPO (Springel 2010) with a primordial chemistry network described in detail in Greif (2014). Here we briefly summarize the procedure utilized in Becerra et al. (2015) and Becerra et al. (2018a), and we refer the reader to those works for more information.

### 5.2.1 Hydrodynamical simulations

We use the resimulation describing the central parts of the collapse of a $10^8\,M_\odot$ atomic cooling halo from Becerra et al. (2018a). This is a 20 pc, zoom-in resimulation extracted from a 2 Mpc (comoving) cosmological box once the highest density cells has reached $10^8\,cm^{-3}$. To achieve such high densities, we impose a refinement strategy in which the Jeans length is resolved by at least 64 cells. Such approach allows the simulation to capture gravitational instabilities (Truelove et al. 1997) and adequately describe the effects of turbulence (Federrath et al. 2011; Safranek-Shrader et al. 2012; Turk et al. 2012; Latif et al. 2013a).

### Chemistry

The chemistry network includes a non-equilibrium solver for five species (H, $H_2$, $H^-$, $H^+$, $e^-$), and reactions such as the formation of $H_2$ via associative detachment as well as three-body reactions, destruction of $H_2$ via collisions and photodissociation, and the formation and destruction of $H^+$ by collisional ionizations and recombinations. Additionally, the module incorporates cooling processes such as $H_2$ line cooling, $H_2$ collision-induced emission, Ly-$\alpha$ cooling, free-free and bound-free $H^-$ continuum cooling, and inverse Compton cooling. Details of the rates for chemical reactions and cooling can be found in Greif (2014) and Becerra et al. (2018b). Finally, we have added a strong Lyman-Werner (LW) background radiation field of $J_{21} = 10^5$ that photodissociates $H_2$ via the Solomon process (Abel et al. 1997)

### Sink particles

We model the central object using a sink particle prescription. For that, we pre-set a threshold density, $n_{\rm th}$, and replace any elements that reaches that value by a so-called sink particle (e.g., Bate et al. 1995; Bromm et al. 2002). To model the accretion radius, $R_{\rm acc}$, of such particle, we follow the formulation of Becerra et al. (2018b), which effectively results in a variable $R_{\rm acc}$ that depends on the mass of the sink particle. The growth in mass of a sink particle occurs through mergers with other sink particles that are inside its accretion radius. In such case, the least massive one is removed

and its mass and momentum are transferred to the most massive one.

### 5.2.2 Radiative transfer

The methodology to solve the radiative transfer equations is based on AREPO-RT (Kannan et al. 2018). Here we present a brief summary of the most important processes involved in the modeling of radiation of SMBH seeds. We start by writing the continuity equations for the propagation of a radiation field:

$$\frac{1}{c}\frac{\partial I_\nu}{\partial t} + \mathbf{n}\cdot\nabla I_\nu = j_\nu - \kappa_\nu\,\rho\,I_\nu\,, \tag{5.1}$$

where $\rho$ is gas density, $j_\nu$ the emission term, $\kappa_\nu$ the absorption coefficient, and $I_\nu(\mathbf{x}, t, \mathbf{n}, \nu)$, at position $\mathbf{x}$ and time $t$, is described as the rate of radiation energy ($E_\nu$) flowing per unit area ($\mathrm{d}\mathbf{A}$), in the direction ($\mathbf{n}$), per unit time ($\mathrm{d}t$), per unit frequency interval ($\mathrm{d}\nu$) centered on frequency $\nu$ and per unit solid angle ($\mathrm{d}\Omega$):

$$\mathrm{d}E_\nu = I_\nu(\mathbf{x}, t, \mathbf{n}, \nu)\ (\mathbf{n}\cdot\mathrm{d}\mathbf{A})\,\mathrm{d}t\,\mathrm{d}\nu\,\mathrm{d}\Omega\,. \tag{5.2}$$

A fluid description of the radiation field can be obtained in terms of the radiation energy density ($E_r$), flux ($\mathbf{F_r}$) and pressure ($\mathbb{P}_r$), defined as

$$\{\tilde{c}E_r,\ \mathbf{F_r},\ \mathbb{P}_r\} = \int_{\nu_1}^{\nu_2}\int_{4\pi}\{1, \mathbf{n},\ (\mathbf{n}\otimes\mathbf{n})\}I_\nu\,\mathrm{d}\Omega\,\mathrm{d}\nu\,. \tag{5.3}$$

Taking the zeroth and first moments of Equation 5.1, we get

$$\frac{\partial E_r}{\partial t} + \nabla \cdot \mathbf{F_r} = S - \kappa_{\rm E}\, \rho\, \tilde{c}\, E_r\,, \tag{5.4}$$

$$\frac{\partial \mathbf{F_r}}{\partial t} + \tilde{c}^2 \nabla \cdot \mathbb{P}_r = -\kappa_{\rm F}\, \rho\, \tilde{c}\, \mathbf{F_r}\,, \tag{5.5}$$

where $S$ denotes the source term which quantifies the amount of radiation energy emitted, $\kappa_{\rm E}$ and $\kappa_{\rm F}$ are the radiation energy density and radiation flux weighted mean opacities within the frequency range defined by $[\nu_1, \nu_2]$, and $\tilde{c}$ is the signal speed of radiation transport, which can be different from the actual speed of light ($c$).

### Photon injection

As the central object evolves and accretes mass, it emits ionizing radiation to the surrounding gas. We can model the ionizing photons rate as

$$\dot{N}_{\rm ion} = \frac{\pi L_{\rm Edd}}{\sigma_{\rm SB} T_{\rm eff}^4} \int_{\nu_{\rm min}}^{\infty} \frac{B_\nu}{h\nu} d\nu \tag{5.6}$$

$$\simeq 2.37 \times 10^{54} {\rm s}^{-1} \left( \frac{M_\star}{10^6\, {\rm M}_\odot} \right), \tag{5.7}$$

where $\sigma_{\rm SB}$ is the Stefan-Boltzmann constant, $B_\nu$ the Planck function, and $h\nu_{\rm min} = 13.6$ eV. For simplicity, here we have assumed a blackbody source with an effective temperature of $T_{\rm eff} = 10^5\,{\rm K}$ emitting at the Eddington luminosity, $L_{\rm Edd} = 4\pi G M_\star m_{\rm H} c/\sigma_T$, where $M_\star$ corresponds to the mass of the sink particle. At each timestep $dt$ that the sink particle becomes active, the total number of photons injected due to emission from the central object is given by

$$N_\gamma^{\rm tot} = \dot{N}_{\rm ion} dt. \tag{5.8}$$

We then distribute the total number of photons among $N_{\rm ngb}$ neighboring cells, inserting a number $N_\gamma^i$ of photons into each cell 'i', given by

$$N_\gamma^i = w_i N_\gamma^{\rm tot}. \tag{5.9}$$

Here, we have employed a weight function $w_i$ defined as

$$w_i = \frac{\phi_i V_i}{\sum_k \phi_k V_k}, \tag{5.10}$$

where $V_i$ is the volume of the gas cell and $\phi_i$ is a softening kernel. We express the kernel as a function of the variable $u = r/h$, which depends on the distance $r$ between

the sink particle and the gas cell 'i', and the smoothing length $h$:

$$\phi(r,h) = \begin{cases} \frac{1}{h^3}\left[2.55 + 15.28(u-1)u^2\right] & \text{if } u < 0.5 \\ \\ \frac{1}{h^3} 5.09(1-u)^3 & \text{if } u \geq 0.5 \end{cases} \tag{5.11}$$

We calculate $h$ using an iterative process until the number of neighbors enclosed by $h$ coincides with $N_{\text{ngb}}$.

### Photon transport

Once the photons have been injected by the sink particle into the neighboring cells, we need to model their propagation. We start by writing the equations modeling the free transport of photons by setting the RHS of Equations 5.4 and 5.5 to zero:

$$\frac{\partial E_r}{\partial t} + \nabla \cdot \mathbf{F_r} = 0\,, \tag{5.12}$$

$$\frac{\partial \mathbf{F_r}}{\partial t} + \tilde{c}^2 \nabla \cdot \mathbb{P}_r = 0\,, \tag{5.13}$$

As a closure relation, we estimate $\mathbb{P}_r$ using the Eddington tensor formalism by defining a proportionality tensor called the Eddington tensor ($\mathbb{D}$), such that

$$\mathbb{P}_r = E_r\, \mathbb{D}\,. \tag{5.14}$$

To compute the Eddington Tensor $\mathbb{D}$ we use the M1 closure, which requires only local quantities of a given cell:

$$\mathbb{D} = \frac{1-\chi}{2}\mathbb{I} + \frac{3\chi-1}{2}\mathbf{n}\otimes\mathbf{n}\,, \tag{5.15}$$

where

$$\mathbf{n} = \frac{\mathbf{F_r}}{|\mathbf{F_r}|},\ \ \chi = \frac{3+4f^2}{5+2\sqrt{4-3f^2}},\ \text{ and } f = \frac{|\mathbf{F_r}|}{\tilde{c}E_r}\,. \tag{5.16}$$

We solve these equations by using the Gauss theorem and expressing them in terms of a combination of the flux over a static interface and an advection step owing to the movement of the interface. We employ the Harte-Lax-van Leer (Harten et al. 1983) framework to solve the approximate Riemann problem normal to the surface, which is used in combination with the Heun's method, a variant of the second order Runge-Kutta scheme, to perform a conservative time integration of the Gauss theorem. The primitive variables on both sides of the interface are obtained using a slope-limited piece-wise linear spatial extrapolation and a first order prediction forward in time, for which the gradient estimates are calculated with the local least square fit. For a more detailed discussion of the methods, we refer the reader to Sections 2 and 3 of Kannan et al. (2018).

### Chemistry coupling

The next step is to calculate the absorption of photons in the surrounding gas. For that purpose, we use the single scattering regime, in which a particular photon interacts with the surrounding medium only once. In such case, we work with photon number densities instead of radiation energy density. We define the photon number density ($N_\gamma^i$), photon number flux ($\mathbf{F}_\gamma^i$), and the associated pressure tensor ($\mathbb{P}_\gamma^i$) in each frequency bin 'i' as

$$\{\tilde{c}N_\gamma^i, \mathbf{F}_\gamma^i, \mathbb{P}_\gamma^i\} = \int_{\nu_{i1}}^{\nu_{i2}} \frac{1}{h\nu}\, d\nu \int_{4\pi} \{1, \mathbf{n}, (\mathbf{n}\otimes\mathbf{n})\} I_\nu \, \mathrm{d}\Omega\,, \tag{5.17}$$

where $\nu_{i1} \leq \nu_i < \nu_{i2}$. In this case, we can formulate the equations for the change in the photon number density and photon number flux as

$$\frac{\partial N_\gamma^i}{\partial t} = -\tilde{c}\, N_\gamma^i n_{\mathrm{H\,I}}\, \bar{\sigma}_{i\mathrm{H\,I}}\,, \tag{5.18}$$

$$\frac{\partial \mathbf{F}_\gamma^i}{\partial t} = -\tilde{c}\, \mathbf{F}_\gamma^i n_{\mathrm{H\,I}}\, \bar{\sigma}_{i\mathrm{H\,I}}\,, \tag{5.19}$$

where $n_{\mathrm{H\,I}}$ is the number density of H I, and $\bar{\sigma}_{i\mathrm{H\,I}}$ is the mean ionization cross section of H I in the frequency bin 'i'

$$\bar{\sigma}_{i\mathrm{H\,I}} = \frac{\int_{\nu_{i1}}^{\nu_{i2}} \frac{4\pi J_\nu}{h\nu} \sigma_{\mathrm{H\,I}_\nu} \, \mathrm{d}\nu}{\int_{\nu_{i1}}^{\nu_{i2}} \frac{4\pi J_\nu}{h\nu} \, \mathrm{d}\nu} \,, \tag{5.20}$$

and

$$J_\nu = \frac{1}{4\pi} \int_{4\pi} I_\nu \, \mathrm{d}\Omega \,. \tag{5.21}$$

Once we have calculated the absorption of photons by the gas around the sink particle, we proceed to couple it with our primordial chemistry network. To model the creation of HII regions, we need to add two more reactions: photoionization by radiation coming from sink

$$\mathrm{H} + \gamma \rightarrow \mathrm{H}^+ + \mathrm{e}^- \,, \tag{5.22}$$

and recombination

$$\mathrm{H}^+ + \mathrm{e}^- \rightarrow \mathrm{H} + \gamma \,. \tag{5.23}$$

The reaction coefficients for both processes are given by

$$q_{\mathrm{ion}} = \tilde{c} \, n_{\mathrm{H\,I}} \sum_i \bar{\sigma}_{i\mathrm{H\,I}} \, N_\gamma^i \,, \tag{5.24}$$

and

$$q_{\rm rec} = \alpha_{\rm B}\, n_{\rm H\,II}\, n_e\,, \tag{5.25}$$

respectively. Here we have used $\alpha_{\rm B} = 2.59 \times 10^{-13} T_4^{-0.7}\,{\rm cm^3 s^{-1}}$ as the effective Case B recombination coefficient with $T_4 = T/10^4\,{\rm K}$.

Furthermore, in addition to ionizing the gas, photons also deposit energy through photoheating. We model the photoheating rate of H I as

$$\Gamma_{\rm H\,I} = \int_{\nu_{t\rm H\,I}}^{\infty} \frac{4\pi J_\nu}{h\nu}\, \sigma_{\rm H\,I\nu}\, (h\nu - h\nu_{t\rm H\,I})\, {\rm d}\nu\,, \tag{5.26}$$

where $h$ is the Planck constant and $\mathcal{E}_{\rm H\,I} = h\nu_{t\rm H\,I}$ is the ionization potential of H I . The total amount of energy deposited into the gas through photoheating is then

$$\mathcal{H} = n_{\rm H\,I} \Gamma_{\rm H\,I}. \tag{5.27}$$

## 5.3 Preliminary results

We use the sink simulations with a threshold density $n_{\rm th} \simeq 10^8\,{\rm cm^{-3}}$ from Becerra et al. (2018a) to implement and test the aforementioned routines. Those simulations follow the collapse of an atomic cooling halo and include the hydrodynamic treatment and the primordial chemistry network described in Section 5.2.1. For our RHD runs, we add the radiative transfer solver step by step: first we turn on photon injection,

and then transport. By separately adding them to our simulations, we verify that photons are being injected and advected as expected before moving to the next stage. Since the evolution of the gas is determined by the radiative transfer timestep, we use a signal speed $\tilde{c} \simeq 3 \times 10^8\,\mathrm{cm\ s^{-1}}$ to avoid reaching prohibitively small values for $dt$.

We start by analyzing photon injection using Figure 5.1, which shows the number density of hydrogen nuclei (top) and photon number density (bottom) projections in a 1 pc box at times $t \simeq 360$ (left), 2200 (middle), and 4000 yr after the creation of the central sink particle. The left column represents the early stages of the evolution, when the sink has a mass $M_\star \simeq 10^3\,\mathrm{M_\odot}$. In those conditions, the photon injection leaves a pattern of small circles of sizes $\lesssim 0.01\,\mathrm{pc}$ as the sink particle moves around every timestep it becomes active. After $\simeq 2200\,\mathrm{yr}$, the sink particle has gone through a very active period of accretion and has increased its mass to $M_\star \simeq 1.7 \times 10^4\,\mathrm{M_\odot}$, thus also increasing by about an order of magnitude the ionizing photons rate. At that point, the morphology of the distribution of photons reveal two main regions of sizes $\simeq 0.1\,\mathrm{pc}$ where photons accumulate, separated by an almost vertical strip of low photon number density where the sink is located. At later times, the sink particle keeps injecting photons while maintaining its position fixed, in which case photons assemble at the center of the cloud reaching values of $n_\gamma \simeq 10^{14}\,\mathrm{cm^{-3}}$.

Once transport is turned on, photons quickly move outwards and the region injected with them grows. The time evolution of such regions can been seen in the photon number density projections presented in Figure 5.2 for times $t \simeq 360$ (top left),

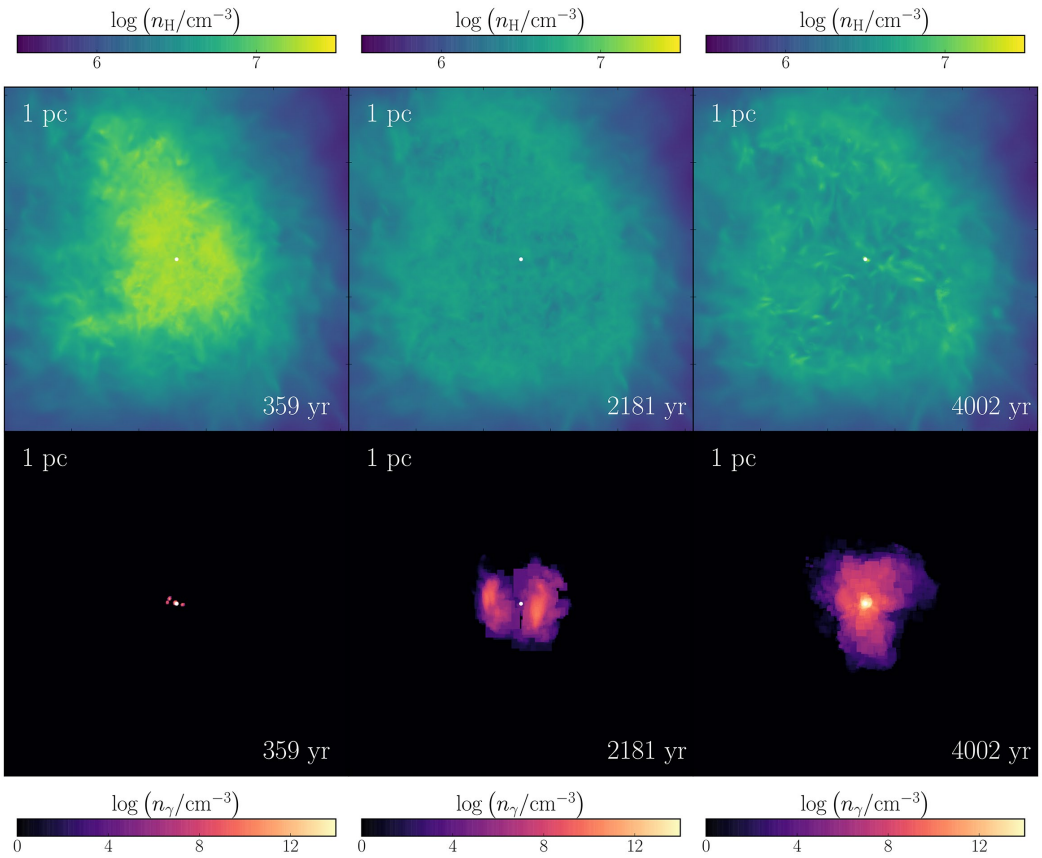


**Figure 5.1:** Injection of ionizing photons due to emission from the central object. Number density of hydrogen nuclei (top) and photon number density (bottom) projections for a box size of 1 pc at $t \simeq 360$ (left), $2200$ (middle), and $4000\,\mathrm{yr}$ (right) after the creation of the sink particle. A few hundred years after the sink particle is formed, the photon imprint is characterized by several small circles of radius $\lesssim 0.01\,\mathrm{pc}$ that represent the regions where photons were injected as the sink moved around. Due to accretion of gas, both the mass and accretion radius of the sink increase, and, as a consequence, photons are deposited in larger regions. As the sink remains roughly at the same position and keeps emitting radiation, photons concentrate at the center of the cloud reaching values $n_\gamma \simeq 10^{14}\,\mathrm{cm}^{-3}$.

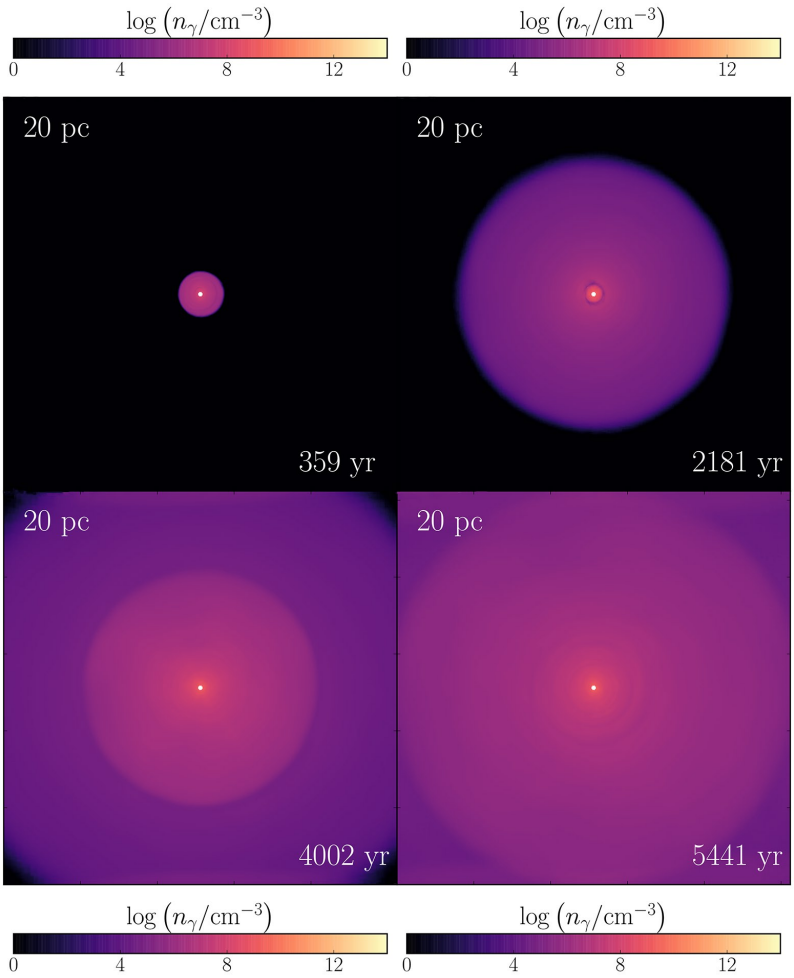


**Figure 5.2:** Time evolution of photon number density for $t \simeq 360$ (top left), $2200$ (top right), $4000$ (bottom left), and $5400\,\mathrm{yr}$ (bottom right) after the creation of the sink. The photons initially injected in small regions of $r \lesssim 0.01\,\mathrm{pc}$ have advected until covering a region with radius $r \simeq 1\,\mathrm{pc}$. The edge of this region keeps expanding to a size $r \simeq 7\,\mathrm{pc}$ at $t \simeq 2200\,\mathrm{yr}$, until finally reaches the border of the simulation box by $t \simeq 4000\,\mathrm{yr}$. In the meantime, a second injection of photons, which is about an order of magnitude larger than the previous one, occurs once the sink has accreted $\simeq 1.7 \times 10^3\,\mathrm{M}_\odot$. Similarly to the first injection episode, this region keeps expanding until it reaches the edge of the simulation box around $t \simeq 5400\,\mathrm{yr}$.

2200 (top right), 4000 (bottom left), and 5400 yr (bottom right) after the sink was formed. At $t \simeq 360$ yr, the initially small patches where photons were injected (see the bottom left panel in Figure 5.1) have grown to an area of radius $r \simeq 1$ pc, which subsequently expands to $r \simeq 7$ pc after $\simeq 2200$ yr. As seen from Figure 5.1, the sink particle undergoes a significant accretion episode around that time and, as a result, a large quantity of photons are injected in the central parts of the cloud. Those photons from the second injection then form an inner region characterized by a photon number density roughly one order of magnitude larger than the outer region, which can be distinguished in the bottom left panel of Figure 5.2. From then on, both the inner and the outer regions expand independently, reaching the edge of the simulation box after a few thousand years.

To complement this picture, we present radial profiles of photon number density at times $t \simeq 360$ (dark blue solid), 2200 (light blue dashed), 4000 (dark red solid), and 5400 yr (light red dashed) in Figure 5.3. The initial injection of photons at $t \simeq 360$ yr reaches photon number density values of $n_\gamma \simeq 10^{14}\,\mathrm{cm}^{-3}$ in the central parts, while decreasing to $n_\gamma \simeq 10^{6.5}\,\mathrm{cm}^{-3}$ at $r \simeq 1$ pc. This region keeps expanding until reaching $n_\gamma \simeq 10^{5}\,\mathrm{cm}^{-3}$ at the border, which, after $\simeq 2200$ yr, is located at $r \simeq 7$ pc. The second photon injection can be distinguished as a bump of almost one order of magnitude in $n_\gamma$ inside the inner $\simeq 7$ pc at $t \simeq 4000$ yr. The expansion of the outer and inner regions occurs independently, and both of them eventually reach the edge of the simulation box by $t \simeq 4000$ yr and $t \simeq 5400$ yr, respectively. In both regions,

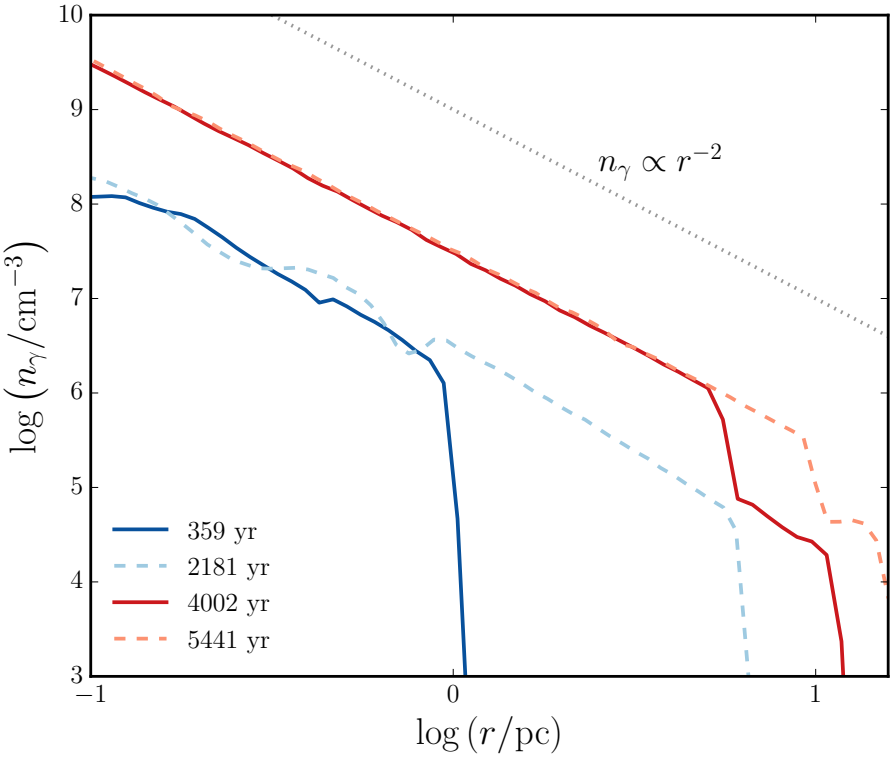


**Figure 5.3:** Radial profiles of the photon number density, $n_\gamma$, for times $t \simeq 360$ (dark blue solid), $2200$ (light blue dashed), $4000$ (dark red solid), and $5400\,\mathrm{yr}$ (light red dashed) after the creation of the sink. The first injection of photons, initially in regions of sizes $\lesssim 0.01\,\mathrm{pc}$, has expanded to $r \simeq 1\,\mathrm{pc}$, while $n_\gamma$ declines from values $\simeq 10^{14}$ cm$^{-3}$ at the center to $\simeq 10^{6.5}$ cm$^{-3}$ at the edge. This tendency is maintained $\simeq 2200\,\mathrm{yr}$ after the sink is formed, in which case the photon number density reaches values $\simeq 10^5$ cm$^{-3}$ once the border has moved to $r \simeq 7\,\mathrm{pc}$. The dark red solid line shows the second injection of photons, which is about one order of magnitude larger than the first injection and extends up to $r \simeq 7\,\mathrm{pc}$ for $t \simeq 4000\,\mathrm{yr}$. In both cases the transport of photons follows a relation of the type $n_\gamma \propto r^{-2}$, represented by the black dotted line.

the transport of photons follows a relation of the kind $n_\gamma \propto r^{-2}$ (black dotted line), as expected for photon advection when it does not interact with the surrounding gas.

## 5.4 Future directions

The next step is to couple the injection and transport of photons with the primordial chemistry network. For that we have already added the photo-ionization and recombination reactions (Equations (5.22) and (5.23)) and are in the process of adding the photo-heating rates (Equation (5.27)). Until this point, we have described how radiation emitted by the central object can ionize hydrogen and form an HII region, but other species can be ionized by those photons as well. For instance, utilizing Equation (5.7) we can also estimate the amount of HeI and HeII ionizing photons produced by a sink particle of mass $M_\star$. The modeling of the HeII and HeIII regions resulting of such interaction would require the addition of the reactions describing photo-ionization and recombination for those species, accompanied by their respective photo-heating rates. We plan to implement all these changes in the future to explore how radiative feedback might affect the growth of SMBH seeds in the early Universe.

*"But it was all right, everything was all right,*
*the struggle was finished. He had won the*
*victory over himself. He loved Big Brother."*

George Orwell

# 6

# Conclusions and future directions

Observations of quasars at redshifts $z \gtrsim 6$ suggest the existence of SMBHs of masses $\simeq 10^9\,\mathrm{M}_\odot$ when the Universe was less than a billion years old. These SMBHs most likely grew from smaller seeds BHs that formed at redshifts $z \gtrsim 15$; however, the origin of such seeds still remains unclear. One of the most promising pathways of the formation of massive BH seeds is the direct collapse of metal-free gas in halos of virial

temperatures $T_{\rm vir} \gtrsim 10^4\,{\rm K}$, so-called atomic cooling halos. In this dissertation we have investigated the formation of SMBH seeds in the direct collapse scenario. In particular, we have presented a detailed study of the formation and evolution of a supermassive protostar at the center of an atomic cooling halo, since its conception with masses $\simeq 0.1\,{\rm M}_\odot$ until it becomes a massive BH seed of $\simeq 10^5\,{\rm M}_\odot$.

## 6.1 Summary

In Chapter 2, we describe the formation of a supermassive protostar using high-resolution hydrodynamical simulations of the collapse of an atomic cooling halo in the early Universe. At the beginning, during the initial collapse, the gas is shock-heated up to temperatures $\simeq 10^4\,{\rm K}$, and then it evolves nearly isothermally due to atomic hydrogen cooling. As the central cloud keeps collapsing and reaches densities $n_{\rm H} \simeq 10^{16}\,{\rm cm}^{-3}$, the gas becomes optically thick to $H^-$ emission and follows an adiabatic evolution, which marks the formation of a protostar with mass $\simeq 0.1\,{\rm M}_\odot$ and accretion rate $\simeq 1\,{\rm M}_\odot\,{\rm yr}^{-1}$. The gas around the protostar settles into a Keplerian disk, which becomes gravitationally unstable and fragments into secondary protostars, forming a protostellar system of 5 - 10 members. Furthermore, the simulation shows the collapse of a second clump a few hundred astronomical units away from the central clump. The secondary clump is still in the early stages of formation, but if it follows a similar evolution than the central cloud it might lead to the formation of a wide

binary system. Regardless of fragmentation and three-body interaction between protostars that momentarily disrupt the central disk, the total accretion rate of the system remains high at $\simeq 1\,\mathrm{M_\odot\,yr^{-1}}$. Based on the high accretion rates reported, we conclude that fragmentation is not a significant barrier to form at least one massive BH seed.

In Chapter 3, we extend our previous work and analyze the evolution of the protostar after the gas has become optically thick to $\mathrm{H^-}$ radiation. We use two methods to describe the initial properties of the gas: one based on thermodynamic consideration, and another one using a detailed one-zone model. Both approaches agree on the characteristic density, $n_\mathrm{F} \simeq 4.6 \times 10^{16}\,\mathrm{cm^{-3}}$, mass, $M_\mathrm{F} \simeq 0.045\,\mathrm{M_\odot}$, and radius, $R_\mathrm{F} \simeq 0.33\,\mathrm{AU}$, of the protostar at that moment. Using the equations for the energy equilibrium, we derived a mass-radius relation of the type $R_\star \propto M_\star^{1/4}$ during the early stages when accretion dominates, which changes to $R_\star \propto M_\star^{1/2}$ once internal sources of radiation become significant. We then used these relations to derive a physically motivated sub-grid model to be used in numerical simulations that lack the resolution to resolve the formation and evolution of the protostar. In particular, we derive a recipe to calculate the accretion radius of a sink particle inserted at a given threshold density as a function of its mass. For high threshold densities, this prescription is based on the isothermal profile of the atomic cooling halo, but, as the sink particle grows in mass, the accretion radius transitions to the Bondi radius. We verify this model results in an accretion rate $\simeq 1\,\mathrm{M_\odot\,yr^{-1}}$, which ensures that the final mass of the central object is $\simeq 10^5 - 10^6\,\mathrm{M_\odot}$.

In Chapter 4, we present a suite of six simulations to study the buildup of a SMBH seed in the early Universe. In order to do that, we limit the resolution of the runs by setting a threshold density above which the central object is modeled using two techniques: sink particles and an artificially-stiffened equation of state. We then use three different thresholds to describe the early, intermediate, and late stages in the assembly of the central protostar. All of the simulations present a similar trend during the initial collapse: the gas is heated up to values below the virial temperature, it follows a roughly isothermal evolution due to atomic hydrogen cooling, and then a central object is formed once it reaches the threshold density. We find that the central object grows from $M_\star \simeq 10\,\mathrm{M}_\odot$ to $M_\star \simeq 6 \times 10^4\,\mathrm{M}_\odot$, with an average accretion rate of $\langle \dot{M}_\star \rangle \simeq 2\,\mathrm{M}_\odot\,\mathrm{yr}^{-1}$ for sink particles, and $\simeq 0.8 - 1.4\,\mathrm{M}_\odot\,\mathrm{yr}^{-1}$ for the stiff equation of state. These values are mainly driven by strong gravitational torques acting on timescales comparable to the free-fall time, which effectively removes angular momentum and feeds gas onto the central object. As the sink accretes mass, it emits ionizing photons that form an ultra-compact, but subsequently expanding, HII region around the protostar. Our estimations suggest that, at the end of the simulations, radiation has long detached from the stellar photosphere, but has not yet escaped from the host halo into the intergalactic medium.

Finally, in Chapter 5, we take one further step towards more realistic, self-consistent simulations by adding radiative transfer to our calculations. We introduce the methods used to perform radiation-hydrodynamical simulations: photon injection and

transport, and coupling to the primordial chemistry network. Then, we perform test runs and show that, as the sink particle accretes mass, the morphology of the region injected with photons changes from scattered patches of sizes $\lesssim 0.01\,\mathrm{pc}$ to a centralized region of size $\gtrsim 0.1\,\mathrm{pc}$. Once we turn advection on, photons expand to the edges of the simulation box following a relation of the kind $n_\gamma \propto r^{-2}$ for the photon number density. Future simulations with fully-coupled, on-the-fly radiation hydrodynamics will give a better description of the effects of radiative feedback from SMBH seeds.

## 6.2 Outlook

This dissertation presents numerical simulations and analytical models that shed light into the details of the formation of supermassive black hole seeds in the first galaxies. Here, we have developed an approach that includes the most important chemical reactions and cooling processes, but there are many other factors that can influence the evolution of supermassive protostars. For instance, Glover (2015a,b) has suggested that the presence of helium might play an important role in the chemical network in atomic cooling halos. The addition of those reactions might affect the temperature evolution and impact the accretion rates onto the central object. Future hydrodynamical simulations should include a proper treatment for helium chemistry to get a more accurate description of the temperature profile of the protostar.

One key factor that can highly influence the development of a massive black hole

seeds is radiation coming from the central source. In collaboration with Aaron Smith, we have studied how Ly-$\alpha$ emission can shape the surrounding gas and affect the long-term evolution (Smith et al. 2017a). Other groups have also explored this kind of radiation and have suggested that it might delay the initial collapse of the halo (Ge & Wise 2017). Unfortunately, these studies used post-processing routines to analyze and estimate this effect. Among other effects of radiation emitted by the protostar, we find the formation of HII, HeII, and HeIII regions around the central object by ionizing photons. In Chapter 5 we have outlined the first steps for a full implementation of radiation hydrodynamical simulations that would allow us to study the development of those regions in detail. Other works have also started to implement radiative transfer in simulations of the collapse of atomic cooling halos (e.g., Luo et al. 2018; Ardaneh et al. 2018; Chon et al. 2018). Future fully-coupled, self-consistent simulations including an on-the-fly treatment for radiation are needed to improve the current picture of the formation of SMBH seeds.

Furthermore, we have ignored the effects of magnetic fields so far, which might provide additional support against gravity and delays the formation of the central protostar (Latif et al. 2014b). Hence, besides radiative feedback, more realistic simulations should also incorporate a treatment for magnetic fields. Ideally, we would like to perform such simulations with a resolution high enough to resolve the formation of a massive protostar and follow its evolution for a few hundred thousand years. In Chapter 2 we showed the limitations of such approach, which forced us to approximate the

central object using sub-grid recipes in Chapter 4. Therefore, achieving such high resolutions in magneto radiation-hydrodynamic simulations will be strongly limited by the power of computational resources and the speed of the numerical codes used to model these problems.

Throughout this dissertation we have focused on the direct collapse scenario for the formation of black hole seeds in the early Universe. Although this seems to be the most promising pathway, future simulations should also explore other alternatives. For example, most of the work investigating the collapse of stellar cluster in massive primordial halos is analytical or using N-body simulations (e.g., Katz et al. 2015). Similarly, there are theoretical studies that propose the formation of massive black hole seeds as a consequence of high-velocity mergers (e.g. Mayer et al. 2010; Inayoshi et al. 2015). Both of these approaches would highly benefit from three-dimensional, hydrodynamical simulations to confirm or discard their feasibility.

Finally, one fundamental ingredient that is still missing is the direct observation of signatures from these black hole seeds. Cosmological simulations are an excellent tool to gain insights on the physical processes governing the formation of these objects and to make predictions about their observational fingerprints. However, any result obtained from our numerical experiments will have to be probed with the next-generation observational facilities, such as the James Webb Space Telescope. Complementarily, a prime target for the Laser Interferometer Space Antenna is the gravitational wave signal accompanying the possible merger of binary black holes, which

would shed light into the process of formation of the first supermassive objects. The synergy between numerical simulations and observations will ultimately provide a complete picture of the formation of supermassive black hole seeds in the early Universe.

REFERENCES

Abel, T., Anninos, P., Zhang, Y., & Norman, M. L. (1997). Modeling primordial gas in numerical cosmology. *NA*, 2, 181–207.

Agarwal, B., Dalla Vecchia, C., Johnson, J. L., Khochfar, S., & Paardekooper, J.-P. (2014). The First Billion Years project: birthplaces of direct collapse black holes. *MNRAS*, 443, 648–657.

Agarwal, B. & Khochfar, S. (2015). Revised rate coefficients for $H_2$ and $H^-$ destruction by realistic stellar spectra. *MNRAS*, 446, 160–168.

Agarwal, B., Khochfar, S., Johnson, J. L., Neistein, E., Dalla Vecchia, C., & Livio, M. (2012). Ubiquitous seeding of supermassive black holes by direct collapse. *MNRAS*, 425, 2854–2871.

Agarwal, B., Smith, B., Glover, S., Natarajan, P., & Khochfar, S. (2016). New constraints on direct collapse black hole formation in the early Universe. *MNRAS*, 459, 4209–4217.

Alexander, T. & Natarajan, P. (2014). Rapid growth of seed black holes in the early universe by supra-exponential accretion. *Science*, 345, 1330–1333.

Alvarez, M. A., Bromm, V., & Shapiro, P. R. (2006). The H II Region of the First Star. *ApJ*, 639, 621–632.

Alvarez, M. A., Wise, J. H., & Abel, T. (2009). Accretion onto the First Stellar-Mass Black Holes. *ApJ*, 701, L133–L137.

Ardaneh, K., Luo, Y., Shlosman, I., Nagamine, K., Wise, J. H., & Begelman, M. C. (2018). Direct Collapse to Supermassive Black Hole Seeds with Radiation Transfer: Cosmological Halos. *ArXiv e-prints*.

Bañados, E., Venemans, B. P., Mazzucchelli, C., Farina, E. P., Walter, F., Wang, F., Decarli, R., Stern, D., Fan, X., Davies, F. B., Hennawi, J. F., Simcoe, R. A., Turner, M. L., Rix, H.-W., Yang, J., Kelson, D. D., Rudie, G. C., & Winters, J. M. (2018). An 800-million-solar-mass black hole in a significantly neutral Universe at a redshift of 7.5. *Nat*, 553, 473–476.

Bate, M. R., Bonnell, I. A., & Bromm, V. (2003). The formation of a star cluster:

predicting the properties of stars and brown dwarfs. *MNRAS*, 339, 577–599.

Bate, M. R., Bonnell, I. A., & Price, N. M. (1995). Modelling accretion in protobinary systems. *MNRAS*, 277, 362–376.

Baumgarte, T. W. & Shapiro, S. L. (1999). Evolution of Rotating Supermassive Stars to the Onset of Collapse. *ApJ*, 526, 941–952.

Becerra, F., Greif, T. H., Springel, V., & Hernquist, L. E. (2015). Formation of massive protostars in atomic cooling haloes. *MNRAS*, 446, 2380–2393.

Becerra, F., Marinacci, F., Bromm, V., & Hernquist, L. E. (2018a). Assembly of supermassive black hole seeds. *ArXiv e-prints*.

Becerra, F., Marinacci, F., Inayoshi, K., Bromm, V., & Hernquist, L. E. (2018b). Opacity Limit for Supermassive Protostars. *ApJ*, 857, 138.

Begelman, M. C. (1978). Black holes in radiation-dominated gas - an analogue of the Bondi accretion problem. *MNRAS*, 184, 53–67.

Begelman, M. C. (2010). Evolution of supermassive stars as a pathway to black hole formation. *MNRAS*, 402, 673–681.

Begelman, M. C., Rossi, E. M., & Armitage, P. J. (2008). Quasi-stars: accreting black holes inside massive envelopes. *MNRAS*, 387, 1649–1659.

Begelman, M. C. & Shlosman, I. (2009). Angular Momentum Transfer and Lack of Fragmentation in Self-Gravitating Accretion Flows. *ApJ*, 702, L5–L8.

Begelman, M. C., Volonteri, M., & Rees, M. J. (2006). Formation of supermassive black holes by direct collapse in pre-galactic haloes. *MNRAS*, 370, 289–298.

Binney, J. & Tremaine, S. (1987). *Galactic dynamics*.

Bonnor, W. B. (1956). Boyle's Law and gravitational instability. *MNRAS*, 116, 351.

Borysow, A., Frommhold, L., & Moraldi, M. (1989). Collision-induced infrared spectra of H2-He pairs involving 0-1 vibrational transitions and temperatures from 18 to 7000 K. *ApJ*, 336, 495–503.

Bromm, V., Coppi, P. S., & Larson, R. B. (2002). The Formation of the First Stars. I. The Primordial Star-forming Cloud. *ApJ*, 564, 23–51.

Bromm, V., Kudritzki, R. P., & Loeb, A. (2001). Generic Spectrum and Ionization Efficiency of a Heavy Initial Mass Function for the First Stars. *ApJ*, 552, 464–472.

Bromm, V. & Loeb, A. (2003). Formation of the First Supermassive Black Holes. *ApJ*, 596, 34–46.

Bromm, V. & Yoshida, N. (2011). The First Galaxies. *ARA&A*, 49, 373–407.

Cen, R. (1992). A hydrodynamic approach to cosmology - Methodology. *ApJS*, 78, 341–364.

Chen, K.-J., Heger, A., Woosley, S., Almgren, A., Whalen, D. J., & Johnson, J. L. (2014). The General Relativistic Instability Supernova of a Supermassive Population III Star. *ApJ*, 790, 162.

Choi, J.-H., Shlosman, I., & Begelman, M. C. (2013). Supermassive Black Hole Formation at High Redshifts via Direct Collapse: Physical Processes in the Early Stage. *ApJ*, 774, 149.

Choi, J.-H., Shlosman, I., & Begelman, M. C. (2015). Supermassive black hole formation at high redshifts via direct collapse in a cosmological context. *MNRAS*, 450, 4411–4423.

Chon, S., Hirano, S., Hosokawa, T., & Yoshida, N. (2016). Cosmological Simulations of Early Black Hole Formation: Halo Mergers, Tidal Disruption, and the Conditions for Direct Collapse. *ApJ*, 832, 134.

Chon, S., Hosokawa, T., & Yoshida, N. (2018). Radiation hydrodynamics simulations of the formation of direct-collapse supermassive stellar systems. *MNRAS*, 475, 4104–4121.

Clark, P. C., Glover, S. C. O., & Klessen, R. S. (2008). The First Stellar Cluster. *ApJ*, 672, 757–764.

Clark, P. C., Glover, S. C. O., Smith, R. J., Greif, T. H., Klessen, R. S., & Bromm, V. (2011). The Formation and Fragmentation of Disks Around Primordial Protostars. *Science*, 331, 1040.

Dayal, P., Choudhury, T. R., Pacucci, F., & Bromm, V. (2017). Warm dark matter constraints from high-z direct collapse black holes using the JWST. *MNRAS*, 472, 4414–4421.

Devecchi, B. & Volonteri, M. (2009). Formation of the First Nuclear Clusters and Massive Black Holes at High Redshift. *ApJ*, 694, 302–313.

Dijkstra, M., Ferrara, A., & Mesinger, A. (2014). Feedback-regulated supermassive black hole seed formation. *MNRAS*, 442, 2036–2047.

Dijkstra, M., Haiman, Z., Mesinger, A., & Wyithe, J. S. B. (2008). Fluctuations in the high-redshift Lyman-Werner background: close halo pairs as the origin of supermassive black holes. *MNRAS*, 391, 1961–1972.

Draine, B. T. & Bertoldi, F. (1996). Structure of Stationary Photodissociation Fronts. *ApJ*, 468, 269.

Ebert, R. (1955). Über die Verdichtung von H I-Gebieten. Mit 5 Textabbildungen. *Z. Astrophys.*, 37, 217.

Eisenstein, D. J. & Loeb, A. (1995). Origin of quasar progenitors from the collapse of low-spin cosmological perturbations. *ApJ*, 443, 11–17.

Fan, X., Strauss, M. A., Becker, R. H., White, R. L., Gunn, J. E., Knapp, G. R., Richards, G. T., Schneider, D. P., Brinkmann, J., & Fukugita, M. (2006). Constraining the Evolution of the Ionizing Background and the Epoch of Reionization with z~6 Quasars. II. A Sample of 19 Quasars. *AJ*, 132, 117–136.

Fan, X., Strauss, M. A., Schneider, D. P., Becker, R. H., White, R. L., Haiman, Z., Gregg, M., Pentericci, L., Grebel, E. K., Narayanan, V. K., Loh, Y.-S., Richards, G. T., Gunn, J. E., Lupton, R. H., Knapp, G. R., Ivezić, Ž., Brandt, W. N., Collinge, M., Hao, L., Harbeck, D., Prada, F., Schaye, J., Strateva, I., Zakamska, N., Anderson, S., Brinkmann, J., Bahcall, N. A., Lamb, D. Q., Okamura, S., Szalay, A., & York, D. G. (2003). A Survey of z>5.7 Quasars in the Sloan Digital Sky Survey. II. Discovery of Three Additional Quasars at z>6. *AJ*, 125, 1649–1659.

Federrath, C., Sur, S., Schleicher, D. R. G., Banerjee, R., & Klessen, R. S. (2011). A New Jeans Resolution Criterion for (M)HD Simulations of Self-gravitating Gas: Application to Magnetic Field Amplification by Gravity-driven Turbulence. *ApJ*, 731, 62.

Ferland, G. J., Peterson, B. M., Horne, K., Welsh, W. F., & Nahar, S. N. (1992). Anisotropic line emission and the geometry of the broad-line region in active galactic nuclei. *ApJ*, 387, 95–108.

Ferrarese, L. & Merritt, D. (2000). A Fundamental Relation between Supermassive Black Holes and Their Host Galaxies. *ApJ*, 539, L9–L12.

Fiacconi, D. & Rossi, E. M. (2016). Bright vigorous winds as signposts of supermassive black hole birth. *MNRAS*, 455, 2–16.

Forrey, R. C. (2013). Rate of Formation of Hydrogen Molecules by Three-body Recombination during Primordial Star Formation. *ApJ*, 773, L25.

Fricke, K. J. (1973). Dynamical Phases of Supermassive Stars. *ApJ*, 183, 941–958.

Galli, D. & Palla, F. (1998). The chemistry of the early Universe. *A&A*, 335, 403–420.

Ge, Q. & Wise, J. H. (2017). On the effect of Lyman $\alpha$ trapping during the initial collapse of massive black hole seeds. *MNRAS*, 472, 2773–2786.

Gebhardt, K., Bender, R., Bower, G., Dressler, A., Faber, S. M., Filippenko, A. V., Green, R., Grillmair, C., Ho, L. C., Kormendy, J., Lauer, T. R., Magorrian, J., Pinkney, J., Richstone, D., & Tremaine, S. (2000). A Relationship between Nuclear Black Hole Mass and Galaxy Velocity Dispersion. *ApJ*, 539, L13–L16.

Glover, S. C. O. (2015a). Simulating the formation of massive seed black holes in the early Universe - I. An improved chemical model. *MNRAS*, 451, 2082–2096.

Glover, S. C. O. (2015b). Simulating the formation of massive seed black holes in the early Universe - II. Impact of rate coefficient uncertainties. *MNRAS*, 453, 2901–2918.

Greene, J. E. (2012). Low-mass black holes as the remnants of primordial black hole formation. *Nature Communications*, 3.

Greif, T. H. (2014). Multifrequency radiation hydrodynamics simulations of $H_2$ line emission in primordial, star-forming clouds. *MNRAS*, 444, 1566–1583.

Greif, T. H. (2015). The numerical frontier of the high-redshift Universe. *Computational Astrophysics and Cosmology*, 2, 3.

Greif, T. H., Bromm, V., Clark, P. C., Glover, S. C. O., Smith, R. J., Klessen, R. S., Yoshida, N., & Springel, V. (2012). Formation and evolution of primordial protostellar systems. *MNRAS*, 424, 399–415.

Greif, T. H., Johnson, J. L., Klessen, R. S., & Bromm, V. (2008). The first galaxies: assembly, cooling and the onset of turbulence. *MNRAS*, 387, 1021–1036.

Greif, T. H., Springel, V., White, S. D. M., Glover, S. C. O., Clark, P. C., Smith, R. J., Klessen, R. S., & Bromm, V. (2011). Simulations on a Moving Mesh: The Clustered Formation of Population III Protostars. *ApJ*, 737, 75.

Habouzit, M., Volonteri, M., Latif, M., Dubois, Y., & Peirani, S. (2016). On the number density of 'direct collapse' black hole seeds. *MNRAS*, 463, 529–540.

Haiman, Z. (2006). The formation of the first black holes and their host halos. *New Astron. Rev.*, 50, 672–676.

Haiman, Z. (2009). *Observing the First Stars and Black Holes*, (pp. 385).

Haiman, Z. (2013). The Formation of the First Massive Black Holes. In T. Wiklind, B. Mobasher, & V. Bromm (Eds.), *The First Galaxies*, volume 396 of *Astrophysics and Space Science Library* (pp. 293).

Hanawa, T. & Matsumoto, T. (2000). Stability of a Dynamically Collapsing Gas Sphere. *PASJ*, 52, 241.

Häring, N. & Rix, H.-W. (2004). On the Black Hole Mass-Bulge Mass Relation. *ApJ*, 604, L89–L92.

Harten, A., Lax, P. D., & van Leer, B. (1983). On upstream differencing and godunov-type schemes for hyperbolic conservation laws. *SIAM Review*, 25(1), 35–61.

Heger, A., Fryer, C. L., Woosley, S. E., Langer, N., & Hartmann, D. H. (2003). How Massive Single Stars End Their Life. *ApJ*, 591, 288–300.

Hindmarsh, A. C., Brown, P. N., Grant, K. E., Lee, S. L., Serban, R., Shumaker, D. E., & Woodward, C. S. (2005). Sundials: Suite of nonlinear and differential/algebraic equation solvers. *ACM Trans. Math. Softw.*, 31(3), 363–396.

Hirano, S. & Bromm, V. (2017). Formation and survival of Population III stellar

systems. *MNRAS*, 470, 898–914.

Hirano, S. & Bromm, V. (2018). Angular momentum transfer in primordial discs and the rotation of the first stars. *MNRAS*, 476, 3964–3973.

Hirano, S., Hosokawa, T., Yoshida, N., Umeda, H., Omukai, K., Chiaki, G., & Yorke, H. W. (2014). One Hundred First Stars: Protostellar Evolution and the Final Masses. *ApJ*, 781, 60.

Hosokawa, T., Hirano, S., Kuiper, R., Yorke, H. W., Omukai, K., & Yoshida, N. (2016). Formation of Massive Primordial Stars: Intermittent UV Feedback with Episodic Mass Accretion. *ApJ*, 824, 119.

Hosokawa, T., Omukai, K., & Yorke, H. W. (2012). Rapidly Accreting Supergiant Protostars: Embryos of Supermassive Black Holes? *ApJ*, 756, 93.

Hosokawa, T., Omukai, K., Yoshida, N., & Yorke, H. W. (2011). Protostellar Feedback Halts the Growth of the First Stars in the Universe. *Science*, 334, 1250.

Hosokawa, T., Yorke, H. W., Inayoshi, K., Omukai, K., & Yoshida, N. (2013). Formation of Primordial Supermassive Stars by Rapid Mass Accretion. *ApJ*, 778, 178.

Hoyle, F. (1953). On the Fragmentation of Gas Clouds Into Galaxies and Stars. *ApJ*, 118, 513.

Inayoshi, K. & Haiman, Z. (2014). Does disc fragmentation prevent the formation of supermassive stars in protogalaxies? *MNRAS*, 445, 1549–1557.

Inayoshi, K., Haiman, Z., & Ostriker, J. P. (2016). Hyper-Eddington accretion flows on to massive black holes. *MNRAS*, 459, 3738–3755.

Inayoshi, K., Hosokawa, T., & Omukai, K. (2013). Pulsational instability of supergiant protostars: do they grow supermassive by accretion? *MNRAS*, 431, 3036–3044.

Inayoshi, K., Omukai, K., & Tasker, E. (2014). Formation of an embryonic supermassive star in the first galaxy. *MNRAS*, 445, L109–L113.

Inayoshi, K., Visbal, E., & Kashiyama, K. (2015). Direct collapse black hole formation via high-velocity collisions of protogalaxies. *MNRAS*, 453, 1692–1700.

Jacobs, T. A., Giedt, R. R., & Cohen, N. (1967). Kinetics of hydrogen halides in shock waves. ii. a new measurement of the hydrogen dissociation rate. *The Journal of Chemical Physics*, 47(1), 54–57.

Janev, R. K., Langer, W. D., & Evans, K. (1987). *Elementary processes in Hydrogen-Helium plasmas - Cross sections and reaction rate coefficients*.

Johnson, J. L. & Bromm, V. (2007). The aftermath of the first stars: massive black holes. *MNRAS*, 374, 1557–1568.

Johnson, J. L. & Dijkstra, M. (2017). Enhanced direct collapse due to Lyman $\alpha$ feedback. *A&A*, 601, A138.

Johnson, J. L. & Haardt, F. (2016). The Early Growth of the First Black Holes. *Publ. Astron. Soc. Australia*, 33, e007.

Johnson, J. L., Khochfar, S., Greif, T. H., & Durier, F. (2011). Accretion on to black holes formed by direct collapse. *MNRAS*, 410, 919–933.

Johnson, J. L., Whalen, D. J., Fryer, C. L., & Li, H. (2012). The Growth of the Stellar Seeds of Supermassive Black Holes. *ApJ*, 750, 66.

Johnson, J. L., Whalen, D. J., Li, H., & Holz, D. E. (2013). Supermassive Seeds for Supermassive Black Holes. *ApJ*, 771, 116.

Kannan, R., Vogelsberger, M., Marinacci, F., McKinnon, R., Pakmor, R., & Springel, V. (2018). AREPO-RT: Radiation hydrodynamics on a moving mesh. *ArXiv e-prints*.

Katz, H., Sijacki, D., & Haehnelt, M. G. (2015). Seeding high-redshift QSOs by collisional runaway in primordial star clusters. *MNRAS*, 451, 2352–2369.

Komatsu, E., Dunkley, J., Nolta, M. R., Bennett, C. L., Gold, B., Hinshaw, G., Jarosik, N., Larson, D., Limon, M., Page, L., Spergel, D. N., Halpern, M., Hill, R. S., Kogut, A., Meyer, S. S., Tucker, G. S., Weiland, J. L., Wollack, E., & Wright, E. L. (2009). Five-Year Wilkinson Microwave Anisotropy Probe Observations: Cosmological Interpretation. *ApJS*, 180, 330–376.

Kormendy, J. & Ho, L. C. (2013). Coevolution (Or Not) of Supermassive Black Holes and Host Galaxies. *ARA&A*, 51, 511–653.

Koushiappas, S. M., Bullock, J. S., & Dekel, A. (2004). Massive black hole seeds from low angular momentum material. *MNRAS*, 354, 292–304.

Kreckel, H., Bruhns, H., Čížek, M., Glover, S. C. O., Miller, K. A., Urbain, X., & Savin, D. W. (2010). Experimental Results for $H_2$ Formation from $H^-$ and H and Implications for First Star Formation. *Science*, 329, 69.

Lai, D. (2000). Global Nonradial Instabilities of Dynamically Collapsing Gas Spheres. *ApJ*, 540, 946–961.

Larson, R. B. (1969). Numerical calculations of the dynamics of collapsing proto-star. *MNRAS*, 145, 271.

Latif, M. A., Bovino, S., Grassi, T., Schleicher, D. R. G., & Spaans, M. (2015). How realistic UV spectra and X-rays suppress the abundance of direct collapse black holes. *MNRAS*, 446, 3163–3177.

Latif, M. A. & Ferrara, A. (2016). Formation of Supermassive Black Hole Seeds. *Publ. Astron. Soc. Australia*, 33, e051.

Latif, M. A. & Schleicher, D. R. G. (2015). The formation of supermassive black holes in rapidly rotating disks. *A&A*, 578, A118.

Latif, M. A., Schleicher, D. R. G., Bovino, S., Grassi, T., & Spaans, M. (2014a). The Formation of Massive Primordial Stars in the Presence of Moderate UV Backgrounds. *ApJ*, 792, 78.

Latif, M. A., Schleicher, D. R. G., & Hartwig, T. (2016). Witnessing the birth of a supermassive protostar. *MNRAS*, 458, 233–241.

Latif, M. A., Schleicher, D. R. G., & Schmidt, W. (2014b). Magnetic fields during the formation of supermassive black holes. *MNRAS*, 440, 1551–1561.

Latif, M. A., Schleicher, D. R. G., Schmidt, W., & Niemeyer, J. (2013a). Black hole formation in the early Universe. *MNRAS*, 433, 1607–1618.

Latif, M. A., Schleicher, D. R. G., Schmidt, W., & Niemeyer, J. (2013b). High-resolution studies of massive primordial haloes. *MNRAS*, 430, 588–598.

Latif, M. A., Schleicher, D. R. G., Schmidt, W., & Niemeyer, J. (2013c). The small-

scale dynamo and the amplification of magnetic fields in massive primordial haloes. *MNRAS*, 432, 668–678.

Latif, M. A., Schleicher, D. R. G., Schmidt, W., & Niemeyer, J. C. (2013d). The characteristic black hole mass resulting from direct collapse in the early Universe. *MNRAS*, 436, 2989–2996.

Lehnert, M. D., Nesvadba, N. P. H., Cuby, J.-G., Swinbank, A. M., Morris, S., Clément, B., Evans, C. J., Bremer, M. N., & Basa, S. (2010). Spectroscopic confirmation of a galaxy at redshift z = 8.6. *Nat*, 467, 940–942.

Li, Y., Hernquist, L., Robertson, B., Cox, T. J., Hopkins, P. F., Springel, V., Gao, L., Di Matteo, T., Zentner, A. R., Jenkins, A., & Yoshida, N. (2007). Formation of z~6 Quasars from Hierarchical Galaxy Mergers. *ApJ*, 665, 187–208.

Lodato, G. & Natarajan, P. (2006). Supermassive black hole formation during the assembly of pre-galactic discs. *MNRAS*, 371, 1813–1823.

Loeb, A. & Rasio, F. A. (1994). Collapse of primordial gas clouds and the formation of quasar black holes. *ApJ*, 432, 52–61.

Low, C. & Lynden-Bell, D. (1976). The minimum Jeans mass or when fragmentation must stop. *MNRAS*, 176, 367–390.

Luo, Y., Ardaneh, K., Shlosman, I., Nagamine, K., Wise, J. H., & Begelman, M. C. (2018). Direct Collapse to Supermassive Black Hole Seeds with Radiative Transfer: Isolated Halos. *MNRAS*.

Madau, P. & Rees, M. J. (2001). Massive Black Holes as Population III Remnants. *ApJ*, 551, L27–L30.

Magorrian, J., Tremaine, S., Richstone, D., Bender, R., Bower, G., Dressler, A., Faber, S. M., Gebhardt, K., Green, R., Grillmair, C., Kormendy, J., & Lauer, T. (1998). The Demography of Massive Dark Objects in Galaxy Centers. *AJ*, 115, 2285–2305.

Marconi, A. & Hunt, L. K. (2003). The Relation between Black Hole Mass, Bulge Mass, and Near-Infrared Luminosity. *ApJ*, 589, L21–L24.

Mayer, L., Kazantzidis, S., Escala, A., & Callegari, S. (2010). Direct formation of supermassive black holes via multi-scale gas inflows in galaxy mergers. *Nat*, 466,

1082–1084.

McDowell, M. R. C. (1961). On the formation of H2 in H I regions. *The Observatory*, 81, 240–243.

McKee, C. F. & Tan, J. C. (2008). The Formation of the First Stars. II. Radiative Feedback Processes and Implications for the Initial Mass Function. *ApJ*, 681, 771–797.

Milosavljević, M., Bromm, V., Couch, S. M., & Oh, S. P. (2009). Accretion onto "Seed" Black Holes in the First Galaxies. *ApJ*, 698, 766–780.

Mo, H. J., Mao, S., & White, S. D. M. (1998). The formation of galactic discs. *MNRAS*, 295, 319–336.

Montero, P. J., Janka, H.-T., & Müller, E. (2012). Relativistic Collapse and Explosion of Rotating Supermassive Stars with Thermonuclear Effects. *ApJ*, 749, 37.

Mortlock, D. J., Warren, S. J., Venemans, B. P., Patel, M., Hewett, P. C., McMahon, R. G., Simpson, C., Theuns, T., Gonzáles-Solares, E. A., Adamson, A., Dye, S., Hambly, N. C., Hirst, P., Irwin, M. J., Kuiper, E., Lawrence, A., & Röttgering, H. J. A. (2011). A luminous quasar at a redshift of z = 7.085. *Nat*, 474, 616–619.

Natarajan, P., Pacucci, F., Ferrara, A., Agarwal, B., Ricarte, A., Zackrisson, E., & Cappelluti, N. (2017). Unveiling the First Black Holes With JWST:Multi-wavelength Spectral Predictions. *ApJ*, 838, 117.

Oesch, P. A., Brammer, G., van Dokkum, P. G., Illingworth, G. D., Bouwens, R. J., Labbé, I., Franx, M., Momcheva, I., Ashby, M. L. N., Fazio, G. G., Gonzalez, V., Holden, B., Magee, D., Skelton, R. E., Smit, R., Spitler, L. R., Trenti, M., & Willner, S. P. (2016). A Remarkably Luminous Galaxy at z=11.1 Measured with Hubble Space Telescope Grism Spectroscopy. *ApJ*, 819, 129.

Oh, S. P. & Haiman, Z. (2002). Second-Generation Objects in the Universe: Radiative Cooling and Collapse of Halos with Virial Temperatures above $10^4$ K. *ApJ*, 569, 558–572.

Omukai, K. (2001). Primordial Star Formation under Far-Ultraviolet Radiation. *ApJ*, 546, 635–651.

Omukai, K. & Inutsuka, S.-i. (2002). An upper limit on the mass of a primordial star due to the formation of an Hii region: the effect of ionizing radiation force. *MNRAS*, 332, 59–64.

Omukai, K. & Nishi, R. (1998). Formation of Primordial Protostars. *ApJ*, 508, 141–150.

Omukai, K. & Palla, F. (2003). Formation of the First Stars by Accretion. *ApJ*, 589, 677–687.

Omukai, K., Schneider, R., & Haiman, Z. (2008). Can Supermassive Black Holes Form in Metal-enriched High-Redshift Protogalaxies? *ApJ*, 686, 801–814.

Omukai, K., Tsuribe, T., Schneider, R., & Ferrara, A. (2005). Thermal and Fragmentation Properties of Star-forming Clouds in Low-Metallicity Environments. *ApJ*, 626, 627–643.

Pacucci, F., Ferrara, A., Volonteri, M., & Dubus, G. (2015). Shining in the dark: the spectral evolution of the first black holes. *MNRAS*, 454, 3771–3777.

Pakmor, R., Bauer, A., & Springel, V. (2011). Magnetohydrodynamics on an unstructured moving grid. *MNRAS*, 418, 1392–1401.

Peebles, P. J. E. (1971). *Physical cosmology.*

Peebles, P. J. E. & Dicke, R. H. (1968). Origin of the Globular Star Clusters. *ApJ*, 154, 891.

Pelupessy, F. I., Di Matteo, T., & Ciardi, B. (2007). How Rapidly Do Supermassive Black Hole "Seeds" Grow at Early Times? *ApJ*, 665, 107–119.

Penston, M. V. (1969). Dynamics of self-gravitating gaseous spheres-III. Analytical results in the free-fall of isothermal cases. *MNRAS*, 144, 425.

Peters, T., Schleicher, D. R. G., Klessen, R. S., Banerjee, R., Federrath, C., Smith, R. J., & Sur, S. (2012). The Impact of Thermodynamics on Gravitational Collapse: Filament Formation and Magnetic Field Amplification. *ApJ*, 760, L28.

Peters, T., Schleicher, D. R. G., Smith, R. J., Schmidt, W., & Klessen, R. S. (2014). Low-metallicity star formation: relative impact of metals and magnetic fields. *MN-*

*RAS*, 442, 3112–3126.

Planck Collaboration, Ade, P. A. R., Aghanim, N., Armitage-Caplan, C., Arnaud, M., Ashdown, M., Atrio-Barandela, F., Aumont, J., Baccigalupi, C., Banday, A. J., & et al. (2014). Planck 2013 results. XVI. Cosmological parameters. *A&A*, 571, A16.

Planck Collaboration, Ade, P. A. R., Aghanim, N., Arnaud, M., Ashdown, M., Aumont, J., Baccigalupi, C., Banday, A. J., Barreiro, R. B., Bartlett, J. G., & et al. (2016). Planck 2015 results. XIII. Cosmological parameters. *A&A*, 594, A13.

Prieto, J., Jimenez, R., & Haiman, Z. (2013). Gas infall into atomic cooling haloes: on the formation of protogalactic discs and supermassive black holes at z $>$ 10. *MNRAS*, 436, 2301–2325.

Rees, M. J. (1976). Opacity-limited hierarchical fragmentation and the masses of protostars. *MNRAS*, 176, 483–486.

Rees, M. J. (1984). Black Hole Models for Active Galactic Nuclei. *ARA&A*, 22, 471–506.

Regan, J. A. & Downes, T. P. (2018). Fragmentation inside atomic cooling haloes exposed to Lyman-Werner radiation. *MNRAS*, 475, 4636–4647.

Regan, J. A. & Haehnelt, M. G. (2009). Pathways to massive black holes and compact star clusters in pre-galactic dark matter haloes with virial temperatures $>$ 10000K. *MNRAS*, 396, 343–353.

Regan, J. A., Johansson, P. H., & Haehnelt, M. G. (2014a). Numerical resolution effects on simulations of massive black hole seeds. *MNRAS*, 439, 1160–1175.

Regan, J. A., Johansson, P. H., & Wise, J. H. (2014b). The Direct Collapse of a Massive Black Hole Seed under the Influence of an Anisotropic Lyman-Werner Source. *ApJ*, 795, 137.

Ripamonti, E. & Abel, T. (2004). Fragmentation and the formation of primordial protostars: the possible role of collision-induced emission. *MNRAS*, 348, 1019–1034.

Ripamonti, E., Haardt, F., Ferrara, A., & Colpi, M. (2002). Radiation from the first forming stars. *MNRAS*, 334, 401–418.

Safranek-Shrader, C., Agarwal, M., Federrath, C., Dubey, A., Milosavljević, M., & Bromm, V. (2012). Star formation in the first galaxies - I. Collapse delayed by Lyman-Werner radiation. *MNRAS*, 426, 1159–1177.

Sakurai, Y., Hosokawa, T., Yoshida, N., & Yorke, H. W. (2015). Formation of primordial supermassive stars by burst accretion. *MNRAS*, 452, 755–764.

Sakurai, Y., Vorobyov, E. I., Hosokawa, T., Yoshida, N., Omukai, K., & Yorke, H. W. (2016). Supermassive star formation via episodic accretion: protostellar disc instability and radiative feedback efficiency. *MNRAS*, 459, 1137–1145.

Salvaterra, R., Della Valle, M., Campana, S., Chincarini, G., Covino, S., D'Avanzo, P., Fernández-Soto, A., Guidorzi, C., Mannucci, F., Margutti, R., Thöne, C. C., Antonelli, L. A., Barthelmy, S. D., de Pasquale, M., D'Elia, V., Fiore, F., Fugazza, D., Hunt, L. K., Maiorano, E., Marinoni, S., Marshall, F. E., Molinari, E., Nousek, J., Pian, E., Racusin, J. L., Stella, L., Amati, L., Andreuzzi, G., Cusumano, G., Fenimore, E. E., Ferrero, P., Giommi, P., Guetta, D., Holland, S. T., Hurley, K., Israel, G. L., Mao, J., Markwardt, C. B., Masetti, N., Pagani, C., Palazzi, E., Palmer, D. M., Piranomonte, S., Tagliaferri, G., & Testa, V. (2009). GRB090423 at a redshift of z~8.1. *Nat*, 461, 1258–1260.

Saslaw, W. C. & Zipoy, D. (1967). Molecular Hydrogen in Pre-galactic Gas Clouds. *Nat*, 216, 976–978.

Schleicher, D. R. G., Palla, F., Ferrara, A., Galli, D., & Latif, M. (2013). Massive black hole factories: Supermassive and quasi-star formation in primordial halos. *A&A*, 558, A59.

Schleicher, D. R. G., Spaans, M., & Glover, S. C. O. (2010). Black Hole Formation in Primordial Galaxies: Chemical and Radiative Conditions. *ApJ*, 712, L69–L72.

Schober, J., Schleicher, D., Federrath, C., Glover, S., Klessen, R. S., & Banerjee, R. (2012). The Small-scale Dynamo and Non-ideal Magnetohydrodynamics in Primordial Star Formation. *ApJ*, 754, 99.

Sesana, A., Gair, J., Berti, E., & Volonteri, M. (2011). Reconstructing the massive black hole cosmic history through gravitational waves. *Phys. Rev. D*, 83(4), 044036.

Shang, C., Bryan, G. L., & Haiman, Z. (2010). Supermassive black hole formation by

direct collapse: keeping protogalactic gas $H_2$ free in dark matter haloes with virial temperatures $T_{vir} \gtrsim 10^4$ K. *MNRAS*, 402, 1249–1262.

Shapiro, S. L. & Teukolsky, S. A. (1983). *Black holes, white dwarfs, and neutron stars: The physics of compact objects*.

Shlosman, I., Choi, J.-H., Begelman, M. C., & Nagamine, K. (2016). Supermassive black hole seed formation at high redshifts: long-term evolution of the direct collapse. *MNRAS*, 456, 500–511.

Shu, F. H. (1977). Self-similar collapse of isothermal spheres and star formation. *ApJ*, 214, 488–497.

Shu, F. H., Lizano, S., Galli, D., Cantó, J., & Laughlin, G. (2002). Self-similar Champagne Flows in H II Regions. *ApJ*, 580, 969–979.

Smith, A., Becerra, F., Bromm, V., & Hernquist, L. (2017a). Radiative effects during the assembly of direct collapse black holes. *MNRAS*, 472, 205–216.

Smith, A., Bromm, V., & Loeb, A. (2017b). The first supermassive black holes. *Astronomy and Geophysics*, 58(3), 3.22–3.26.

Smith, R. J., Glover, S. C. O., Clark, P. C., Greif, T., & Klessen, R. S. (2011). The effects of accretion luminosity upon fragmentation in the early universe. *MNRAS*, 414, 3633–3644.

Spaans, M. & Silk, J. (2006). Pregalactic Black Hole Formation with an Atomic Hydrogen Equation of State. *ApJ*, 652, 902–906.

Spergel, D. N., Verde, L., Peiris, H. V., Komatsu, E., Nolta, M. R., Bennett, C. L., Halpern, M., Hinshaw, G., Jarosik, N., Kogut, A., Limon, M., Meyer, S. S., Page, L., Tucker, G. S., Weiland, J. L., Wollack, E., & Wright, E. L. (2003). First-Year Wilkinson Microwave Anisotropy Probe (WMAP) Observations: Determination of Cosmological Parameters. *ApJS*, 148, 175–194.

Springel, V. (2010). E pur si muove: Galilean-invariant cosmological hydrodynamical simulations on a moving mesh. *MNRAS*, 401, 791–851.

Springel, V., White, S. D. M., Jenkins, A., Frenk, C. S., Yoshida, N., Gao, L., Navarro, J., Thacker, R., Croton, D., Helly, J., Peacock, J. A., Cole, S., Thomas,

P., Couchman, H., Evrard, A., Colberg, J., & Pearce, F. (2005). Simulations of the formation, evolution and clustering of galaxies and quasars. *Nat*, 435, 629–636.

Stacy, A., Bromm, V., & Lee, A. T. (2016). Building up the Population III initial mass function from cosmological initial conditions. *MNRAS*, 462, 1307–1328.

Stacy, A., Greif, T. H., & Bromm, V. (2010). The first stars: formation of binaries and small multiple systems. *MNRAS*, 403, 45–60.

Stacy, A., Greif, T. H., & Bromm, V. (2012). The first stars: mass growth under protostellar feedback. *MNRAS*, 422, 290–309.

Stacy, A., Greif, T. H., Klessen, R. S., Bromm, V., & Loeb, A. (2013). Rotation and internal structure of Population III protostars. *MNRAS*, 431, 1470–1486.

Stahler, S. W., Palla, F., & Salpeter, E. E. (1986). Primordial stellar evolution - The protostar phase. *ApJ*, 302, 590–605.

Sugimura, K., Omukai, K., & Inoue, A. K. (2014). The critical radiation intensity for direct collapse black hole formation: dependence on the radiation spectral shape. *MNRAS*, 445, 544–553.

Sur, S., Schleicher, D. R. G., Banerjee, R., Federrath, C., & Klessen, R. S. (2010). The Generation of Strong Magnetic Fields During the Formation of the First Stars. *ApJ*, 721, L134–L138.

Susa, H. (2013). The Mass of the First Stars. *ApJ*, 773, 185.

Susa, H., Hasegawa, K., & Tominaga, N. (2014). The Mass Spectrum of the First Stars. *ApJ*, 792, 32.

Tanvir, N. R., Fox, D. B., Levan, A. J., Berger, E., Wiersema, K., Fynbo, J. P. U., Cucchiara, A., Krühler, T., Gehrels, N., Bloom, J. S., Greiner, J., Evans, P. A., Rol, E., Olivares, F., Hjorth, J., Jakobsson, P., Farihi, J., Willingale, R., Starling, R. L. C., Cenko, S. B., Perley, D., Maund, J. R., Duke, J., Wijers, R. A. M. J., Adamson, A. J., Allan, A., Bremer, M. N., Burrows, D. N., Castro-Tirado, A. J., Cavanagh, B., de Ugarte Postigo, A., Dopita, M. A., Fatkhullin, T. A., Fruchter, A. S., Foley, R. J., Gorosabel, J., Kennea, J., Kerr, T., Klose, S., Krimm, H. A., Komarova, V. N., Kulkarni, S. R., Moskvitin, A. S., Mundell, C. G., Naylor, T., Page, K., Penprase, B. E., Perri, M., Podsiadlowski, P., Roth, K., Rutledge,

R. E., Sakamoto, T., Schady, P., Schmidt, B. P., Soderberg, A. M., Sollerman, J., Stephens, A. W., Stratta, G., Ukwatta, T. N., Watson, D., Westra, E., Wold, T., & Wolf, C. (2009). A $\gamma$-ray burst at a redshift of z~8.2. *Nat*, 461, 1254–1257.

Toomre, A. (1964). On the gravitational stability of a disk of stars. *ApJ*, 139, 1217–1238.

Truelove, J. K., Klein, R. I., McKee, C. F., Holliman, II, J. H., Howell, L. H., & Greenough, J. A. (1997). The Jeans Condition: A New Constraint on Spatial Resolution in Simulations of Isothermal Self-gravitational Hydrodynamics. *ApJ*, 489, L179.

Turk, M. J., Norman, M. L., & Abel, T. (2010). High-entropy Polar Regions Around the First Protostars. *ApJ*, 725, L140–L144.

Turk, M. J., Oishi, J. S., Abel, T., & Bryan, G. L. (2012). Magnetic Fields in Population III Star Formation. *ApJ*, 745, 154.

Turner, J., Kirby-Docken, K., & Dalgarno, A. (1977). The Quadrupole Vibration-Rotation Transition Probabilities of Molecular Hydrogen. *ApJS*, 35, 281.

Umeda, H., Hosokawa, T., Omukai, K., & Yoshida, N. (2016). The Final Fates of Accreting Supermassive Stars. *ApJ*, 830, L34.

Valiante, R., Agarwal, B., Habouzit, M., & Pezzulli, E. (2017). On the Formation of the First Quasars. *Publ. Astron. Soc. Australia*, 34, e031.

Valiante, R., Schneider, R., Zappacosta, L., Graziani, L., Pezzulli, E., & Volonteri, M. (2018). Chasing the observational signatures of seed black holes at z $>$ 7: candidate observability. *MNRAS*, 476, 407–420.

Van Borm, C., Bovino, S., Latif, M. A., Schleicher, D. R. G., Spaans, M., & Grassi, T. (2014). Effects of turbulence and rotation on protostar formation as a precursor of massive black holes. *A&A*, 572, A22.

Van Borm, C. & Spaans, M. (2013). The influence of magnetic fields, turbulence, and UV radiation on the formation of supermassive black holes. *A&A*, 553, L9.

Visbal, E., Haiman, Z., & Bryan, G. L. (2014). A no-go theorem for direct collapse black holes without a strong ultraviolet background. *MNRAS*, 442, L100–L104.

Volonteri, M. (2012). The Formation and Evolution of Massive Black Holes. *Science*, 337, 544.

Volonteri, M. & Begelman, M. C. (2010). Quasi-stars and the cosmic evolution of massive black holes. *MNRAS*, 409, 1022–1032.

Volonteri, M. & Bellovary, J. (2012). Black holes in the early Universe. *Reports on Progress in Physics*, 75(12), 124901.

Volonteri, M., Lodato, G., & Natarajan, P. (2008). The evolution of massive black hole seeds. *MNRAS*, 383, 1079–1088.

Volonteri, M. & Rees, M. J. (2005). Rapid Growth of High-Redshift Black Holes. *ApJ*, 633, 624–629.

Wang, F. Y., Bromm, V., Greif, T. H., Stacy, A., Dai, Z. G., Loeb, A., & Cheng, K. S. (2012). Probing Pre-galactic Metal Enrichment with High-redshift Gamma-Ray Bursts. *ApJ*, 760, 27.

Wang, H.-H., Klessen, R. S., Dullemond, C. P., van den Bosch, F. C., & Fuchs, B. (2010). Equilibrium initialization and stability of three-dimensional gas discs. *MNRAS*, 407, 705–720.

Wise, J. H. & Abel, T. (2007). Resolving the Formation of Protogalaxies. I. Virialization. *ApJ*, 665, 899–910.

Wise, J. H., Turk, M. J., & Abel, T. (2008). Resolving the Formation of Protogalaxies. II. Central Gravitational Collapse. *ApJ*, 682, 745–757.

Wolcott-Green, J. & Haiman, Z. (2012). Feedback from the infrared background in the early Universe. *MNRAS*, 425, L51–L55.

Wolcott-Green, J., Haiman, Z., & Bryan, G. L. (2011). Photodissociation of $H_2$ in protogalaxies: modelling self-shielding in three-dimensional simulations. *MNRAS*, 418, 838–852.

Woods, T. E., Heger, A., Whalen, D. J., Haemmerlé, L., & Klessen, R. S. (2017). On the Maximum Mass of Accreting Primordial Supermassive Stars. *ApJ*, 842, L6.

Wu, X.-B., Wang, F., Fan, X., Yi, W., Zuo, W., Bian, F., Jiang, L., McGreer, I. D.,

Wang, R., Yang, J., Yang, Q., Thompson, D., & Beletsky, Y. (2015). An ultraluminous quasar with a twelve-billion-solar-mass black hole at redshift 6.30. *Nat*, 518, 512–515.

Xu, H., O'Shea, B. W., Collins, D. C., Norman, M. L., Li, H., & Li, S. (2008). The Biermann Battery in Cosmological MHD Simulations of Population III Star Formation. *ApJ*, 688, L57–L60.

Yoshida, N., Omukai, K., & Hernquist, L. (2008). Protostar Formation in the Early Universe. *Science*, 321, 669–.

Yoshida, N., Omukai, K., Hernquist, L., & Abel, T. (2006). Formation of Primordial Stars in a ΛCDM Universe. *ApJ*, 652, 6–25.